FIRST INTERNATIONAL CONFERENCE ON ELECTRON MICROSCOPY OF NANOSTRUCTURES

ELMINA 2018

ПРВА МЕЂУНАРОДНА КОНФЕРЕНЦИЈА О ЕЛЕКТРОНСКОЈ МИКРОСКОПИЈИ НАНОСТРУКТУРА

САНУ

August 27-29, 2018, Belgrade, Serbia
27–29. август 2018. Београд, Србија

FIRST INTERNATIONAL CONFERENCE

ELMINA 2018

PROGRAM

&

BOOK OF ABSTRACTS

Rectorate of the University of Belgrade, Belgrade, Serbia
August 27-29, 2018
http://elmina.tmf.bg.ac.rs

Organized by:
Serbian Academy of Sciences and Arts and Faculty of Technology and Metallurgy, University of Belgrade

Endorsed by:
European Microscopy Society and Federation of European Materials Societies

FIRST INTERNATIONAL CONFERENCE
ELMINA 2018
Program and Book of Abstracts

Publisher:	Serbian Academy of Sciences and Arts Knez Mihailova 35, 11000 Belgrade, Serbia Phone: +381 11 2027200 https://www.sanu.ac.rs/en/
Editor:	Velimir R. Radmilović and Vuk V. Radmilović
Technical Editor:	Vuk V. Radmilović
Cover page:	Vuk V. Radmilović
Printed in:	Serbian Academy of Sciences and Arts Knez Mihailova 35, 11000 Belgrade, Serbia Phone: +381 11 2027128 stamparija@sanu.ac.rs
Circulation:	50 copies

ISBN 978-86-7025-785-6

At the beginning we wish you all welcome to Belgrade and ELMINA2018 International Conference organized by the Serbian Academy of Sciences and Arts and the Faculty of Technology and Metallurgy, University of Belgrade. We are delighted to have such a distinguished lineup of plenary speakers who have agreed to accept an invitation from the Serbian Academy of Sciences and Arts to come to the first in a series of electron microscopy conferences: Electron Microscopy of Nanostructures, ELMINA2018. We will consider making it an annual event in Belgrade, due to this year's overwhelming response of invited speakers and young researchers. The scope of ELMINA2018 will be focused on electron microscopy, which provides structural, chemical and electronic information at atomic scale, applied to nanoscience and nanotechnology (physics, chemistry, materials science, earth and life sciences), as well as advances in experimental and theoretical approaches, essential for interpretation of experimental data and research guidance. It will highlight recent progress in instrumentation, imaging and data analysis, large data set handling, as well as time and environment dependent processes. The scientific program contains the following topics:

- Instrumentation and New Methods
- Diffraction and Crystallography
- HRTEM and Electron Holography
- Analytical Microscopy (EDS and EELS)
- Nanoscience and Nanotechnology
- Life Sciences

To put this Conference in proper prospective, we would like to remind you that everything related to nanoscience and nanotechnology started 30 to 40 years ago as a long term objective, and even then it was obvious that transmission electron microscopy (TEM) must play an important role, as it was the only method capable of analyzing objects at the nanometer scale. The reason was very simple - at that time, an electron microscope was the only instrument capable of detecting the location of atoms, making it today possible to control synthesis of objects at the nanoscale with atomic precision. Electron microscopy is also one of the most important drivers of development and innovation in the fields of nanoscience and nanotechnology relevant for many areas of research such as biology, medicine, physics, chemistry, etc. We are very proud that a large number of contributions came from young researchers and students which was one of the most important objectives of ELMINA2018, and which indicates the importance of electron microscopy in various research fields. We are happy to present this book, comprising of the Conference program and abstracts, which will be presented at ELMINA2018 International Conference. We wish you all a wonderful and enjoyable stay in Belgrade.

TABLE OF CONTENTS

ORGANIZERS

SERBIAN ACADEMY OF SCIENCES AND ARTS

Knez Mihailova 35, 11000 Belgrade, Serbia

Phone: +381 11 2027200 / https://www.sanu.ac.rs/

FACULTY OF TECHNOLOGY AND METALLURGY, UNIVERSITY OF BELGRADE

Karnegijeva 4, 11000 Belgrade, Serbia

Phone: +381 11 3370425 / https://www.tmf.bg.ac.rs/

ELMINA 2018

CONFERENCE CHAIR

Velimir R. Radmilović

CONFERENCE MANAGER

Vuk V. Radmilović

INTERNATIONAL ADVISORY BOARD

Chair: Robert Sinclair (USA)

Members: Sara Bals (Belgium), Gianluigi Botton (Canada), Vladimir Bumbaširević (Serbia), Fu-Rong Chen (Taiwan), Vladica Cvetković (Serbia), Rafal Dunin-Borkowski (Germany), Rolf Erni (Switzerland), Hamish Fraser (USA), Ferdinand Hofer (Austria), Randi Holmestad (Norway), Đorđe Janaćković (Serbia), Wayne D. Kaplan (Israel), Vesna Lačković (Serbia), Joachim Mayer (Germany), Paul Midgley (UK), Eva Olsson (Sweden), Stephen Pennycook (Singapore), Dejan Popović (Serbia), Tamara Radetić (Serbia), Quentin Ramasse (UK), Frances Ross (USA), Etienne Snoeck (France), Erdmann Spiecker (Germany), Leposava Šiđanin (Serbia), Maria Varela del Arco (Spain), Johan Verbeeck (Belgium).

PROGRAM COMMITTEE

Chair: Velimir R. Radmilović (Serbia)

Members: Nataša Bibić (Serbia), Vladimir Bumbaširević (Serbia), Zoran Đurić (Serbia), Jasmina Grbović Novaković (Serbia), Aleksandra Korać (Serbia), Zoran Popović (Serbia).

ORGANIZING COMMITTEE

Chair: Petar Uskoković

Vice-chair: Zlatko Rakočević

Members: Anđelika Bjelajac, Vladan Ćosović, Ivana Cvijović-Alagić, Željko Kamberović, Smilja Marković, Nataša Nestorović, Irena Nikolić, Mirjana Novaković, Vladimir Pavlović, Vuk Radmilović, Dragan Rajnović, Milica Ševkušić, Đorđe Veljović.

TECHNICAL COMMITTEE

Chair: Đorđe Veljović

Members: Anđelika Bjelajac, Jovana Dimitrijević, Ivana Drvenica, Špiro Đurđević, Tamara Matić, Daniel Mijailović, Katarina Nešović, Vladimir Pavkov, Jelena Petrović, Anđela Radisavljević, Mia Radonjić, Željko Radovanović, Ivana Radović, Milena Stevanović.

GENERAL INFORMATION

DATE AND VENUE: The conference will be held August 27-29, 2018 at the Rectorate of the University of Belgrade, Studentski Trg 1, 11000 Belgrade, Serbia with the beginning at 8:30 AM on August 27th, 2018, in the Solemn Hall.

REGISTRATION: At the registration desk, located and the ground floor hall of the conference venue. Registration desk working hours are: Sunday, August 26th, from 16:00 to 18:00, Monday, August 27th, from 08:00 to 18:30, Tuesday, August 28th, from 08:00 to 13:00, Wednesday, August 29th, from 08:00 to 11:00. Registered participants will receive a nametag and a conference bag.

INSTRUCTIONS FOR AUTHORS: The conference will feature plenary sessions and poster sessions as well as vendor presentations during lunch breaks. Presentations during plenary sessions will last 30 minutes each, including discussion. Standard and hands-free microphones will be on site. No A-V equipment will be provided for any poster presentations. Poster presenters must remain at their poster on their assigned day during the required poster session. Each poster will be allocated a 130 cm high and 95 cm wide (130X95) display area.

CONFERENCE AWARDS: Poster presentations will be reviewed according to the following criteria: (a) relevance to a specific symposium, (b) scientific content, quality and innovative proposals, (c) clarity of the text, and (d) compliance with the format. During the conference, the best three (3) posters, selected by a poster award committee, will receive awards.

PROGRAM

First International Conference: "Electron Microscopy of Nanostructures", ELMINA 2018, August 27 – 29, Belgrade, SERBIA

Sunday, August 26, Ground Floor Hall

19:00-21:00	Welcome Reception for Invited Plenary Speakers

Monday, August 27, Main Lecture Hall

8:30-9:00	**Opening Ceremony** Velimir Radmilović, Conference Chair Vladimir Kostić, President of Serbian Academy of Sciences and Arts Vladimir Bumbaširević, Rector of Belgrade University Vladimir Popović, State secretary, Ministry of Education, Science and Technological Development Robert Sinclair, Chair of International Advisory Board
9:00	**Plenary Session 1** Chair: Robert Sinclair & Tamara Radetić
9:00-9:30	**Hannes Lichte:** "Electron Waves for Comprehensive Analysis of Structures and Fields in Solids"
9:30-10:00	**Rafal Dunin-Borkowski:** " Model-Based Iterative Reconstruction of Charge Density and Electric Field using Off-Axis Electron Holography "
10:00-10:30	**Fu-Rong Chen:** "Low Dose in-Line Electron Holography: Toward Revealing Atomic Resolution Dynamics for MoS_2 Nanoparticles and Soft Materials"
10:30-11:00	Coffee Break

11:00	**Plenary Session 2** Chair: Rafal Dunin-Borkowski & John Verbeeck
11:00-11:30	**Erdmann Spiecker:** "Scanning Transmission Electron Microscopy and Diffraction in SEM: Novel Approaches and Applications"
11:30-12:00	**Peter Denes:** "High-Speed Direct Electron Detection: Past, Present and Future"
12:00-12:30	**Gianluigi Botton:** "Applications of Direct Electron Detectors and Machine Learning with Neural Networks in Energy Loss Spectroscopy and Mapping"
12:30-14:00	Lunch Break
	Vendor Presentations Small Lecture Hall 8:
13:00-13:30	**Thermo Fisher Scientific:** Dominique Delille
13:30-13:45	**NanoMEGAS SPRL:** Stavros Nicolopoulos
14:00	**Plenary Session 3** Chair: Erdmann Spiecker & Peter Denes
14:00-14:30	**Stephen Pennycook:** "Materials Under the Microscope: the Atomic Origin of Functionality"
14:30-15:00	**David Bell:** "Advancing Topological Materials for Quantum Computing Applications with Electron Microscopy"
15:00-15:30	**Wayne D. Kaplan:** "Incoherent Interfaces: Strain, Adsorption, and Reconstruction"
15:30-16:00	**Laurence Marks:** "Profile Imaging: 35 years Old and Still Truckin"
16:00-16:30	Coffee Break
16:30	**Plenary Session 4** Chair: Stephen Pennycook & Wayne D. Kaplan
16:30-17:00	**Robert Sinclair:** “In Situ High Resolution and Transmission Environmental Electron Microscopy of Material Reactions”
17:00-17:30	**Tamara Radetić:** "Atomic Mechanisms of Grain Boundary Migration in Au Bicrystals"
17:30-18:00	**Wolfgang Jäger:** "Advanced and In Situ TEM of Functional Nanomaterials"
18:00-20:00	**Poster Session 1**

Tuesday, August 28, Main Lecture Hall

8:30	**Plenary Session 5** Chair: David Bell & Jürgen Plitzko
8:30-9:00	**Rolf Erni:** "Possibilities of Differential Phase Contrast STEM to Study Functional Oxides"
9:00-9:30	**Maria Varela del Arco:** "High Resolution STEM-EELS Mapping of Magnetic Quantities Across Oxide Multiferroic Interfaces"
9:30-10:00	**Miran Čeh:** "Microstructure Tailoring of Oxide Thermoelectrics to Increase the Figure of Merit (ZT) Value"
10:00-10:30	**Johan Verbeeck:** "The Road Towards a Versatile Programmable Phase Plate for Electrons"
10:30-11:00	Coffee Break
11:00	**Plenary Session 6** Chair: Maria Varela del Arco & Rolf Erni
11:00-11:30	**Kazu Suenaga:** "Single Atom Spectroscopy in Low-Dimensional Materials Using Low-voltage STEM"
11:30-12:00	**Ferdinand Hofer:** “Quantitative Electron Microscopy At Atomic Resolution”
12:00-12:30	**Jürgen Plitzko:** "Cryo-Electron Tomography - The Past, the Present and the Future"
12:30-14:00	Lunch Break
	Vendor Presentation Small Lecture Hall 8:
13:00-13:15	**JEOL-SCAN:** Guillaume Brunetti
14:00-16:00	**Poster Session 2**
19:00-22:00	Invited speakers boat tour and dinner

Wednesday, August 29, Main Lecture Hall

8:30	**Plenary Session 7** Chair: Kazu Suenaga & Wolfgang Jäger
8:30-9:00	**Paulo Ferreira:** "On the Degradation of PtNi Nanocatalysts for PEM Fuel Cells: An Identical Location Aberration-corrected TEM Study"
9:00-9:30	**Hamish Fraser:** "The Role of Structural Instabilities on Micro-structural Evolution in Metastable Beta Titanium Alloys"
9:30-10:00	**Jan Neethling:** "Applying Cs-corrected TEM/STEM to Long-standing Materials Science Problems"
10:00-10:30	Coffee Break
10:30	**Plenary Session 8** Chair: Hamish Fraser & Ferdinand Hofer
10:30-11:00	**Joachim Mayer:** PICO – Chromatic Aberration Correction and Applications in Materials Science
11:00-11:30	**Zoran Mišković:** " Theoretical Modeling of Electron Energy Loss Spectroscopy of Graphene: Comparing Ab initio Calculations and Empirical Models with Experiments "
11:30-12:00	**Dominique Delille:** "Sub-Å STEM Resolution From 30 to 300kV: Themis Z Opens a New Era for Ultra-high Resolution in Low kV Imaging and Analysis"
12:00-12:15	**Poster Awards & Closing Ceremony**

POSTER SESSION 1

Monday, August 27th, 2018, 18:00-20:00h

• PO1.1

Measuring and Controlling Out-of-Plane Shape of Free-Standing Two-Dimensional Materials

Ursula Ludacka, Mohammad R. A Monazam, Toma Susi, Christian Rentenberger, Jannik C. Meyer and Jani Kotakoski

Faculty of Physics, University of Vienna, Austria

• PO1.2

Structural Characterization of Organic and Perovskite Solar Cells

Vuk V. Radmilović[1], Yi Hou[2], Fei Guo[2], Christoph J. Brabec[2], Erdmann Spiecker[3], Velimir R. Radmilović[4,5]

[1]*Innovation Center, Faculty of Technology and Metallurgy, University of Belgrade, Karnegijeva 4, 11120 Belgrade, Serbia,* [2]*Institute of Materials for Electronics and Energy Technology (i-MEET), Friedrich-Alexander-University Erlangen-Nuremberg, Martensstrasse 7, 91058 Erlangen, Germany,* [3]*Center for Nanoanalysis and Electron Microscopy (CENEM), Friedrich-Alexander-University of Erlangen-Nuremberg, Cauerstrasse 6, 91058 Erlangen, Germany,* [4]*Faculty of Technology and Metallurgy, University of Belgrade, Karnegijeva 4, 11120 Belgrade, Serbia,* [5]*Serbian Academy of Sciences and Arts, Knez Mihailova 35, 11000 Belgrade, Serbia*

• PO1.3

Silicon Nanostructuring by Ag Ions Implantation Through Polystyrene Nanomask

Almedina Modrić-Šahbazović[1], Mirjana Novaković[2], Izet Gazdić[1], Nataša Bibić[2] and Zlatko Rakočević[2]

[1]*University of Tuzla, Faculty of Natural Sciences and Mathematics, 75000 Tuzla, BiH,* [2]*University of Belgrade, Institute of Nuclear Sciences Vinća, 11351 Belgrade, Serbia*

• PO1.4

XRD and HRTEM Study of Rutile Precipitates in Chrysoberyl Crystals

Aleksander Rečnik[1], Sandra Drev[2], Matjaž Mazaj[3] and Nina Daneu[4]

[1]*Department for Nanostructured Materials, Jožef Stefan Institute, Ljubljana, Slovenia,* [2]*Center for Electron Microscopy and Microanalysis, Jožef Stefan Institute, Ljubljana, Slovenia,* [3]*Laboratory for Inorganic Chemistry, National Institute of Chemistry, Ljubljana, Slovenia,* [4]*Advanced Materials Department, Jožef Stefan Institute, Ljubljana, Slovenia*

• **PO1.5**

Electrospun Hybrids of Carbon Nanofibers with Cobalt and Manganese Oxide Nanoparticles as High-Performance Electrodes for Supercapacitors

Daniel M. Mijailović[1], Uroš Č. Lačnjevac[2], Vuk V. Radmilović[1], Dušica B. Stojanović[3], Velimir R. Radmilović[3,4], Vladimir D. Jović[2], Petar S. Uskoković[3]

[1]Innovation Center, University of Belgrade, Faculty of Technology and Metallurgy, Karnegijeva 4, 11120, Belgrade, Serbia, [2]Institute for Multidisciplinary Research, University of Belgrade, Kneza Višeslava 1, 11030 Belgrade, Serbia, [3]University of Belgrade, Faculty of Technology and Metallurgy, Karnegijeva 4, 11120, Belgrade, Serbia, [4]Serbian Academy of Sciences and Arts, Knez Mihailova 35, 11000 Belgrade, Serbia

• **PO1.6**

Atomic Scale Investigations of 1D-2D Heterostructures

Kimmo Mustonen[1], Heena Inani[1], Viera Skakalova[1], Christoph Hofer[1], Mohammad R.A. Monazam[1], Toma Susi[1], Esko Kauppinen[2], Jannik C. Meyer[2] and Jani Kotakoski[1]

[1]Faculty of Physics, University of Vienna, Boltzmanngasse 5, A-1090 Vienna, Austria, [2]Department of Applied Physics, Aalto University School of Science, 15100, FI-00076 Aalto, Finland

• **PO1.7**

Solubility Limits and Micro-Structural Changes Induced by Ca Content in the $Ba_{1-x}Ca_xTiO_3$ Perovskite-Type Particles

Ionel F. Mercioniu[1], Marjeta Maček Kržmanc[2], Daniela Ghica[1], Adrian V. Maraloiu[1] and Ioana D. Vlaicu[1]

[1]National Institute of Materials Physics, Magurele-Ilfov, Romania, 1Advanced Materials Department, Jožef Stefan Institute, Ljubljana, Slovenia

• **PO1.8**

A Quantitative EDXS Analysis of Oxide Ceramic-Electrode Systems

Judith Lammer[1,2], Evelin Fisslthaler[1], Martina Dienstleder[1], Sebastian Rauch[1] and Werner Grogger[1,2]

[1]Graz Centre for Electron Microscopy, Steyrergasse 17, 8010 Graz, Austria, [2]Institute of Electron Microscopy and Nanoanalysis, Graz University of Technology, Steyrergasse 17, 8010 Graz, Austria

• **PO1.9**

Comprehensive Characterization of Multiferroic $BiFeO_3$ Powder Fabricated by the Hydrothermal Procedure

Maria Čebela[1], Radmila Hercigonja[2], Milena Rosić[1], Dejan Zagorac[1], Jelena Luković[1], Jelena Zagorac[1], Dragana Jordanov[1] and Branko Matović[1]

[1]Institute for Nuclear Sciences, Centre of Excellence-CextremeLab Vinca, University of Belgrade, Belgrade, Serbia, [2]University of Belgrade, Faculty of Physical Chemistry, Serbia

• **PO1.10**

The Effect of Particle Shape and Composition on the Electrochemical Behavior of Pt-based Nanostructured Catalysts for Fuel Cells

Mila N. Krstajić Pajić[1], Sanja I. Stevanović[2], Vuk V. Radmilović[3], Piotr Zabinski[4], Nevenka R. Elezović[5], Aleksandra Gavrilović-Wohlmutter[6], Velimir R. Radmilović[1,7], Snežana Lj. Gojković[1] and Vladislava M. Jovanović[2]

[1]Faculty of Technology and Metallurgy, University of Belgrade, Serbia, [2]Institute for Chemistry, Technology and Metallurgy, Department of Electrochemistry, University of Belgrade, Serbia, [3]Innovation Center, Faculty of Technology and Metallurgy, University of Belgrade, Serbia, [4]AGH University of Science and Technology, Faculty of Non-Ferrous Metals, Krakow, Poland, [5]Institute for Multidisciplinary Research, University of Belgrade, Serbia, [6]CEST Competence Center for Electrochemical Technologies, Vienna, Austria, [7]Serbian Academy of Sciences and Arts, Belgrade, Serbia

• **PO1.11**

Formation of Ag Nanoparticles in CrN by Using Ag Ion Implantation and Thermal Annealing

Mirjana Novaković[1], Maja Popović[1], Emanuel Schmidt[2], Philipp Schöppe[2], Miodrag Mitrić[1], Nataša Bibić[1], Carsten Ronning[2], Zlatko Rakočević[1]

[1]University of Belgrade, Institute of Nuclear Sciences VINČA, 11351, Belgrade, Serbia, [2]Institute of Solid State Physics, Friedrich Schiller University Jena, Max-Wien-Platz 1, D-07743, Jena, Germany

• **PO1.12**

Ion Implantation and Electron-beam Modification of Graphene

Mukesh Tripathi[1], Cong Su[2,3], Roman Böttger[4], Stefan Facsko[4], Ju Li[2], Juan-Carlos Idrobo[5], Jani Kotakoski[1] and Toma Susi[1]

[1]University of Vienna, Faculty of Physics, Vienna 1090, Austria, [2]Department of Nuclear and Materials Science and Engineering, Massachusetts Institute of Technology, Cambridge MA 02139, USA, [3]Research Lab of Electronics, Massachusetts Institute of Technology, Cambridge MA 02139, USA, [4]Helmholtz-Zentrum Dresden-Rossendorf, Institute of Ion Beam Physics and Materials Research, 01314 Dresden, Germany, [5]Center for Nanophase Materials Sciences, Oak Ridge National Laboratory, Oak Ridge TN 37831, USA

• **PO1.13**

Advanced TEM Characterization of Interfaces and Strain-Related Distortions in Epitaxial Perovskite Heterostructures

Raluca F. Negrea and Corneliu Ghica

National Institute of Materials Physics, Magurele, Romania

• **PO1.14**

ABF-STEM Investigations of Taaffeite $Be_xMg_yAl_{2(x+y)}O_{4(x+y)}$ Structures

Sandra Drev[1], Aleksander Rečnik[2], Matej Komelj[2], Christian Gspan[3], Goran Dražić[4], Vesna Šrot[5], Miran Čeh[1,2], Ferdinand Hofer[3], Peter A. van Aken[5], Nina Daneu[2]

[1]Center for Electron Microscopy and Microanalysis, Ljubljana, Slovenia, [2]Department for Nanostructured Materials, Jožef Stefan Institute, Ljubljana, Slovenia & Jožef Stefan International Postgraduate School, Ljubljana, Slovenia, [3]Institute for Electron Microscopy and Nanoanalysis, Graz University of Technology, Graz, Austria [4]Laboratory for Materials Chemistry, Institute of Chemistry, Ljubljana, Slovenia, [5]Stuttgart Center for Electron Microscopy, Max Planck Institute for Solid State Research, Stuttgart, Germany

• **PO1.15**

Temperature Dependent Quasimolten Crystallinity of Sub-nm Pt and Au Clusters Observed in 3D by Fast Dynamic STEM

Trond Henninen, Marta Bon, Daniele Passerone, Rolf Erni

Empa, Swiss Federal Laboratories for Materials Science and Technology, CH-8600 Dübendorf, Switzerland

• **PO1.16**

Efficient First Principles Simulation of Electron Scattering Factors for Transmission Electron Microscopy

Toma Susi[1], Jacob Madsen[2], Ursula Ludacka[1], Jens J. Mortensen[2], Timothy J. Pennycook[1,3], Zhongbo Lee[4], Jani Kotakoski[1], Ute Kaiser[4] and Jannik C. Meyer[1]

[1]University of Vienna, Faculty of Physics, 1090 Vienna, Austria, [2]Technical University of Denmark, Department of Physics, Kgs. Lyngby, Denmark, 3Max Planck Institute for Solid State Research, Center for Electron Microscopy, Stuttgart, Germany, [4]Ulm University, Electron Microscopy Group of Materials Sciences, Ulm, Germany

• **PO1.17**

HRTEM and HAADF–STEM Study of Translation States and Cation Ordering on Basal Plane Inversion Boundaries in ZnO with III+, VI+ and V+ Dopants

Vesna Ribić[1], Aleksander Rečnik[2], Goran Dražić[3], Zorica Branković[1], Goran Branković[1] and Nina Daneu[4]

[1]Institute for Multidisciplinary Research, University of Belgrade, Belgrade, Serbia, [2]Department for Nanostructured Materials, Jožef Stefan Institute, Ljubljana, Slovenia, [3]Department of Materials Chemistry, National Institute of Chemistry, Ljubljana, Slovenia, [4]Advanced Materials Department, Jožef Stefan Institute, Ljubljana, Slovenia

• **PO1.18**

Study of Ge and SiGe Nanoparticles Formed by RTA and Laser Pulse Annealing of SiGeO Amorphous Films Obtained by RF Sputtering

Valentin S. Teodorescu[1], Adrian V. Maraloiu[1], Corneliu Ghica[1], Andrei Kuncser[1],

Ionel Stavarache[1], Ana-Maria Lepadatu[1], Magdalena L. Ciurea[1], Nicu D. Scarisoreanu[2], Andreea Andrei[2] and Maria Dinescu[2]
[1]National Institute for Materials Physics, Bucharest-Magurele, Romania, [2]National Institute for Lasers, Plasma and Radiation, Bucharest-Magurele, Romania

• **PO1.19**

Study of Structural Defects in $Ga_{2-x}Fe_xO_3$ Thin Layers

Corinne Bouillet[1], Xavier Devaux[2], Anna Demchenko[1], Christophe Lefevre[1], François Roulland[1], Nathalie Viart[1]
[1]Institut de Physique et Chimie des Matériaux de Strasbourg (IPCMS), UMR 7504 CNRS, Université de Strasbourg, 23 rue du Læss BP 43, 67034 Strasbourg, France, [2]Institut Jean Lamour, UMR 7198 CNRS-Université de Lorraine, Campus ARTEM 2, allée André Guinier, BP 50840 F54011 NANCY Cedex, France

• **PO1.20**

Analysis of Coatings With Scented Microcapsules

Rastko Milošević[1], Nemanja Kašiković[1], Živko Pavlović[1], Urška Stanković Elesini[2], Tomislav Cigula[3] and Raša Urbas[2]
[1]University of Novi Sad, Faculty of Technical Sciences, Department of Graphic Engineering and Design, Novi Sad, Serbia, [2]University of Ljubljana, Faculty of Natural Sciences and Engineering, Department of Textiles, Graphic Arts and Design, Ljubljana, Slovenia, [3]University of Zagreb, Faculty of Graphic Arts, Department of Printing Plates, Zagreb, Croatia

• **PO1.21**

Potentials, Implementation and Perspectives of Atomic Force Microscopy for Characterization of Drug Delivery Nanosystems

Ines Nikolic[1], Danijela Randjelovic[2], Snezana Savic[1]
[1]University of Belgrade, Faculty of Pharmacy, Department of Pharmaceutical Technology and Cosmetology, Belgrade, Serbia, [2]University of Belgrade, Institute of Chemistry, Technology and Metallurgy, Department of Microelectronic Technologies, Belgrade, Serbia

• **PO1.22**

Epitaxial Growth of Metastable (P–type) Al–Mn–Si Quasicrystal from the Stable (F–type) Al–Cu-Fe Quasicrystalline Surface

Blaž Leskovar[1], Sašo Šturm[2], Zoran Samardžija[2], Bojan Ambrožič[2], Boštjan Markoli[1], Iztok Naglič[1]
[1]University of Ljubljana, Faculty of Natural Sciences and Engineering, Department of Materials and Metallurgy, Aškerčeva cesta 12, 1000 Ljubljana, Slovenia, [2]Jožef Stefan Institute, Department for Nanostructured Materials, Jamova cesta 39, 1000 Ljubljana, Slovenia

• **PO1.23**

Morphology and Structure of TiO_2 Thin Films and Nanostructures Deposited on ZnO Nanorods for Photovoltaic Application

Andreja Gajović[1], Ivana Panžić[1], Krunoslav Juraić[1], Nikša Krstulović[2], Domagoj Belić[1], Milivoj Plodinec[1,3], Davor Gracin[1], Ana Šantić[1], Marc Gregor Willinger[3]

[1]Ruđer Bošković Institute, Bijenička 54, 10000 Zagreb, Croatia, [2]Instutute of Physics, Zagreb, Croatia, [3]Fritz Haber Institute of Max Planck Society, Berlin, Germany

• **PO1.24**

Mapping Twins in B_4C using ASTAR Electron Precession System on Transmission Electron Microscope

Andrei C. Kuncser[1], Corneliu Ghica[1], Ionel Mercioniu[1], Oleg Vasylkiv[2] and Petre Badica[3]

[1]National Institute of Materials Physics, Laboratory of Atomic Structures and Defects in Advanced Materials, Magurele, Romania, [2]National Institute of Materials Science, Tsukuba, Ibaraki, Japan, [3]National Institute of Materials Physics, Laboratory of Magnetism and Superconductivity, Magurele, Romania

• **PO1.25**

Influence of Zr Concentration on the Morphology and Structure of $BaTi_{1-y}Zr_yO_3$ Particles

Valentin A. Maraloiu[1], Ioana D. Vlaicu[1], Marjeta M. Maček Kržmanc[2], Ionel Mercioniu[1] and Daniela Ghica[1]

[1]National Institute of Materials Physics, 405A Atomistilor Str., 077125 Magurele-Ilfov, Romania, [2]Advanced Materials Department, Jožef Stefan Institute, Jamova cesta 39, Ljubljana 1000, Slovenia

• **PO1.26**

From Titania to Titanates: Phase and Morphological Transition

Bojana Simović[1], Aleksandra Dapčević[2], Jelena Zdravković[3], Jugoslav Krstić[4] and Goran Branković[1]

[1]Institute for Multidisciplinary Research, University of Belgrade, Belgrade, Serbia, [2]Faculty of Technology and Metallurgy, University of Belgrade, Belgrade, Serbia, [3]Innovation Centre Faculty of Technology and Metallurgy, University of Belgrade, Belgrade, Serbia, [4]Institute of Chemistry, Technology and Metallurgy, Department of Catalysis and Chemical Engineering, University of Belgrade, Belgrade, Serbia

• **PO1.27**

Sunlight-driven Photocatalytic and Photo-electrochemical Activity of ZnO/SnO_2 Composite

Smilja Marković[1], Ivana Stojković Simatović[2], Ana Stanković[1], Srečo Škapin[3], Lidija Mančić[1], Slavko Mentus[2,4] and Dragan Uskoković[1]

[1]Institute of Technical Sciences of SASA, Belgrade, Serbia, [2]University of Belgrade,

Faculty of Physical Chemistry, Belgrade, Serbia, [3]Institute Jožef Stefan, Ljubljana, Slovenia, [4]Serbian Academy of Sciences and Arts, Knez Mihajlova 35, 11000 Belgrade, Serbia

• **PO1.28**

Synthesis and Characterization of $Na_{0.4}MnO_2$ as a Positive Electrode Material for an Aqueous Electrolyte Sodium-ion Energy Storage Device

Lazar Rakočević[1], Mirjana Novaković[2], Jelena Potočnik[2], Dragana Jugović[3] and Ivana Stojković Simatović[1]

[1]University of Belgrade, Faculty of Physical Chemistry, Belgrade, Serbia, [2]University of Belgrade, Vinča Institute of Nuclear Sciences, Serbia, [3]Institute of Technical Sciences of SASA, Belgrade, Serbia

• **PO1.29**

Metal Nanoparticles-PANI Nanocomposites and their Applications

Una Stamenović[1], Vesna Vodnik[1] and Mojca Otoničar[2]

[1]Vinča Institute of Nuclear Sciences, University of Belgrade, P. O. Box 522, 11001 Belgrade, Serbia, [2]Jožef Štefan Institute, Department of Advanced Materials, Jamova 39, 1000 Ljubljana, Slovenia

• **PO1.30**

Morphology of Nanotubular Oxide Layer Formation on Titanium and Titanium Alloy Using Electrochemical Anodization

Dragana R. Barjaktarević[1], Ivana D. Dimić[1], Ivana Lj. Cvijović-Alagić[2], Veljko R. Đokić[1] and Marko P. Rakin[1]

[1]Faculty of Technology and Metallurgy, University of Belgrade, Karnegijeva 4 11120 Belgrade, Serbia, [2]Institute of Nuclear Sciences "Vinča", University of Belgrade, P.O. Box 522, 11001, Belgrade, Serbia

• **PO1.31**

Depth Analysis of Thin Films Using StrataGem Program

Jelena Potočnik, Maja Popović, Mirjana Novaković, Davor Peruško, Zlatko Rakočević

University of Belgrade, INN Vinča, Mike Petrovića Alasa 12-14, 11351 Belgrade, Serbia

• **PO1.32**

Improvement of Density and Influence of Sb Doping on Structural Properties of Perovskite $BaSnO_3$

Jelena Vukašinović[1], Milica Počuča-Nešić[1], Danijela Luković Golić[1], Slavica M. Savić[2], Zorica Branković[1], Nikola Tasić[1], Aleksandra Dapčević[3], Slavko Bernik[4], Matej Kocen[4] and Goran Branković[1]

[1]Institute for Multidisciplinary Research, University of Belgrade, Belgrade, Serbia, [2]Biosense Institute, University of Novi Sad, Novi Sad, Serbia, [3]Faculty of Technology and Metallurgy, University of Belgrade, Belgrade, Serbia, [4]Jožef Stefan Institute, Ljubljana, Slovenia

• **PO1.33**

Perovskite Thin Films in Tunable Microwave Technologies

Jelena Vukmirovic[1], Elvira Djurdjic[2], Andrea Nesterovic[1], Ante Bilusic[3], Zeljka Cvejic[2] and Vladimir V. Srdic[1]

[1]Department of Materials Engineering, Faculty of Technology, Novi Sad, Serbia, [2]Department of Physics, Faculty of Sciences, Novi Sad, Serbia, [3]Department of Physics, Faculty of Science, University of Split, Croatia

• **PO1.34**

Synthesis, Structure, Morphology and Properties of Biphasic ZnO–$ZnMn_2O_4$

Lidija Radovanović[1], Predrag Vulić[2], Željko Radovanović[1], Bojana Balanč[1], Bojana Simović[3], Ivana Zeković[4], Miroslav Dramićanin[4] and Jelena Rogan[5]

[1]Innovation Center of the Faculty of Technology and Metallurgy, University of Belgrade, Belgrade, Serbia, [2]Faculty of Mining and Geology, Department of Crystallography, Petrology and Geochemistry, University of Belgrade, Belgrade, Serbia, [3]Institute for Multidisciplinary Research, University of Belgrade, Belgrade, Serbia, [4]Vinča Institute of Nuclear Sciences, University of Belgrade, Belgrade, Serbia, [5]Faculty of Technology and Metallurgy, Department of General and Inorganic Chemistry, University of Belgrade, Belgrade, Serbia

POSTER SESSION 2

Tuesday, August 28th, 2018, 14:00-16:00h

• PO2.1

Electron Microscopy Characterization of TiO_2 Nanotubes Sensitized with CdS Quantum Dots

Andjelika Bjelajac[1], Rada Petrović[2], Veljko Djokic[2], Kassioge Dembele[3], Simona Moldovan[3,4], Ovidiu Ersen[3], Gabriel Socol[5], Ion N. Mihailescu[5], Djordje Janaćković[2]
[1]University of Belgrade, Innovation center of Faculty of Technology and Metallurgy, Karnegijeva 4, 11000 Belgrade, Serbia, [2]University of Belgrade, Faculty of Technology and Metallurgy, Karnegijeva 4, 11000 Belgrade, Serbia, [3]Institut de Physique et Chimie des Materiaux de Strasbourg, UMR 7504CNRS - Université de Strasbourg, 23 rue du Loess, BP 43, 67037 Strasbourg cedex 02, France, [4]Groupe de Physique des Matériaux UMR CNRS 6634, Université de Rouen, INSA Rouen, Avenue de l'Université – BP12, 76801 Saint Etienne du Rouvray, France, [5]National Institute for Lasers, Plasma, and Radiation Physics, Lasers Department, "Laser-Surface-Plasma Interactions" Laboratory, PO Box MG-54, RO- 77125, Magurele, Ilfov, Romania

• PO2.2

Cathodically Protonated TiO_2 Nanotube Arrays Decorated with Pd Nanoparticles as Highly Efficient and Stable Electrocatalysts for the Hydrogen Evolution Reaction

Uroš Lačnjevac[1], Rastko Vasilić[2], Tomasz Tokarski[3], Grzegorz Cios[3], Piotr Żabiński[4], Nevenka Elezović[1] and Nedeljko Krstajić[5†]
[1]Institute for Multidisciplinary Research, University of Belgrade, Kneza Višeslava 1, 11030 Belgrade, Serbia, [2]Faculty of Physics, University of Belgrade, Studentski trg 12-16, 11000 Belgrade, Serbia, [3]Academic Centre for Materials and Nanotechnology, AGH University of Science and Technology, al. A. Mickiewicza 30, 30-059 Krakow, Poland, [4]Faculty of Non-Ferrous Metals, AGH University of Science and Technology, al. A. Mickiewicza 30, 30-059 Krakow, Poland, [5]Faculty of Technology and Metallurgy, University of Belgrade, Karnegijeva 4, 11000 Belgrade, Serbia

• PO2.3

Elemental Mapping in (Alpha2/O)-Phase Lamellae of a Gamma-TiAl Alloy

Heike Gabrisch[1], Tobias Krekeler[2], Uwe Lorenz[1], Marcus Willi Rackel[1], Martin Ritter[1], Florian Pyczak[1] and Andreas Stark[1]
[1]Helmholtz-Zentrum Geesthacht, Department of Metal Physics, Max-Planck-Str.1, 21502 Geesthacht, Germany, [2]Technische Universität Hamburg, Betriebseinheit Elektronenmikroskopie BEEM, Eißendorfer Straße 42, 21073 Hamburg, Germany

• **PO2.4**

Various Structures of ZnO Grown by Vapor - Liquid - Solid Method

Danilo D. Kisić, Miloš T. Nenadović, Jelena M. Potočnik and Zlatko Lj. Rakočević
University of Belgrade, Vinča Institute of Nuclear Sciences, Laboratory of Atomic Physics, Belgrade, Serbia

• **PO2.5**

Influence of Generation Time on Optical Properties of Gold Nanoparticles

Nataša Nastić, Jaroslava Švarc-Gajić and Zorica Stojanović
Department of Applied and Engineering Chemistry, Faculty of Technology, University of Novi Sad, Novi Sad, Serbia

• **PO2.6**

Problems in Obtaining High-Density, Pure-Phase $BiFeO_3$ Ceramics

Nikola I. Ilić, Jelena D. Bobić, Adis S. Džunuzović, Mirjana M. Vijatović Petrović and Biljana D. Stojanović
Institute for Multidisciplinary Research, University of Belgrade, Materials Science Department, Belgrade, Serbia

• **PO2.7**

Synthesis, Calcination and Characterization of $CoMoO_4$ Nanopowders by GNP Method

Milena Rosić[1], Dejan Zagorac[1], Maria Čebela[1], Dragana Jordanov[1], Jelena Zagorac[1], Jelena Luković[1], Aleksandra Zarubica[2] and Branko Matović[1]
[1]Institute for Nuclear Sciences, Centre of Excellence-CextremeLab Vinca, University of Belgrade, Belgrade, Serbia, [2]Department of Chemistry, Faculty of Science and Mathematics, University of Niš, Višegradska 33, 18000 Niš, Serbia

• **PO2.8**

Polyacrilic Acid and Chitosan Assisted Solvothermal Synthesis of Up-converting $NaYF_4$: Yb,Er Particles

Marina Vuković[1], Ivana Dinić[1], Lidija Mančić[2], Marko Nikolić[3], Mihailo Rabasović[3] and Olivera Milošević[2]
[1]Innovation Center of the Faculty of Chemistry, University of Belgrade, Serbia, [2]Institute of Technical Sciences of SASA, Belgrade, Serbia, [3]Photonic Center, Institute of Physics Belgrade, University of Belgrade, Belgrade, Serbia

• **PO2.9**

Alkali Activated Slag as Adsorbents for Cu^{2+} Removal from Wastewaters

Irena Nikolić[1,2], Dijana Đurović[2], Ivana Milašević[2], Smilja Marković[3], Ljiljana Veselinović[3], Vuk V. Radmilović[4], Ivona Janković-Častvan[5], Velimir R. Radmilović[5,6]
[1]University of Montenegro, Faculty of Metallurgy and Technology, Podgorica, Montenegro, [2]Institute of Public Health of Montenegro, Podgorica, Montenegro, [3]Institute of Technical Sciences of SASA, Belgrade, Serbia, [4]Innovation Centre, Faculty

of Technology and Metallurgy, University of Belgrade, Belgrade, Serbia, [6]Faculty of Technology and Metallurgy, University of Belgrade, Belgrade, Serbia, [7]Serbian Academy of Sciences and Arts, Belgrade, Serbia

• **PO2.10**

Nanostructured Boehmite Powders as Efficient Absorbent in Water Treatments

Marija Milanović[1], Ivan Stijepović[1], Vesna Vasić[2], Dragana Kukić[2], Marina Šćiban[2]

[1]University of Novi Sad, Faculty of Technology, Department of Materials Engineering, Bulevar cara Lazara 1, 21000 Novi Sad, Serbia, [2]University of Novi Sad, Faculty of Technology, Department of Biotechnology and Pharmaceutical Engineering, Bulevar cara Lazara 1, 21000 Novi Sad, Serbia

• **PO2.11**

The Effect of Alkaline Activator Molarity and Aging Time on the Structure of Inorganic Polymer

Marija Ivanović[1], Ljiljana Kljajević[1], Jelena Gulicovski[1], Bratislav Todorović[2], Adela Egelja[1], Vladimir Pavlović[3] and Snežana Nenadović[1]

[1]Institute of Nuclear Sciences Vinča, Department of Materials Science, University of Belgrade, Serbia, [2]Faculty of Technology of Leskovac, University of Niš, Serbia, [3]Institute of Technical Sciences of the Serbian Academy of Sciences and Arts, Knez Mihailova 35/IV, University of Belgrade, 11000 Belgrade, Serbia

• **PO2.12**

SEM-EDS and AFM Study of a Novel Magnetic Polymer/Bentonite Nanocomposite

Bojana M. Marković[1], Ivan S. Stefanović[1], Jasna V. Džunuzović[1], Danijela V. Ranđelović[1], Bojan Kostić[2], Aleksandra B. Nastasović[1]

[1]University of Belgrade, Institute of Chemistry, Technology and Metallurgy, Njegoševa 12, Belgrade, Serbia, [2]University of Belgrade, Faculty of Mining and Geology, Đušina 7, 11000 Belgrade, Serbia

• **PO2.13**

Ultra-fine Grained Structure and Fracture Mode in Low Carbon Steel Subjected to Severe Plastic Deformation

Marko Vilotić, Leposava Šidjanin and Dragan Rajnović

Department of Production Engineering, Faculty of Technical Sciences, University of Novi Sad, Novi Sad, Serbia

• **PO2.14**

Microstructure of Nanolayered CrAlN/TiSiN Coating

Aleksandar Miletić[1], Peter Panjan[2], Miha Čekada[2], Lazar Kovačević[1], Pal Terek[1] and Branko Škorić[1]

[1]Faculty of Technical Sciences, University of Novi Sad, Novi Sad, Serbia, [2]Jožef Stefan Institute, Ljubljana, Slovenia

• **PO2.15**

Synthesis and Characterization of $MnCo_2O_4$ Porous Spinel Oxide

Vesna Antunović[1], Dijana Jelić[1], Zoran Nedić[2], Marija Ilić[3], Aleksandar Lolić[4]

[1]Department of Pharmacy, Faculty of Medicine, University of Banja Luka, Banja Luka, Bosnia and Herzegovina, [2]Faculty of Physical Chemistry, University of Belgrade, Belgrade, Serbia, [3]Faculty of Mining and Geology, University of Belgrade, Belgrade, Serbia, [4]Faculty of Chemistry, University of Belgrade, Belgrade, Serbia

• **PO2.16**

Fabrication of $NiFe_2O_4$ Nanofibers/Net Via Combined Sol-Gel and Electrospinning Method

Aleksandar Grujić[1], Vladan Ćosović[1], Jasna Stajić-Trošić[1], Aleksandar Ćosović[2], Mirko Stijepović[2] and Tomáš Žák[3]

[1]Institute of Chemistry, Technology and Metallurgy, University of Belgrade, Belgrade, Serbia, [2]Faculty of Technology and Metallurgy, University of Belgrade, Belgrade, Serbia, [3]Institute of Physics of Materials of the Czech Academy of Sciences, Brno, Czech Republic

• **PO2.17**

TiO_2 Nanoparticle Deposition on Solid CP-Ti Substrate through Spraying Water Colloid in the Arc Plasma

Vladimir Pavkov[1], Milovan M. Stoiljković[2], Vesna M. Maksimović[1], Ivana Lj. Cvijović-Alagić[1], Jovan Ciganović[2] and Mila R. Vranješ[3]

[1]Laboratory of Material Science, Vinča Institute of Nuclear Sciences, University of Belgrade, Belgrade, Serbia, [2]Laboratory of Physical Chemistry, Vinča Institute of Nuclear Sciences, University of Belgrade, Belgrade, Serbia, [3]Laboratory of Radiation Chemistry and Physics-Gamma, Vinča Institute of Nuclear Sciences, University of Belgrade, Belgrade, Serbia

• **PO2.18**

Bioactive Hydroxyapatite/Chitosan/Gentamicin Composite Coating Electrodeposited on Titanium

Milena Stevanović[1], Marija Đošić[2], Ana Janković[1], Maja Vukašinović-Sekulić[3], Vesna Kojić[4] and Vesna Mišković-Stanković[3]

[1]Innovation center of Faculty of Technology and Metallurgy, Karnegijeva 4, Belgrade, Serbia, [2]Institute for Technology of Nuclear and Other Mineral Raw Materials, Bulevar Franš d'Eperea 86, Belgrade, Serbia, [3]Faculty of Technology and Metallurgy, University of Belgrade, Karnegijeva 4, Belgrade, Serbia, [4]Faculty of Medicine, Oncology Institute of Vojvodina, University of Novi Sad, Dr Goldmana 4, Sremska Kamenica, Serbia

• **PO2.19**

Electrochemical Deposition of Ni in the Liquid Cell: Groundwork Experimental Approach Prior to LC TEM Experiments

Maja Koblar[1,3], Kristina Žužek Rožman[2], Sašo Šturm[3], Miran Čeh[1,2]

[1]Center for Electron Microscopy and Microanalysis (CEMM), Jožef Stefan Institute, Jamova 39, 1000 Ljubljana, Slovenia, [2]Department for Nanostructured Materials (K7), Jožef Stefan Institute, Jamova 39, 1000 Ljubljana, Slovenia, [3]Jožef Stefan International Postgraduate School, Jamova 39, 1000 Ljubljana, Slovenia

• **PO2.20**

Characterization Of Composite Polymer Membranes Modified By Electrospinning Method

Lana Putić[1], Jasna Stajić-Trošić[1], Branka Pilić[2], Vladan Ćosović[1], Aleksandar Grujić[1]

[1]Institute of Chemistry, Technology and Metallurgy, University of Belgrade, Belgrade, Serbia, [2]Faculty of Technology, University of Novi Sad, Novi Sad, Serbia

• **PO2.21**

Morphology of Poly(urethane-siloxane)/Montmorillonite Nanocomposites

Ivan S. Stefanović, Bojana M. Marković, Aleksandra B. Nastasović, Marija V. Pergal and Jasna V. Džunuzović

Institute of Chemistry, Technology and Metallurgy, Center of Chemistry, University of Belgrade, Njegoševa 12, 11000 Belgrade, Serbia

• **PO2.22**

Morphology, Biocompatibility and Antimicrobial Activity of Hydroxyapatite Simultaneously Doped with Silver and Strontium Ions

Djordje Veljovic[1], Zeljko Radovanovic[1], Suzana Dimitrijevic-Brankovic[1], Vesna Kojic[2], Rada Petrovic[1] and Djordje Janackovic[1]

[1]University of Belgrade, Faculty of Technology and Metallurgy, Department of Inorganic Chemical Technology, Karnegijeva 4, 11120 Belgrade, Serbia, [2]University of Novi Sad, Faculty of Medicine, Oncology Institute of Vojvodina, Put Dr Goldmana 4, 21204 Sremska Kamenica, Serbia

• **PO2.23**

Nanocomposite Hydrogels Based on Poly(vinyl alcohol) and Chitosan with Silver Nanoparticles and Graphene Aimed for Wound Dressing Applications

Katarina Nešović[1], Ana Janković[1], Maja Vukašinović-Sekulić[2], Aleksandra Perić-Grujić[2] and Vesna Mišković-Stanković[2]

[1]Innovation center of the Faculty of Technology and Metallurgy, Karnegijeva 4, Belgrade, Serbia, [2]Faculty of Technology and Metallurgy, University of Belgrade, Karnegijeva 4, Belgrade, Serbia

• **PO2.24**

Bacteria-Based Self-Healing System for Concrete Structures

Snežana Vučetić[1], Andrijana Sever Škapin[2], John M. van der Bergh[2], Bojan Miljević[1], Ivan Ristić[1], Siniša Markov[3], Ana Vidaković[3], Olja Šovljanski[3] and Jonjaua Ranogajec[1]

[1]University of Novi Sad, Faculty of Technology, Dept. of Materials Engineering, Novi Sad, Serbia, [2]Slovenian National Building and Civil Engineering Institute, Ljubljana, Slovenia, [3]University of Novi Sad, Faculty of Technology, Dept. of Biotechnology and Pharmaceutical Engineering, Novi Sad, Serbia

• **PO2.25**

Processing and Characterization of Hydroxyapatite/tricalcium Phosphate Biomaterials for Obtaining Scaffolds

Željko Radovanović[1], Saša Vasilijić[2], Djordje Veljović[3], Ivona Janković-Častvan[3], Slavica Lazarević[3], Rada Petrović[3], Djordje Janaćković[3]

[1]University of Belgrade, Innovation Center of the Faculty of Technology and Metallurgy, Karnegijeva 4, Belgrade 11070, Serbia, [2]University of Defense, Institute for Medical Research Military Medical Academy, Faculty of Medicine of Military Medical Academy, Crnotravska 17, Belgrade 11000, Serbia, [3]University of Belgrade, Faculty of Technology and Metallurgy, Karnegijeva 4, Belgrade 11070, Serbia

• **PO2.26**

Synthesis of Phosphate Based Bioactive Glass-ceramics Scaffolds

Vladimir S. Topalović[1], Srđan D. Matijašević[1], Jelena D. Nikolić[1], Marija S. Đošić[1], Veljko V. Savić[1], Sonja V. Smiljanić[2], Snežana R. Grujić[2]

[1]Institute for the Technology of Nuclear and Other Mineral Raw Materials, 86 Franchet d' Esperey St, 11000 Belgrade, Serbia, [2]Faculty of Technology and Metallurgy, University of Belgrade, Karnegijeva 4, 11000 Belgrade, Serbia

• **PO2.27**

Assessment of Three Microscopic Techniques in Observing Morphology of Pygidial Glands of Ground Beetles

Marija Nenadić[1], Aleksandar Krmpot[2], Nikola Vesović[1], Mihailo Rabasović[2], Srećko Ćurčić[1], Danica Pavlović[2], Vesna Lačković[3], Svetlana Savić-Šević[2] and Dejan Pantelić[2]

[1]Institute of Zoology, University of Belgrade-Faculty of Biology, Belgrade, Serbia, [2]Institute of Physics, University of Belgrade, Belgrade, Serbia, [3]Institute of Histology and Embryology "Aleksandar Đ. Kostić", University of Belgrade - Faculty of Medicine, Belgrade, Serbia

• **PO2.28**

Electron Tomography Analysis of Human Islet Amyloid Polypeptide Crystalline Structures in *Drosophila Melanogaster*

Ling Xie[1], Xiaohong Gu[2], Kenta Okamoto[3], Gunilla T Westermark[2] and Klaus Leifer[1]

[1]Department of Engineering Sciences, Applied Materials Sciences, Uppsala University, SE-75121, Uppsala, Sweden, [2]Department of Medical Cell Biology, Uppsala University, SE-75123, Uppsala, Sweden, [3]Department of Biology Physics, Uppsala University, SE-75123, Uppsala, Sweden

• **PO2.29**

Metformin and Itraconazole Combination is Effective Against Fibrosarcoma in Hamsters

Kosta J. Popović[1], Dušica J. Popović[2], Dušan Lalošević[2], Dejan Miljković[2], Ivan Čapo[2], Jovan K. Popović[3]

[1]Department of Pharmacy, Faculty of Medicine, University of Novi Sad, Novi Sad, Republic of Serbia, [2]Department of Histology and Embryology, Faculty of Medicine, University of Novi Sad, Novi Sad, Republic of Serbia, [3]Department of Pharmacology, Toxicology and Clinical Pharmacology, Faculty of Medicine, University of Novi Sad, Novi Sad, Republic of Serbia

• **PO2.30**

Synergistic Anticancer Interaction of Metformin and Caffeine on Fibrosarcoma in Hamsters

Dušica J. Popović[1], Dušan Lalošević[1], Dejan Miljković[1], Kosta J. Popović[2], Ivan Čapo[1], Jovan K. Popović[3]

[1]Department of Histology and Embryology, Faculty of Medicine, University of Novi Sad, Novi Sad, Republic of Serbia, [2]Department of Pharmacy, Faculty of Medicine, University of Novi Sad, Novi Sad, Republic of Serbia, [3]Department of Pharmacology, Toxicology and Clinical Pharmacology, Faculty of Medicine, University of Novi Sad, Novi Sad, Republic of Serbia

• **PO2.31**

Differential Polarization Laser Scanning Microscopy (DP-LSM) - Technique for Rapid Screening of Cell Walls of Different Plant Species

Jasna Simonović Radosavljević[1], Daniela Djikanović[1], Gabor Steinbach[2], Aleksandra Lj. Mitrović[1], Jelena Bogdanović Pristov[1], Győző Garab[3], Ksenija Radotić[1]

[1]Institute for multidisciplinary study, University of Belgrade, Kneza Višeslava 1, 11000 Belgrade, Serbia, [2]Institute of Biophysics, Biological Research Center, Szeged 6701, Hungary, [3]Institute of Plant Biology, Biological Research Center, Szeged 6701, Hungary

• **PO2.32**

Transmission Electron Microscopy in Evaluation of Curcumin Nanoparticles Cellular Uptake

Tamara Kravic-Stevovic[1], Tamara Martinovic[1], Darko Ciric[1], Verica Paunovic[2], Biljana Ristic[2], Zoran Markovic[3], Biljana Todorovic-Markovic[4], Milica Kosic[2], Jovana Prekodravac[4], Matej Micusik[3], Zdeno Spitalsky[3], Vladimir Trajkovic[2], Ljubica Harhaji-Trajkovic[5] and Vladimir Bumbasirevic[1]

[1]Institute of Histology and Embryology, School of Medicine, University of Belgrade, Visegradska 26, Belgrade 11000, Serbia, [2]Institute of Microbiology and Immunology, School of Medicine, University of Belgrade, Dr Subotica 1, Belgrade 11000, Serbia, [3]Polymer Institute, Slovak Academy of Sciences, Dubravska cesta 9, 84541 Bratislava, Slovakia, [4]Vinca Institute of Nuclear Sciences, University of Belgrade, P.O. Box522, Mike Petrovica Alasa 12-14, Belgrade 11001, Serbia, [5]Institute for Biological Research "Sinisa Stankovic", University of Belgrade, Despot Stefan Blvd. 142, Belgrade 11000, Serbia

• **PO2.33**

Polyethylene Glycol Coated Gold Nanoparticles Nerve Tissue Uptake After Spinal Cord Injury

Tamara Martinovic[1], Darko Ciric[1], Tamara Kravic-Stevovic[1], Florentia Papastefanaki[2], Igor Jakovcevski[3,4], Nafsika Poulia[2], Nevena Djogo[3], Florian Schulz[5], Gabrielle Loers[3], Tobias Vossmeyer[5], Horst Weller[5,6], Melitta Schachner[7], Rebecca Matsas[2] and Vladimir Bumbasirevic[1]

[1]Institute of Histology and Embryology, School of Medicine, University of Belgrade, Visegradska 26, Belgrade 11000, Serbia, [2]Laboratory of Cellular and Molecular Neurobiology, Hellenic Pasteur Institute, 127 Vassilissis Sofias Avenue, 11521 Athens, Greece, [3]Zentrum für Molekulare Neurobiologie, Universitätsklinikum Hamburg-Eppendorf, Universität Hamburg, Martinistrasse 52, 20246 Hamburg, Germany, [4]Experimental Neurophysiology, University Hospital Cologne, Joseph-Stelzmann-Str. 9, 50931 Köln, Germany; German Center for Neurodegenerative Diseases, Ludwig-Erhard-Allee 2, 53175 Bonn, Germany, [5]Institut für Physikalische Chemie, Universität Hamburg, Grindelallee 117, 20146 Hamburg, Germany, [6]Department of Chemistry, Faculty of Science, King Abdulaziz University, Jeddah, Saudi Arabia, [7]Center for Neuroscience, Shantou University Medical College, 22 Xin Ling Road, Shantou, Guandong 515041, People's Republic of China

• **PO2.34**

Ultrastructural Analysis of Large Graphene Quantum Dots Internalization in Hepatocytes

Darko Ciric[1], Tamara Martinovic[1], Tamara Kravic-Stevovic[1], Vladislav Volarevic[2], Verica Paunovic[3], Zoran Markovic[4], Bojana Simovic Markovic[2], Maja Misir-

kic-Marjanovic[3,5], Biljana Todorovic- Markovic[4], Sanja Bojic[2], Ljubica Vucicevic[3,5], Svetlana Jovanovic[4], Nebojsa Arsenijevic[2], Ivanka Holclajtner-Antunovic[6], Momir Milosavljevic[4], Miroslav Dramicanin[4], Miodrag L. Lukic[2], Vladimir Trajkovic[3] and Vladimir Bumbasirevic[1]

[1]Institute of Histology and Embryology, School of Medicine, University of Belgrade, Visegradska 26, Belgrade 11000, Serbia, [2]Centre for Molecular Medicine and Stem Cell Research, Faculty of Medical Sciences, University of Kragujevac, 69 Svetozara Markovica St., 34000 Kragujevac, Serbia, [3]Institute of Microbiology and Immunology, School of Medicine, University of Belgrade, Dr Subotica 1, Belgrade 11000, Serbia, [4]Vinca Institute of Nuclear Sciences, University of Belgrade, P.O. Box 522, Mike Petrovica Alasa 12-14, Belgrade 11001, Serbia, [5]Institute for Biological Research "Sinisa Stankovic", University of Belgrade, Despot Stefan Blvd. 142, Belgrade 11000, Serbia, [6]Faculty of Physical Chemistry, University of Belgrade, Studentski trg 12-16, 11000 Belgrade, Serbia

PLENARY ABSTRACTS

Electron Holography for Comprehensive Analysis of Structures and Fields in Solids

Hannes Lichte, Felix Börrnert, Bernd Einenkel, Andreas Lenk, Axel Lubk, Falk Röder, Jan Sickmann, Sebastian Sturm, Karin Vogel and Daniel Wolf

Formerly at Triebenberg Laboratory, Technische Universität Dresden, Dresden, Germany *closed by TU Dresden in September 2016*

Transmission Electron Microscopy is wave optics. The object information is found both in amplitude and phase of the object exit wave. Alas, the intensity image recorded on a detector only represents the amplitude distribution whereas the phase distribution is lost. This means a substantial loss of object information, e.g. about the intrinsic electromagnetic fields in an object, which largely determine the properties.

Phases can only be measured by interference. Therefore, holography offers a powerful means for analyzing the complete electron wave including all object properties encoded in the electron phase, such as electric and magnetic fields. Due to the restrictions of electron coherence, the most powerful method up to now is off-axis image plane electron holography. It allows measuring the object phase shift on the scale reaching from several micrometers down to atomic resolution (Fig.1 and Fig.2). Recent developments in Holographic Tomography give access to the 3D-distribution of electromagnetic fields.

At medium resolution with details larger than about 2 nm, the aberrations of the electron lenses can be neglected, and hence the reconstructed wave agrees with the object wave. Thus, the reconstructed phase distribution can directly be interpreted in terms of the object. This is the basis for achieving perfect phase contrast without defocusing or staining hence for determining

- Mean Inner Potentials in solids
- Functional potentials such as drift-diffusion potentials across pn-junctions
- Electric potentials across interfaces
- Trapping of charges at surfaces and interfaces

- Electric potential distributions in charge-modulated structures
- Magnetic fields in and around magnetic structures down to a nanoscale
- Magnetic leakage fields at structural inhomogeneities
- Ordering of magnetic nanoparticles
- Mechanical strain

and others. All these details are significant parts of the object structure, since they determine the functionality, e.g. in semiconductors and magnetics, and hence are indispensable for a comprehensive understanding of their properties.

At atomic resolution, because of the aberrations, amplitude and phase of the reconstructed wave differ considerably from the object wave and hence cannot be interpreted directly. First, the aberrations have to be corrected by appropriate processing. Then, both in amplitude and phase, lateral resolution can be achieved as high as determined by the information limit offered by the TEM used for recording the hologram. The resulting phase images allow details of the atomic structure to be revealed, such as

- Atomic potentials
- Difference of atomic numbers of different constituents
- Number of atoms in an atomic column

Recent developments

- Holographic Tomography. To obtain full 3D-information, the methods of holography and tomography are combined: A tilt series of holograms is recorded, from which the corresponding 2D-phase image series is reconstructed. Following tomographic procedures, from these 2D-images, the 3D-representation is reconstructed, which allows uniquely determining 3D electric potential distributions and magnetic fields as well as elastic and inelastic attenuation coefficients.
- In situ Holography. The better the performance, the more object details contributing to the phase shift have to be considered. Therefore, we have to strengthen in-situ experiments where only the parameter of interest is varied, and hence a better defined insight in solid state science is gained and used for a more detailed and accurate modeling of the substance under investigation.
- Inelastic Holography. By inelastic processes, coherence with respect to the elastic electrons is destroyed. However, the electron wave “newborn” by an inelastic event, such as excitation of a plasmon, has an appreciable area of coherence of about 30nm diameter in the object. This was measured by inelastic holography in

an EFTEM path of rays. Strictly speaking, due to entanglement of the electrons with the object, these phenomena can only be described correctly by density matrices, which incorporate the propagation of coherence through the TEM.

In summary, one can say that, after 60 years of development, electron holography is an established method for comprehensive wave optical characterization of solids including their intrinsic electromagnetic fields. The performance, essentially restricted by quantum noise, allows atomic resolution both laterally and in signal. Any improvement of electron microscopes, such as of lateral resolution and of brightness of the electron gun, will enhance the capabilities of this unrivalled method for nanocharacterization.

For further reading, we recommend the textbook "Transmission Electron Microscopy" edited by C. Barry Carter and David B. Williams, chapter 7 on "Electron Waves, Interference and Coherence" and chapter 8 on "Electron Holography" (Springer ISBN 978-3-319-26649-7).

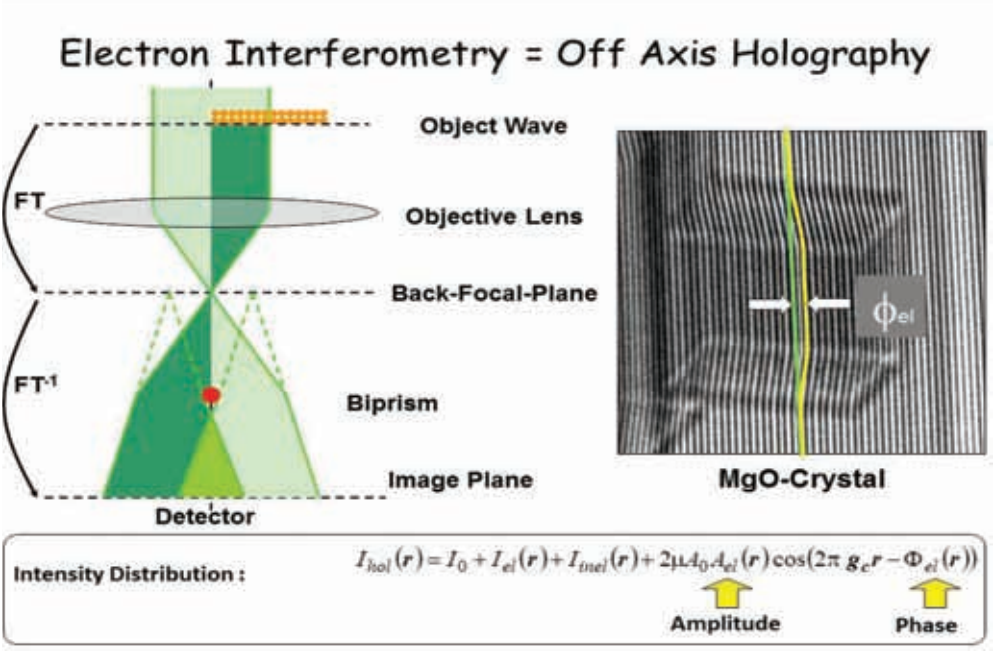

Figure 1. Recording an Off-Axis Hologram. By means of the electron biprism, a plane reference wave is superimposed on the object wave in the image plane. In the hologram, interference fringes are found, which are modulated in contrast by the object amplitude and in position by the object phase. So, the complete wave is recorded by amplitude and phase.

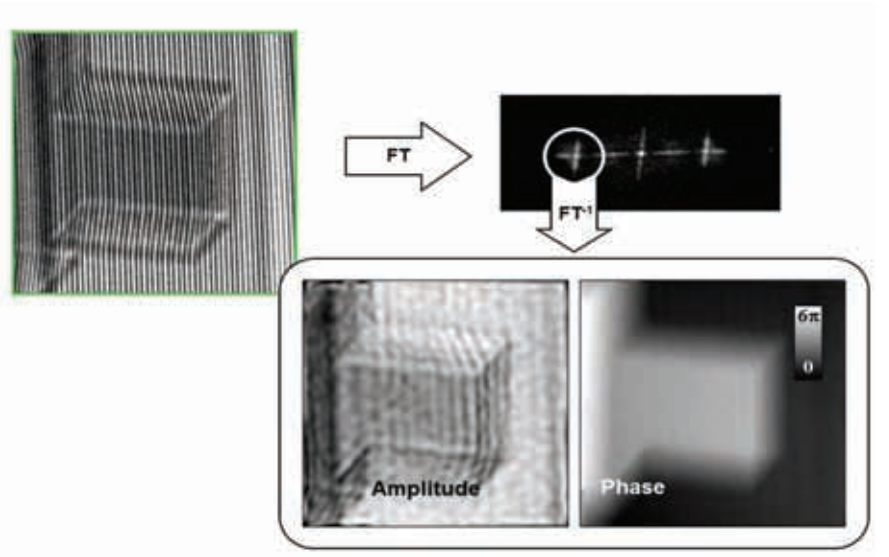

Figure 2. Reconstructing the electron wave. In the hologram, the wave is recorded on a cosinoidal fringe pattern with a controllable carrier frequency. Therefore, in the Fourier transform (FT) one finds two off axis sideband at the carrier frequency, with the FT of the object wave convoluted around each of them. Masking out one of these sidebands, after inverse FT, one finds amplitude and phase distribution of the object wave in real space. Here, the phase represents the Mean Inner Potential in the MgO-crystal.

Model-Based Iterative Reconstruction of Charge Density and Electric Field using Off-Axis Electron Holography

Fengshan Zheng[1], Jan Caron[1], Vadim Migunov[1, 2] and Rafal E. Dunin-Borkowski[1]

[1] *Ernst Ruska-Centre for Microscopy and Spectroscopy with Electrons and Peter Grünberg Institute, Forschungszentrum Jülich, 52425 Jülich, Germany*

[2] *Central Facility for Electron Microscopy, RWTH Aachen University, 52074 Aachen, Germany*

The ability to measure local variations in charge density in the transmission electron microscope would provide a valuable tool for the study of functional materials, including ferroelectrics and semiconductors. Similarly, the ability to measure local variations in electric field outside electrically-biased needle-shaped samples would be of great importance for understanding the fidelity of reconstructions of microstructure and chemical composition achieved using atom probe tomography [1, 2], in particular for samples that contain multiple phases or insulating materials.

Off-axis electron holography is a powerful technique that provides direct access to the phase of the high energy electron wave that has passed through a sample in the transmission electron microscope [3]. In the absence of magnetic fields, the phase is sensitive to the electrostatic potential in the specimen projected in the electron beam direction. The local projected charge density in the specimen can in principle be determined directly from the Laplacian of a recorded phase image. However, such a model-independent approach suffers from poor signal-to-noise, as well as from artefacts associated with local variations in mean inner potential and specimen thickness [4].

Here, we describe a model-based iterative technique that can be used to reconstruct the projected charge density inside a specimen from a single electron optical phase image recorded using off-axis electron holography, or alternatively the three-dimensional charge density distribution from a tomographic tilt series of phase images [5]. We use a forward model in an iterative algorithm to solve the inverse problem of reconstructing the charge density in the specimen, as shown in Fig. 1. Additional constraints and physical laws can be incorporated in the algorithm. For

the three-dimensional problem, the use of such a model-based approach avoids many of the artifacts that are associated with the use of backprojection-based tomographic techniques. The projected or three-dimensional electric field can be determined numerically from the reconstructed charge density.

Figure 2 illustrates the reconstruction of the projected charge density distribution inside an atom probe tomography needle, which contains a conducting base and an insulating Al_2O_3 apex. In the present example, the needle has become charged in the absence of an applied voltage simply as a result of exposure to electron beam irradiation. Off-axis electron holograms of the needle were acquired at 300 kV using a Gatan K2 camera in an FEI Titan microscope equipped with two electron biprisms. Experimental equiphase contours are shown in Fig. 2(a). Corresponding simulated equiphase contours, which were generated from the best-fitting reconstructed charge density distribution, are shown in Fig. 2(b) and are consistent with the experimental phase image in the vacuum region outside the specimen. The challenges of developing the reconstruction algorithm, as well the uniqueness of the solution and its sensitivity to boundary conditions, will be discussed [6].

References:

[1] TF Kelly and MK Miller, Rev. Sci. Instrum. **78** (2007), 031101.
[2] SS Katnagallu *et al*, J. Phys. D: Appl. Phys. **51** (2018), 105601.
[3] H Lichte and M Lehmann, Rep. Prog. Phys. **71** (2008), 016102.
[4] G Matteucci *et al*, Ultramicroscopy **45** (1992), *77*.
[5] J Caron *et al*, Proceedings of the PICO 2015 Conference on Frontiers of Aberration Corrected Electron Microscopy, Kasteel Valsbroek, The Netherlands, 19-23 April 2015, p. PB04.
[6] The authors thank J Ungermann, *M Riese , M Beleggia and G* Pozzi for valuable contributions.

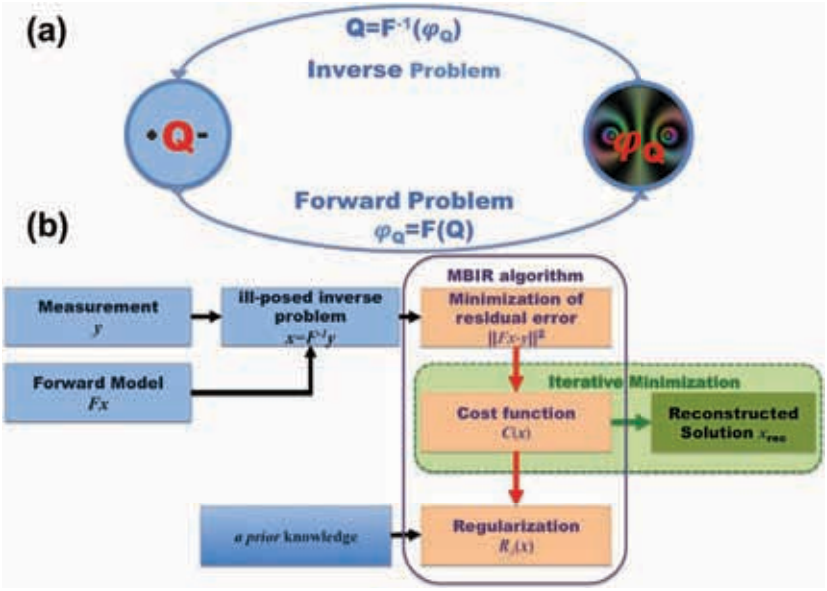

Figure 1. (a) Schematic diagram illustrating the forward and inverse problems that link the charge distribution Q in a specimen with the recorded phase shift φ_Q. (b) Workflow of the reconstruction process used here to solve the ill-posed inverse problem.

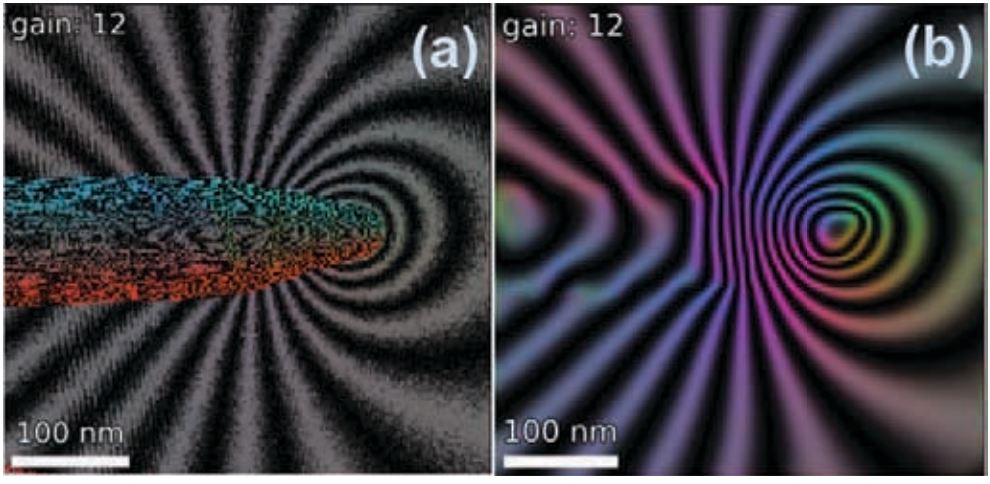

Figure 2. Example of the reconstruction of the charge density in an atom probe tomography needle that has an insulating Al_2O_3 apex. (a) Experimental phase contour map. Contours inside the needle are affected by the mean inner potential of the specimen. (b) Simulated contour map determined from the best-fitting charge density distribution in the specimen, which was reconstructed from the phase shift measured in vacuum outside the needle. The contour spacing is $\pi/6$ radians.

10

Low Dose Electron in-Line Electron Holography: Toward Revealing Atomic Resolution Dynamics for MoS_2 Nanoparticle and Soft Materials

Fu-Rong Chen[1], Dirk van Dyck[3], Christian Kisielowski[4], Stig Helveg[2]

[1] *Department of Materials Science and Engineering, City University, Hong Kong*
[2] *Haldor Topsoe A/S, Haldor Topsøes Allé 1, DK-2800 Kgs. Lyngby, Denmark*
[3] *Departments of Physics, EMAT, University of Antwerp, 2020 Antwerp, Belgium*
[4] *Molecular Foundry, Lawrence Berkeley National Laboratory, Berkeley CA 94720, USA*

Over the past decade, electron microscopy has become indispensable for studying heterogeneous catalysts at the atomic-scale [1]. The ability to acquire atomic-resolution images with single-atom sensitivity has opened up for unprecedented insight into catalyst structures and dynamics. However, the progress has also shown that observations at the atomic-level require an intense electron illumination that generally alters the catalyst during observation. The electron-induced alterations are particular pronounced at the catalyst surface as they expose a variety of sites of reduced atomic coordination. In the quest to suppress electron-induced alterations and to enable chemical meaningful observations, it therefore becomes mandatory to exercise control over the electron dose, dose-rate and energy.

Here, we demonstrate low dose-rate in-line electron holography as a viable concept for atomic-resolution observations of catalysts in the genuine state [2-4]. The imaging scheme employs bright field transmission electron microscopy (TEM) as the most efficient way to detect single atoms using the fewest elastically scattered electrons. The image acquisition is done with low electron dose-rates of down to 1-100 $e^{-}Å^{-2}s^{-1}$ to inflict the weakest object excitation and to offer time for reversible object restoration between successively delivered electrons. As a result, the individual atomic-resolution images are dominated by noise, and recovery of image signal can be accomplished by averaging over a series of consecutively acquired images of the

object. For this purpose, in-line holography based on focal image series is particular attractive as residual aberrations are corrected and the exit wave (EW) function recovered with enhanced signal that is quantitatively interpretable.

Applications of the concept of low dose-rate in-line electron holography in catalysis research will outlined. Figure 1 shows EW phase images of carbon-supported single-layer MoS_2 nanocrystals with edge-attached Co promoter atoms [6]. This catalyst is relevant for hydrodesulfurization processes in oil refineries. A systematically examination of the MoS_2 structures at different dose-rates reveal that lower dose-rates sharpen up the atomic column contrast and reduce smearing of the edge contrast. This suppression of beam-induced atom dynamics enables a quantitative analysis of the exit wave for retrieving the stoichiometric arrangement in the Co-Mo-S nanocrystals in three dimensions. The low dose-rate concept also benefits *in situ* electron microscopy observations. Figure 2 shows EW phase images of VO_x supported on anatase-TiO_2 nanoparticles (VO_x/TiO_2), which are widely applied for reducing NO_x emissions that are harmful to human health and ecosystems [7]. Specifically, the image series were recorded using low dose-rates for which the V L_3 ionization edge remained constant, indicating that electron-induced oxide alterations were suppressed. Surprisingly, the images reveal a facet-dependent and reversible order-disorder transformation of the outermost atomic layers of the VO_x/TiO_2 catalyst under alternating oxidizing and reducing environments (Figure 2).

References:

[1] S Helveg, J. Catal. 328 (2015), 102.
[2] C Kisielowski *et al*, Phys Rev B 88 (2013), 024305.
[3] S Helveg *et al*, Micron 68 (2014), 176.
[4] C Kisielowski *et al*, Adv. Struct. Chem. Imag. 2 (2016), 13.
[5] F-R Chen *et al* (2018) in prep.
[6] M Ek *et al*, Nature Comm. 8 (2017), 305.

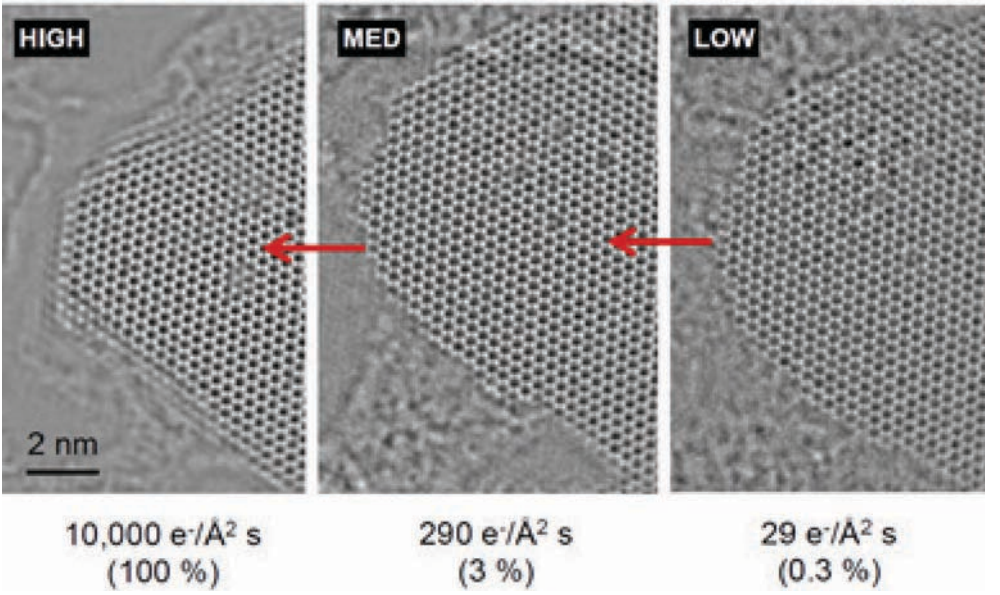

Figure 1. Exit wave phase images of Co-promoted MoS_2 nanocrystal supported on carbon. The individual images are recorded at 80 keV under variable electron dose-rates. At the lower dose-rates atomic column contrast sharpens up and edge contrast smearing is reduced. Adapted from [5].

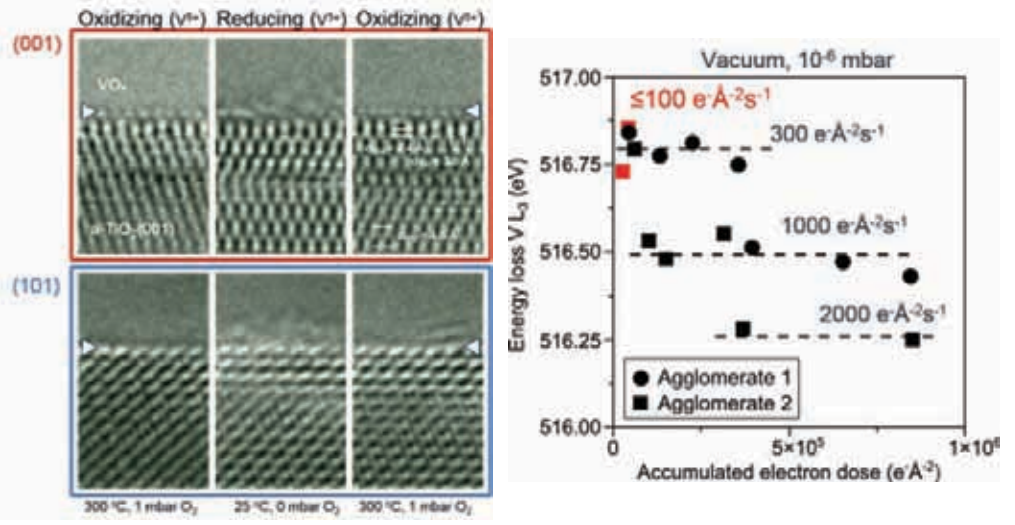

Figure 2. Exit wave phase images of VO_x/TiO_2 reveal a facet-dependent order-disorder transformation under alternating oxidizing and reducing conditions. The individual images are recorded at 300 keV with 300 $e^-Å^{-2}s^{-1}$. Under those conditions, the V L_3 ionization edge is constant indicating that electron-induced oxide alterations are suppressed. Adapted from [6].

High-Speed Direct Electron Detection: Past, Present and Future

Peter Denes

Lawrence Berkeley National Laboratory, Berkeley, CA USA

The use of CMOS Active Pixel Sensors for electron detection has had a dramatic effect on Transmission Electron Microscopy. The detector-enabled "Resolution Revolution" has led to explosive growth in the use of cryoEM for structural biology – with the technique being named "Method of the Year" in 2015 by Nature Methods, just two years after the first significant results[1], followed by the Nobel Prize in Chemistry in 2017. Similarly, high-speed recording opens new vistas for in-situ studies of materials and novel imaging modes. This talk will describe how these detectors work, together with opportunities and constraints for further improvements. Characteristics will be illustrated by the TEAM detector[2] (2008, 1 Mpix at 400 frames/s) and the subsequent K2 detector[3] (2011, 16 Mpix, 400 frame/s) as well as a 100,000 frame/s detector currently being deployed at Lawrence Berkeley National Laboratory.

References:

[1] M Liao *et al*, Nature **504** (2013) 107-12.
[2] M Battaglia *et al*, Nucl. Instrum. and Meth. **622A** (2010) 669-677.
[3] D Contarato *et al*, Nucl. Instrum. and Meth. **635A** (2011) p. 69-73.

14

Applications of Direct Electron Detectors and Machine Learning with Neural Networks in Energy Loss Spectroscopy and Mapping

Hanshuo Liu[1], Michael Chatzidakis[1], Gianluigi A. Botton[1,2]

[1] *Department of Materials Science & Engineering, McMaster University, Hamilton, ON, Canada*
[2] *Canadian Center for Electron Microscopy, Hamilton, ON, Canada*

Electron energy loss spectroscopy (EELS) is an invaluable technique to study the detailed structure and the chemical state of materials at unprecedented spatial resolution. Today, this technique is used "routinely" to characterize nanoscale materials used in a myriad of applications from energy storage and conversion, to solid-state devices and biomaterials interfaces. This technique also has the potential to provide insight into much more fundamental problems where the valence state of atoms and their location in the lattice is of critical importance. However, whilst there have been dramatic improvements in the characteristics of the electron probe (size, current) and energy resolution of microscope, there is still a significant need to improve the quality of the spectroscopic data in order to reduce the limitations induced by electron beam damage.

Recently, there have been major developments in detection approaches for scanning transmission electron microscopy (STEM) through pixelated detectors, and in EELS using direct electron detectors [1,2]. Direct electron detectors have significant benefits in terms of noise levels and point spread function resulting in major improvement in the quality of spectra. Here, we use a retractable Gatan K2 IS camera adapted to a Quantum spectrometer installed on a Titan 80-300 Cubed monochromated microscope to demonstrate the impact of such detectors on materials science applications.

First of all, the better the point spread function results in significant improvements in the quality of spectra and signal, due to the use of lower dispersion during spectral acquisition. Secondly, the noise characteristics are dramatically improved due to the single electron counting mode. This leads to much lower dose for the acquisition of spectra. As a consequence, such instrumentation allows improvements in data

acquisition of beam sensitive samples and the detection of core losses signals at energies not normally easily accessible with regular cameras.

Several examples of application of direct electron detectors for spectroscopy will be given in the field of Li ion battery materials to study materials in the $Li_{1+x}(NiMnCo)_{1-x}O2$ ($0 \leq x \leq 1/3$) and spinel families[3-6]. Here atomic resolved spectroscopy, not normally possible with regular detectors due to the beam damage will be shown (figure 1). Furthermore, significant change in the electronic structure could be detected from the lithium and oxygen K-edges when probing the active material and the cathode- electrolyte interphase (CEI). The application of energy loss spectroscopy to Sr iridate phases, as prospective new superconductors is also shown, thus providing much better insight on the electronic structure of these materials. Further examples related to the use of high energy edges (above 2000eV) will be shown for the study of noble metal nanoparticles and nanostructures.

The spectroscopy data, combined with machine learning approaches to identify spectra, will be discussed and used to demonstrate single atom spectroscopy and valence state mapping. [7]

References:

[1] JL Hart *et al*, Sci. Rep. **7** (2017), 8243.
[2] A Maigné and M Wolf, Microscopy (2018) (doi: 10.1093/jmicro/dfx088)
[3] H Liu *et al*, Phys. Chem. Chem. Phys. **18** (2016), 29064.
[4] J Li *et al*, J. Electrochem. Soc. **164** (2017), A655.
[5] H Liun *et al*, ACS Nano (2018) (doi: 10.1021/acsnano.7b08945)
[6] B Xiao *et al*, Adv. Mater. **29** (2017), 1703764.
[7] This work is supported by NSERC and the Canada Foundation for Innovation. The experimental data was acquired at the Canadian Centre for Electron Microscopy, a National Facility supported by NSERC, the Canada Foundation for Innovation and McMaster University.

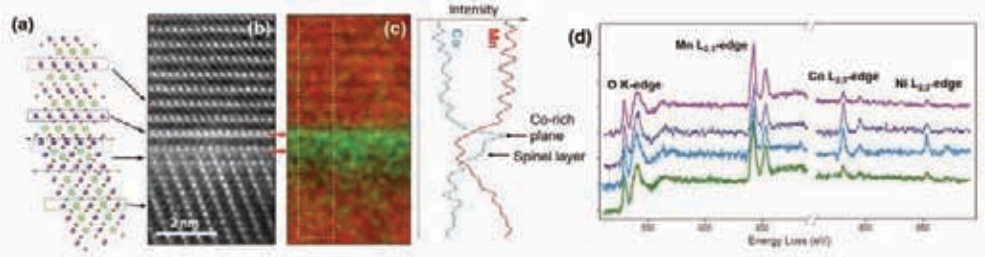

Figure 1. High-resolution STEM-EELS mapping showing the TM segregation at the impurity phase in pristine Li-rich cathode material. (a) atomic model for the HAADF image shown in (b), where, green spheres: Li; purple: TM; red: O. (c) EELS mapping of Co (green) and Mn (red), and the intensity profile showing Co segregation. (d) EELS spectra acquired from regions highlighted in (a).

16

The Road Towards a Versatile Programmable Phase Plate for Electrons

Johan Verbeeck, Armand Béché, Giulio Guzzinati, Daen Jannis and Knut Müller-Caspary

EMAT, University of Antwerp, Groenenborgerlaan 171, Antwerp, Belgium

In modern light optics, spatial light modulators allow full control over the phase of optical waves which has led to a rapidly expanding field of applications ranging from astrophysics to advanced light microscopy, endoscopy, laser cutting, data encryption, free space communication, , quantum information and many more. These spatial modulators rely on different working principles including deformable mirror surfaces and liquid crystals locally altering their refractive index, but all have in common that a computer can now control the optical transfer function in a programmable way, similar to pixels on a computer screen.

In electron optics, one could say that such control over the optical transfer function is common to all electron optical devices as the optical properties naturally depend on potentials on electrodes and currents through solenoids. Especially in modern aberration correctors, a high degree of flexibility in tuning the phase transfer is available and used to cancel aberrations up to a certain order by means of a complicated setup of multipolar lenses requiring a large number of computer controlled current sources. These correctors approach the flexibility of a spatial light modulator in light optics, yet still pose constraints on the kind of phase plate that can be realized. Indeed, Maxwell equations put rather severe restrictions on realizable fields in free space and the resulting phase transfer tends to be a smooth function that is ideal for aberration correction, but less so for other applications requiring rapid changes of phase in central regions of the device.

A good example of a phase plate with a rapid phase jump is the so-called Zernike phase plate that can be used to increase the contrast in weak phase object imaging. Many different realizations and variants of such phase plates were made with some making use of a miniaturized electrostatic einzel lens allowing to control the phase shift in a small region in the center of the phase plate by applying a voltage to the central electrode of the lens.

The downside of such designs is that they are typically placed in the objective aperture to provide a phase filter on the exit wave in the back focal plane where the material of the lens system will inevitable block some part of this exit wave creating loss of information and leading to image artefacts.

In this talk we extend this idea to an array of einzel lenses which we use as a probe forming aperture. We demonstrate a proof of concept realization with a 2x2 array of einzel lenses leading to a phase controlled 4 slit interference experiment in an existing transmission electron microscope. We discuss the design and behaviour of the proof of concept including its effect on coherence and the role of delocalized inelastic scattering.

We further will discuss the upscaling of the current device, which is the goal of a recently started ERC proof of concept grant (ADAPTEM) aiming for at least a 5x5 demonstrator. We discuss the possible uses of such a device as a tool for the study of exotic electron waves, including electron vortex beams, Bessel beams, Airy beams, snake Beams, helicon beams and many more. We demonstrate that even with relatively few phase elements, a highly desirable device can be produced for studying such waves.

Alternatively, the device could also show promise as a low-cost aberration corrector for TEM and SEM and we demonstrate that even with a relatively low amount of well-chosen phase elements such correctors could find their use for specific applications [2].

References:

[1] J Verbeeck *et al*, Ultramicroscopy **190** (2018), 58–65.

[2] JV and AB acknowledge funding from the Fund for Scientific Research Flanders FWO project G093417N and the European Research Council, ERC Starting Grant 278510 VORTEX and ERC proof of concept project DLV- 789598 ADAPTEM. The Qu-Ant-EM microscope was partly funded by the Hercules fund from the Flemish Government.

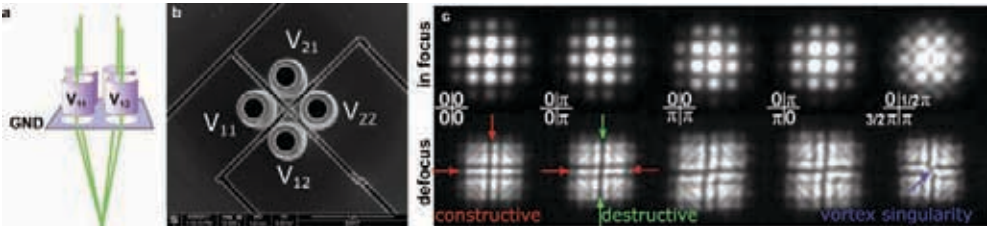

Figure 1. a) schematic set up of the 2x2 phase programmable array. b) SEM image of the device showing 4 cylindrical electrodes that can be put on separate electrostatic potentials Vij. c) Resulting interference pattern when mounted in the TEM showing the complete control of the phase of the 4 interfering beams resulting in different patterns.

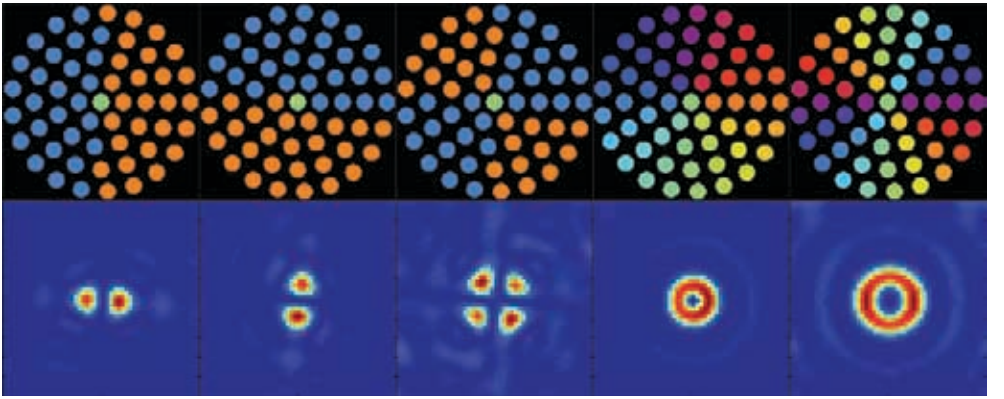

Figure 2. A simulated upscaled version of this device could serve as an attractive tool to study exciting electron beams. From left to right HG_{10}, HG_{01}, HG_{11} LG_{01}, LG_{02} beams.

Scanning Transmission Electron Microscopy and Diffraction in SEM: Novel Approaches for *In situ* Studies

Erdmann Spiecker, Christian Dolle, Peter Schweizer, Peter Denninger

Center for Nanoanalysis and Electron Microscopy (CENEM) & Institute of Micro- and Nanostructure Research, Department of Materials Science and Engineering, Friedrich-Alexander-Universität Erlangen-Nürnberg, 91058 Erlangen, Germany

Current trends in electron microscopy point towards low-voltage applications. The reduction of beam energy offers several benefits like reduced beam damage and higher scattering cross sections, especially beneficial for the investigation of light elements. Widely recognized examples of light element-materials are graphene and carbon nanotubes, which have been thoroughly investigated by electron microscopy demanding primary beam energies below 80 keV to exclude knock-on damage. While dedicated low-voltage TEMs are only slowly entering the commercial market, scanning electron microscopes (SEM) already use primary electron energies of 0.5-30 keV and thus offer an easy access to low-voltage microscopy.

The SEM is a highly versatile tool for the investigation of novel materials by offering a complex set of applicable techniques, less spatial limitations compared to TEM, high throughput and the possibility to use a wide range of available add-on tools (e.g. manipulators, gas injection systems, *in situ* equipment) while still maintaining resolution in the nm-range and high material contrast. Besides the well-established imaging of surfaces by secondary electrons and chemical contrast/composition by backscattered electrons and X-Ray spectroscopy, a SEM gives direct access to low-voltage scanning transmission electron microscopy (STEM). State-of-the-art segmented STEM detectors are very versatile and well suited for material and diffraction contrast imaging. However, a more quantitative interpretation of the STEM contrast (bright-field and dark-field) requires the knowledge of the electron diffraction pattern in the plane of the STEM-detector.

Here we report on a custom-built diffraction setup in the SEM enabling the simultaneous acquisition of real space and reciprocal space information *in situ*. Low

Energy Nano Diffraction (LEND) in transmission is based on the combination of a fluorescent screen positioned below the sample with a dedicated CMOS camera. The technique has been implemented and successfully tested on graphene, silicon and polycrystalline gold. For graphene a hexagonal spot like diffraction pattern can be obtained due to the small convergence angle typically encountered in SEM [1]. The exemplary LEND pattern depicted in Fig. 2a has been taken from twisted bilayer graphene and allows for straightforward determination of the local twist angle (here ~ 30°). By acquiring LEND patterns on a 2D array of sample positions the twisting angle can be mapped across large areas of twisted bilayer graphene. This is similar to 4D-STEM in TEM. However, with our setup we could already successfully demonstrate LEND down to electron energies of 0.5 keV which opens up new opportunities in characterization of ultrathin low-Z materials.

The combination of STEM and LEND is furthermore important for reliable interpretation of STEM contrast in SEM since LEND allows to directly reveal the electron intensity that is collected by the different segments of the STEM detector. This enabled us to directly reveal basal plane dislocations in bilayer graphene and correctly interpret their contrast in dark-field STEM ([2], Fig. 2b). By combining this with the *in situ* capabilities of our SEM setup (Fig. 1) we could successfully manipulate the dislocations while simultaneously image them in dark-field STEM ([2], Fig. 2b, right). Further *in situ* STEM and LEND studies in SEM are ongoing. For instance, we recently installed a chip-based *in situ* heating device which we now use for investigation of phase transformation phenomena in thin films.

References:

[1] C Dolle, P Schweizer and E Spiecker, Proceedings of the Microscopy Conference MC2017, Lausanne (Switzerland), 498-499.

[2] P Schweizer, C Dolle and E Spiecker, Proceedings of the International Microscopy Congress IMC19, Sydney (Australia), accepted.

[3] The authors acknowledge funding from the German Research Foundation (DFG) through the Research Training Group GRK 1896 „In situ microscopy with electrons, X-rays and scanning probes“ and the Collaborative Research Center SFB 953 „Synthetic carbon allotropes”.

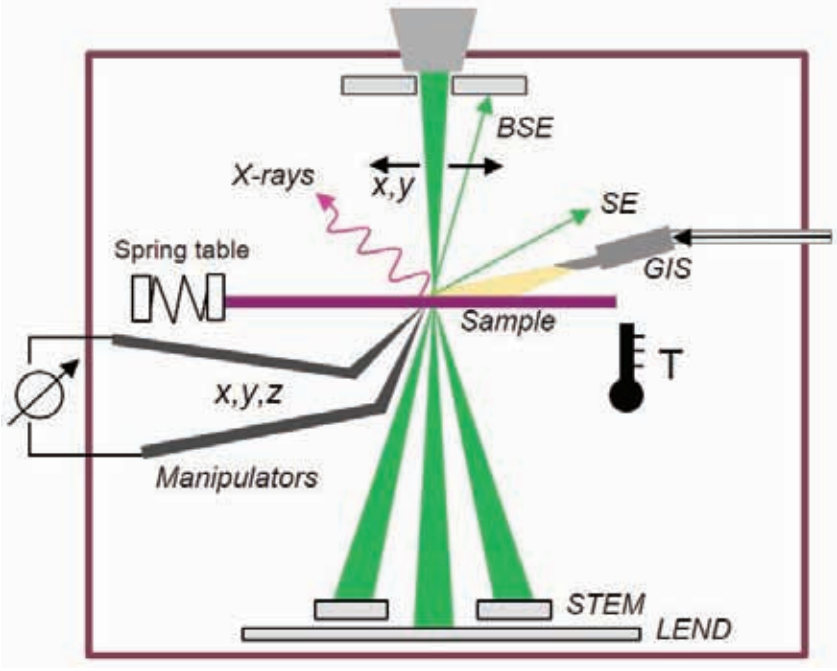

Figure 1. Versatile SEM setup combining STEM and LEND with various *in situ* tools including micro-manipulators, spring table for force measurement, gas injection system and heating device (schematic).

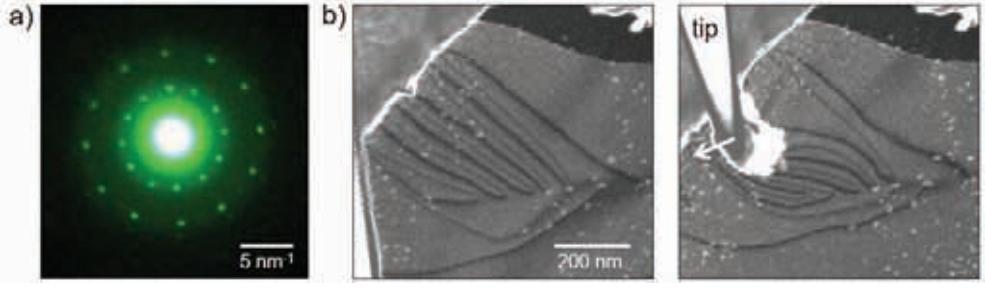

Figure 2. a) LEND pattern of rotated bilayer graphene taken with custom-built diffraction setup in SEM at 20 keV primary electron energy. b) Dark-field STEM image in SEM showing diffraction contrast from basal plane dislocations in bilayer graphene. c) *In situ* mechanical manipulation of dislocations using a micro-manipulation with sharp tip.

22

Advancing Topological Materials for Quantum Computing Applications with Electron Microscopy

David C. Bell[1,2]

[1] *Harvard John A. Paulson School of Engineering and Applied Sciences, Harvard University Cambridge MA 02138*
[2] *Center for Nanoscale Systems, Harvard University Cambridge MA 02138*

Depending on the composition, Quantum Materials may act as conductors, insulators, semiconductors or even as superconductors. Combinations of different quantum materials are of high interest to explore new phenomena and act as the foundation for future electronic devices at the nanometer scale. Our quantum materials research reaches from defect formation in graphene to the characterization of hybrid quantum materials. I will present our work utilizing Low-Voltage Monochromated EELS and Low-Voltage High-Resolution Electron Microscopy (LV HREM). Together, these often improve the contrast to damage ratio obtained on a large class of samples. The exploration and synthesis constitute only one aspect of the challenges in the development of new topological materials, another challenge is their characterization. Since the phenomena appear at very restricted and dedicated conditions, the characterization method must have very high sensitivity, resolution, localization and precision.

Transmission electron microscopy is a powerful technique to investigate structural, compositional or electromagnetic properties of topological materials. Especially, recent implementation of aberration correction in the transmission electron microscopy made chemical and structural characterization with very high spatial resolution (in the range of picometers) and sensitivity possible. This in turn allows detailed analysis of superconductor and topological materials, where small compositional variations have large effects on the material properties.

For topological materials 2005 was an important milestone as a consequence the realization of the existence of a metallically conductive surface state in an insulator material. Within couples of years, the experimental evidences of the surface state followed the theory studies. A high spin orbit coupling creates edge states where

quantum spin Hall Effect can exist in the absence of an external magnetic field. The discovery of the new phenomenon opened up intensive discussions in condensed matter, and even very well-known conventional material systems such as $Bi2(Te,Se)_3$, BiSb alloys etc., became "exotic" and highly investigated materials again.

One idea is using the kagome lattice as a topological switch. The kagome lattice is a two-dimensional network of corner-sharing triangles known as a platform for exotic quantum magnetic states. Theoretical work has predicted that the kagome lattice may also host Dirac electronic states that could lead to topological and insulating phases, but these have evaded experimental detection to date. Fe_3Sn_2 is a rare metallic Kagome ferromagnet, which synthesis as a single crystal has not previously been reported. We study this single crystal as well as other topological insulators with the particular interest in the correlated behavior in topologically non-trivial materials.

[1] This work was supported by the STC, Center for Integrated Quantum Materials, NSF Grant No. DMR-1231319. This work was performed at the Center for Nanoscale Systems (CNS), a member of the National Nanotechnology Coordinated Infrastructure Network (NNCI), which is supported by the National Science Foundation under NSF award no. 1541959.

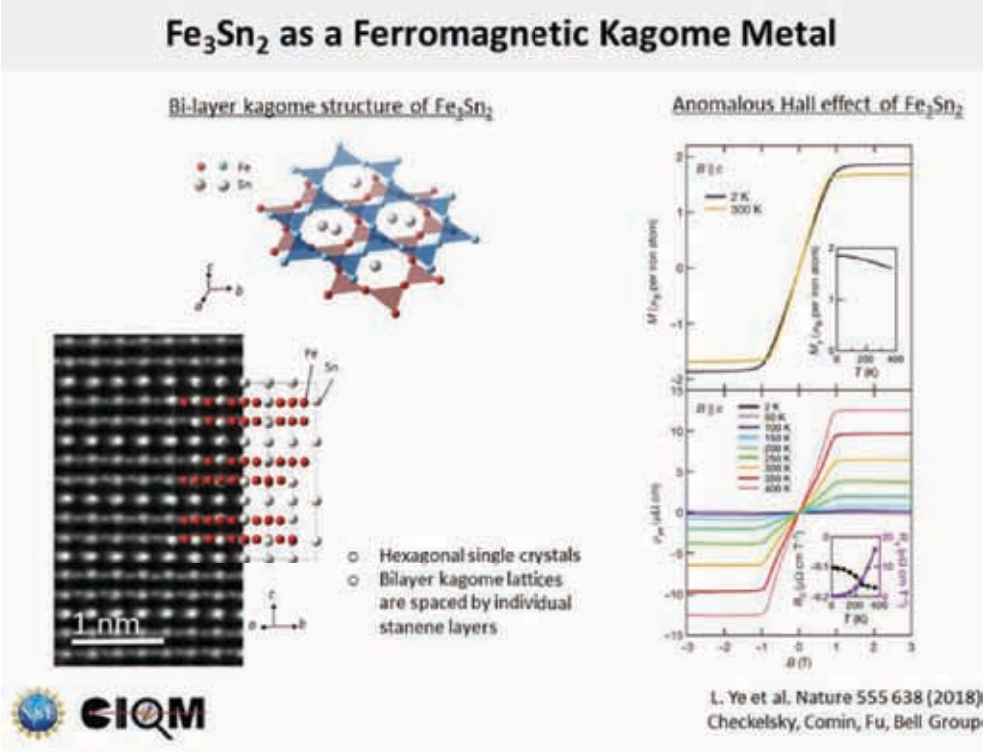

24

Incoherent Interfaces: Strain, Adsorption, and Reconstruction

Hadar Nahor and Wayne D. Kaplan

Department of Materials Science and Engineering, Technion - Israel Institute of Technology, Haifa 32000, Israel

Atomistic structural characterization of interfaces mostly focuses on systems having low mismatch and a low index orientation relationship between the phases, where semi-coherent interfaces can be described as regions of coherency separated by misfit dislocations. However, many systems form incoherent interfaces due to significant difference in lattice parameters and/or lattice symmetry. Mechanisms for strain energy reduction at incoherent interfaces have not been fully addressed.

In this work, solid-state dewetting of continuous Ni films deposited on the (111) and (001) surfaces of yttrium stabilized zirconia (YSZ) was used to produce equilibrated Ni particles on the substrates. Orientation relationships were determined using selected area diffraction patterns and transmission electron microscopy (TEM), and the solid-solid interfacial energy was measured for each of the low-index orientations using Winterbottom analysis [1]. The orientation distribution was determined using electron backscattered diffraction (EBSD) and X-ray diffraction (XRD), and the solid-solid interface structure of the Ni(111)-YSZ(111) interface was determined using aberration corrected TEM and scanning transmission electron microscopy (STEM). The results reveal that despite the 31% lattice mismatch between Ni and YSZ, the nominally incoherent interface reconstructs to form a 2-D array of high density, semi-periodic misfit dislocations [2,3].

In addition, Ni particles were doped with Cr and with Fe and Cr. Chemical analysis of the interfaces was conducted using energy dispersive spectroscopy (EDS) in STEM, and the equilibrium crystal shapes (ECS) were simulated using “Wulffmaker” software. Cr was found to adsorb to the Ni-YSZ interface, and in parallel to create a Cr_2O_3 phase which partially wets the interface. The presence of Fe in solution in the Ni was found to reduce the activity of the Cr atoms, thus reducing the amount of adsorption to the interface, and preventing the formation of Cr_2O_3. Furthermore, the same orientation relationship was found in both doped systems as in the un-doped system, regardless of the significant change in the equilibrium crystal shape.

These results strengthened the conclusion that the concept of coherent-incoherent interfaces as a means for describing interface atomistic structure is over simplified, where the concept of interfacial reconstruction is more complete, and serves to connect the atomistic structure to a thermodynamic description of the equilibrium interface state. These findings will be compared to the *reconstructed* Ni-Al_2O_3 interface, and the concept of diffuse order at interfaces within the general diffuse interface model.

References:

[1] WL Winterbottom, Acta Metallurgica **15** (1967), 303.
[2] H Nahor, H Meltzman and WD Kaplan, Journal of Materials Science **49** (2014), 3943.
[3] H Nahor and WD Kaplan, Journal of the American Ceramic Society **99** (2016), 1064.
[4] This research was partially supported by the Israel Science Foundation (grant 381/14).

Profile Imaging: 35 years Old and Still Truckin

Laurence D. Marks

Department of Materials Science and Engineering, Northwestern University, Evanston, IL 60201, USA

When the first high resolution electron microscopes started to come on line in the early 1980's, it became possible to image most to all materials at the atomic scale. Fairly rapidly it was recognized that one could view materials in a profile imaging mode and obtain detailed atomic structure including, for instance, surface reconstructions. This was because the lanthanum hexaboride sources used in those days did not suffer from delocalization (which modern, more coherent field sources do), and because of channeling.

While the method quickly became a staple in heterogeneous catalysis research, most metals have rather boring 1×1 surfaces so there is nothing particularly exciting to image. Over the last several years, there has been an increase in interest in a different class of materials, oxides. Part of this is because it is easier to obtain images with aberration-corrected microscopes, although sometimes the images are no better than those from decades ago. More significantly, oxides for their own sake have been growing in importance. Oxides often have much more complex surface structures, and in some cases more classic surface science approaches have difficulties decoding the atomic details.

In this talk I will look at some of the recent progress, mainly work from within my own group on the surfaces of $SrTiO_3$, $LnScO_3$ (Ln=rare earth), $KTaO_3$ and others. Provided one can overcome the (not new) issue of radiation damage, particularly radiolytic damage, there is a vast amount to do -- not just electron microscopy imaging but also understanding why different types of surfaces form. Some of the current unknowns, including discrepancies between measured positions and the results of density functional calculations will be briefly discussed.

In Situ High Resolution and Transmission Environmental Electron Microscopy of Material Reactions

Robert Sinclair, Yunzhi Liu, Sang Chul Lee and Ai Leen Koh

Dept. of Materials Science & Engineering, Stanford University, Stanford, CA 94305-4034, U.S.A.

There has been a steady growth in the applications and breadth of in situ transmission electron microscopy (TEM) since the 1980's [1]. At that time, the procedures to carry out meaningful experiments were described (e.g. [2]) but it was thought that high voltage TEM and thick specimens were required to reproduce bulk behavior. However, in a series of studies, we established that this was not necessarily the case and that even high resolution TEM recordings could be made in real time, in situ and that the atomic behavior associated with materials reactions at interfaces could be deduced (e.g. [3], [4]). Moreover, with the advent of thin film and nanotechnology, the investigation of thin and nano-scale materials became a necessity (e.g. [5]). In recent years, there has been an additional proliferation, most notably from in situ TEM in controlled environments such as in gases and liquids (e.g. [1], [6]).

This paper reviews the application of in situ high resolution TEM to investigate material reactions. An overarching theme of our work has been to ensure that the in situ studies are truly representative of the real behavior of the material system, and we have advanced a number of guidelines to ensure this. [3,7] Moreover, we have also expanded our approach to environmental material-gas reactions such as carbon nanotube (CNT) oxidation [8], hydrogen reactions with molybdenum sulphide catalysts, etc. [9] (e.g. Fig.1). The influence of the imaging electron beam is more important for the gaseous reactions, as the beam ionizes the reacting gas species, and it is necessary to develop protocols to take this into account. [10,11] The procedures we have adopted to do this will be described.

References:

[1] R Sinclair, Mats. Res. Soc. Bull. **38** (2013) 1065-1071.

[2] EP Butler and KF Hale in "Practical Methods in Electron Microscopy", Vol. 9, ed. AM Glauert (North-Holland Pub. Com., New York).

[3] R Sinclair *et al*, Acta Crystallogr. Sec. A **44** (1988), 965-975.
[4] TJ Konno and R Sinclair, Philos. Mag. B **71** (1995), 179-199.
[5] K. H. Min *et al*, Philos. Mag. **85** (2005), 2049-2063.
[6] AL Koh, SC Lee and R Sinclair in "Controlled Atmosphere Transmission Electron Microscopy - Principles and Practice", eds. TW Hansen and JB Wagner (Springer Publishing Company, New York), 2016, pp.3-43.
[7] DH Ko and R Sinclair, Ultramicroscopy, **54** (1994), 166-178.
[8] AL Koh *et al*, ACS Nano **7** (2013), 2566-2572.
[9] SC Lee *et al*, ACS Nano **10** (2016). 624-632.
[10] AL Koh *et al*, Nano Lett. **16** (2016), 856-863.
[11] AL Koh and R Sinclair, Ultramicroscopy **176** (2017), 132-138.
[12] Financial support from the CCNE-TD (NCI-NIH Grant # U54 CA151459) and Toyota Research Institute – Accelerated Materials Design and Discovery program (Stanford University) is much appreciated.

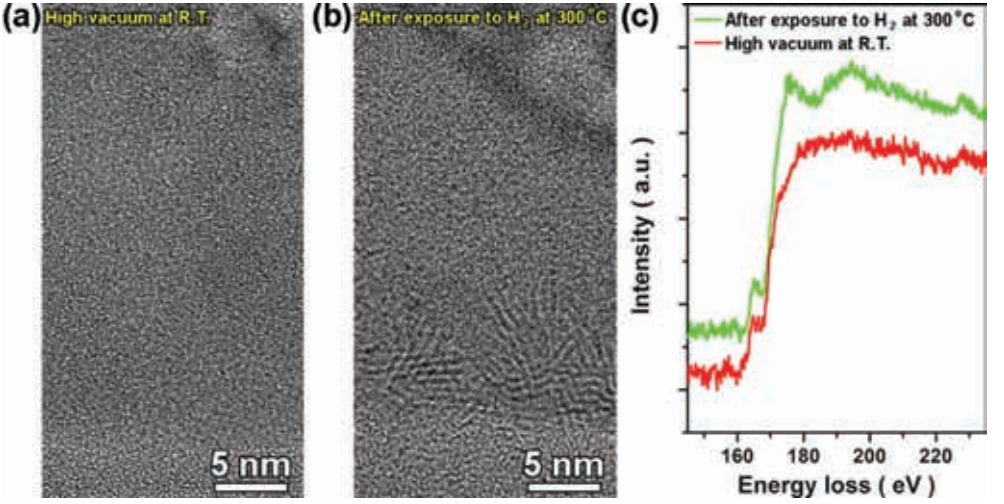

Figure 1. High resolution TEM images of amorphous molybdenum sulphide before (a) and after (b) hydrogenation in the environmental TEM, showing the formation of crystalline disulphide regions. (c) Electron energy loss spectra showing the characteristic sulphur edge for crystalline MoS_2 in the latter.

Atomic Mechanisms of Grain Boundary Migration in Au Bicrystals

Tamara Radetic[1] and Ulrich Dahmen[2]

[1] Faculty of Technology and Metallurgy, University of Belgrade, Serbia
[2] Molecular Foundry - NCEM, LBNL, Berkeley California 94720 USA

The mobility of interfaces is critical for the stability of a material microstructure and properties. In-situ observations of grain boundary motion by transmission electron microscopy provide direct insight into underlying migration modes and mechanisms. In this work, we report on observations of the motion of grain boundaries in Au thin films on the atomic scale. Study of the migration dynamics of grain boundaries in {110} and {111} mazed bicrystal films [1] covers the behavior of the boundaries at opposite ends of coincidence lattice space: low coincidence site Σ99 and low energy Σ3 boundaries.

In {110} mazed bicrystal films, misorientation of the grains is defined by 90° around the <110> axis. A pronounced anisotropy enforces pure tilt character for all boundaries. Morphology of grains ranges from complex convoluted shapes with both concave and convex sections to small convex island-like grains. Statistical analysis of grain boundary shape on mesoscopic and microscopic levels showed a tendency toward faceting on low-index crystal planes (Figure 1). During thermal annealing, under capillary forces, grain boundaries migrate eliminating the high curvature or unfavorable inclinations. HREM observations [2] showed that grain boundaries in Au and Al move by a glide, step motion and cooperative shuffles. All three mechanisms were observed to be active during a grain boundary migration in {110} mazed bicrystal grains. Glide has been observed during migration of B-facets as 9R dissociation provides continuity of {111} planes in both crystals and dislocation nature of the grain boundary [3]. However, step motion appears to be most prominent mode and rate controlling mechanism.

The dynamics of boundary motion was found to be limited by nucleation and propagation of steps on C-facets, an asymmetrical {110}|{100} grain boundary (Figure 1). The boundary is incommensurate since a ratio of interplanar spacing of (001) and (110) planes meeting at the interface is irrational √2. The migration

of the C-facet can take place by lateral motion of steps heterogeneously nucleated at the facet junctions. Characterization over hundred steps showed that the heights range from 1|1 to 7|10 (*in n|m notation n and m are the numbers of {100} and {011} planes in the two grains ending at the step*). The mobility of the steps appears to be a function of their height. The steps with small height and odd|even parity such as 1|2 and 2|3, show greater mobility and ability to fluctuate back and forth, while steps such as 4|6 and pure step 5|7 are more stationary and move unidirectionally.

In addition to lateral motion of the steps, the C-facets can advance perpendicularly to itself in discrete jumps of 7|5 or 6|4 {110}|{001} interplanar spacing. The jumps occur within a single frame of TV rate camera (33 ms), so temporal resolution of Gatan K2-IS direct electron detection camera (2.5 ms per frame) was necessary to gain more detailed insight. The appearance of Moiré pattern in the internment frames between the beginning and the end of the jump (Figure 2) indicates that an overlap between two grains takes place during the jump. It looks like that the jump proceeds by formation and progression of a buried step in the grain boundary plane perpendicular to the film surface.

The microstructure of <111> mazed bicrystal films consists of strongly faceted grains in two twin-related variants. Morphology of the film is more complex with the majority of the boundaries being tilt {112} incoherent twin boundaries connected by the short stretches of horizontal facets parallel to the standard {111} coherent twin plane. In the initial stages of the grain boundary migration occurs by lateral step motion. In contrast to the {110} bicrystals, the height of step is not limiting factor for its mobility, and multiatomic layer steps are not only highly mobile and can fluctuate, but, due to the equivalency of the planes forming a ledge, lateral motion can take place along the either of facets at the junction. Once steps are eliminated and facets coarsen, they can become immobile for an extended period until sudden motion of a whole facet is triggered. Recent simulations of migration of flat and stepped boundaries show that in the migration is controlled the nucleation of islands or double kinks [4]. The absence of experimental evidence for step formation in the imaging plane, suggests for the role of buried steps in triggering the motion as in case of C-facets of <110> island grains.

References:

[1] KH Westmacott, S Hinderberger and U Dahmen, Phil. Mag. **A81** (2001), 1291.
[2] K Merkle, L Thompson and F Phillipp, Interface Sci. **12** (2004), 277.
[3] DL Medlin, SM Foiles and D Cohen, Acta Mater. **49** (2001), 3689.
[4] R Hadian *et al*, Phys. Rev. B **94** (2016), 165413.
[5] This work, at the Molecular Foundry – NCEM, was supported by the Office of Science, Office of Basic Energy Sciences , of the U.S. DOE under Contract No. DE-AC02-05CH11231.

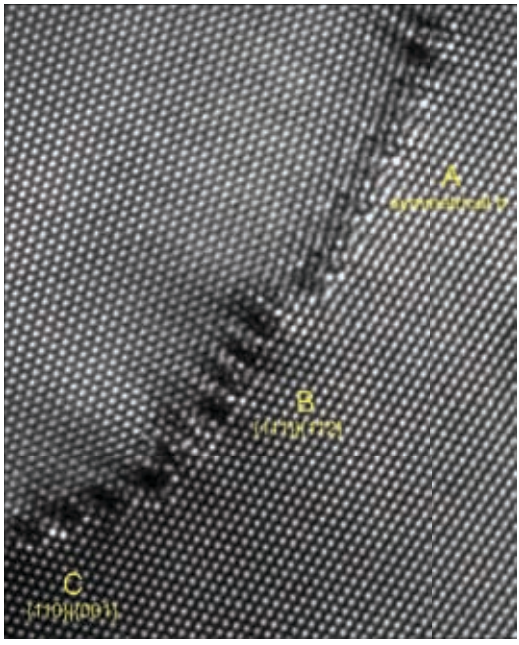

Figure 1 The boundary in {110} mazed bicrystal with 3 major facet inclinations.

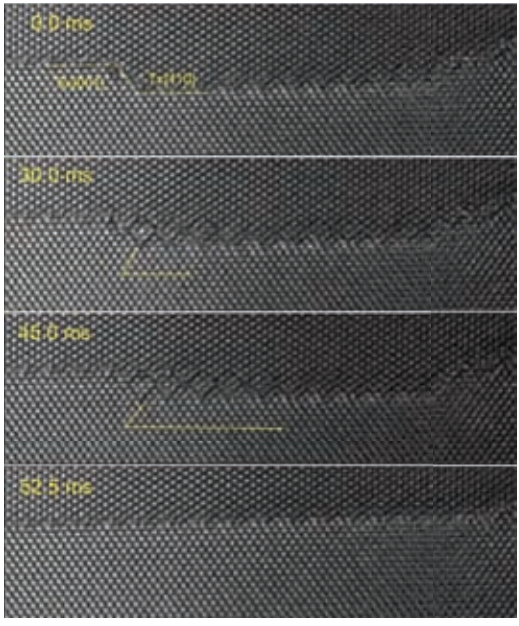

Figure 2 Facet jump recorded by K2 camera and propagation of the buried step.

On the Degradation of PtNi Nanocatalysts for PEM Fuel Cells: An Identical Location Aberration-corrected TEM Study

Somaye Rasouli[1], Tsuyohiko Fujigaya[2], Naotoshi Nakashima[2], Paulo Ferreira[1,3,4]

[1]*Materials Science and Engineering Program, University of Texas at Austin, Austin TX 78712, USA*
[2] *Department of Applied Chemistry, Kyushu University, Fukuoka 819, Japan*
[3] *INL-International. Iberian Nanotechnology Laboratory, Braga, Portugal*
[4] *Mechanical Engineering Department and IDMEC, Instituto Superior Técnico, University of Lisbon, Lisboa, Portugal*

Proton exchange membrane fuel cells (PEMFCs) are promising energy conversion devices for transport and stationary applications. Pt nanoparticles (NPs) are currently used as the catalyst to promote the kinetics of the hydrogen oxidation and oxygen reduction reactions in the anode and cathode of the fuel cell, respectively. However, Pt-based alloys are being investigated to replace Pt on the cathode as a way to improve the efficiency of the fuel cell, and reduce cost [1]. Although the enhancement in the ORR activity of Pt alloys is well established, the durability of the catalysts remains the main issue for their commercialization.

In this context, the focus of this work is to understand the behavior of Pt-Ni nanoparticles during the various stages of fuel cell cycling. For this purpose a set-up was developed to simulate the effect of voltage cycling on the cathode side of the fuel cell. In this set up, Pt-Ni catalyst NPs supported on carbon were deposited on a gold TEM grid attached to a gold plate, which is used as a working electrode in a three electrode electrochemical cell. The NPs were cycled between 0.6 and 1.0 V in a N_2 saturated 0.1M $HClO_4$ liquid electrolyte. In this fashion, pre-defined locations of the electrocatalyst on the TEM grid were analyzed before and after cycling using an aberration-corrected JEOL ARM 200F.

Fig. 1a shows that single atoms and atomic clusters appeared on the surface of the carbon support after voltage cycling as a result of surface dissolution of nanoparticles. As a result, single atoms move on the surface of the carbon support and redeposit on the surface of larger particles through modified Ostwald ripening [2]. Fig. 1b shows the surface re-deposition of single atoms on a (111) plane of a large particle. In

some cases, a NP exhibits both dissolution and re-deposition at the same time. This is illustrated in Fig. 2, where atoms on surface steps are dissolved during voltage cycling, while new (111) facets are formed on the surface of the NP.

These experiments also showed the heterogeneous deposition of Pt on NPs, as shown in Figures 3a and 3b (red squares 1 and 2). Initially, as there are no other particles nearby, the deposition of single atoms should have occurred, instead of coalescence. This heterogeneous deposition is likely due to the type of available surfaces in each NP. A high magnification image of the particle depicted in square 2 (Fig. 3b) is shown in Fig 3c. EDS mapping of this particle (Fig. 3d) confirms that the atomic re-deposition that occurred consisted of Pt and not Ni. Due to the low Ni/Ni^{2+} redox potential and low enthalpy of mixing of Pt-Ni, re-deposition of Ni on the particles is not thermodynamically favorable.

References:

[1] SC Ball *et al*, ECS Transactions **11** (2007), 1267.
[2] S Chen *et al*, J. Phy. Chem. *C.* **113** (2009), 1109.

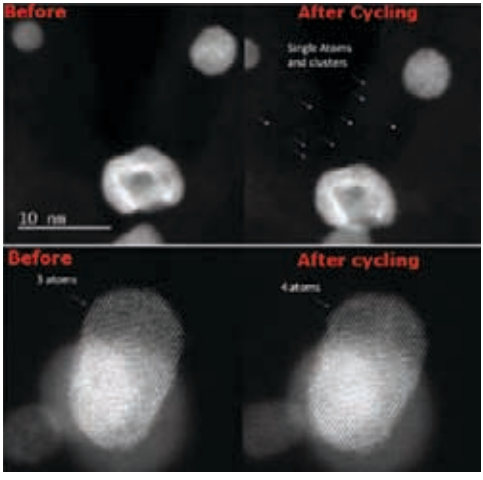

Figure 1. a) Appearance of single atoms and atomic clusters on the carbon support after voltage cycling, b) Deposition of a single atom on the surface of a nanoparticle.

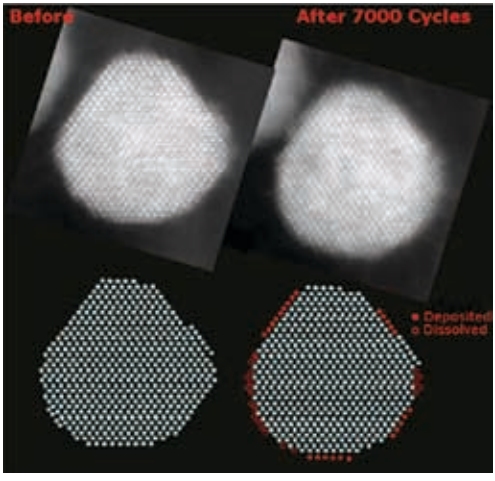

Figure 2. Dissolution and re-deposition of surface atomic layers before and after cycling.

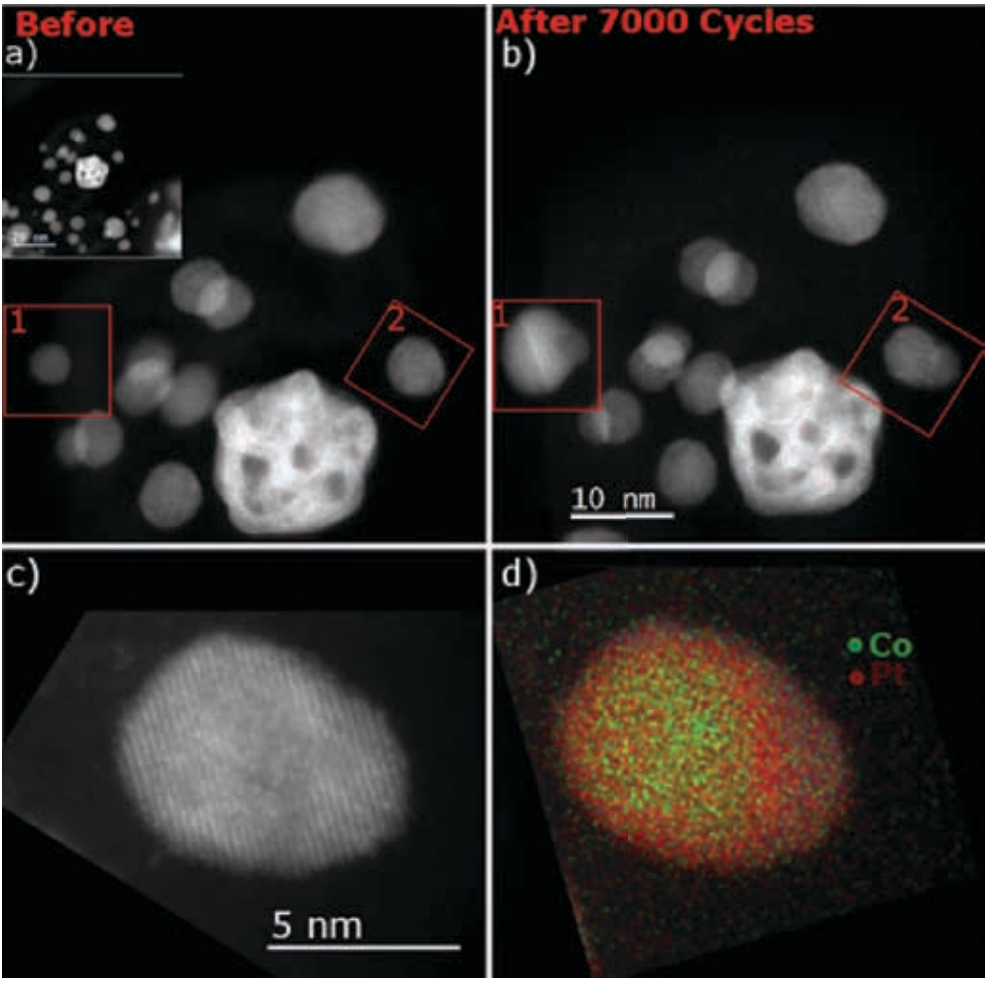

Figure 3. Aberration corrected HAADF images of PtNi nanoparticle a) before and b) after 7000 voltage cycles, c) and d), HAADF image and EDS mapping of the PtNi nanoparticle after 7000 voltage cycles.

Materials Under the Microscope: the Atomic Origin of Functionality

Stephen J. Pennycook, Xiaoxu Zhao, Jiadong Dan, Haijun Wu, Mengsha Li, Chunhua Tang, Changjian Li and Shoucong Ning

National University of Singapore, Department of Materials Science and Engineering, Block EA #07-24, 9 Engineering Drive 1, Singapore 117575

The aberration-corrected scanning transmission electron microscope (STEM) provides real space imaging and spectroscopy with unprecedented sensitivity down to the single atom level [1]. Thoroughly understanding and tailoring structural defects is extremely significant for understanding the structure-property relations of existing high-performance materials, and more importantly, guiding the design of new materials with improved properties. Several representative studies will be presented using the recently installed JEOL ARM200F at the National University of Singapore, which incorporates a cold field emission gun, ASCOR aberration corrector, UHR pole piece, Gatan Quantum ER spectrometer, OneView camera, hybrid detector and Oxford Aztec EDS system. In 2D materials, sub-Ångstrom information transfer can be achieved at only 40 kV, and point defects and their local environments directly identified to correlate with properties (Fig. 1). New edge structures in nanoporous MoS_2 are found to exhibit excellent catalytic properties [2], and 2D Mo metal membranes can be fabricated from $MoSe_2$ films via beam induced sputtering of Se [3]. In addition, beam induced healing of holes can also be observed under certain conditions.

In piezoelectrics, owing to growing environmental concerns, the development of lead-free materials with enhanced properties is urgently required. Key to the academic problem is a lack of fundamental understanding of the actual mechanisms involved at the microscopic (unit cell) level. While it is understood that giant responses occur near structural phase boundaries, there has been no atomistic understanding of the origin of the response. Precise mapping of atomic displacements reveals a hierarchical nanodomain structure as the origin of excellent properties, the coexistence of ferroelectric phases inside nanodomains and gradual polarization rotation between

them (Fig. 2). Density functional calculations and phase field modelling confirm this scenario [4,5].

Similarly, in thermoelectrics, nanostructuring has been widely acknowledged as the most universal strategy to enhance thermoelectric properties. However, atomic-scale defects have usually been ignored due to the difficulty of quantifying them via traditional methods. With the new generation of aberration-corrected STEMs this has now become possible. For example, one of our recent achievements is to directly observe the intrinsic Pb vacancies and extrinsic Cu interstitials in the classic PbTe thermoelectric, so revealing the "magic" roles of Cu on synergistic optimization of phonon and carrier transport.[6] The hierarchical structure ranging from point defects through nanoscale and microscale precipitates results in a high-performance material with lattice thermal conductivity approaching the theoretical minimum [6].

Today's 5th-order aberration correctors can provide probe semi-angles up to 60 mrad which allows depth resolution at the nm-scale [7]. In a TiO_2 film grown on $LaAlO_3$, La is seen to have preferentially diffused along stacking fault intersections originating at an interface step. Simply by changing focus views at different depths can be directly resolved and compared to build a 3D structure model. Through image simulations the local La environment can be identified enabling modelling of its diffusion pathway.

References:

[1] W Zhou et al, Phys Rev Lett. 109 (2012), 206803.
[2] X Zhao et al, Nano Lett 18 (2017), 482–490.
[3] X Zhao et al, Adv. Mater. (2018), 1707281.
[4] T Zheng et al, Energy Environ. Sci. 10 (2017), 528–537.
[5] B Wu et al, J Am Chem Soc. 138 (2016), 15459–15464.
[6] Y Xiao et al, J Am Chem Soc. 139 (2017), 18732–18738.
[7] R Ishikawa et al, Applied Physics Letters 109 (2016), 163102.
[8] The authors would like to acknowledge funding from the National University of Singapore, and the Ministry of Education, Singapore under its Tier 2 Grant (Grant No. MOE2017-T2-1-129). The authors are grateful to their many collaborators on these projects.

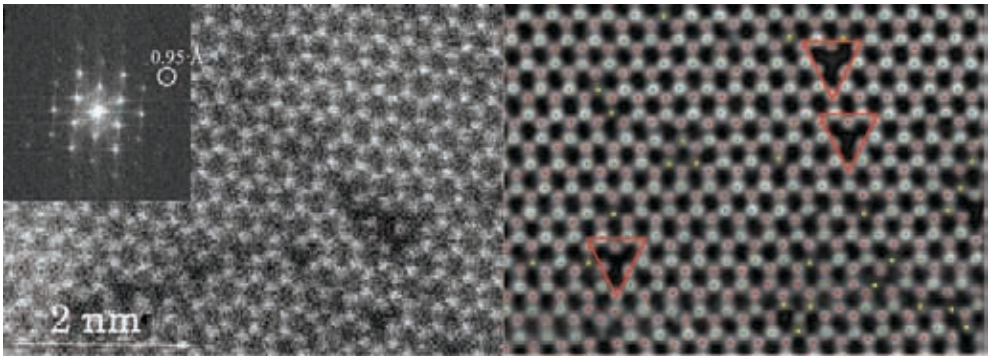

Figure 1. Left: STEM image of $MoSe_2$ obtained at 40 kV showing information transfer to 0.95 Å (inset fast Fourier transform). Right: A filtered image (not the same sample) showing identification of Mo (red), Se_2 (green), Se (yellow, single vacancy), and Se divacancies (red triangles). Data taken on a JEOL ARM200F with ASCOR corrector at 40 kV, courtesy Xiaoxu Zhao and Jiadong Dan.

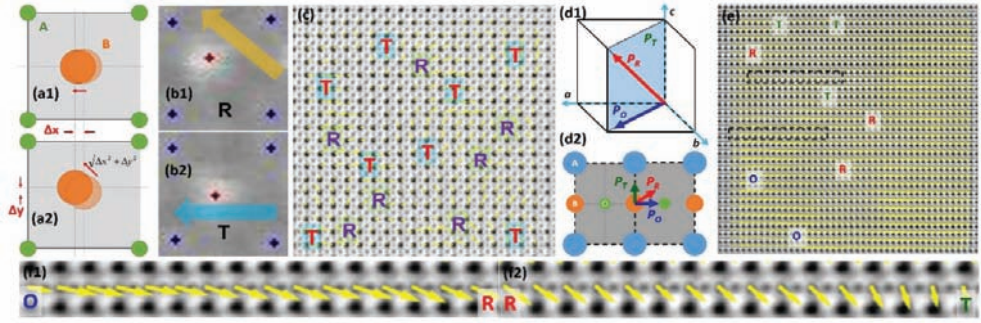

Figure 2. Structural models showing phase coexistence and gradual polarization rotation, (a1,a2) and (d1,d2); (b1,b2) STEM HAADF and (c) ABF images of KNN-based material with polarization map showing R+T phases; (e) ABF image of BT-based material with polarization map showing R+T+O; (f1,f2) Gradual polarization rotation between R, O, and T. Adapted from [4,5].

38

Possibilities of Differential Phase Contrast STEM to Study Functional Oxides

Rolf Erni, Marco Campanini, Marta Bon and Marta D. Rossell

Electron Microscopy Center, Swiss Federal Laboratories for Materials Science and Technology – Empa, Dübendorf, Switzerland

With the realization of segmented annular detectors for scanning transmission electron microscopy (STEM), differential phase contrast (DPC) has become a valuable method to study magnetic and electrostatic fields, complementing other methods with the same purpose such as off-axis and in-line electron holography. An electrostatic field in the sample plane leads to a shift of the center of mass of the transmitted beam. Acquiring an annular STEM signal split in four azimuthal segments allows for qualitatively measuring the change of the center of mass and thus for mapping phase and amplitude of the electrostatic field. Integration (iDPC) and differentiation (dDPC) of the DPC signal yields the projected electrostatic potential and the electric charge, respectively.

In order to shed light on the contrast of DPC images we investigated differential DPC (dDPC) STEM images of $DyScO_3$ (DSO). The complex pattern observed in experimental data of DSO is difficult to relate to the material's charge distribution and thus indicates that the image formation in DPC STEM might significantly be affected by dynamic scattering. We carried out extensive simulations using a custom-written frozen-phonon multi-slice algorithm [1] which we expanded to use as input total-potential electronic-structure data from density functional theory (DFT) calculations. These DFT-based DPC STEM simulations are compared with conventional simulations based on the independent atom model (IAM) using scattering factors of Weickenmeier and Kohl [2]. While there is marginal difference between simulations based on DFT data and the IAM, defocus, absorption, Debye-Waller factor and thermal diffuse scattering show a strong effect on dDPC images (see Fig. 1). We find that simulations based on the IAM including thermal diffuse scattering based on frozen phonons provide the best match with the experimental data.

Being aware of the complexity of the image formation of DPC STEM, we aimed at investigating to what level relevant data can be extracted from complex functional oxides. Using annular bright field (ABF) and high-angle annular dark field (HAADF) STEM, we find that Ca-doped $BiFeO_3$ (BFO) exhibits a complex modulated and locally ordered structure which is due to the arrangements of Ca ions and the corresponding oxygen vacancies [3]. While in Ca-rich areas, the ferroelectric polarization of BFO is largely suppressed, in Ca-poor areas the native ferroelectric polarization of BFO is maintained. As a consequence, the ferroelectric polarization of Ca-doped BFO is modulated yielding a giant polarization gradient of up to 70 μC cm^{-2} across the 3 nm thick domains.

While the ferroelectric polarization was mapped indirectly by measuring local atomic displacements by ABF and HAADF STEM, atomic-resolution DPC STEM should provide an alternative way to measure ferroelectric domains directly. The atomically resolved DPC signal of Ca-doped BFO shows in the Ca-rich areas, i.e. where the ferroelectric polarization is suppressed, doughnut-shaped signals at each atomic column, while in the Ca-poor areas the azimuthal symmetry of the doughnuts is broken, particularly pronounced at Bi sites (see Fig. 2). As the ferroelectric polarization in BFO is caused by a lone electron pair of the Bi ions, the origin of the DPC pattern of BFO can be a complex interplay between the “macroscopic” ferroelectric polarization and the local electronic structure at each atomic site.

We find that experimental parameters (aberrations and sample tilt) can destroy the symmetry of the doughnut-shaped atomic column DPC signal, but superimposing the macroscopic electrostatic field on the atomic column potential provides the most likely reason for the observed asymmetry.

References:

[1] R Erni, H Heinrich and G Kostorz, Ultramicroscopy **94** (2003), 125.
[2] A Weickenmeier and H Kohl, Acta Cryst. A**47** (1991), 590.
[3] M Campanini *et al*, Nano Lett. **18** (2018), 717.
[4] This project has received funding from the European Research Council (ERC) under EU’s Horizon 2020 research and innovation program (Grant Agreement No. 681312). Carlo Pignedoli and Kristjan Eimre of the computational group at Empa are acknowledged for providing support for the DFT data.

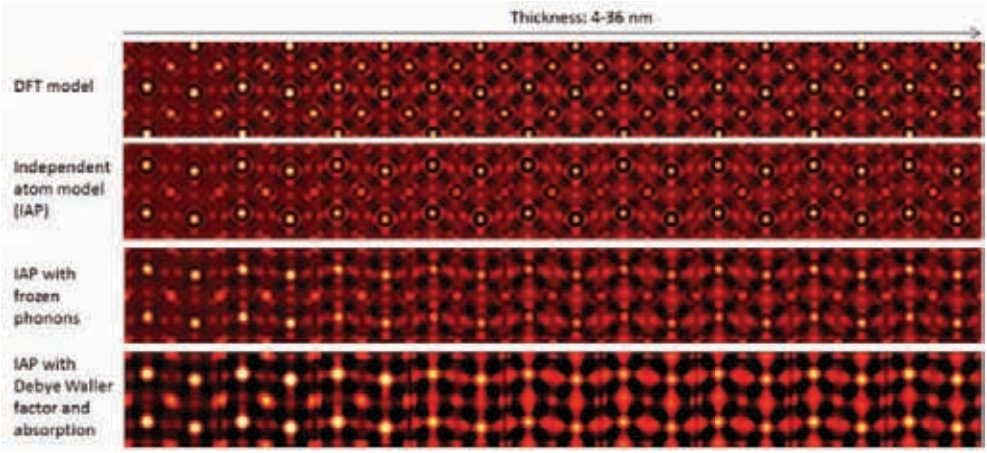

Figure 1. Multi-slice simulations of dDPC images of $DyScO_3$ using different approaches.

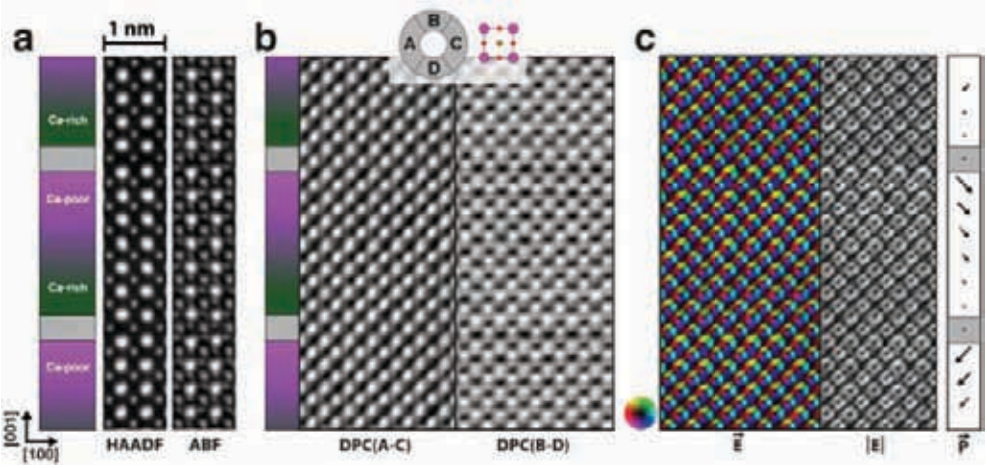

Figure 2. Experimental DPC-STEM analysis of the polar structure of the $BiFeO_3$ film. (a) HAADF and ABF signals, (b) DPC differential signals, c) plot of the electric field vector and amplitude.

High Resolution STEM-EELS Mapping of Magnetic Quantities Across Oxide Multiferroic Interfaces

Javier Grandal[1], Juan I. Beltran[1], Gabriel Sanchez-Santolino[2], Fernando Gallego[2], Javier Tornos[1], Carlos Leon[1], Jacobo Santamaria[1], M. Carmen Muñoz[2], and Maria Varela[1]

[1] *GFMC, Dept. de Fisica de Materiales, Universidad Complutense de Madrid, 28040 Madrid, Spain*

[2] *Instituto de Ciencia de Materiales de Madrid, Consejo Superior de Investigaciones Científicas, Cantoblanco 280409, Madrid. Spain*

Complex oxides with a perovskite structure show a wide range of interesting properties due to a strong interplay and competition between lattice, spin, and charge degrees of freedom. In these systems, subtle changes in local structure or chemistry may result in colossal responses in macroscopic physical behaviors. In addition, high quality epitaxial heterostructures based on perovskite complex oxides can be grown where novel macroscopic functionalities arise. This is the case when oxide materials exhibiting different ferroic orders are combined. In this talk we will apply atomic resolution aberration corrected scanning transmission electron microscopy (STEM) and electron energy-loss spectroscopy (EELS) to the study of the structure and properties of magnetic oxide heterostructures. Thanks to spherical aberration correction, both spatial resolution and sensitivity limits attainable in the STEM have improved down to the single-atom level, resulting in unprecedented contrast and signal-to-noise ratio improvements in both imaging and EELS. Here, we will discuss a few examples where these techniques hold the key to understanding macroscopic functionalities in these systems.

A first example involves local measurements of electronic and magnetic properties of ferromagnetic manganite $La_{0.7}Sr_{0.3}MnO_3$ (LSMO) epitaxial ultrathin films grown by high-pressure O2 sputtering on single crystal $SrTiO_3$ (STO) substrates. We will combine STEM-EELS with density-functional calculations to study local structural distortions and electronic phenomena associated with interfacial magnetism. Atomic resolution images exhibit an increase of the out-of-plane lattice parameter at the LSMO/STO interface plane, pointing to a local reconstruction of the charge density

and, hence, physical properties. We use energy-loss magnetic chiral dichroism (EMCD) [1], a technique directly sensitive to the local magnetic moment, to track magnetic quantities across the interface with sub-unit cell resolution. The dichroic signal at both the Mn L2,3 and the Ti L2,3 edges is enhanced near the interface, pointing to a local increase of the Mn and Ti magnetic moments. These results agree with density-functional theory simulations including interfacial oxygen vacancies, which enhance charge transfer and antiferromagnetic coupling between the Ti and the Mn.

A second example can be found in the study of the electronic and magnetic properties of ferromagnetic /ferroelectric interfaces where ultrathin ferroelectric BaTiO3 (BTO) barriers are sandwiched between ferromagnetic LSMO electrodes. We will use atomic resolution STEM-EELS to obtain maps of the local electronic and magnetic properties in order to understand the phenomena giving rise to coupling across the interfaces and, hence, multiferroic behavior. Real space measurements of local polarization will be compared to magnetic quantities. Again, high spatial resolution EMCD measurements obtained at low temperature (<100K) allow studying the local magnetization of the interfaces in a unit cell–by–unit cell fashion [1, 2], see Figure 1. On the other hand, the quantification of local ferroelectric polarization is possible through the analysis of atomic resolution annular bright field images [3]. Both local magnetization and polarization measurements will be discussed in the light of electronic properties such as interface charge transfer and orbital anisotropy through density-functional theory calculations.

References:

[1] P Schattschneider *et al*, Nature **441** (2006), 486-488.
[2] J Salafranca *et al*, Nanoletters **12** (2012), 2499-2503.
[3] G Sanchez-Santolino *et al*, Nature Nanotechnolgy **12** (2017), 655-662.
[4] Research at UCM sponsored by Fundación BBVA and Spanish MINECO/ FEDER MAT2015-66888-C3-1-R & MAT2015-66888-C3-3-R and by the ERC Proof of Concept Grant POLAR-EM.

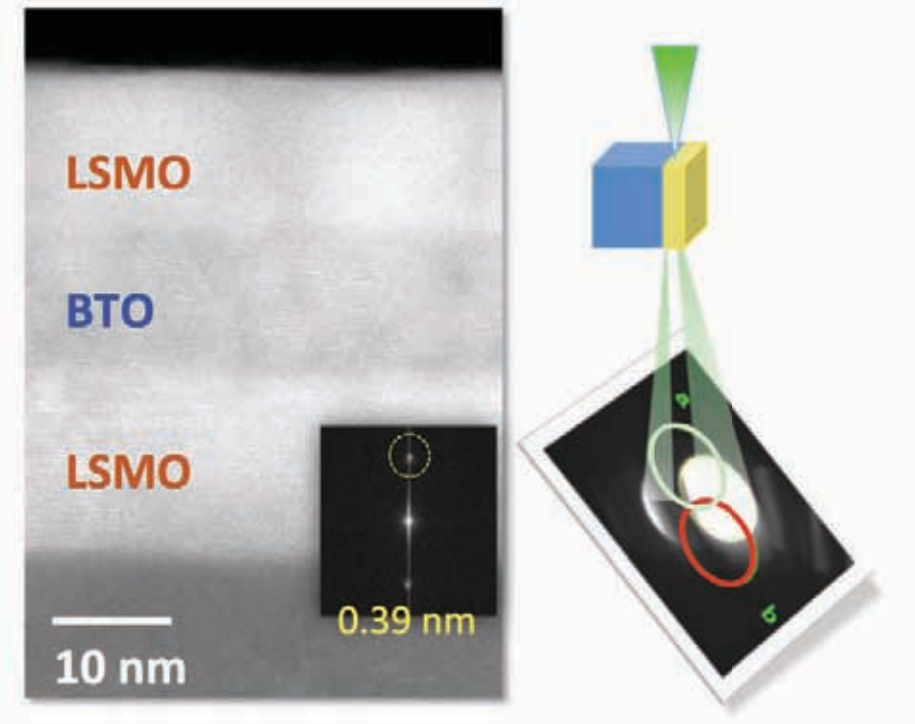

Figure 1. (left) High angle annular dark field image of a LSMO/BTO/LSMO epitaxial trilayer grown on a STO substrate interface acquired at 97K after setting up the electron microscope for an EMCD experiment. The inset exhibits the Fourier transform of the image. (Right) Schematic describing the experimental set up. The convergent electron beam reaches the sample after tilting the specimen to find two beam diffraction conditions. The two beam polarizations are then obtained by effectively coupling the two different conjugate positions in the nanodiffraction pattern (a and b) to the EEL spectrometer. Data acquired in an aberration corrected JEOL ARM200cF operated at 200 kV.

Microstructure Tailoring of Oxide Thermoelectrics to Increase the Figure of Merit (ZT) Value

Miran Čeh[1,3], Marja Jerič[1,2], Johannes de Boor[4], Mateja Košir[1], Slavko Bernik[1], Cleva Ow-Yang[5], Mehmet Ali Gülgün[5]

[1] *Department for nanostructured materials, Jožef Stefan Institute, Ljubljana, Slovenia.*
[2] *Jožef Stefan Postgraduate School, Ljubljana, Slovenia.*
[3] *Center for Electron Microscopy and Microanalysis, Jožef Stefan Institute, Ljubljana, Slovenia.*
[4] *Department of Thermoelectric Materials and Systems, Institute of Materials Research, Cologne, Germany.*
[5] *Materials Science & Engineering, Sabanci University, Tuzla, Istanbul, Turkey.*

Figure of merit (ZT) of oxide-based TE materials can be improved by modifying the microstructure of these materials in order to influence the crucial factors affecting the ZT, i.e. Seebeck coefficient, electrical conductivity and thermal conductivity. It has been shown that by introducing planar faults into the microstructure one can significantly reduce the thermal conductivity of oxide thermoelectric materials thus increasing the ZT value. In our work we studied the influence of incorporated planar faults on thermal conductivity in the following materials: $Sr(Ti_{0.8}Nb_{0.2})O_3$ (STN) and ZnO. In the STN the planar faults were incorporated with the addition of CaO and SrO, while in ZnO the planar faults were obtained with the addition of In_2O_3/Al_2O_3. All microscopic investigations were performed in Jeol 2010F and Jeol ARM-200CF with Cs probe corrector while thermoelectric measurements were carried out as described in reference [1].

The microstructure analysis of the STN samples revealed that the addition of CaO into the STN resulted in the formation of Ruddlesden-Popper-type (RP) planar faults with a rock salt-type structure. These RP that formed either random 3D networks consisting of single RP faults along {001} STN crystallographic planes or formed more or less ordered polytypoidic sequences with a general formula $(Sr,Ca)O_{*}n(Sr(Ti,Nb)O_3)$ (Fig. 1a). HAADF analysis of the perovskite matrix additionally

showed that the Nb content on the Ti sites in this perovskite structure largely varied and that no ordering on B-sites was observed. Furthermore, the concentration of Ca at the RP faults was always higher as compared to the STNO matrix (Fig. 1b). This was attributed to preferential incorporation of smaller Ca ions into the rock-salt-type structure of the RP faults. The thermoelectric measurements showed that thermal conductivities of CaO-doped STN samples were app. twice lower as compared with the undoped STN (Figure 1c).

In In_2O_3-doped ZnO ceramics pure indium monolayers were readily observed by the HAADF STEM. These basal inversion domain boundaries (IDB's) run parallel to the {0001} ZnO lattice planes and separate domains with different orientation (Fig. 2a). Thermoelectric measurements confirmed that the thermal conductivity of the ZnO decreased with the increasing addition of In_2O_3 which resulted in increased ZT value (Fig. 2b). Our investigation showed that in-growth planar faults reduced thermal conductivity in both investigated materials systems and that by such nanostructured modifications of the material it is possible to improve the ZT value in oxide-based thermoelectric materials.

References:

[1] M Jerič *et al*, J. Eur. Ceram. Soc. **36** (2016), 1177.
[2] M Košir *et al*, J. Am. Ceram. Soc. **100** (2017), 3712.
[3] M Jerič *et al*, J. Mater. Sci. **51** (2016), 7660.

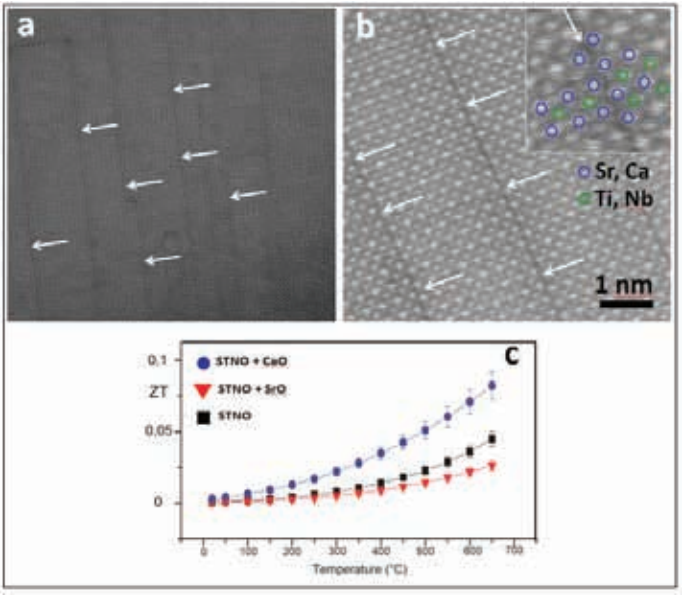

Figure 1. (a,b) HAADF STEM images of CaO-doped STN showing Ruddlesden-Popper-type planar faults in STN grains, and (c) ZT values of pure and doped STN.

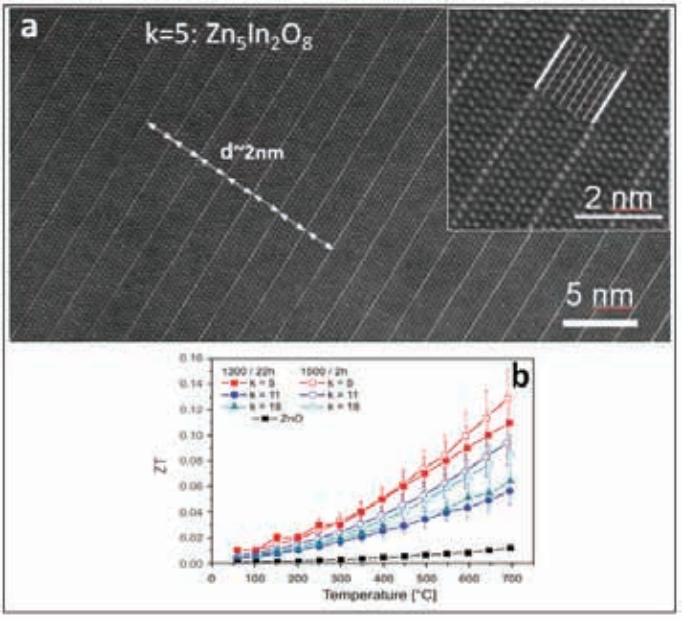

Figure 2. (a) HAADF STEM images of In-doped ZnO. Ordered In-rich IDB's are clearly resolved by higher intensity. (b) ZT values for different In_2O_3 content show increased value as compared with pure ZnO.

Single Atom Spectroscopy in Low-Dimensional Materials Using Low-voltage STEM

Yung-Chang Lin, Ryosuke Senga, Junhao Lin, Luiz Tizei and Kazu Suenaga

National Institute of Advanced Industrial Science and Technology (AIST), Central 5, 1-1-1 Higashi, Tsukuba, Ibaraki 305-8565, Japan

In this presentation, single atom spectroscopy by means of EELS and EDX will be demonstrated to discriminate individual atoms in low-dimensional materials. It has remained a challenge for scientists to see and identify individual atoms since Dalton first proposed distinct atoms in his atomic theory [1]. It is emphasized here that information on the bonding/electronic states has become accessible for single atoms through the EELS fine-structure analysis as well as the spin state. Such analysis was not possible until recently because of an intrinsic limitation, namely, the inevitable irradiation damage due to the huge number of electrons required to realize a high enough signal-to-noise ratio for fine-structure analysis from a single atom.

Properties of low-dimensional materials are largely influenced by its structural imperfections, such as defects, impurities, edges or boundaries. Hence, analytical technique at single atom level is becoming crucial to fully understand the physical/chemical performance of nano-devices. In my presentation, single atom spectroscopy by means of electron energy-loss spectroscopy (EELS) will be shown to discriminate individual atoms in low-dimensional materials at their interrupted periodicities. It is emphasized here that information of the bonding/electronic states has become accessible for single atoms through the EELS fine-structure analysis [1] as well as the spin state [2]. Large variations of local electronic properties of 1D and 2D materials with different atomic coordinates will be shown [3]. Such an analysis was applied to understand catalytic behavior of Co doped MoS_2 for hydrodeoxygenation reaction [4]. Furthermore, a high-energy resolution EELS offers us possibilities to obtain local optical/vibrational properties. Some of the recent examples for such experiments on low-dimensional nanomaterials will be also presented [5].

References:

[1] Y-C Lin *et al*, Nano Letters **15** (2015), 7408-7413; L Tizei *et al*, Phys. Rev. Lett. 114 (2015), 197602; R Senga *et al*, Nature Mat. **13** (2014), 1050.
[2] Y-C Lin *et al*, Phys. Rev. Lett. **115** (2015), 206803.
[3] Y-C Lin *et al*, Nano Lett. **17** (2017), 494-500; R Senga and K Suenaga, Nature Communications **6** (2015), 7943.
[4] G Liu *et al*, Nature Chem. **9** (2017) 810.
[5] J Lin *et al*, Nano Lett. **16** (2016), 7198-7202; L Tizei *et al*, Phys. Rev. Lett. **114** (2015), 107601; R Senga *et al*, Nano Lett. **16** (2016), 3661-3667.
[6] This research was supported by JSPS KAKENHI (JP16H06333 and JP25107003).

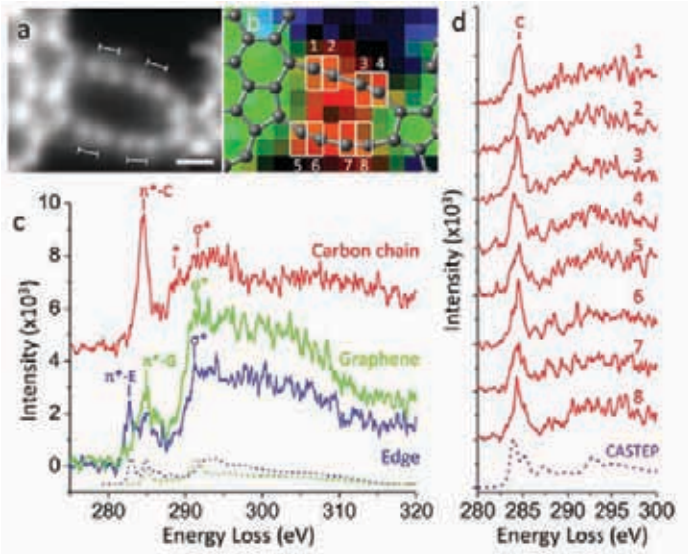

Figure 1. Atom-by-atom EELS on the carbon atomic chains. (a) ADF image of two parallel carbon chains. Scale bar is 2Å. (b) The corresponding EELS color mapping overlapped with the extracted atomic model. The 2D spectrum imaging contains 13 x 10 pixels in EELS map and simultaneous ADF image consists of subpixel scan (16 x 16). Three color indexes in the EELS color integrated with different energy widths correspond to sp1-chain (red, 283.4−284.5 eV), sp2-graphene (green, 284.6−299.6 eV), and graphene edges (blue, 281.4−282.9 eV). The acquisition time for each spectrum is 0.2s/pixel. (c) Spectra shown are extracted from the sum of 10 pixels from the EELS map shown in (b). The simulated EEL spectra of graphene and edge are presented by green and blue dashed lines, respectively. (d) Atom-by-atom EEL spectra corresponding to each atom in the carbon chain.

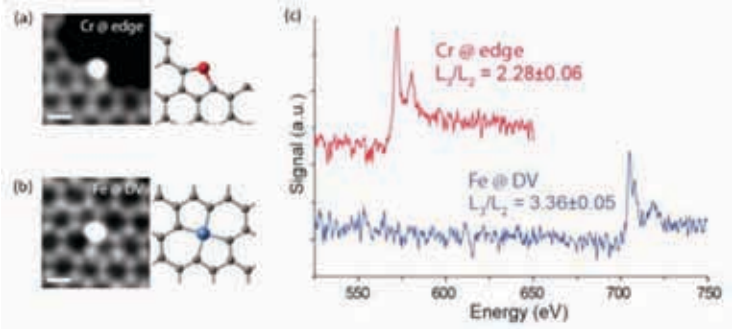

Figure 2. Single atom spin-stage spectroscopy [6]. (a)(b) Experimental ADF images and atomic structures of the Cr atom at the graphene edge (Cr@edge) and the Fe atom at divacancy (Fe@DV), respectively. (c) The EEL spectra of single TM atoms, Cr@edge, and Fe@DV. These two single TM atoms all exhibit a high-spin state based on the analysis of the L_3/L_2 branching ratio.

Quantitative Electron Microscopy At Atomic Resolution

Ferdinand Hofer[1,2], Daniel Knez[1,2], Werner Grogger[1,2], Georg Haberfehlner[1,2], Franz Schmidt[3], Mihaela Albu[2], Christian Gspan[2], Gerald Kothleitner[1,2]

[1] *Institute of Electron Microscopy and Nanoanalysis, Graz University of Technology, Graz, Austria*
[2] *Graz Centre for Electron Microscopy, Graz, Austria*
[3] *Institute of Physics, University of Graz, Graz, Austria*

Over the last years, aberration-corrected transmission electron microscopy (TEM) has revolutionized our understanding of nanostructured materials, devices and nanoparticles. At the centre of these developments is the scanning TEM (STEM), not only by the introduction of new and improved hardware and its flexibility, but also by the development of new techniques for data acquisition and analysis. In the meanwhile, many laboratories are equipped with Cs-corrected STEMs, which are able to provide atomic resolution imaging using HAADF and ABF detectors.

The Cs-corrected STEM also enables atomic-resolution mapping of chemical elements in materials thus allowing a direct correlation of structural and chemical information by means of EELS and EDX spectroscopy. While the principal acquisition of the data has become more straightforward, the data processing and interpretation are more challenging. For example, most atomically resolved elemental maps are only interpreted in a qualitative way. Therefore, we will show how it is possible to determine elemental concentrations in terms of volumetric densities [1]. This methodology allows quantifying the number of atoms in individual atom columns in a crystal, but only if all dynamical scattering effects are fully considered [2].

Additionally, we will show how electron tomography can be used for 3D elemental mapping using simultaneous EELS and EDX spectroscopy. This voxel spectroscopy approach has been first demonstrated at nanometre resolution [3], but in the meanwhile electron tomography has been even driven to atomic resolution. For example, recently we could elucidate the 3D morphology and composition of Ag/Au core/shell nanoparticles; the atomic positions were estimated without using any prior information and with minimal filtering [4]. The introduction of tomographic 3D EELS imaging is a new approach to study the plasmonic properties of 3D

nanostructures, such as the investigation of the photonic local density of states parallel to the electron trajectory [5,6].

Finally, we will describe new STEM studies about the dynamics of metallic clusters and single atoms on amorphous and crystalline surfaces. These experiments were performed on supported clusters grown inside superfluid He-droplets. For example, we could study the transformation of extremely small Ni-clusters into single crystalline NiO rings by an electron beam induced nanoscale Kirkendall effect (Fig.2) [7]. Furthermore, we present a new methodology for the simulation of beam damage processes of metallic clusters at atomic resolution using an algorithm based on molecular dynamics and Monte Carlo techniques [8].

References:

[1] G Kothleitner *et al*, Microsc. Microanal. **20** (2014), 678.
[2] G Kothleitner *et al*, Phys. Rev. Letters **112** (2014) 085501.
[3] G Haberfehlner *et al*, Nanoscale **6** (2014), 14563.
[4] G Haberfehlner *et al*, Nature Comm. **6** (2015), 8779.
[5] G Haberfehlner *et al*, Nano Letters **15** (2015), 7726.
[6] G Haberfehlner *et al*, Nano Letters **17** (2017), 6773.
[7] D Knez *et al*, Ultramicroscopy **176** (2017), 105.
[8] D Knez *et al*, Ultramicroscopy (in print).
[9] The authors acknowledge funding from the European Union within the 7th Framework Program (FP7/2007-2013).

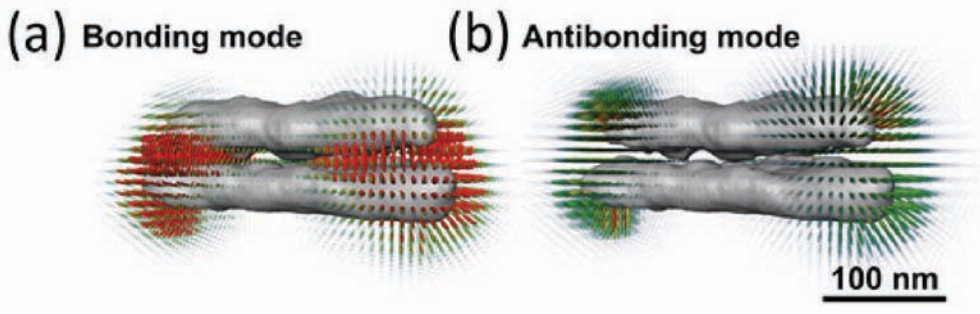

Figure 1 (a) 3D reconstruction of the photonic LDOS of gold nanoparticle dimers from tomographic STEM-EELS mapping; (a) low-energy (bonding) mode and (b) high-energy (anti-bonding) mode [6].

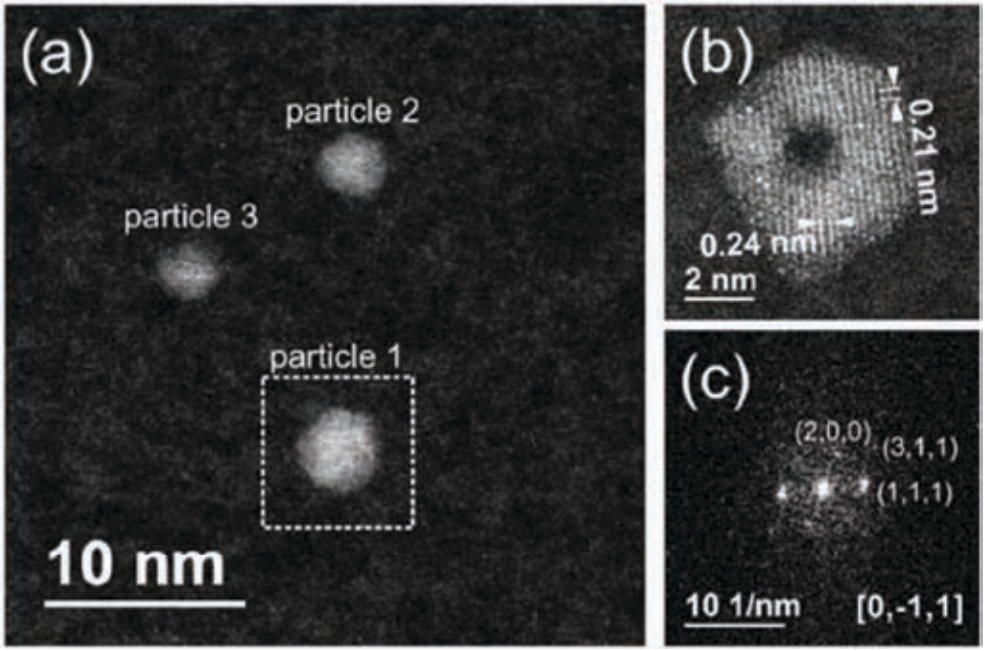

Figure 2 (a) HAADF overview image of three clusters on amorphous carbon before oxidation; (b) enlarged image of particle 1 after full transformation into a single crystalline NiO ring; (c) corresponding FFT from (b) [7].

Cryo-Electron Tomography - The Past, the Present and the Future

Juergen M. Plitzko

Max Planck Institute of Biochemistry, Department of Molecular Structural Biology, 82152 Martinsried, Germany

As a consequence of the 'resolution revolution' cryo-electron microscopy (cryo-EM) has become the most versatile method for structural biology. Advances made in instrumentation, in automation and in image processing over the recent past have expanded the capabilities of cryo-EM in a profound manner. Single particle cryo-EM (SPA) of isolated particles (*ex situ*) can deliver near-atomic resolution structures for large macromolecular complexes as well as for rather small proteins. SPA can be seen nowadays as an established method and has been awarded with the Nobel prize in chemistry in 2017. Although cryo-EM is not yet one of the high-throughput methods, the requirements in terms of user experience and measurement time are becoming ever less demanding. Equivalent to the beamlines in protein crystallography the first cryo-EM facilities/centers are being build up and put into operation. Of course, there is still room for further improvements in cryo-EM. The latest development of the Volta phase plate is a good example of this [1]. The clear phase contrast improves the selection and classification of the individual particles and thus also enables the structural determination of very small proteins that were previously inaccessible.

However, proteins have their biological function in the complex environment of the cell and interact with other macromolecules. The exciting potential of cryo-EM therefore lies in cryo-electron tomography (CET), the three-dimensional analysis of macromolecular and supramolecular structures in their functional cellular context (i. e. *in situ*). This method closes the gap between molecular and cytological structural research.

Thin samples are mandatory for any high-resolution tomographic study. 'Slicing' in the 21st century, to obtain electron transparent lamellas, can be done gently and in a targeted fashion with the focused-ion-beam instrument. Perhaps it is too early

to say that cryo-focused ion beam milling (cryo-FIB) is now the method of choice for obtaining 150-300 nm thin slices from a wide variety of cell types ranging from larger bacteria to neuronal primary cultures [2,3]. However, the method is certainly gaining momentum and in combination with direct detection and phase-plate assisted tomography, we are now able to explore the 'wonders' of the inner space of cells at molecular detail [4].

After a brief look back this lecture will present our recent work in the field of cryo-electron tomography and *in situ* structural biology and highlights technological developments, limitations and their opportunities. Furthermore, we will give a prospective towards obtaining structural insights from an *in situ* context at molecular resolution.

References:

[1] R Danev *et al*, PNAS USA **111** (2014), 15635-40.
[2] M Schaffer *et al*, Journal of Structural Biology **197** (2017), 73-82.
[3] J Mahamid *et al*, Journal of Structural Biology **192** (2015), 262-269.
[4] J Mahamid *et al*, Science **351** (2016), 969-972.
[5] P Erdmann, JM Plitzko and W Baumeister, Current Opinion in Coloid and Interface Science, Article in press (2018).

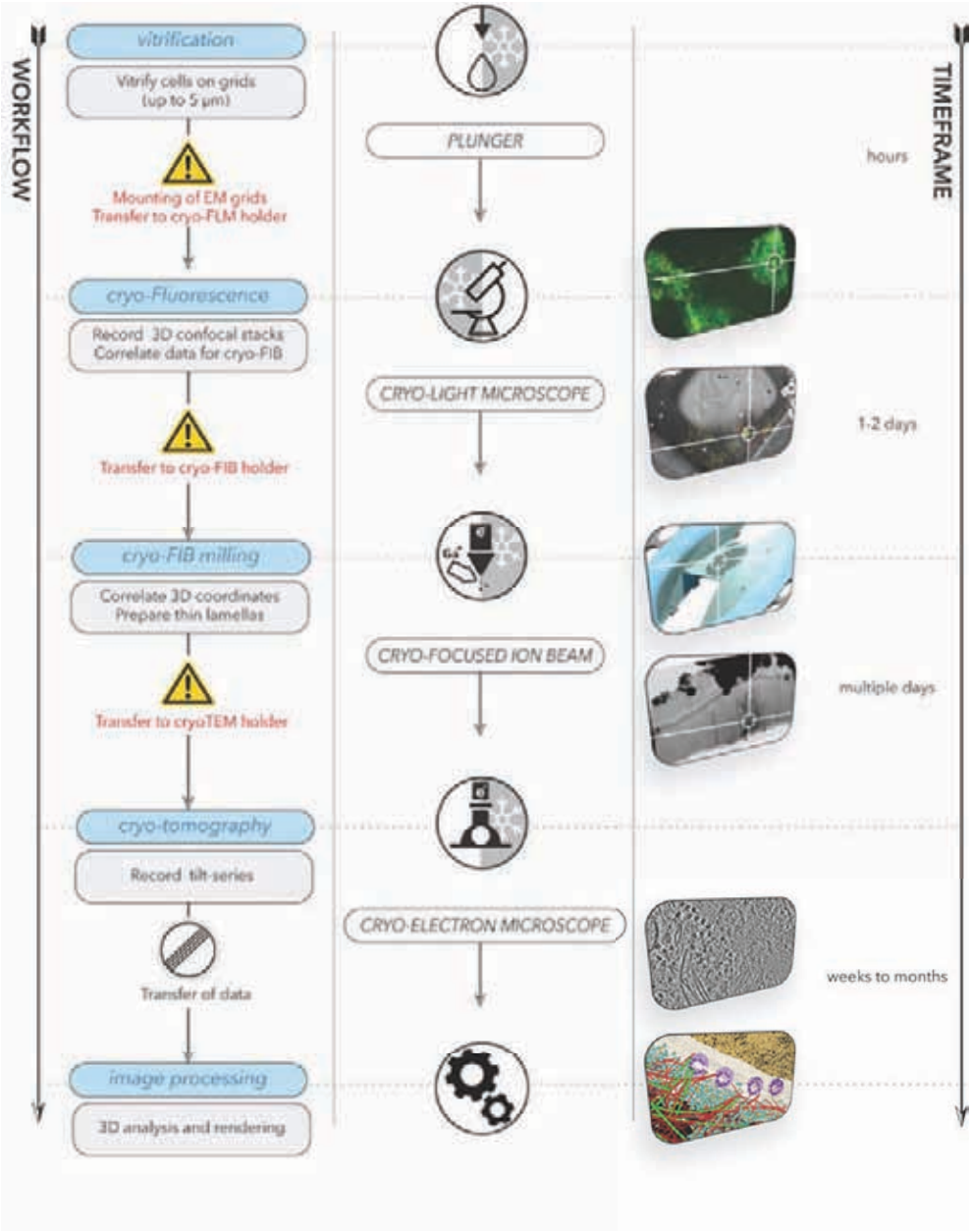

Figure 1. Cryo-electron tomography workflow including image analysis and computational processing [image adapted from 5].

PICO – Chromatic Aberration Correction and Applications in Materials Science

Joachim Mayer[1,2], Juri Barthel[2], Lothar Houben[2], Rafal Dunin-Borkowski[2] and Knut Urban[2]

[1] *Central Facility for Electron Microscopy, RWTH Aachen University, 52074 Aachen, Germany*
[2] *Ernst Ruska-Centre for Microscopy and Spectroscopy with Electrons, Research Centre Juelich, 52425 Juelich, Germany*

The invention of aberration correctors has revolutionized the development of TEM and STEM instrumentation. Only shortly after the development and installation of the first TEM with a corrector for the spherical aberration [1], commercial instruments with aberration correctors are now offered by all major manufacturers. In order to provide a platform for these novel developments and based on the experience with the first aberration corrected TEM [2-4], Research Centre Juelich and RWTH Aachen University have jointly founded the Ernst Ruska-Centre for Microscopy and Spectroscopy with Electrons (ER-C) [5]. At the Ernst Ruska-Centre we have recently installed the FEI Titan 60-300 PICO. PICO is a fourth-generation transmission electron microscope capable of obtaining high-resolution transmission electron microscopy images approaching 50 pm resolution in the C_C- and C_S-corrected mode at 300 keV. It is currently one of only two microscopes in the world capable of chromatic aberration correction [6-8].

In the present contribution we will report on the initial results obtained with the PICO instrument (Fig. 1b). In the PICO instrument, HRTEM images can be obtained with simultaneous correction of the spherical and the chromatic aberration. Furthermore, a spherical aberration corrector also exists in the illumination system for Cs-corrected STEM imaging. The blurring caused by the chromatic aberration C_c is proportional to the energy spread ΔE and inversely proportional to the primary electron energy E:

$$d_c = \frac{1}{2} C_c \frac{\Delta E}{E} \theta$$

where θ represents the aperture angle. The benefits of chromatic aberration corrected imaging are thus particularly large for HRTEM imaging at low accelerating voltages

and for energy filtered (EFTEM) imaging with large energy window width. In the present contribution we will focus on these two applications and will present results from our recent work, Fig. 1b.

References:

[1] M Haider *et al*, Nature **392** (1998), 768.
[2] M Lentzen *et al*, Ultramicroscopy **92** (2002), 233.
[3] CL Jia, M Lentzen, and K Urban, Science **299** (2003), 870.
[4] CL Jia and K Urban, Science **303** (2004), 2001.
[5] http://www.er-c.org
[6] B Kabius *et al*, J. Electron Microsc. **58** (2009), 147.
[7] H Rose, Philos.Trans.R.Soc.A: Math.Phys.Eng.Sci. **367** (2009), 3809–3823.
[8] M Haider *et al*, Microsc.Microanal. **16** (2010), 393–408.

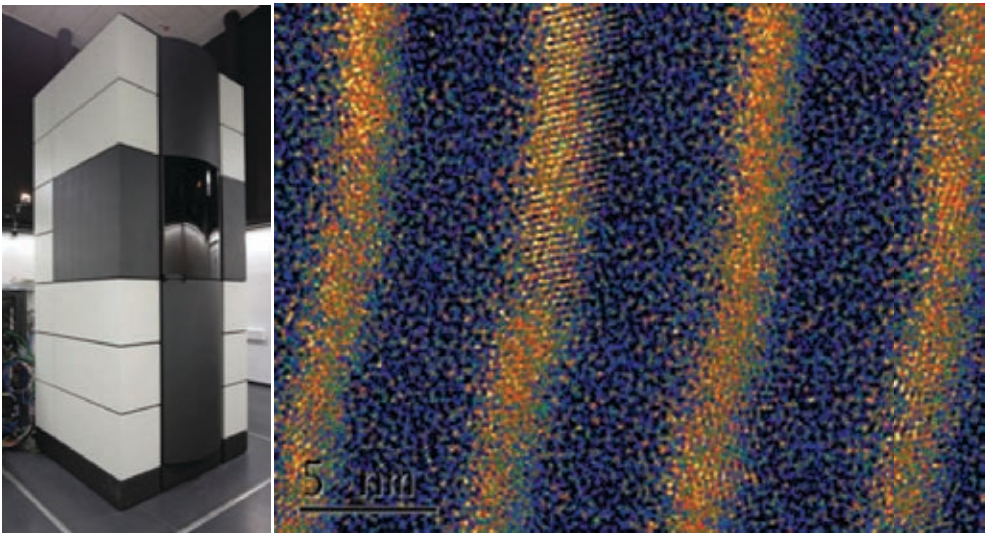

a **b**

Figure 1. The PICO instrument (a) and an EFTEM map of the Si distribution in a multi-quantum-well solar cell (b).

The Role of Structural Instabilities on Microstructural Evolution in Metastable Beta Titanium Alloys

Yufeng Zheng[1], Rongpei Shi[1], Talukder Alam[2], Rajarshi Banerjee[2], Yunzhi Wang[1], Hamish L. Fraser[1]

[1] *Center for the Accelerated Maturation of Materials and Department of Materials Science and Engineering, The Ohio State University, 1305 Kinnear Road, Columbus, OH 43212, USA*

[2] *Department of Materials Science and Engineering, University of North Texas, Discovery Park Suite E-132, Denton, TX 76203, USA*

Beta titanium alloys have been used in a wide range of areas such as aerospace and bio-medical field due to the combination of attractive mechanical properties such as high strength, corrosion resistance and bio-compatibility. Such unique combinations of properties can be tailored by the different microstructures developed under various thermal mechanical processing techniques. In the current work, in order to improve the overall strength, precipitation strengthening by *hcp* structure alpha phase precipitation in *bcc* structure beta phase matrix is effected in a metastable beta titanium alloy, Ti-5Al-5Mo-5V-3Cr (Ti-5553), exploiting differing roles of the structural instabilities (athermal and isothermal omega phase of *hexagonal* structure) during specifically designed heat treatments [1-3]. The microstructural evolution has been explored using advanced electron microscopy, and validated using phase field simulation [1-3].

The first set of experiment involved samples of Ti-5553 (having first been solution heat treated and quenched) being heated to 600°C at the heating rate of 100°C/min and isothermally held for 2 hours before being fast cooled to room temperature. The microstructure was characterized using an FEI Sirion SEM at an accelerating voltage of 12kV and shown in Fig. 1(a). This heat treatment produced a fine distribution of the alpha phase and aerial number density of alpha phase precipitates was analyzed using MIPAR™ software package [4] as ~2 ppts/um^2. The refined alpha microstructure appears to be very similar to those formed by step-quenching from above the beta transus to 600°C [5], formed via the pseudo-spinodal mechanism [6]. At 600°C, the alpha phase precipitates were formed without the influence of athermal

omega phase, directly from beta phase matrix by pseudo-spinodal decomposition mechanism [1,5,6].

The second set of experiment involved samples being heated to 600°C at a much slower rate, 5°C/min, and isothermally held for 2 hours before being fast cooled to room temperature. As shown in Fig. 1(b) a super-refined alpha microstructure was produced with a much higher aerial number density of 40 ppts/ um^2 [2]. This super-refined alpha microstructure is formed by the direct influence of pre-formed isothermal omega phase particles shown in the HAADF-STEM image in Fig. 2(a). The pre-formed isothermal omega phase particles can change the local concentration (by rejecting solutes of Al, Mo, V and Cr into beta matrix) and structure (from *bcc* to *hexagonal*), shown in Fig. 2(b-c) [2]. Therefore, isothermal omega phase can provide extra driving force for subsequent alpha phase precipitation and pre-formed omega/ beta interface can act as favorable nucleation sites for the alpha phase. The large number of isothermal omega phase particles provide the large number sites for the nucleation of super-refined alpha precipitates.

The third set of experiments involved samples heated to 350°C at a rate of 5°C/min, and subsequently up-quenched to 600°C and isothermally held for 2 hours before being fast cooled to room temperature. The produced microstructure exhibits an aerial number density in between as ~20 ppts/um^2, which is named as more-refined alpha microstructure, shown in Fig. 1(c) [3]. Such more-refined alpha microstructure was produced via the indirect influence of pre-formed isothermal omega phase particles. Isothermal omega phase was formed firstly during isothermal aging at 350°C and fine scale alpha phase precipitates nucleated and grew after long time aging at 350°C. But the fine scale alpha phase precipitates transformed back to beta phase matrix during up-quenching to 600°C and also created solute inhomogeneity in beta matrix that would restrain the nucleation of subsequent alpha precipitation at 600°C [3]. Therefore, the number density of more-refined alpha microstructure was directly influenced by the compositional inhomogeneity in the beta phase matrix which was indirectly influenced by the pre-formed isotheral omega phase [3].

References:

[1] Y Zheng et al, Scripta Materialia 111 (2016) 81-84.
[2] Y Zheng et al, Acta Materialia 103 (2016) 850-858.
[3] Y Zheng et al, Acta Materialia 103 (2016) 165-173.
[4] JM Sosa et al, Integrated Materials and Manufacturing Innovation, 2014 3:10
[5] S Nag et al, Acta Materialia 60 (2012) 6247-6256
[6] A Boyne et al, Acta Materialia 64 (2014) 188-197

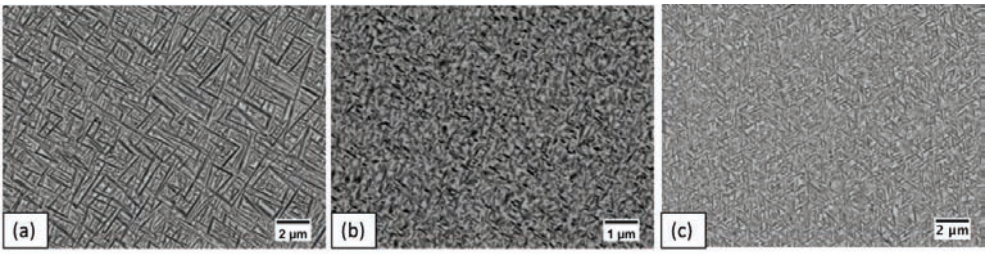

Figure 1. SEM images showing refined (a) [1], super-refined (b) [2] and more-refined (c) [3] alpha microstructures obtained in the metastable beta titanium alloy, Ti-5553 under different heat treatments.

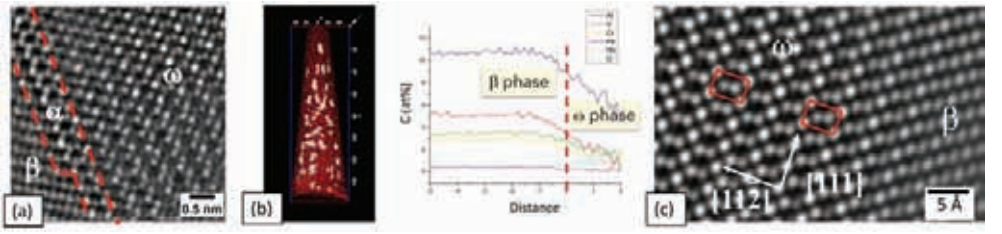

Figure 2. (a) HAADF-STEM image showing the pre-formed omega/beta interface acting as nucleation site of super-refined alpha precipitate; (b) Atom probe reconstruction showing iso-thermal omega particle and composition profile of Al, V, Mo, Cr, O, Fe across the omega/beta interface; (c) HAADF-STEM image showing the structure of isothermal omega particle [3].

Advanced and *in situ* Transmission Electron Microscopy of Functional Nanomaterials

Wolfgang Jaeger

Institute for Materials Science, Christian-Albrechts-University of Kiel, 24143 Kiel, Germany

Advanced high-resolution imaging and spectroscopic techniques of transmission electron microscopy (TEM) and scanning TEM (STEM) play a crucial role for characterizations of the synthesis and optimization of novel materials and of the structure-property relationships of materials and interfaces. This brief review will illustrate examples related to the synthesis of nanostructured oxide semiconductors, to interface properties of high-efficiency multi-junction solar cells, and to multilayer systems for X-ray optical applications.

Nanostructured oxide semiconductors, such as ZnO or In_2O_3, are of interest for device applications in nanoelectronics, for gas sensing, or in photovoltaic devices. High-resolution and scanning TEM were used to characterize the growth and doping phenomena of ZnO nanorod structures fabricated by a thermal method from powder precursor materials. For ZnO grown with Sn-precursors nanorods with core-shell morphologies form whose core regions contain dislocations, precipitates, or tubular voids partly filled with liquid Sn. Thin surface layers of a spinel phase indicate that interfacial reactions take place during crystal growth. Cathodoluminescence (CL) recorded from ZnO nanorods reflects the inhomogeneous defect distributions by a spatially varying CL emission whereas the CL spectra show a blue-shifted ZnO band gap luminescence which can be attributed to the effects of doping [1]. By applying in-situ (S)TEM experiments Sn-rich core material is identified and found to reversibly melt and expand under varying thermal load exerted by the electron beam [2]. Complex hierarchical phenomena are observed for growth with Al or Ga precursors and are found to be correlated with dopant incorporation. An example is the observation of planar defects enriched in Ga and their spatial connection with a variation of the rod diameter, indicating a possible origin for an oscillatory growth behaviour [3]. Various phenomena are observed for crystal growth of In_2O_3

nanorods, most strikingly the presence of nanotubes or nanopipes with constant diameter extending along the nanorods. Their formation can be understood as evidence for a crystal growth mode which involves a screw dislocation [4].

High-efficiency multi-junction solar cells based on III-V compound semiconductors reach the highest conversion efficiencies and are currently used primarily in terrestrial concentrator photovoltaics and for power generation on satellites and spacecraft. Different semiconductor cell materials are generally combined to absorb solar radiation of different wavelengths and to convert it into electric power. Solar-electric conversion efficiencies of up to 46 % have been obtained with multi-junction cells fabricated by metal-organic vapour phase epitaxy (MOVPE) of III-V semiconductors [5]. To overcome the challenge of integration of III–V compound semiconductors with Ge and Si caused by the large differences in lattice constant and thermal expansion two different process technologies were investigated by using advanced and in-situ (S)TEM techniques: direct epitaxial growth involving buffer layer concepts [6] and layer transfer combined with semiconductor wafer bonding [7]. An example is the wafer bond processing of transparent and electrically conductive interfaces between different III-V semiconductors, such as n-GaSb/n-GaInP bond interfaces. TEM characterizations of the atomic structure and of the elemental distribution at and near these bond interfaces enabled to understand the effects of fast atom beam activation treatments on the formation of amorphous interface layers, their recrystallization during thermal annealing, and the resulting effects on the electrical current-voltage characteristics, thus supporting the optimized engineering of wafer-bond interfaces for solar cells [8].

Periodic and aperiodic multilayer coatings consisting of ultrathin bilayers are essential components of X-ray optics for advanced X-ray analytical equipment and for synchrotron beam lines. Examples are filters of small or large spectral bandwidth, components for shaping high-intensity X-ray beams, or mirrors for light sources. The functionality of these components is based on X-ray scattering from a stack of alternating amorphous or nanocrystalline layers of materials with large differences in atomic number. Modern thin film deposition technologies allow to fabricate such multilayer systems with reproducible control of layer thickness on the nanometer scale and resulting excellent reflectivity properties. TEM characterizations of multilayer cross-sections have proven to be successful for monitoring the layer thickness, the layer periodicity and uniformity, and the interface quality on different length scales [e.g., 9, 10]. An example of aperiodic Mo-B_4C multilayers will be used to illustrate the potential of electron tomography in combination with advanced imaging and spectroscopic techniques of aberration-corrected STEM for extracting quantitative information, especially about the interface roughness of individual ultrathin layers in such multilayer systems [11, 12].

References:

[1] Y Ortega *et al*, Nanotechnology **21** (2010), 225604.
[2] Y Ortega *et al*, J. Phys. D: Appl. Phys. **46** (2013), 395301.
[3] Y Ortega *et al*, Phys. Stat. Sol. A **209** (2012), 1487
[4] D Maestre *et al*, Cryst. Growth. Des. **11** (2011), 1117.
[5] F Dimroth *et al*, IEEE Journal of Photovoltaics **6** (2016), 343.
[6] J Schöne *et al*, Journal of Physics: Conference Series **471** (2013), 012008.
[7] D Häussler *et al*, Ultramicroscopy **134** (2013), 55.
[8] F Predan *et al*, Journal of Applied Physics **122** (2017), 135307.
[9] D Haeussler *et al*, Phys. Stat. Sol. **202** (2005), 2299.
[10] D Haeussler *et al*, Surface & Coatings Technology **204** (2010), 1929.
[11] G Haberfehlner *et al*, in preparation (2018).
[12] The author acknowledges with pleasure the contributions of all colleagues and co-authors to the various research projects.

Applying Cs-corrected TEM/STEM to Long-standing Materials Science Problems

Jan H. Neethling, Jaco E. Olivier and Jacques H. O'Connell

Centre for HRTEM, Nelson Mandela University, Port Elizabeth, South Africa

Cs-corrected HRTEM and STEM have become essential techniques for the analysis of materials at the nanoscale. The range of useful techniques includes atomic scale and Z-contract imaging, diffraction and chemical analysis. This paper discusses three examples of long-standing materials problems of technological interest that were solved by using a double Cs-corrected JEOL ARM200F operated at 200 kV. HRTEM specimens were prepared by using a Helios Nanolab 650 FIB SEM.

A detailed understanding of the silver (Ag) transport mechanism in polycrystalline 3C-SiC is important for the design of advanced tristructural isotropic (TRISO) coated fuel particles to be used in high temperature gas cooled reactors. SiC is the main fission product barrier coating in the fuel particle. The finding, more than three decades years ago, that silver (a radioactive fission product) can be released by reputedly intact TRISO particles has led to significant research efforts to determine the silver transport mechanism in SiC [1]. This was due to the fact that out-of-reactor experiments did not reveal any significant silver migration in SiC [1]. Neethling and co-workers discovered that palladium, another high yield fission product, significantly enhances the transport of silver along grain boundaries in SiC [2]. The Pd assisted Ag transport mechanism was confirmed in a recent paper by Van Rooyen, Olivier and Neethling [3]. In this paper analytical and high resolution STEM was used to examine the microstructure and location of fission products (Pd and Ag) in SiC obtained from a neutron irradiated TRISO particle. Fig. 1(a) and (b) show BF and HAADF STEM images respectively of 3C-SiC irradiated at 1072°C and exposed to the fission products Pd and Ag. It can be seen that the Pd formed a palladium silicide layer (indicated by arrows) of thickness about 2 nm along the SiC grain boundaries. It was concluded that palladium penetrates the SiC along grain boundaries and reacts with the SiC to form palladium silicide, which creates fast

diffusion paths for Ag. These results explain why the Ag release rates obtained from irradiated and annealed TRISO particles are in good agreement with that measured in this study for a combined Pd-Ag transport mechanism in 3C-SiC.

The nitrogen containing {001} platelet defect in type 1a diamond have been studied for more than 60 years. In order to image the atomic arrangement across a platelet, a spatial resolution better than 89 pm is required to resolve the atomic columns of the defect along the <110> direction. Fig. 2 shows (a) HRTEM and (b) HAADF STEM images of the platelet defect viewed along the <110> direction [4]. Comparisons of the HAADF STEM images with simulated platelet model images revealed that it agrees closely with a structural model called the zigzag model [4]. The electron energy-loss near-edge fine structure data of both carbon K- and nitrogen K-edges obtained from the platelet core is consistent with the proposed zigzag structure [4].

The correct phase diagram of the Ag-Pt alloy is essential for the identification of new novel uses of this alloy. However, despite many years of research on the silver-platinum system, it was until recently not well understood since earlier attempts to determine its crystal structure were not successful [5]. However, by using HAADF STEM, we were able to show that the Ag-Pt alloy consists of nanometre-sized domains with $L1_1$ ordering together with disordered FCC domains [5].

In all three abovementioned examples, Cs-corrected HAADF STEM was used to solve the long-standing problems. These three examples will be discussed in detail during the presentation.

References:

[1] H Nabielek, PE Brown and P Offerman, Nucl. Technol. **35** (1977), 483.
[2] JH Neethling, JH O'Connell and EJ Olivier, Nucl. Eng. and Design **251** (2012), 230.
[3] IJ Van Rooyen, EJ Olivier and JH Neethling, J. Nucl. Mater. **476** (2016), 93.
[4] EJ Olivier *et al*, Nature Materials, **17** (2018), 243.
[5] GLW Hart *et al*, Acta Materialia, **124** (2017), 325
[6] The authors gratefully acknowledge the National Research Foundation and Department of Science and Technology for financial support.

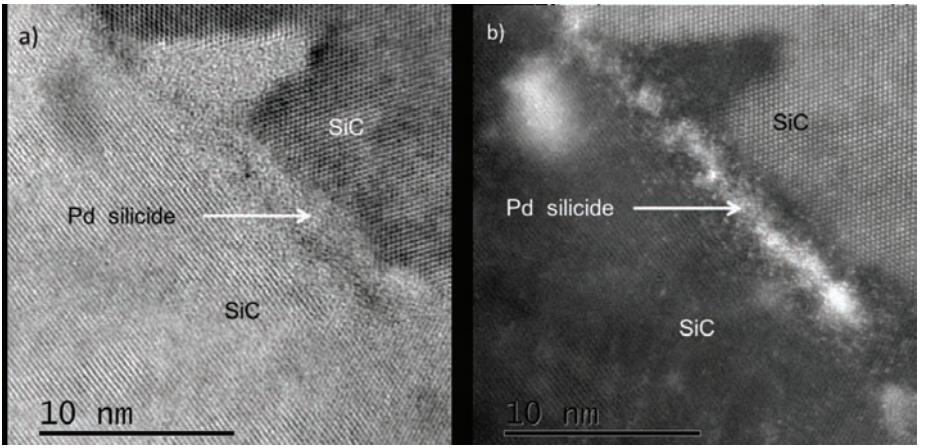

Figure 1. (a) and (b) show BF and HAADF STEM images respectively of 3C-SiC irradiated at 1072°C and exposed to Pd and Ag. The palladium silicide regions are indicated by the arrows.

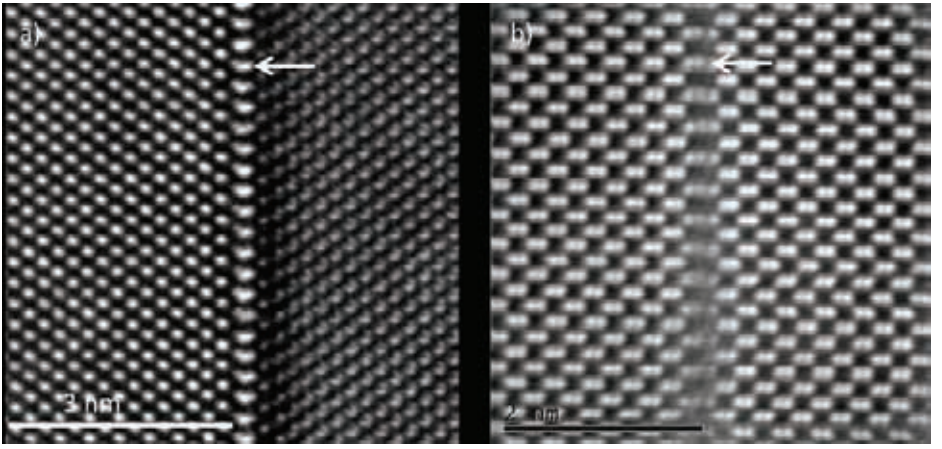

Figure 2. (a) HRTEM image of a {001} diamond platelet (indicated by arrow) viewed along the <110> direction. (b) HAADF STEM image of a {001} diamond platelet (indicated by arrow) viewed along the <110> direction (from ref. 4).

Theoretical Modeling of Electron Energy Loss Spectroscopy of Graphene: Comparing *Ab initio* Calculations and Empirical Models with Experiments

Zoran Miskovic

Department of Applied Mathematics and Waterloo Institute for Nanotechnology, University of Waterloo, Waterloo, Ontario, Canada

Graphene has come to focus of recent research efforts for applications in plasmonic devices in a broad range of frequencies, from the terahertz (THz) to the far ultraviolet. In that respect, Electron Energy Loss Spectroscopy (EELS) has been recognized as one of the most effective techniques for probing electronic excitations in graphene, both in the low-energy range using High-Resolution EELS (HREELS) [1] and in the range of energy losses of ~ 1 – 50 eV using Scanning Transmission Electron Microscopy (STEM) [2]. In my talk, I shall give a progress report on the work done in my group and with my collaborators on theoretical modelling of various aspects of the EELS of graphene.

We have developed a theoretical model for the energy and momentum transfer from an incident charged particle to graphene, treated as a two-dimensional (2D) electron gas characterized by a polarization function or a 2D dynamic conductivity [3]. We have initially modeled the polarization function of graphene at high frequencies by using a two-fluid, 2D hydrodynamic (HD) model for the inter-band excitations involving graphene's π and σ electronic bands [4], giving rise to essentially a two-term Drude-Lorentz model. This model gave surprisingly good results in comparison with the experiments using HREELS of graphene deposited on metallic substrates in the range of energy losses ~ 4 – 10 eV, which includes the so-called graphene's π plasmon peak [5,6]. Subsequent applications of the HD model gave excellent comparisons [7,8] with the experimental data for EELS of free-standing graphene in STEM in the range of energy losses ~ 2 – 50 eV, which includes both the π and $\sigma+\pi$ peak features, for single-layer [8] and multi-layer graphene [9].

However, the EELS data for graphene in STEM obtained by different groups reveal inconsistencies for electron energy losses below some 2 – 3 eV [8-11], which are

presumably related to the method used by those groups to treat the zero-loss peak. In order to shed some light on this range of energy losses from a theoretical perspective, we have extended our HD model to low frequencies by adding the so-called Dirac term to the conductivity of graphene [12]. We have further gauged empirical parameters that appear in such extended HD (eHD) model by comparing it with *ab initio* calculations of the optical conductivity of free-standing graphene [13,14]. A subsequent comparison of both the eHD model and the *ab initio* calculations with the experiments from Refs.[8,9,10] revealed that, indeed, the Dirac term in graphene's conductivity may give important contribution to the energy losses below 2 – 3 eV [12]. On the other hand, we have observed in Ref. [12] that high-energy losses above ~ 20 eV, i.e., above the $\sigma+\pi$ spectral peak, reveal a strong influence of the size of the collection aperture of the transmitted electrons in STEM.

In order to further focus on the role of the collection aperture, we have turned our attention to experiments using momentum-resolved EELS of graphene [11], where relativistic effects should play a role in how the incoming electrons scatter on the graphene monolayer in STEM. To that effect, we have generalized our model of Refs. [3,7] to include retardation effects in the energy loss of a ~ 100 keV incident electron [15,16]. While we have found that the retardation plays an important role at very low energy losses, corresponding to the THz frequency range [15,16], its effect in the ~ 1 – 50 eV range of energy losses mostly increases the magnitude of the spectra by up to ~ 10% [15,17]. A direct comparison of the eHD model and *ab initio* calculations for the conductivity of graphene with the experimental EELS data from Ref. [11] was attempted in Ref. [17]. However, only partial success was achieved in reproducing basic features of the spectra, e.g., the ratio of the heights of the π and $\sigma+\pi$ peaks, even when the retardation effects are included in the energy loss model [17]. I shall discuss in my talk possible reasons for the unexpected difficulties in modelling the momentum-resolved EELS and routes to overcome them.

References:

[1] A Politano and G Chiarello, Nanoscale **6** (2014), 10927.
[2] JC Idrobo and W Zhou, Ultramicroscopy **180** (2017), 156.
[3] KF Allison and ZL Miskovic, Nanotechnology **21** (2010), 134017.
[4] DJ Mowbray *et al*, Phys. Rev. B **82** (2010), 035405.
[5] A Politano *et al*, Carbon **96** (2016), 91.
[6] A Politano *et al*, Carbon **114** (2017), 70.
[7] VB Jovanovic *et al*, Phys. Rev. B **84** (2011), 155416.
[8] FJ Nelson *et al*, Nano Lett. **14** (2014), 3827.
[9] T Eberlein *et al*, Phys. Rev. B **77** (2008), 233406.
[10] P Wachsmuth *et al*, Phys. Rev. B **88** (2013), 075433.

[11] SC Liou *et al* , Phys. Rev. B **91** (2015), 045418.
[12] T Djordjevic *et al*, Ultramicroscopy **184** (2018), 134.
[13] D Novko, M Sunjic and V Despoja, Phys. Rev. B **93** (2016), 125413.
[14] V Despoja *et al*, Phys. Rev. B **96** (2017), 075433.
[15] ZL Miskovic *et al*, Phys. Rev. B **94** (2016**),** 125414.
[16] K Akbari *et al*, ACS Photonics **4** (2017**),** 1980.
[17] K Lyon, DJ Mowbray and ZL Miskovic, Radiat. Eff. Defects Solids **173** (2018), 8.
[18] The author acknowledges funding from the Natural Sciences and Engineering Research Council of Canada (RGPIN-2016-03689).

Sub-Å STEM Resolution From 30 to 300kV: Themis Z Opens a New Era for Ultra-high Resolution in Low kV Imaging and Analysis

Dominique Delille

Thermo Fisher Scientific - Materials & Structural Analysis, Achtseweg Noord 5, P.O. Box 80066 - 5600KA Eindhoven, The Netherlands

Interest in low-kV STEM imaging and analysis keeps being fueled by increasing research on novel materials such as carbon-based nano-materials and other low-dimensional structures. Atomic resolution imaging of these classes of materials is known to be seriously affected by radiation damage and weak signals leading to low contrast in the images. Therefore high contrast, beam-damage-free imaging can often only be achieved at low to very low accelerating voltages. Imaging below the critical knock-on damage threshold is the key to success and for some materials this can be well below 60kV.

To maintain optical performance at lower voltages, higher opening angles of the probe have to be used (diffraction limit). Hence the higher order aberrations of the optics, which increase dramatically with higher opening angles and lower voltages, need to be measured and corrected with high precision and long enough stability. Monochromation of the electron beam has proven to be an effective way to reduce chromatic blurring and the Thermo Scientific monochromator - although not specifically developed for imaging - has demonstrated to be a good fit for the purpose of low-kV imaging. The probe corrector can potentially eliminate, or at least significantly reduce, the resolution-limiting aberrations even at low accelerating voltages but some limitations still remain. The corrector must be able to correct higher order aberrations over the entire high tension range of the system (300-30kV) so that optimum imaging performance can be achieved for the high tension selected to best suit the material being investigated. Additionally, for correction, the biggest remaining challenge is measuring the aberrations with sufficient confidence to come to reproducible results during daily operation.

We will discuss in this presentation how to achieve optimized imaging performance for a wide high tension range, excellent reproducibility of operation and ultimate

precision in atomic imaging. With all aberrations corrected, sub-Ångström STEM imaging results will be shown to be routinely achievable on a system with full high tension flexibility.

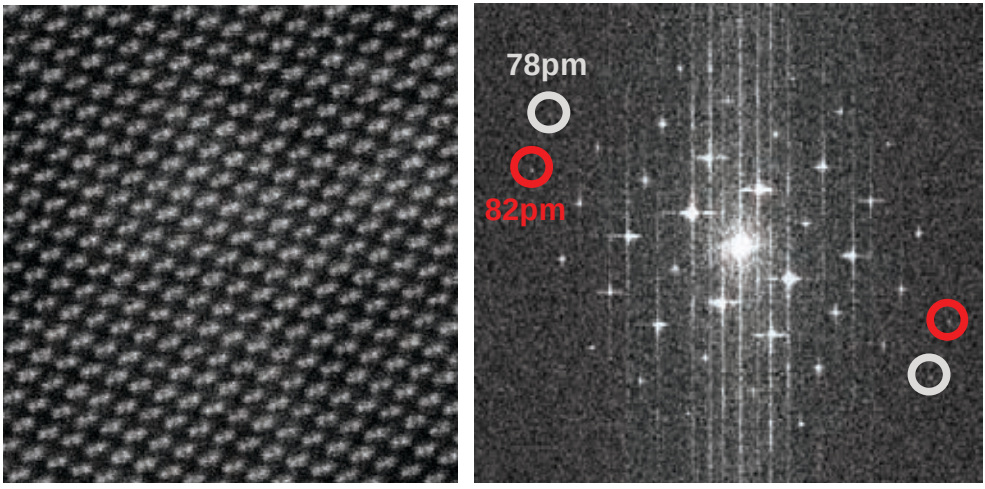

Figure 1. 60kV ADF of Si <110> (left) with FFT of the image (right).

Figure 2. 40kV Ronchigram with 51mrad convergence semi-angle.

POSTER ABSTRACTS

Measuring and Controlling Out-of-Plane Shape of Free-Standing Two-Dimensional Materials

Ursula Ludacka, Mohammad R. A Monazam, Toma Susi, Christian Rentenberger, Jannik C. Meyer and Jani Kotakoski

Faculty of Physics, University of Vienna, Austria

In this work, we show through transmission electron microscope (TEM) and atomistic simulations that the non-flatness of free-standing graphene, hBN, and MoS_2, as well as their heterostructures varies depending on the material.

TEM offers the possibility to investigate the materials properties without mechanically perturbing it. This is especially important if the aim of the investigations is to study out-of-plane corrugations. Unfortunately, in the case of two-dimensional materials, one cannot purely rely on the imaging mode, as the corrugations are not high enough as compared to the available depth of field. But a TEM offers a second mode, the diffraction mode, where these corrugations can be easily teased out. Diffraction pattern of two-dimensional materials are represented by poles orthogonal to the membrane. Therefore, corrugated two-dimensional materials exhibit a superposition of surface normals in their diffraction pattern. Figure 1 (left) shows a typical diffraction pattern of graphene at 0° sample tilt, whereas figure 1 (right) shows a diffraction pattern of graphene at 21° sample tilt. Because the spreading of diffraction spots as a function of the sample tilt increases for increasing roughness of the sample, this allows the direct measurement of the corrugations.

Out of all materials studied here, graphene is the least flat, followed by hBN and finally MoS_2. For heterostructures made of two different two-dimensional materials, the overall shape is determined to a large extent by the stiffer one. Thomsen *et al.* [1] already suggested that hBN causes a flattening of graphene in a heterostructure of these two materials.

In addition to measuring the out-of-plane shape, we can also control it *in situ* in one direction using a TEM stretching holder. For these experiments, we glued the samples, transferred onto gold TEM grids with a perforated amorphous carbon film, onto the holder and applied mechanical strain with small incremental steps to avoid

breaking the film during the experiment. Figure 2 shows the results of one such study. Diffraction pattern recorded at different stages of the experiment: (a) at the beginning, (b) towards the end and (c) at the end. All shown patterns were recorded at sample tilt $\alpha = 21°$. The dashed lines show the approximate tilt axis and the overlaid hexagons highlight the first set of diffraction peaks. The panels on the right show a zoom-in of the indicated diffraction spots in false color. (d) Orientation of the ellipse fitted to the diffraction patterns (Θ) and that of the diffraction spots (ϑ) during the experiment. (e) Ellipticity of the diffraction patterns (B/A, right y-axis) and spots (b/a, left y-axis). Standard errors from the fits to the measured values are contained within the markers. All diffraction pattern values are for $\alpha = 0°$ and spot values for $\alpha = 21°$. In panels (d) and (e), the values corresponding to the diffraction patterns shown in panels a-c are marked with corresponding labels. The x-axis values ($\Delta G/G0$) indicate the relative change in the size of the gap in the sample carrier over which the sample was suspended.

In conclusion one can say that the deviation of circular symmetry of the diffraction pattern and the shape of the individual diffraction spots give us insight on the strain in the material and its out-of-plane shape, respectively. Our results show that this simple method can be used to completely flatten the 2D materials in the direction of the applied force. At this point, the material exhibits an aligned set of one-dimensional corrugations. After the structure has been flattened, continuous mechanical deformation leads to a measurable strain in the structure.

References:

[1] J. Thomson *et al*, Phys. Rev. B **96** (2017), 014101.

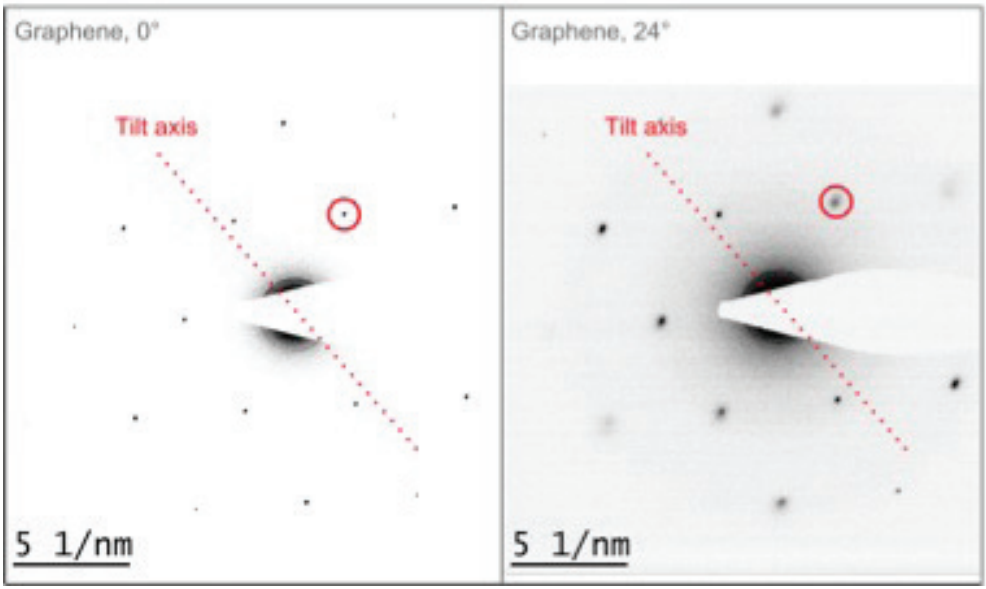

Figure 1. Diffraction pattern of graphene at 0° sample tilt (left) and 21° sample tilt (right).

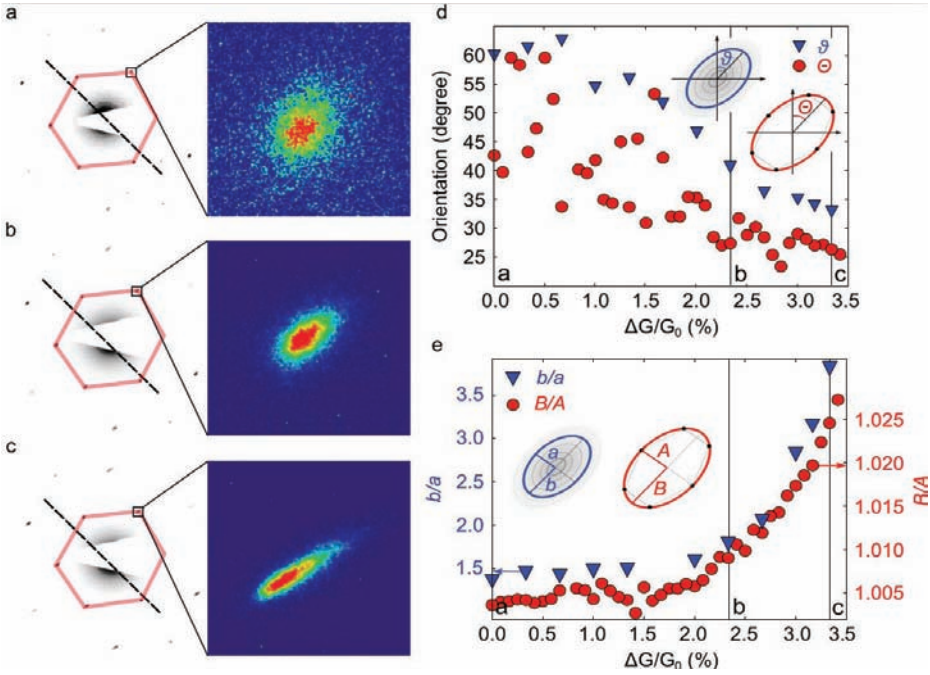

Figure 2. Evolution of the diffraction pattern of graphene and individual diffraction spots during the experiment.

Structural Characterization of Organic and Perovskite Solar Cells

Vuk V. Radmilović[1], Yi Hou[2], Fei Guo[2], Christoph J. Brabec[2], Erdmann Spiecker[3], Velimir R. Radmilović[4,5]

[1] *Innovation Center, Faculty of Technology and Metallurgy, University of Belgrade, Karnegijeva 4, 11120 Belgrade, Serbia*
[2] *Institute of Materials for Electronics and Energy Technology (i-MEET), Friedrich-Alexander-University Erlangen- Nuremberg, Martensstrasse 7, 91058 Erlangen, Germany*
[3] *Center for Nanoanalysis and Electron Microscopy (CENEM), Friedrich –Alexander -University of Erlangen- Nuremberg, Cauerstrasse 6, 91058 Erlangen, Germany*
[4] *Faculty of Technology and Metallurgy, University of Belgrade, Karnegijeva 4, 11120 Belgrade, Serbia*
[5] *Serbian Academy of Sciences and Arts, Knez Mihailova 35, 11000 Belgrade, Serbia*

Although the photovoltaic market is still dominated by crystalline Si solar cells, there is a rising demand for thin film devices which has sparked extensive research in the field of third generation (3G) solar cells, most notably organic based as well as hybrid organic-inorganic (perovskite). These cells present a very attractive area of research because of their ability to overcome the Shockley-Queisser limit [1] of power efficiency for single bandgap solar cells as well as to fulfill industry demands like flexibility, scalability and simple/cost efficient processing.

In organic solar cells (OSC), organic materials like polymers (electron donors/p-type materials) and carbonaceous nanostructures like fullerenes (electron acceptors/n-type materials) can be blended together forming interpenetrating network i.e. a nanocomposite with the polymer as the matrix and the fullerene as the nanofiller called a bulk heterojunction (BHJ). Advantage of this structure is that charge separation can occur over the entire bulk of the film, effectively removing the problem of exciton diffusion through the entire film thickness. Light absorption can occur throughout the entire film and, as such, charge transport is benefitted. One of the

best ways to increase power conversion efficiency (PCE) is by connecting multiple light absorbers, with various band gaps and complementary light absorption spectra. This concept, known as the tandem cell (multi-junction), simultaneously addresses absorption and thermalization losses.

In this work, the cell characterized was a tandem OSC, with the architecture (from substrate on) PEDOT coated glass/printed Ag/PEDOT:PSS polymer/GEN-2:PC61BM BHJ layer 1/ZnO/N-PEDOT/pDPP5T-2-PC61BM BHJ layer2/ZnO/Ag nanowires (NWs), seen in Figure 1 (LEFT). The cell was processed ENTIRELY from solution (thereby making this procedure very cheap) by doctor blading on glass and PET substrates although only cell on glass could have been characterized in the microscope. Results suggested that most of the layers comprising the OSC have very uniform thickness and fairly low roughness. Reported PCE of 5.81% was the highest for a fully solution processed double junction OSC at that moment which demonstrated the potential of low cost and environmentally friendly low energy production [2].

Perovskite based SC have been one of the hottest topics in the PV research field as they have shown enormous potential for reaching high PCE in just a few years, going from only 3% just 9 years ago to as high as ~20% presently. These cells utilize the unique structure of the perovskite crystal ABX_3, with methylammonium lead halides as the most notable examples, which allows for high PCE due to very efficient light harvesting, fast charge separation ability, long carrier separation lifetimes, long diffusion lengths, high dielectric constants etc. Coupled with the fact that the cost of the materials and their processing is very low, it is clear why these SCs have a leading role in PV research. Recent research suggests that the porous structures can enhance device stability compared to planar structured devices. High synthesis temperatures and the limited selection of adequate materials are the main reasons why, although exhibiting record PCE for perovskite SC, alternatives to metal oxide based porous materials need to be studied.

In this work, a novel organic-based interfacial layer was produced for a perovskite SC by low-temperature green solvent based process. Cost efficient and scalable organics are the most promising alternatives to inorganic interfaces, produced by demanding synthesis methods. With this novel organic layer, the perovskite effectively infiltrates into this mesoporous structure, and with enhanced wetting of surface, the perovskite dramatically increases its homogeneity, thus leading leads to the enhancement PCE and thermal stability. The cell characterized included a perovskite as the light conversion layer, with the “n-i-p” architecture (from substrate on): Glass/ITO/ SnO_2/ $PC_{61}BM$/FAMAPbIBr/PDCBT/Ta-WO_X/Ag (Figure 2 RIGHT). Excluding the Ag electrode, the cell was processed entirely from solution (thereby making this procedure very cheap) by spin coating. Reported power conversion efficiency value of ~20% [3].

Solar cells characterized in this study were investigated by SEM/FIB dual beam system and by conventional and scanning transmission electron microscopy (CTEM and STEM) in combination with energy dispersive X-ray spectroscopy (EDS). To our knowledge, this was the first time cross-sections of these kinds of solar cells have been characterized by (scanning) transmission electron microscopy.

References:

[1] W Shockley and H Queisser, Journal of Applied Physics **32** (1961), 510-519.
[2] F Guo *et al*, Energy & Environmental Science **8** (2015), 1690-1697.
[3] Y Hou *et al*, Submitted (2018).
[4] Support acknowledged from the Ministry of Education, Science and Technological Development of the Republic of Serbia, contract No. III45019, Serbian Academy of Sciences and Arts under contract #F-141 as well as the DFG Research Training Group GRK1896 and the Cluster of Excellence EXC315 at the University of Erlangen-Nürnberg, Germany.

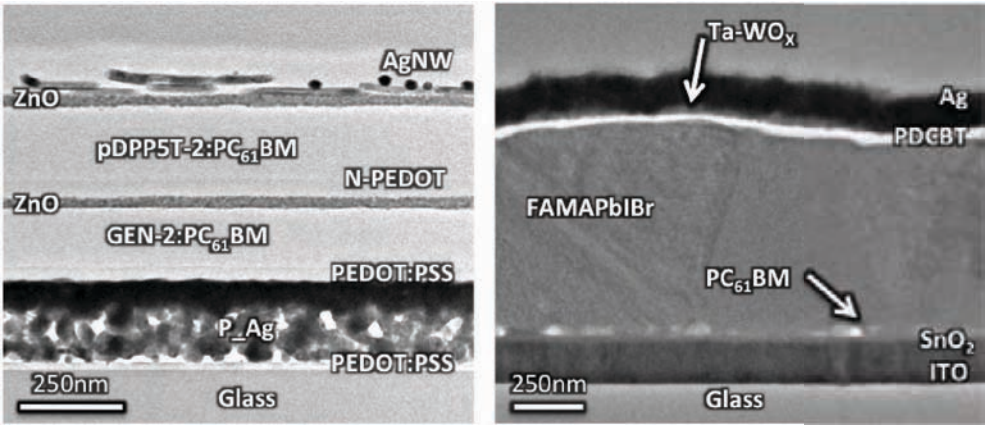

Figure 1. (LEFT) BF TEM with noted layers of tandem OSC cross-section; (RIGHT) BF TEM with noted layers of perovskite SC cross-section.

Silicon Nanostructuring by Ag Ions Implantation Through Polystyrene Nanomask

Almedina Modrić-Šahbazović[1], Mirjana Novaković[2], Izet Gazdić[1], Nataša Bibić[2] and Zlatko Rakočević[2]

[1] *University of Tuzla, Faculty of Natural Sciences and Mathematics, 75000 Tuzla, BiH*
[2] *University of Belgrade, Institute of Nuclear Sciences VINČA, 11351 Belgrade, Serbia*

Mask-assisted ion beam processing of insulating substrates is a versatile tool for achieving nanopatterning of a material through the formation of ordered nanostructures. The possibility of producing self-assembled monolayers of silica or polystyrene (PS) nanospheres with size in the 100–1000 nm range on the substrate to be patterned is much simpler and cheaper alternative to conventional lithographic techniques, for the synthesis of 2D ordered arrays of nanostructures [1,2]. In some cases, after the nanosphere mask deposition, ion implantation can be used to selectively modify the substrate through the triangular holes left among adjacent spheres, providing that these are thick enough to stop incoming ions before reaching the substrate. In this work, we used ion implantation through self-assembled PS mask to directly and regularly modify the subsurface layer of silicon substrate with Ag ions.

The monocrystalline (100) p-type Si wafers with thicknesses of ~550 μm were covered with ~150 nm diameter PS spheres and implanted by singly charged Ag ions with energy of 60 keV and fluences of 1×10^{15}, 5×10^{15}, 1×10^{16} and 2×10^{16} ions/cm^2. The projected range of 60 keV Ag ions in polystyrene is 64 nm according to the SRIM-2008 [3] simulations, with the range straggling of 12 nm. Therefore, the ions hitting the center of PS spheres are expected to be completely stopped inside the spheres, and should penetrate the substrate only through the holes in the monolayer mask or at areas very close to the mask openings. Morphological and crystallographic analysis of the patterned Si after the mask removal was done by cross-sectional transmission electron microscopy (XTEM), using FEI Talos F200X microscope.

XTEM bright-field image of sample implanted to the dose of 1×10^{16} ions/cm^2 is presented in Fig. 1(a). Energy dispersive spectrometry microanalysis (in the inset) taken from the area given at the micrograph is characterized by a spectrum with Si and Ag peaks in the energy range of 1.5-3.5 keV. A large-scale area of the sample of several hundreds of nanometers indicates a periodic microstructure with the homogeneously arranged half-squared fragments. These fragments present the position of mask openings, where Ag ions penetrated into the Si substrate. They are roughly of same dimensions, with the width of about 190 nm and are arranged in a similar manner with 60-100 nm spacing in between. The micrograph in Fig. 1(b) presents XTEM bright-field image of the one of the irradiated Si regions with the surrounding non-irradiated substrate. One notes the presence of NPs below the top-surface of the implanted region of the Si substrate. Closer analysis of the substrate surface reveals that the Ag nanoparticles are situated only at the irradiated Si fragment, while beyond the edges of this region no Ag particles could be observed. The position of the implanted areas exhibit a weak contrast under the imaging conditions used, indicating that amorphisation of the Si substrate has occurred. High-resolution micrograph taken at the periphery of the amorphized Si region of the sample is given in the upper part in Fig. 1(c). As can be observed, the interface between a-Si and c-Si is characterized with the defect-rich zone (dark-contrast region), with a thickness of a few nanometers.

Figure 1(c) in the bottom shows high-resolution image of a typical Ag particle in the sample. It can be seen that the silver nanoparticle is crystalline in nature. The measured lattice spacing is 0.236 nm, which is in a good agreement with the theoretical value for cubic Ag [4].

It is demonstrated that the 60 keV Ag ions implantation into silicon through the nanomask consisting of ~150 nm diameter polystyrene spheres can be used for well-ordered nanostructuring of Si substrate. The Ag is implanted into the silicon at the openings between adjacent PS spheres, thus creating an array of amorphized Si regions with Ag nanoparticles formed. A major conclusion is that this technique may proof useful for nanostructuring surfaces in general, since the PS mask is fast to make and inexpensive while the implantation process is precisely controllable [5].

References:

[1] CL Haynes and RP Van Duyne, J Phys Chem B **105** (2001), 5599.
[2] J Jensen *et al*, Nucl Instr Meth Phys Res B **266** (2008), 3113.
[3] JF Ziegler, JP Biersack and U Littmark, (Pergamon Press, New York); code SRIM2003: http://www.srim.org.
[4] NH Winchell and AN Winchell in “Elements of Optical Mineralogy II”, (Wiley & Sons, New York).

[5] The authors acknowledge funding from the Ministry of Education and Science of the Republic of Serbia (Project No. III 45005). Igor Peterka is thanked for his assistance at 500 kV ion implanter.

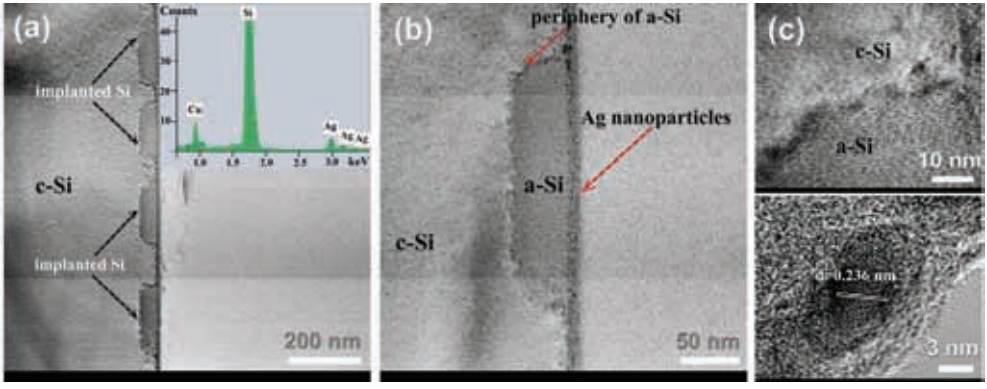

Figure 1. XTEM analysis of Si substrate irradiated to 1×10^{16} Ag/cm^2 through ~150 nm PS nanomask.

XRD and HRTEM Study of Rutile Precipitates in Chrysoberyl Crystals

Aleksander Rečnik[1], Sandra Drev[2], Matjaž Mazaj[3] and Nina Daneu[4]

[1] *Department for Nanostructured Materials, Jožef Stefan Institute, Ljubljana, Slovenia*
[2] *Center for Electron Microscopy and Microanalysis, Jožef Stefan Institute, Ljubljana, Slovenia*
[3] *Laboratory for Inorganic Chemistry, National Institute of Chemistry, Ljubljana, Slovenia*
[4] *Advanced Materials Department, Jožef Stefan Institute, Ljubljana, Slovenia*

Natural chrysoberyl ($BeAl_2O_4$) crystals often contain inclusions of different minerals that precipitate during its growth. When oriented, these inclusions scatter light along the specific orientation within the hosting crystal, known as the cat's-eye effect or *chatoyancy*. In chrysoberyl, this effect is often caused by oriented precipitation of rutile (TiO_2). Oriented precipitation of rutile is possible due to the similarity of the two structures [1]. Chrysoberyl crystallizes in an olivine-type structure with slightly distorted hexagonal close-packed (*hcp*) O–sublattice along the crystallographic c–axis (in the space group 62, Pmnb), where cations (Al^{3+} and Be^{2+}) partially occupy (½) of the octahedral and (¼) of the tetrahedral interstices. On the other hand, the rutile has tetragonally distorted O–sublattice with *hcp* stacking along the crystallographic a– and b–axes (No.136, $P4_2/mnm$), where cations (Ti^{4+}) occupy octahedral interstices. Owing to this structural similarity oriented exsolution of rutile in chrysoberyl is possible [2]. Until the present, real structural relations have not yet been studied in detail.

To solve structural relations between chrysoberyl and rutile we used X–ray (XRD) diffractometry for determination of bulk crystal properties and transmission electron microscopy (TEM) to determine crystallographic relations and the atomic–scale structure of interfaces. Powder XRD patterns were recorded using a high-resolution X-ray diffractometer (PANalytical X'Pert PRO) under a continuous scanning mode in 2θ range from 15 to 90° and a recording time of 300 sec/step of 0.016°. The crystal

structures were refined by Rietveld analysis of experimental X-ray diffractograms using the TOPAS-Academic V4 software package (Coelho Software). Refined unit-cell parameters of the chrysoberyl crystals are: a = 5.4825(1) Å, b = 9.4163(2) Å, c = 4.4308(1) Å (Pmnb), whereas those of rutile have converged to a = 4.7331(4) Å, c = 2.880(2) Å ($P4_2/mnm$), that considerably deviates from the lattice parameters of regular rutile. The refinement of rutile included in chrysoberyl was less reliable due to broad and weak reflections of rutile, that can be attributed to relatively low concentration of rutile (2 mol%), its small crystal size (~ 50 nm), and possibly large structural anisotropy. TEM study of rutile precipitates shows that they are oriented along specific crystallographic direction in the chrysoberyl structure. Electron diffraction analysis of several rutile precipitates showed that rutile is exsolved in two orientations, following orientation relationship of $[001]_{Ch}\{120\}_{Ch}|[010]_R\{103\}_R$. HRTEM study of the precipitates confirmed large distortion of the rutile lattice, as indicated by the Rietveld analysis of bulk sample. Using chrysoberyl lattice as a reference, unit–cell parameters of rutile, determined by HRTEM analysis are a = 4.725 Å, c = 2.875 Å. Such a large expansion of the rutile structure along the a–axis and contraction along the c–axis (Henderson *et al*. 2009; a = 4.5922 Å and c = 2.9576 Å at RT) is unusual, and suggest that rutile exsolved from chrysoberyl at elevated temperature, when the two structures were perfectly matching. On cooling, the thin rutile precipitates were deformed by the contraction of chrysoberyl lattice. Based on this assumption, we can calculate an approx. exsolution temperature of 970°C, where the rutile precipitated from the chrysoberyl lattice [3].

References:

[1] TE Mitchell and JM Marder, Proceedings of the Electron Microscopy Society of America (1982).
[2] K Schmetzer in “Russian Alexandrites” (Schweizerbart Science Publishers, Stuttgart).
[3] S Drev *et al*, American Mineralogist **100** (2015), 861–871.

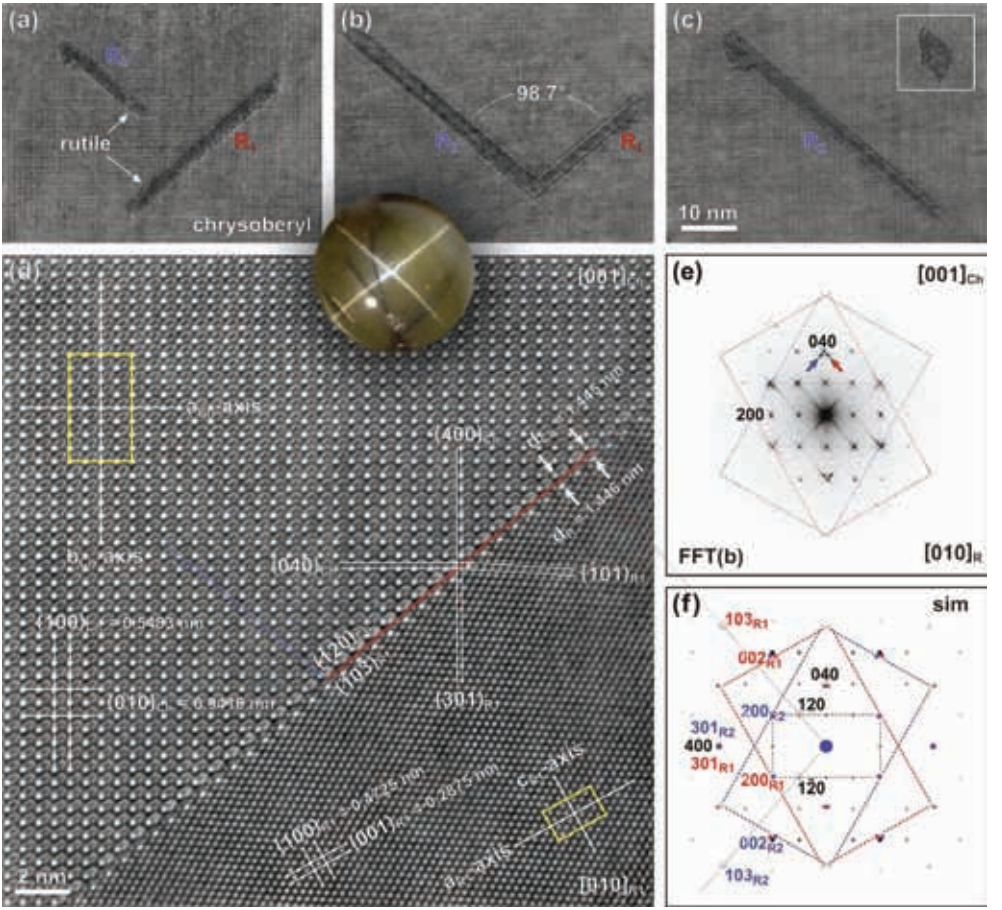

Figure 1. TEM study of anisotropic rutile precipitates in chrysoberyl. (**a**) Two orientations are observed (R_1 and R_2). (**b**) L-shaped cluster composed of two impinging rutile precipitates enclosing an angle of 98.7°. (**c**) Isolated rutile precipitate with small xenomorphic grains of faulted rutile (*see* the inset). (**d**) Structural analysis of the chrysoberyl–rutile interface. Crystallographic axes of chrysoberyl and rutile are indicated for determination of orientation relationship $[001]_{Ch}(120)_{Ch} \parallel [010]_R(103)_R$. (**e**) Fast Fourier transform (FFT) of the HRTEM image from Fig. (b) displaying additional reflections from rutile R_1 and R_2 precipitates (indicated by arrows). (**f**) Reconstructed EDP of chrysoberyl and rutile precipitates calculated with lattice parameters of deformed rutile from the HRTEM analysis.

Electrospun Hybrids of Carbon Nanofibers with Cobalt and Manganese Oxide Nanoparticles as High-Performance Electrodes for Supercapacitors

Daniel M. Mijailović[1], Uroš Č. Lačnjevac[2], Vuk V. Radmilović[1], Dušica B. Stojanović[3], Velimir R. Radmilović[3,4], Vladimir D. Jović[2], Petar S. Uskoković[3]

[1] *Innovation Center, University of Belgrade, Faculty of Technology and Metallurgy, Karnegijeva 4, 11120, Belgrade, Serbia*
[2] *Institute for Multidisciplinary Research, University of Belgrade, Kneza Višeslava 1, 11030 Belgrade, Serbia*
[3] *University of Belgrade, Faculty of Technology and Metallurgy, Karnegijeva 4, 11120, Belgrade, Serbia*
[4] *Serbian Academy of Sciences and Arts, Knez Mihailova 35, 11000 Belgrade, Serbia*

Supercapacitors have sparked widespread attention as efficient energy storage devices due to high power capability, excellent cycling stability, simple principles and low maintenance costs. These properties have made them attractive in a wide range of applications, such as portable electronic devices, energy back-up systems and hybrid electric vehicles. Further development of supercapacitors will strongly depend on novel advanced materials which can achieve higher energy densities without sacrificing their power characteristics [1,2].

In this work, a facile two-step process has been used to synthesize various hybrid materials consisting of carbon nanofibers (CNFs) decorated with nanoparticles of cobalt and manganese oxides. In the first step, composite solutions containing two polymers and different quantities of metal precursors were electrospun into nanofibers. In the second step, these metal salt-incorporated nanofibers were converted into hybrid structures by heating at 280 °C and 600 °C in air and argon atmosphere, respectively.

Scanning electron microscopy (SEM) analysis confirmed the formation of interbonded CNFs with nanoparticles deposited on the surface of these fibers (Figure 1). However, scanning transmission electron microscopy (STEM) in combination with energy dispersive X-ray spectroscopy (EDS) of cross-sections of these hybrids

revealed that metal oxide nanoparticles are present inside the CNFs as well as on the surface (Figure 2). Fourier transform infrared spectroscopy (FTIR) analysis suggested phase separated structures of as-spun nanofibers as typical peaks of polymers used were noted in the FTIR spectrum.

Benefiting from the unique structural features, the hybrid electrodes demonstrate high specific capacitance, good cycling stability and rate capability. For instance, the hybrid electrode CNFs / cobalt oxide exhibits specific capacitance of ~400 F g^{-1}, at a current density of 1 A g^{-1} in 3 M KOH, which is four times higher than neat CNFs. Additionally, the electrode retained 85% of its initial capacitance after one thousand cycles of galvanostatic charge/discharge at 10 A g^{-1}. On the other hand, the hybrid with combined cobalt and manganese oxides delivers a specific capacitance of ~1000 F g^{-1}, ten times higher than neat CNFs, at the current density of 1 A g^{-1} with a still impressive cyclic stability of 76% capacity retention after one thousand cycles at 3 A g^{-1}. These remarkable electrochemical performances of our hybrid structures make them a very desirable candidate for high-performance supercapacitor applications.

References:

[1] F Zhang *et al*, Adv. Funct. Mat. **23** (2013), 3909-3915.
[2] S Peng *et al*, ACS Nano **9** (2015), 1945-1954.
[3] The authors acknowledge funding from the Ministry of Education, Science and Technological Development of the Republic of Serbia (III45019). V.V. Radmilovic and V.R. Radmilovic acknowledge the Center for Nanoanalysis and Electron Microscopy (CENEM), Friedrich-Alexander-University of Erlangen-Nurnberg, Germany, where electron microscopy characterization has been performed.

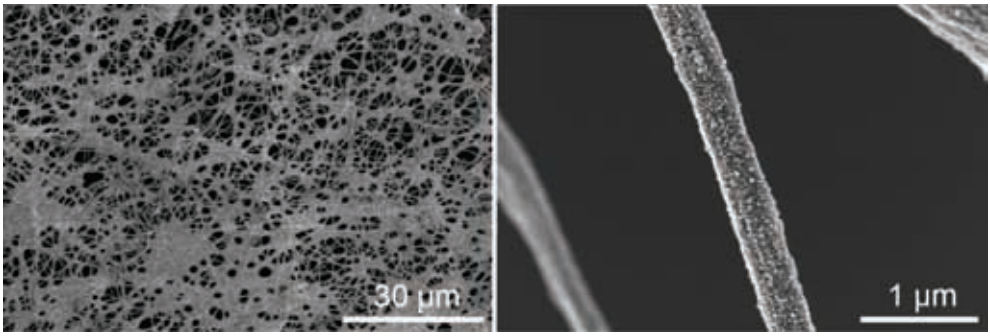

Figure 1. SEM micrographs of hybrid sample at different magnifications.

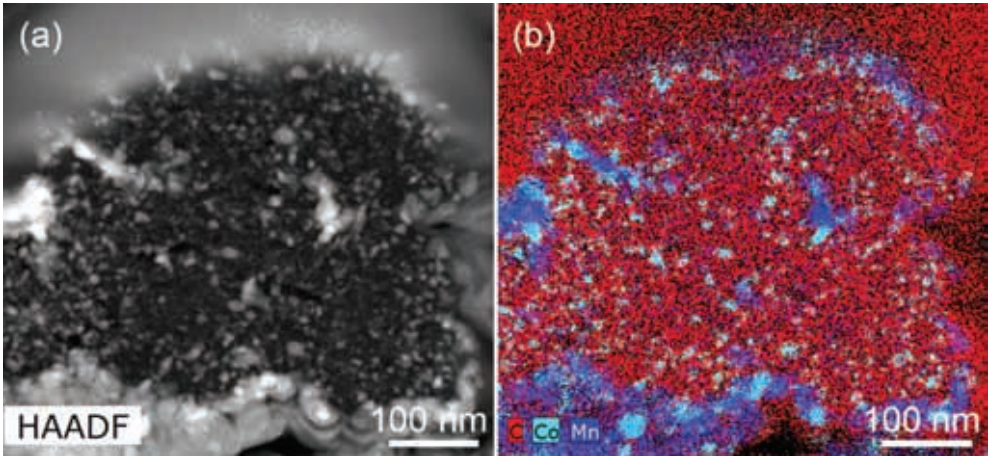

Figure 2. (a) HAADF STEM of hybrid sample and (b) EDS composite map of C, Co and Mn elemental distribution.

Atomic Scale Investigations of 1D-2D Heterostructures

Kimmo Mustonen[1], Heena Inani[1], Viera Skakalova[1], Christoph Hofer[1], Mohammad R.A. Monazam[1], Toma Susi[1], Esko Kauppinen[2], Jannik C. Meyer[1] and Jani Kotakoski[1]

[1] *Faculty of Physics, University of Vienna, Boltzmanngasse 5, A-1090 Vienna, Austria*

[2] *Department of Applied Physics, Aalto University School of Science, 15100, FI-00076 Aalto, Finland*

Low-dimensional materials exist with different dimensionalities, for example as two-dimensional (2D) atomically thin layers such as graphene and as quasi-one-dimensional (1D) structures such as nanotubes and nanowires. Although they already have interesting properties individually, when combined into stacked heterostructures, held together by van der Waals forces, they enable creating completely new building blocks for novel devices [1].

Graphene, one-atom-thick layer of carbon atoms, with exceptional electronic and mechanical properties has made a lasting mark in the field of material science. Graphene can be rolled into carbon nanotubes (CNT), which have diameters in the range of nanometers while being several micrometers long. Beyond graphene, which is a zero-band-gap semiconductor, another important class of 2D materials are transition metal dichalcogenides (TMD) that exhibit semiconducting band gaps. 2D TMDs have a three-atom-thick structure, where a transition metal (such as W) layer is sandwiched between two layers of chalcogen atoms (such as S). Similar to carbon nanotubes, also these materials can be rolled up into tubes.

We use aberration corrected scanning transmission electron microscopy (STEM) to study 1D-2D heterostructures of graphene and nanotubes (carbon and WS_2) at the atomic level. Our CNT-graphene heterostructures were synthesized by floating catalyst chemical vapor deposition [2] on commercial graphene grown via chemical vapor deposition (CVD). The structures were cleaned in the microscope column with laser irradiation in order to get rid of contamination around nanotubes. The atomic scale images show that the randomly deposited nanotubes become self-aligned on a suspended extremely clean graphene monolayer, due to minimization of the

interface energy. The interfacial interaction also leads to deformation of nanotubes and wrapping of the graphene around them.

The inorganic WS_2 nanotubes were suspended on CVD-grown graphene by the direct transfer method. STEM images show the large diameter multiwalled WS_2 nanotubes. Due to the much larger diameter of the WS_2NTs, such deformations as observed with CNTs are absent in the WS_2NT-graphene heterostructures.

As a conclusion, graphene support allows the randomly suspended single walled carbon nanotubes to be observed with unprecedented accuracy and with their structure down to an individual atom. However, for WS_2-NTs, no direct signs of interaction with graphene were observed due to their size.

References:

[1] D Jariwala, TJ Marks and MC Hersam, Nat. Materials **16** (2016), 170.
[2] K Mustonen *et al*, Appl. Phys. Lett. **107** (2015), 013106.

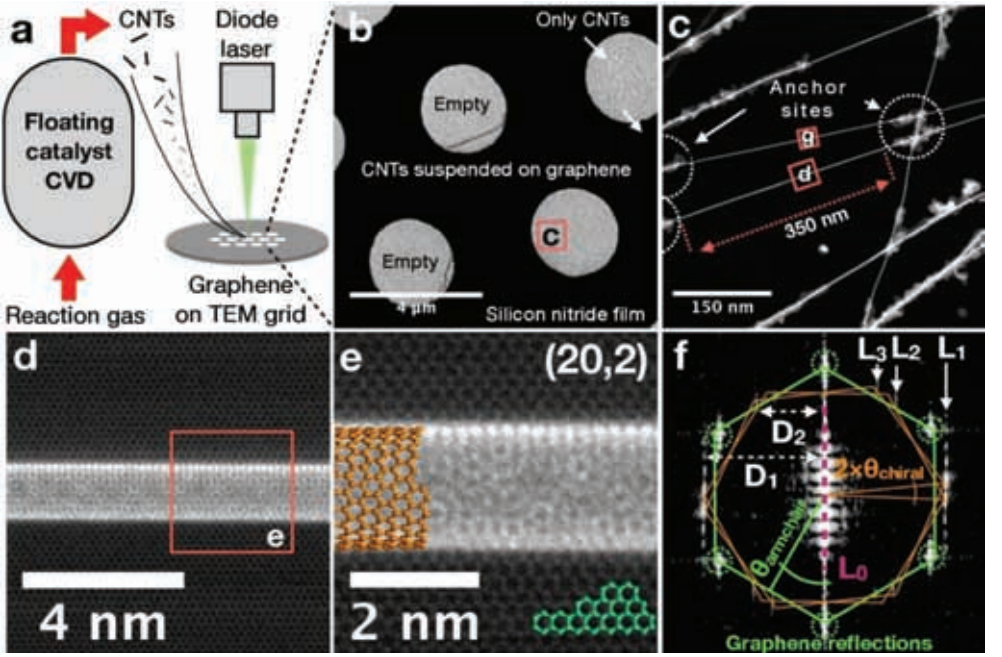

Figure 1. (a) Setup for CNT-graphene sample preparation. (b-c) (Scanning) Transmission electron microscopy (S)TEM images of a CNT-graphene heterostructure. (d-e) Atomic resolution images of single-walled CNT. (f) The corresponding Fourier transform.

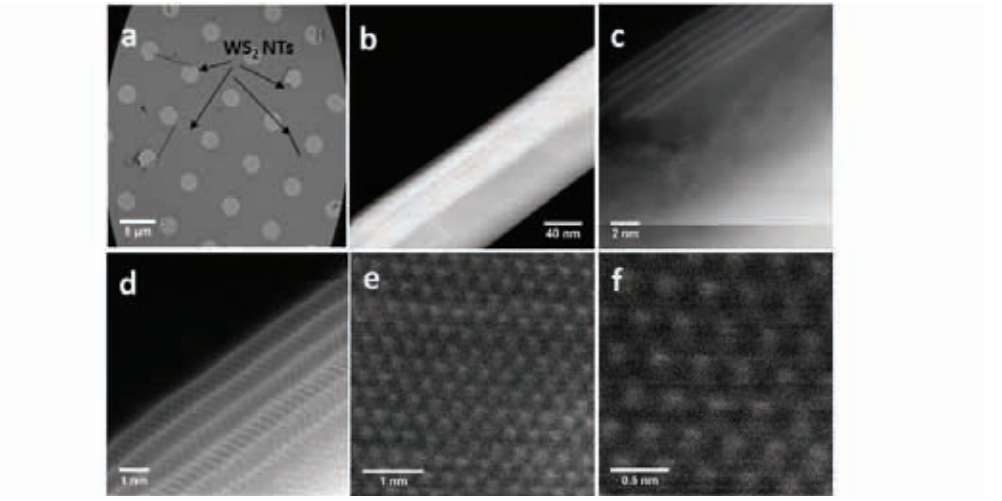

Figure 2. (a) TEM overview image of WS_2-NT-graphene heterostructure. (b) STEM image of a WS_2-NT nanotube. (c-d) Close up view of the walls of a multi-walls WS_2-NT. (e-f) Atomic resolution images of the nanotube.

Solubility Limits and Micro-Structural Changes Induced by Ca Content in the $Ba_{1-x}Ca_xTiO_3$ Perovskite-Type Particles

Ionel F. Mercioniu[1], Marjeta Maček Kržmanc[2], Daniela Ghica[1], Adrian V. Maraloiu[1] and Ioana D. Vlaicu[1]

[1] *National Institute of Materials Physics, Magurele-Ilfov, Romania*
[2] *Advanced Materials Department, Jožef Stefan Institute, Ljubljana, Slovenia*

An increasing attention was dedicated towards ferroelectric perovskite particles with a well-defined anisotropic shape because of their unique properties which are shape and size dependent at low dimensions. As it was observed by others, in order to grow oriented and defined shape particles of ABO_3 perovskites one should use a template which possess a two-dimensional structure and already contains perovskite units, like Ruddlesden-Popper-type layered perovskite $Sr_3Ti_2O_7$ and layered perovskite Aurivillius phases ($Bi_4Ti_3O_{12}$, $MBi_4Ti_4O_{15}$, M = Ba, Sr, Pb). It was found that (001) oriented $MTiO_3$ plates can be grown from 10 µm sized plates Aurivillius $MBi_4Ti_4O_{15}$ phases which serve as a template in a grain growth process [1-3].

Following a similar principle of growth and design as Kržmanc *et al* [4] have used $Bi_4Ti_3O_{12}$ micron-plates in order to tailor the shape, size, crystal structure and preferential growth orientation of $BaTiO_3$ plates, solid solutions with the composition $Ba_{1-x}Ca_xTiO_3$ (x is the calcium content which was varied from 0 to 1) have been prepared. Ba^{2+} and Ca^{2+} precursors were roughly mixt with NaCl/KCl salts and afterwards mixt with $Bi_4Ti_3O_{12}$ template plates. All this mixture was put in an alumina crucible and the topochemical conversion from molten salt solution of the $Ba_{1-x}Ca_xTiO_3$ particles carried out in an oven with a temperature regime well controlled, at 900ºC. The washing procedure was performed in a way that the $Ba_{1-x}Ca_xTiO_3$ particles were isolated from the other side products by repeated washing-centrifugation operations. For only one sample to be ready for all experimental analyses three days were allocated.

How the morpho-structural characteristics of the $Ba_{1-x}Ca_xTiO_3$ particles are affected by increasing the calcium content have been present herein. By powder

XRD measurements have been determined both the structure and tetragonality degree of the products with the composition $Ba_{1-x}Ca_xTiO_3$. Rietveld refinements enabled observation how the lattice parameters of the host material is affected with respect to the increasing calcium content, thus providing information regarding the solubility of calcium in the $BaTiO_3$ lattice in the given experimental conditions. With Ca content increasing the lattice parameters tend to the same value as for cubic structure. At a nominal Ca content of 0.3, there is already a secondary phase which was identified to be $CaTiO_3$, thus indicating the fact that calcium solubility in $BaTiO_3$ lattice was reached. The side products resulted for the Ca nominal content x=0.5 indicate somehow that the template plates get disintegrated in the initial compounds of which they were synthesized, Bi_2O_3 and TiO_2 (rutile, the crystalline phase stable at high temperature).

Transmission Electron Microscopy (TEM) techniques provided information regarding the micro-structural properties of the particles, information which completes the x-ray diffraction (XRD) statements. Energy dispersive x-ray (EDX) spectroscopy provided information about the presence of the desired elemental composition and the real compositions of the $Ba_{1-x}Ca_xTiO_3$ particles could be determined. Also, Scanning Electron Microscopy (SEM) data show that the thickness of the particles appears to increase with Ca content increasing. Until a certain calcium content, the perovskite-type particles with the composition $Ba_{1-x}Ca_xTiO_3$ follow a growth pattern preserving more or less the shape of the template, but above a critical Ca content both structure and morphology of the particles are drastically affected.

References:

[1] Y Chang *et al*, Inorganic Chemistry **53** (2014), 11060.
[2] SF Poterala *et al*, Chemistry of Materials **22** (2010), 2061.
[3] D Liu, Y Yan and H Zhou, Journal of the American Ceramic Society **90** (2007), 1323.
[4] M Maček Kržmanc *et al*, Crystal Growth & Design **17** (2017), 3210.
[5] The authors ID Vlaicu, D Ghica, AV Maraloiu and IF Mercioniu acknowledge that studies in this work were supported by a grant of the Romanian National Authority for Scientific Research and Innovation, CCCDI-UEFISCDI, project number 49/2016 within PNCDI III - M-ERA NET Program.

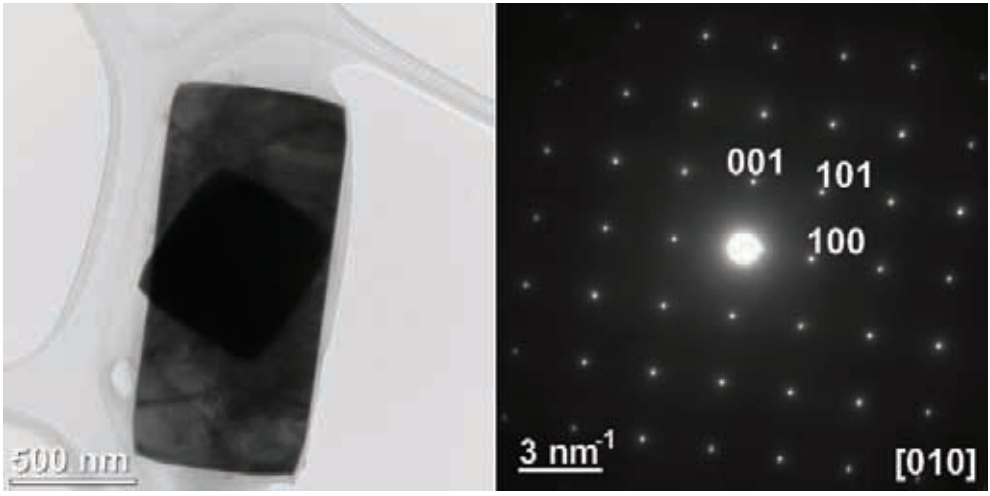

Figure 1. TEM image at low-magnification and the corresponding SAED pattern (insets) for $Ba_{1-x}Ca_xTiO_3$ (x=0) sample.

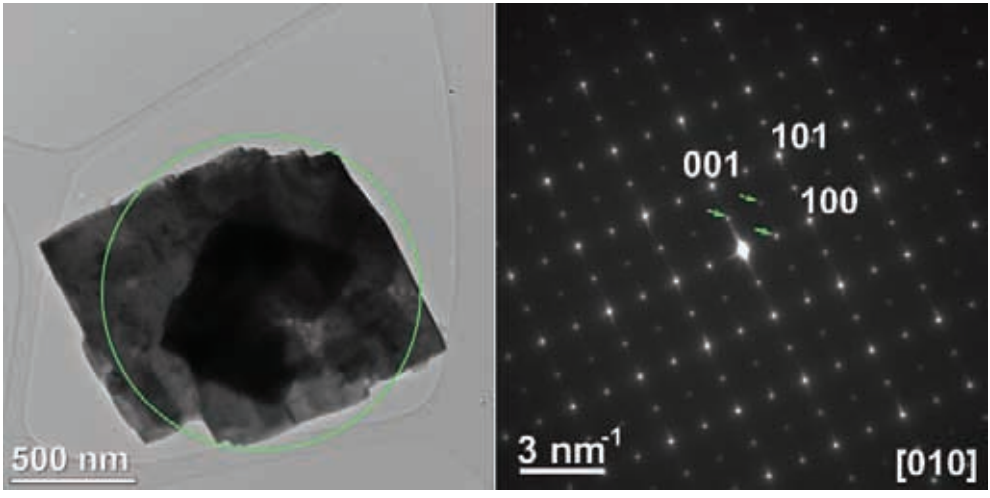

Figure 2. TEM image at low-magnification and the corresponding SAED pattern (insets) for Ba1-xCaxTiO3 (x=0.3) sample.

A Quantitative EDXS Analysis of Oxide Ceramic-Electrode Systems

Judith Lammer[1,2], Evelin Fisslthaler[1], Martina Dienstleder[1], Sebastian Rauch[2] and Werner Grogger[1,2]

[1] Graz Centre for Electron Microscopy, Steyrergasse 17, 8010 Graz, Austria
[2] Institute of Electron Microscopy and Nanoanalysis, Graz University of Technology, Steyrergasse 17, 8010 Graz, Austria

Energy-dispersive X-ray spectroscopy (EDXS) is an essential method in chemical analysis using transmission electron microscopy, especially since the recent introduction of large-area detectors. Thanks to this increase in collection efficiency, even signals from single atoms have become detectable. Quantification tools, using the Cliff-Lorimer method combined with software embedded theoretical k-factors, offer a quick and easy way to obtain the composition of materials. However, such quantification results must be treated with caution since absorption effects in the sample [1] as well as shadowing effects due to sample holder - detector geometry [2] might influence the outcome.

In this work, we analysed the shadowing behaviour of several sample holders in combination with a ChemiSTEM system (Super-X) with four detectors situated symmetrically around the sample within an FEI 60–300 Titan³ microscope. In order to do so, we used the model developed by Kraxner et al. [3] which coughs out detector positions as well as shadow images dependent on holder tilt angles by combining measured X-ray intensities as a function of specimen tilt angle α and simulations including geometric models of the TEM holders and the four detectors (see Figure 1). Thereby, we are able to correct shadowing effects depending on the sample holder.

Concerning absorption effects in the sample we used the so-called Zeta-factor method [4], which remediates for this issue when using flat specimen geometries. It comes along with an integrated absorption correction for low energy X-rays and therefore improves quantification for light elements.

As an application example, we analysed an oxide ceramic implemented in various engineering applications: lanthanum-doped lead zirconate titanate (PLZT) multi-

layers deposited between copper electrodes. We investigated diffusion processes, dopant behaviour and perturbing effects in stoichiometry. We used our model for shadowing correction and the Zeta-factor method to improve the accuracy of the quantification results. Our multiscale analyses reveal a Cu diffusion in the material close to the electrodes as well as an enrichment of zirconium oxide grains at the interface between the electrode and the ceramic. Furthermore, we detected several single PLZT grains with inhomogeneous composition: an increase of lead and a reduction of titanium and lanthanum in grain centres. Additionally, we examined thermally driven changes of the material. *In situ* heating experiments revealed a severe change in the ceramic material at 700°C, where strong elemental shifts appeared: areas of zirconium oxide formed (see Figure 2).

Our subsequent work will focus on the material behaviour at the atomic scale, e.g. dopant position in the crystal lattice. Therefore, we have already started to perform HR-STEM measurements (see Figure 3) in combination with EDX spectrum imaging.

References:

[1] J Philibert in “X-Ray Optics and X-Ray Microanalysis”, ed. HH Pattee, VE Cosslett and A Engström, (Elsevier Science, Burlington), p. 379–392.
[2] TJA. Slater *et al*, Ultramicroscopy **162** (2016), 61–73.
[3] J Kraxner *et al*, Ultramicroscopy **172** (2017), p. 30–39.
[4] M Watanabe and DB Williams, J. Microsc. **221** (2) (2006), p. 89–109.
[5] The authors thank EPCOS OHG a TDK Group Company for the samples, DENS Solutions for the holder models and the Austrian Research Promotion Agency FFG (project 850220/859238) for funding.

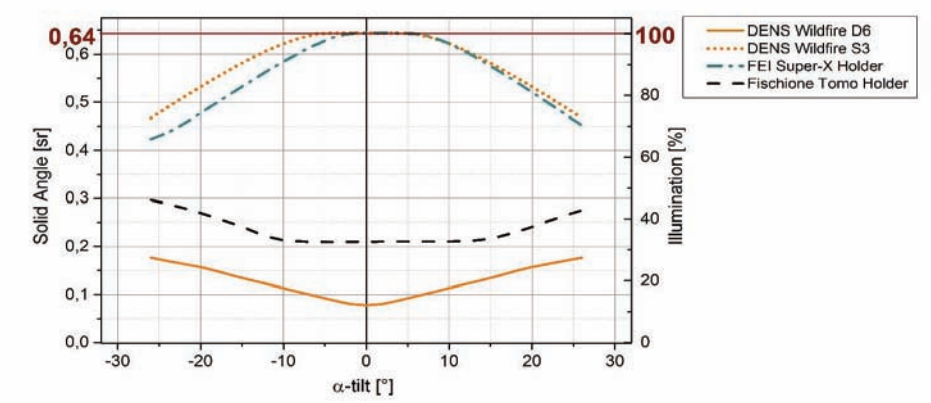

Figure 1. Detector illumination using several sample holders as a function of sample tilt angle.

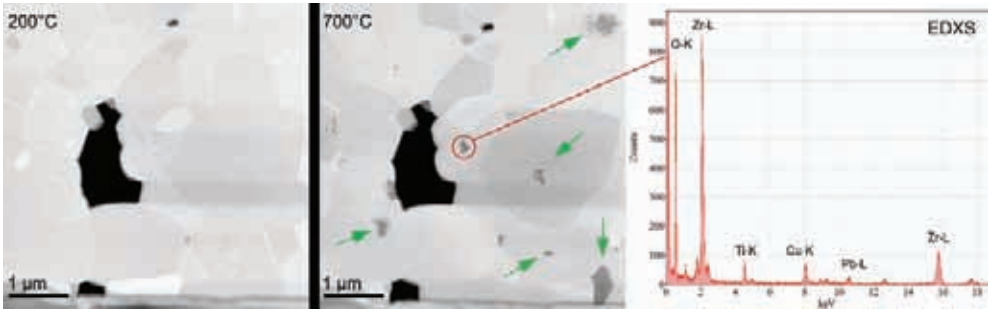

Figure 2. Formation of zirconium oxide regions at 700°C (arrows in HAADF image).

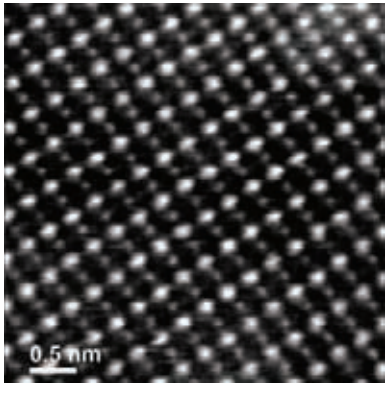

Figure 3. HR-STEM HAADF image of PLZT.

Comprehensive Characterization of Multiferroic $BiFeO_3$ Powder Fabricated by the Hydrothermal Procedure

Maria Čebela[1], Radmila Hercigonja[2], Milena Rosić[1], Dejan Zagorac[1], Jelena Luković[1], Jelena Zagorac[1], Dragana Jordanov[1] and Branko Matović[1]

[1] *Institute for Nuclear Sciences, Centre of Excellence-CextremeLab Vinca, University of Belgrade, Belgrade, Serbia*
[2] *University of Belgrade, Faculty of Physical Chemistry, Serbia*

Bismuth ferrite ($BiFeO_3$) has recently drawn attention due to its outstanding multi-functional properties, as well as for being a lead-free ceramic material. In the current study, BiFeO3 nanoparticles were synthesized by strictly controlled hydrothermal process. High geometric molded particles of a small size and with high degree of purity (99.74 %) were obtained. We used nitrates of bismuth and iron as well as 8M potassium hydroxide as a basis for synthesis. The results of the X-ray diffraction study of the obtained polycrystalline material show single-phase bismuth ferrite that crystallizes with a rhombohedral lattice. Using the Rietveld method it has been determined that the particles of the synthesized powder are in a nanometric range with a particle size of about 30 nm. It was found that all reflections of the obtained bismuth ferrite belong to the rhombohedral α-$BiFeO_3$ phase which crystallizes in the space group R3c (No. 161). In addition, electronic and magnetic properties of $BiFeO_3$ were investigated using combination of experimental and theoretical methods. HRTEM analysis confirmed existence of twin stacking faults, which are responsible for enhanced magnetic properties. EPR measurements suggested existence of electrons trapped by vacancies or defects. It has been proposed that $Fe^{3+}-O_V$ defect complex could be created at elevated temperatures followed by formation of trivalent Fe ions, which intensely provide local 3d moments. The magnetic behavior of the synthesized material was studied by means of SQUID device and using a vibrating sample magnetometer (VSM). The temperature dependence of the magnetization shows the antiferomagnetic-paramagnetic phase transition at the temperature of TN = 220K, while below this temperature weak ferromagnetic behavior has been detected. Theoretical studies were performed using a full potential linearized augmented plane-waves plus local orbital (FP(L)APW+lo)

method, based on the density functional theory (DFT). In addition, a structure prediction has been performed and 11 additional $BiFeO_3$ modifications have been proposed. In the next stage, an *ab initio* optimization of predicted structures has been performed and the structure of the γ-phase has been elucidated.

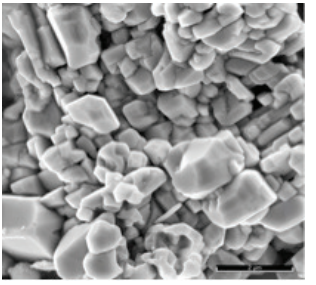

Figure 1. SEM image of BFO synthesized with 8 M KOH for 6 h at 200 °C (bar length is 2μm).

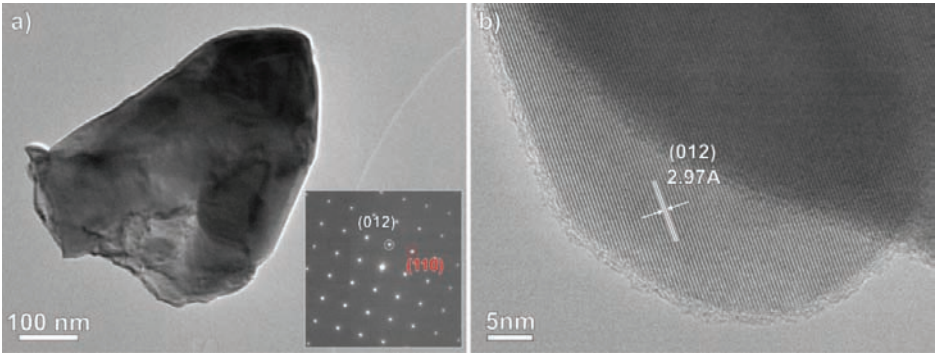

Figure 2. TEM image of a typical BFO particle (insert - SAED pattern over one grain) (a) and HRTEM image with characteristic d-spacing value (b).

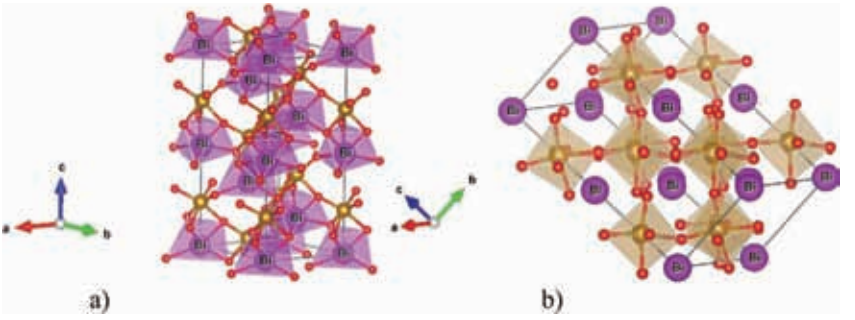

Figure 3. Visualization of the synthesized and calculated α-BiFeO3 structure: (a) sixfold coordination (CN=6) of the Bi atom by O atom; (b) sixfold coordination (CN=6) of the Fe atom by O atom.

The Effect of Particle Shape and Composition on the Electrochemical Behavior of Pt-based Nanostructured Catalysts for Fuel Cells

Mila N. Krstajić Pajić[1], Sanja I. Stevanović[2], Vuk V. Radmilović[3], Piotr Zabinski[4], Nevenka R. Elezović[5], Aleksandra Gavrilović-Wohlmutter[6], Velimir R. Radmilović[1,7], Snežana Lj. Gojković[1] and Vladislava M. Jovanović[2]

[1] *Faculty of Technology and Metallurgy, University of Belgrade, Serbia*
[2] *Institute for Chemistry, Technology and Metallurgy, Department of Electrochemistry, University of Belgrade, Serbia*
[3] *Innovation Center, Faculty of Technology and Metallurgy, University of Belgrade, Serbia*
[4] *AGH University of Science and Technology, Faculty of Non-Ferrous Metals, Krakow, Poland*
[5] *Institute for Multidisciplinary Research, University of Belgrade, Serbia*
[6] *CEST Competence Center for Electrochemical Technologies, Vienna, Austria*
[7] *Serbian Academy of Sciences and Arts, Belgrade, Serbia*

Nanostructured Pt and bimetallic PtAu catalysts supported on high area carbon Vulcan XC 72 R for fuel cell applications were synthesized by water in oil microemulsion method. HCl was used as a capping agent to affect the particle shape. The aim of the research was to investigate the effect of particle surface structure and composition on their electrochemical behavior in supporting electrolyte and in oxidation reactions of small organic molecules, as reactions of interest for low temperature fuel cells.

Pt/C and PtAu/C catalysts prepared without and with various concentrations of capping agent were characterized by several microscopic and spectroscopic techniques, in order to investigate their structure, morphology and composition: X-ray diffraction (XRD), high resolution transmission electron microscopy (HRTEM), energy dispersive X-ray spectroscopy (EDS) and X-ray photoelectron spectroscopy (XPS). In the case of Pt/C catalysts (Fig.1), these analyses have shown that the addition of a capping agent, and proper adjustment of synthesis conditions can affect the nanoparticle shape [1,2]. When the optimal amount of the capping agent is used, concave cu-

bic particles are formed (Fig.1 B). The particle size, calculated from XRD and TEM data, turned out to be around 8 nm. Particles with such a shape have a higher share of [100] oriented planes, convenient for oxidation of small organic molecules, due to their high resistivity to CO poisoning, which is a common problem in such systems. If the amount of capping agent is further increased, the deterioration of cubic shape occurs and more branched-like structures can be observed. Additionally, particle agglomeration is present on the carbon support.

Low-loading bimetallic PtAu/C nanocatalysts were synthesized by the same procedure, with the simultaneous reduction of the precursors (Fig. 2) from a single micromulsion and with successive reduction methodology. Particle size of the bimetallic catalysts, calculated from XRD and TEM data with values 2-6 nm, is smaller compared to Pt samples. XPS and EDS results confirm the presence of both, Pt and Au in the samples, which indicates a successful synthesis procedure. Au content in PtAu samples, according to EDS analysis, is in the 10 – 20 at% on average, which is very low, having in mind that the PtAu ratio for this kind of application is usually 1:4, or with even higher Au contribution. However, due to very fine dispersion of Au, and the incorporation of a certain amount of Au into the Pt crystal lattice, Au has an exaggerated beneficial effect on the catalyst as if much more Au is present in the structure that it is in reality.

References:

[1] MN Krstajić Pajić *et al*, Applied Catalysis B: Environmental **196** (2016), 174-184

[2] MN Krstajić Pajić *et al*, Journal of Solid State Electrochemistry **20** (2016), 3405-3414

[3] The authors acknowledge funding from the Ministry of Education, Science and Technological Development of the Republic of Serbia and networking support by COST action MP1407.

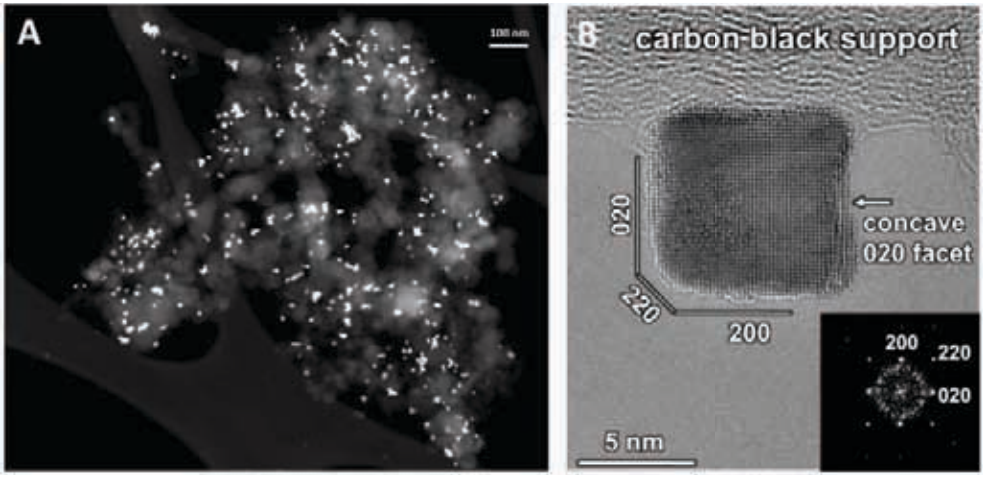

Figure 1. Pt/C catalyst prepared with optimal (25%) amount of capping agent: A – low magnification HAADF STEM; B – HRTEM image of a concave cubic Pt particle; inset is an FFT of the particle [1].

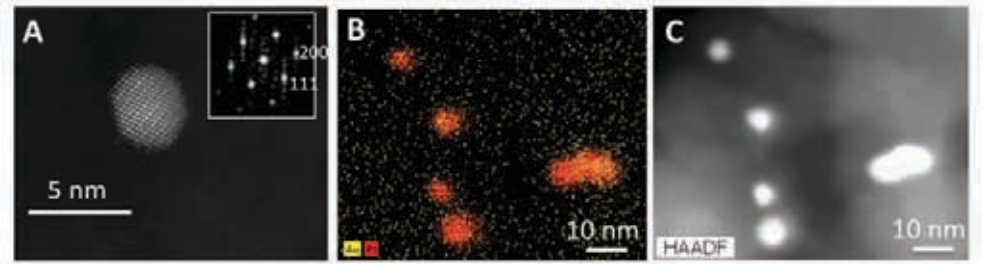

Figure 2. PtAu/C catalyst prepared by simultaneous reduction without capping agent: A - HRTEM image with FFT inset of the PtAu/C catalyst; B - EDS map of the PtAu/C catalyst; C- HAADF STEM image from which the EDS map has been taken.

Formation of Ag Nanoparticles in CrN by Using Ag Ion Implantation and Thermal Annealing

Mirjana Novaković[1], Maja Popović[1], Emanuel Schmidt[2], Philipp Schöppe[2], Miodrag Mitrić[1], Nataša Bibić[1], Carsten Ronning[2], Zlatko Rakočević[1]

[1] *University of Belgrade, Institute of Nuclear Sciences VINČA, 11351, Belgrade, Serbia*

[2] *Institute of Solid State Physics, Friedrich Schiller University Jena, Max-Wien-Platz 1, D-07743, Jena, Germany*

In the recent years, there has been a great interest in metal nanoparticles (NPs) embedded in different host matrices due to the wide range of their potential applications [1,2]. Methods, which are the most frequently used for the production of the nanocomposites with metal nanoparticles, are in situ doping during growth of the material or subsequent ion implantation. Experiments involving ion implantation are commonly performed at elevated temperatures or they are followed by high temperature annealing or high-energy (MeV) irradiations [3]. In this study we examine the influence of silver ion implantation and subsequent annealing on the behavior of CrN layers, where the variation of these parameters is expected to play an important role for the formation of Ag nanoparticles. As it will be seen from the results, Ag nanoparticles are formed for the particular used set of experimental parameters of 2×10^{16} ions/cm^2 and 700 ºC annealing temperature.

CrN films thickness of ~280 nm deposited by means of d.c. reactive ion sputtering on commercial Si (100) wafers were implanted with silver ions with incident ion energy of 200 keV to the fluences of $0.5\text{-}2\times10^{16}$ ions/cm^2. For such an incident ion energy, the SRIM code [4] gave an average ion implanted depth of R_P=40 nm with a straggling of ΔR_P=14 nm. Subsequent to the implantation the films were annealed for 2 h either at 200 ºC and 400 ºC or at 700 ºC. Lamellas for transmission electron microscopy (TEM) were prepared via focused ion beam (FIB) using a FEI Helios Nanolab 600i dual

beam system. High-resolution TEM microscope TALOS F200X was used for characterization of the samples.

A high-magnification image and corresponding EDS elemental mapping of CrN film implanted to the fluence of 2×10^{16} ions/cm^2 and annealed 2h at 700ºC is presented in Fig. 1. The HRTEM image shows the inhomogeneous depth distribution of the NPs. The smaller Ag nanoparticles are found in the top sublayer, while the largest ones are in the bottom sublayer, at a depth corresponding to the maximum Ag distribution in the sample. The NPs size was measured in the cross-section image and the resulting size distribution is shown in the inset of Fig. 1a. The maximum particle diameter is 14 nm, but most of them are very small. In fact, 90% of the counted Ag nanoparticles were less than 5 nm in diameter. Fig. 1b presents elemental color mapping of the rectangular area taken from the cross-sectional image. Chromium, nitrogen, and silver are presented in different colors: Cr (green), N (deep blue) and Ag (sky blue). The Figure reveals the uniform spatial distribution of Cr and N in the film area, whereas the silver is entirely located within the nanoparticle areas.

It is demonstrated that the Ag metallic nanoparticles, with a spherical shape and grain diameter up to 14 nm were formed within the CrN films after silver ions implantation. The particles are inhomogenously distributed through the layer and the largest ones are found at a depth corresponding to the projected range of Ag ions. The results of this study are interesting towards developing radiation tolerant materials based on multiple layered structures.

References:

[1] HA Atwater and A Polman, Nat. Mater. **9** (2010), 205.
[2] M Torrell *et al*, Surf. Coat. Technol. **204** (2010), 1569.
[3] S Wolf *et al*, Nanotechnology **27** (2016), 145202.
[4] J F Ziegler, J P Biersack and U Littmark, (Pergamon Press, New York) code SRIM2003: http://www.srim.org.
[5] The authors acknowledge funding from the Ministry of Education and Science of the Republic of Serbia (Project No. III 45005) and the German-Serbian DAAD bilateral collaboration (Project No. 451-03-01038/2015-09118/18). We would like to thank Igor Peterka for his assistance at 500 kV ion implanter and Carmen Voigt for her help during STEM experiments in Jena.

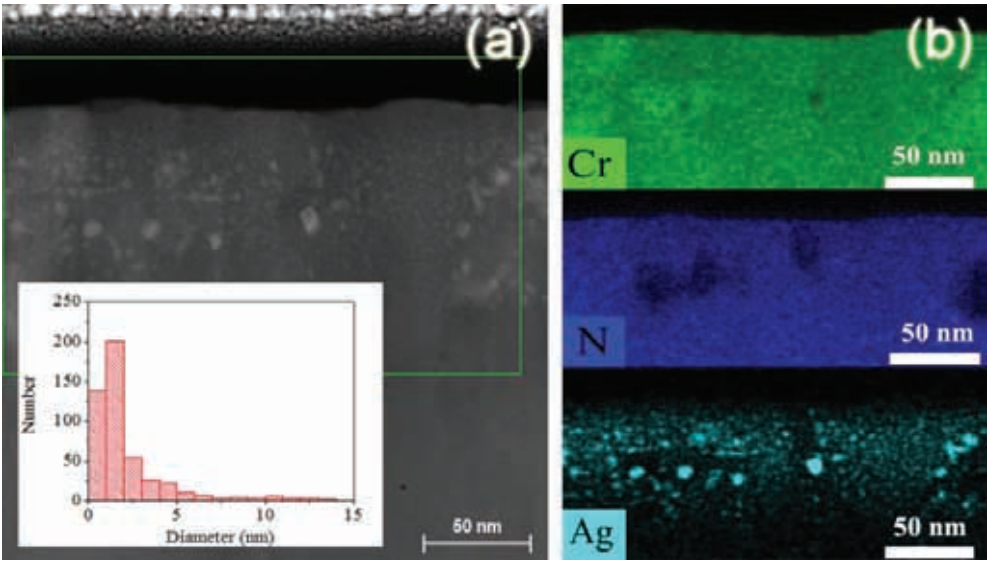

Figure 1. (a) High-magnification cross-sectional image of subsurface of CrN layer implanted to the fluence of 2×10^{16} ions/cm^2 and annealed 2h at 700ºC with the particle size distribution in the inset and (b) EDS element color mapping.

Ion Implantation and Electron-beam Modification of Graphene

Mukesh Tripathi[1], Cong Su[2, 3], Roman Böttger[4], Stefan Facsko[4], Ju Li[2], Juan-Carlos Idrobo[5], Jani Kotakoski[1] and Toma Susi[1]

[1] *University of Vienna, Faculty of Physics, Vienna 1090, Austria*
[2] *Department of Nuclear and Materials Science and Engineering, Massachusetts Institute of Technology, Cambridge MA 02139, USA*
[3] *Research Lab of Electronics, Massachusetts Institute of Technology, Cambridge MA 02139, USA*
[4] *Helmholtz-Zentrum Dresden-Rossendorf, Institute of Ion Beam Physics and Materials Research, 01314 Dresden, Germany*
[5] *Center for Nanophase Materials Sciences, Oak Ridge National Laboratory, Oak Ridge TN 37831, USA*

Incorporating heteroatoms in the graphene lattice can drastically alter its electronic, mechanical and chemical properties. These dopants can be introduced either during materials growth, or using a separate modification route. Until recently, directly observed substitutions have been limited to incidental Si impurities, and low-energy ion implanted B and N [1]. Last year, we have extended implantation studies to also include P [2].

Here we show the so far heaviest reported impurity, Ge, also implanted through ion irradiation, and demonstrate the manipulation of Si and P impurities in graphene using the Ångström-sized electron beam of an aberration corrected scanning transmission electron microscope (STEM).

In the first study, we implanted low-energy $^{74}Ge^{+}$ ions into single-layer graphene [3]. Although sample contamination introduced during irradiation remains an issue, atomic resolution STEM imaging and quantitative image simulations reveal that Ge can either directly substitute single carbon atoms, bonding to three C neighbors in a buckled out-of-plane configuration, or occupy an in-plane position in a double vacancy. First principles molecular dynamics provides further atomistic insight into the implantation process, revealing a strong chemical interaction between incoming Ge ion and the neighbors of the displaced C atom that enables implantation below the graphene displacement threshold energy. Our results demonstrate that the elements

from the fourth period can be implanted into the graphene lattice, suggesting that substitutions from group 3-13 with advanced applications such as single-atom catalysis and magnetism with graphene as the template may also be possible.

In the second study, we employed STEM to image, identify and manipulate Si [4] and P dopants in monolayer graphene synthesized via chemical vapor deposition (CVD), which is found to be largely free of contamination. For Si, we show atomically precise manipulation over dozens of jumps within the graphene lattice [4]. In the case of P, we observe various dynamics, such as direct exchange and Stone-Wales transitions, knock-out of a C neighbor, and replacement of a P atom by C and explain the mechanism for each process by first-principle calculations. Our simulations show that the P atom will not move unless there is an out-of plane momentum transfer from an incoming electron to a C atom neighboring the dopants. We also demonstrate the possibility of electron-beam manipulation of P in graphene, although this is significantly more challenging compared to Si. Our work presented here can further help designing techniques for controlling P and other dopants in graphene at room temperature and with atomic precision using STEM [5].

References:

[1] U Bangert *et al*, Nano Letters **13** (2013), 4902.
[2] T Susi *et al*, 2D Materials **4** (2017), 021013.
[3] M Tripathi *et al*, ACS Nano **12** (2018), 4641.
[4] T Susi *et al*, Ultramicroscopy **180** (2017), 163.
[5] We acknowledge funding by the Austrian Science Fund (FWF) through project P 28322-N36 and European Research Council (ERC) under the European Union's Horizon 2020 research and innovation programme (grant agreement No. 756277-ATMEN).

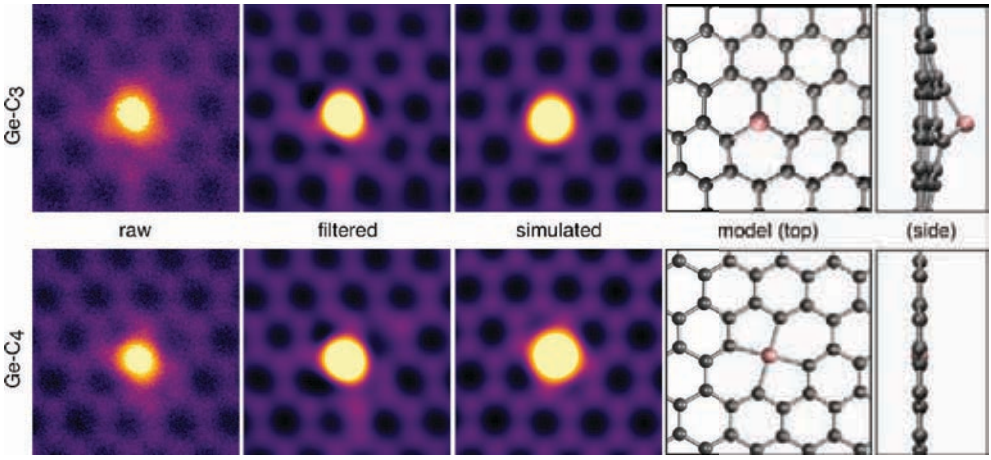

Figure 1. Germanium substitutions in graphene (top: 3-fold single-atom substitution, bottom: 4-fold substitution in a double vacancy). Quantitative STEM simulation using our experimental parameters reproduces in both cases the high intensity of the Ge impurity. DFT simulations show that while the Ge-C_3 impurity buckles out of the graphene plane, the Ge-C_4 site is flat. The fields of view are ~ 1×1 nm^2.

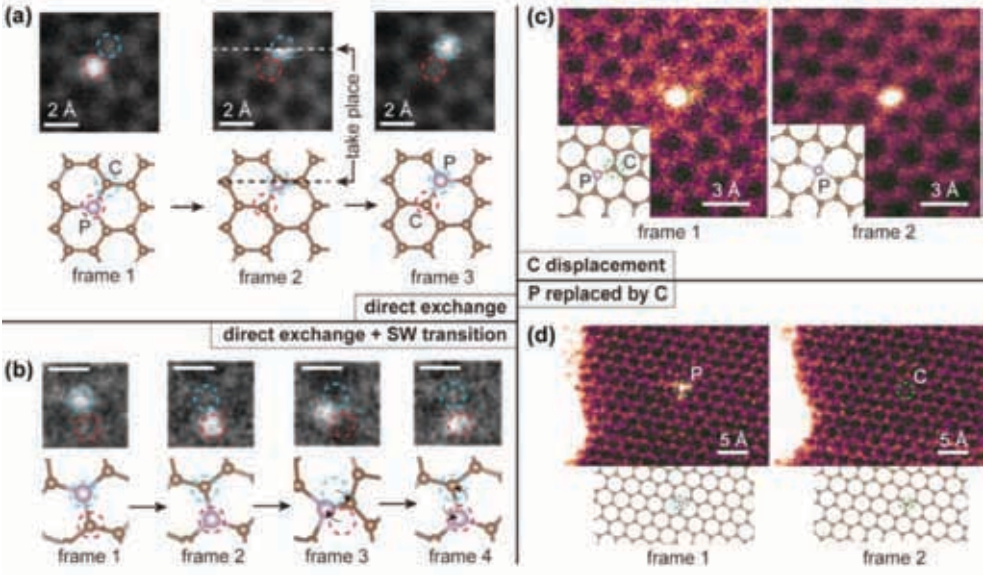

Figure 2. Competing P dopant dynamics in graphene. (a) 3 frames showing direct exchange with the initial (frame 1), transition (frame 2), and final configurations (frame 3). (b) 4 frames showing both direct exchange (frame 1 to 2) and Stone-Wales transition (frame 2 to 4). (c) Neighboring C atom knocked out by electron beam, turning the threefold P into fourfold. (d) P dopant being replaced by a C atom. Scale bars in (b): 2 Å.

Advanced TEM Characterization of Interfaces and Strain-Related Distortions in Epitaxial Perovskite Heterostructures

Raluca F. Negrea and Corneliu Ghica

National Institute of Materials Physics, Magurele, Romania

Most of the currently studied artificial multiferroic systems are based on epitaxial multilayers grown onto SrTiO3 (001) single crystals (STO), using SrRuO3 (SRO) epitaxial layers as bottom electrode. In the ferroelectric heterostructures, the microstructural characteristics of the deposited thin films as well as the interfaces between the ferroelectric layers and the electrodes play a fundamental role in the electrical behavior of the heterojunction (polarization hysteresis loops, C-V and I-V characteristics). Atomic scale structural and chemical characterization brings a major contribution in further understanding the extrinsic contributions to the electrical characteristics. In this study a Cs probe corrected JEM ARM 200F electron microscope was used to investigate the interface structure and strain driven structural distortions in the PZT/SRO/STO and BTO/SRO/STO systems, where PZT stands for $PbZr_{0.2}Ti_{0.8}O_3$ and BTO for $BaTiO_3$. Pulsed Laser Deposition (PLD) has been used for the deposition of the epitaxial SRO, PZT and BTO layers onto STO (001) substrates.

The Scanning Transmission Electron Microscopy (STEM) and the Electron Energy Loss Spectroscopy (EELS) were performed for the atomic resolution characterization of the SRO-PZT and SRO-BTO interfaces (Figure 1). The atomic interdiffusion at the interface has been studied using the Z contrast in STEM imaging by High-Angle Annular Dark Field (HAADF) and Annular Bright Field (ABF). The studies reveal an atomic interdiffusion across a region of up to 7 atomic planes around the SRO-PZT and SRO-BTO interfaces. Atomic scale EELS – Spectrum Imaging (EELS-SI) reveals the nature and position of the atomic species at the interface. SAED patterns from areas including the SRO layer exhibit faint diffraction spots appearing in positions which are not allowed by the reflection conditions in the space groups of SRO, PZT, BTO or STO. FFT of the corresponding HRTEM micrographs prove

that the concerned spots are generated from nanometric areas inside the SRO layer (Figure 2). A quantitative HRTEM study was performed in order to measure and map the strain fields inside the SRO layer at the nanometric scale. The study, supported by quantitative image processing using Geometrical Phase Analysis (GPA) and image simulation, clearly proves a strain-driven monoclinic distortion in nanometric domains inside the thin SrRuO3 epitaxial layers, thus explaining the presence of the diffraction spots in forbidden positions in the SAED patterns [1].

References:

[1] C Ghica *et al*, Journal of Applied Physics **116** (2014), 023516.

[2] The authors acknowledge UEFSCDI for financial support through the PN- III-P4-ID-PCE-2016-0529 project.

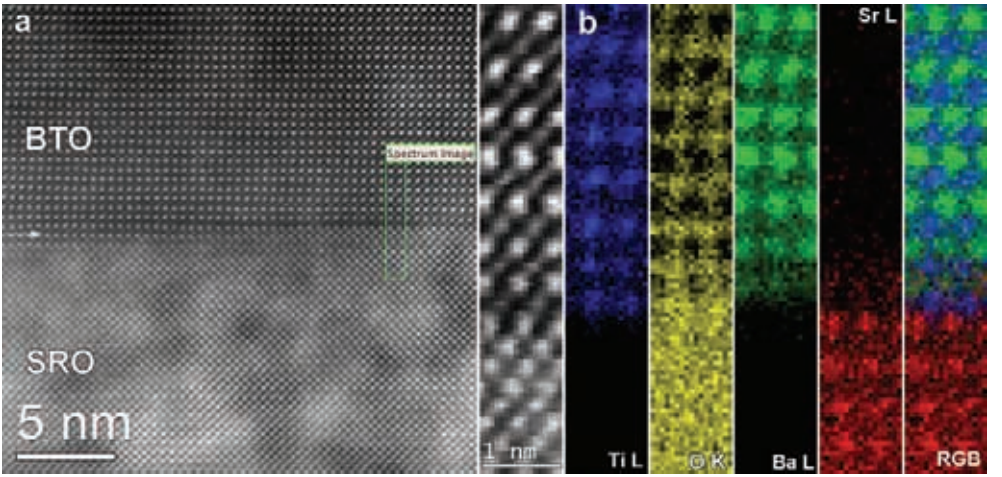

Figure 1. (a) HAADF – STEM image showing the BTO – SRO interface; (right – magnified DF image extracted from Spectrum Image area) and (b) atomic resolution elemental mapping extracted from EELS–SI area in the HAADF image showing the elemental distribution at the SRO – BTO interface. The Ba, Ti and Sr maps reveal atomic interdiffusion at the interface across 1 atomic plan.

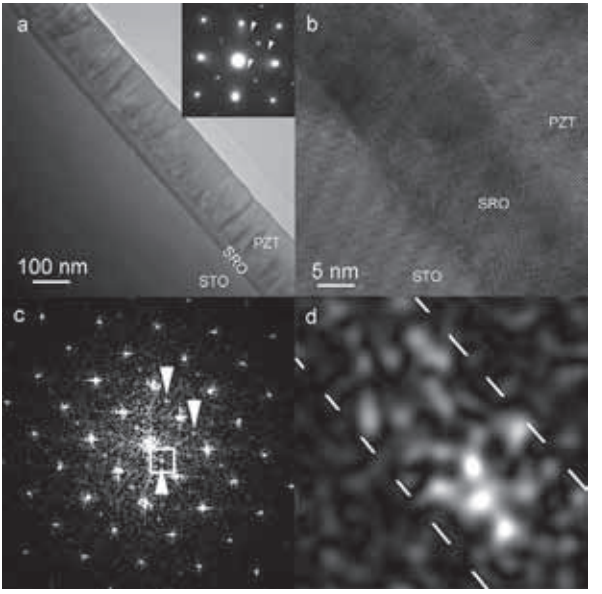

Figure 2. (a) Low-magnification TEM image of a PZT/SRO/STO sample featuring SRO diffraction spots in forbidden positions (marked by arrows on inserted SAED pattern). (b) HRTEM image showing the epitaxial growth of the PZT and SRO layers. (c) Power spectrum of the HRTEM image exhibiting diffraction spots in forbidden positions. (d) GPA amplitude image using the selected forbidden spot 010 (white square) in (c).

ABF-STEM Investigations of Taaffeite $Be_xMg_yAl_{2(x+y)}O_{4(x+y)}$ Structures

Sandra Drev[1], Aleksander Rečnik[2], Matej Komelj[2], Christian Gspan[3], Goran Dražić[4], Vesna Šrot[5], Miran Čeh[1,2], Ferdinand Hofer[3], Peter A. van Aken[5], Nina Daneu[2]

[1] *Center for Electron Microscopy and Microanalysis, Ljubljana, Slovenia*
[2] *Department for Nanostructured Materials, Jožef Stefan Institute, Ljubljana, Slovenia & Jožef Stefan International Postgraduate School, Ljubljana, Slovenia*
[3] *Institute for Electron Microscopy and Nanoanalysis, Graz University of Technology, Graz, Austria*
[4] *Laboratory for Materials Chemistry, Institute of Chemistry, Ljubljana, Slovenia*
[5] *Stuttgart Center for Electron Microscopy, Max Planck Institute for Solid State Research, Stuttgart, Germany*

Four compounds of the $Be_xMg_yAl_{2\cdot(x+y)}O_{4\cdot(x+y)}$ series have been reported based on XRD analysis of natural taaffeites: $BeMgAl_4O_8$ [1], $Be_3Mg_5Al_{16}O_{32}$, $BeMg_2Al_6O_{12}$ [2] and $BeMg_3Al_8O_{16}$ [3]. Along the crystallographic c-axis, oriented normal to close-packed planes, these structures comprise different periods of spinel-cubic (*ccp*) and chrysoberyl-hexagonal (*hcp*) sequences. Depending on local stoichiometry deviations these layered structures often lose their regular periodicity, which is readily reflected in uncertainty in determination of site occupancies in tetrahedral sites (Be^{2+} and Mg^{2+}), as well as in octahedral sites (Mg^{2+} and Al^{3+}).

In order to prove our work hypothesis, we decided to grow spinel twins in flux or in the presence of liquid phase (PbF_2) from initial oxides (MgO, Al_2O_3, BeO). While no twins were observed in the binary MgO-Al_2O_3 system, twinning was abundant in the samples with BeO addition. The presence of Be in the initial stage of crystal growth leads to the formation of *hcp* stacking on the surface of octahedral $MgAl_2O_4$ crystals (*ccp*) leading to twin formation. In the first stage, i.e. until beryllium is available for the formation of the *hcp* stacking, such grain grows very fast (exaggeratedly) in the direction of the twin boundary. This leads to the formation of plate-like

composite grains. When the twin-forming dopant is no longer present, the growth in this direction is stopped and the crystal starts to thicken according to the Ostwald ripening law. Electron microscopy analyses have shown that the samples contain simple twins, complex twins and complex modulated taaffeite $Be_xMg_yAl_{2(x+y)}O_{4(x+y)}$ phases, where the *ccp* and *hcp* sequences are interchanging. The taaffeite phases may form separate grains or epitaxial layers with the spinel.

To resolve these inconsistencies, we investigated synthetic taaffeites. Three compositions with different rations of MgO:BeO have been sintered in appropriate amounts with Al_2O_3 [4]. We have shown that taaffeite grows epitaxially on the octahedral faces of the primary spinel crystals in the $[1\bar{1}0]\cdot\{111\}_{sp} \parallel [11\bar{2}0]\cdot\{0001\}_{taf}$ orientation relationship [4]. All observed modulations are in perfect structural coherency with respect to spinel and each other. Intergrowths are accomplished through a common *ccp* O-sublattice interrupted with *hcp* faults extending in all four $\langle 111\rangle_{sp}$ directions. In order to identify individual modulations, occupancy of tetrahedral and octahedral sites was accurately determined using probe-corrected FEG-STEM microscopy. Atomically-resolved HAADF and ABF images showed that *hcp* sequences are directly related to the presence of Be atoms in adjacent tetrahedral sites (black contrast); whereas in *ccp* blocks these sites are occupied by Mg atoms (weak bright dots). Detection of Be has been shown to be quite challenging due to its low atomic number and presence of Al atoms in neighboring octahedral sites. Combination of HAADF-STEM and ABF-STEM imaging with box measurements-EELS confirmed presence of weak Be-K edge. In this way we demonstrated for the first time that Be exclusively occupies the *hcp* tetrahedral sites of the structure.

References:

[1] CC Peng and KJ Wang, Scientia Sinica **12** (1963), 276-278.
[2] B Nuber and K Schmetzer, N. Jb. Miner. Mh**. 9** (1983), 393-402.
[3] R Moor *et al*, Schweiz. Mineral. Petrogr. Mitt. **61** (1981), 13-21.
[4] S Drev *et al*, CrystEngComm **15** (2013), 2640-2647.
[5] The research leading to these results has received funding from the EU 7th Framework Programme under Grant Agreement 312483: ESTEEM2 (I3) and TA to TUG and MPI-IS (WP13).

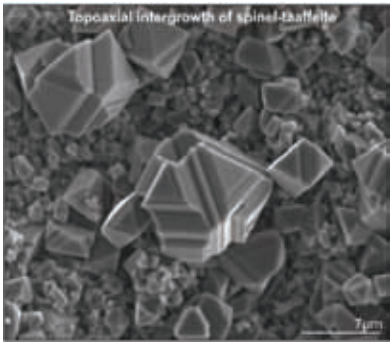

Figure 1. SEM image of topoaxial intergrowth of spinel-taaffeite crystals.

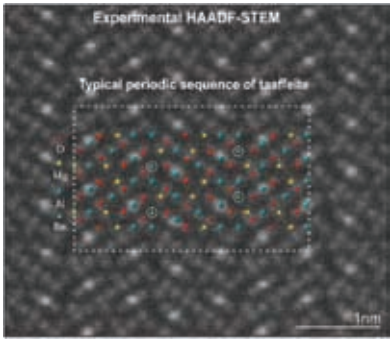

Figure 2. Experimental HAADF-STEM image of typical periodic sequence of taaffeite $BeMg_3Al_8O_{16}$.

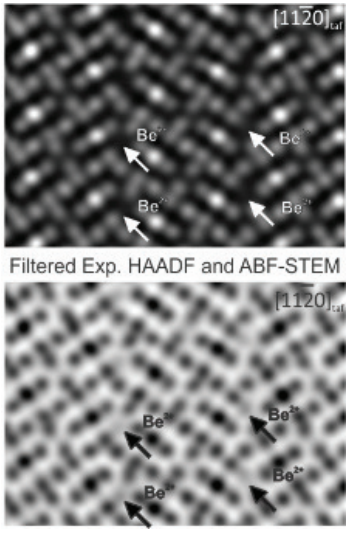

Figure 3. Filtered HAADF-STEM and ABF-STEM images of taaffeite $BeMg_3Al_8O_{16}$.

Temperature Dependent Quasimolten Crystallinity of Sub-nm Pt and Au Clusters Observed in 3D by Fast Dynamic STEM

Trond Henninen, Marta Bon, Daniele Passerone, Rolf Erni

Empa, Swiss Federal Laboratories for Materials Science and Technology, CH-8600 Dübendorf, Switzerland

The formation of solid matter is typically modelled by classical nucleation theory, assuming the solid forms a spherical nucleus. However, during the initial phase at sub-nm scale, non-spherical atomic clusters form, with atomic structures deviating from bulk crystals. Thus understanding the dynamics of this regime requires considering individual atoms. Knowledge of this initial cluster formation enables improved control of nanomaterial fabrication and potentially the creation of new materials.The aim of this work is to study the metastable structures and atomic dynamics of sub-nm clusters, as individual atoms combine to form stable nm-sized clusters.Aberration corrected scanning transmission electron microscopy (STEM) has sufficient resolution to directly image this system. The atomic dynamics and structure of the clusters are affected by the e-beam, as have been studied for clusters of Ge and Si [1,2]. However, to study cluster formation *in-situ*, the effect of the e-beam should be minimized. By using a heating stage, the effect of the e-beam is evaluated, so thermal effects can dominate the system instead.

Samples were made by plasma sputtering Pt or Au onto Protochips Fusion thermal chips, giving homogeneous coverage of single atoms and small clusters up to ~2 nm on an amorphous c-film. The clusters were studied using a probe corrected FEI Titan Themis at 300 kV, optimized for fast dynamic STEM imaging and low radiation dose. Heating experiments were performed using a Protochips Fusion heating holder, from room temperature up to 500°C. STEM image series were recorded at ca 2.5, 15 and 150 fps with doses ranging correspondingly from $5*10^3$ e/Å^{2}s to $2*10^6$ e/Å^{2}s. 3D reconstruction was done by building atomic models assisted by StatSTEM[3] atom counting based on images from multiple orientations, recorded as the clusters rotate.

In our experiments with sub-nm sized clusters of Pt or Au on a carbon surface, we observe the clusters to have an amorphous structure at room temperature. These

clusters are largely flat, 1-2 atoms tall, as if the clusters wet the carbon surface in droplet-like manner. Counterintuitively, the clusters crystallize when heated up; forming close-packed quasi-molten crystals with a more spherical shape, almost as tall as wide. This crystallization is due to the clusters being at elevated temperature, as it is reversible upon cooling the clusters to room temperature. This shows that the amorphous and crystalline phases are equilibrium phases at their respective temperatures, and independent of the temperature history of the clusters.

Our work demonstrates direct observation of multiple different structures, forming from the same specific atomicity clusters. For example, in the range of 11 to 15 atoms, Pt_n clusters form four different structures, as shown in the figure. Notably, the cuboid and cubooctahedral fcc structures are more stable during e-beam irradiation and appear more frequently, compared to the others. The cuboid structures are the most stable up to ca 30 atoms in size. This type of cubic clusters has been simulated by Nie et al. [4] to be the favoured growth pathway for Pt clusters; however, this is in contrast to the majority of theoretical work which agree that spherical closed shell icosahedral-type clusters are the most stable.

References:

[1] S Bals *et al*, Nature Communications **3** (2012), 897.
[2] J Lee *et al*, Nature Communications **4** (2013), 1650.
[3] A De Backer *et al*, Ultramicroscopy **171** (2016), 104.
[4] A Nie *et al*, International Journal of Quantum Chemistry **107** (2007), 219.
[5] We acknowledge funding from the European Research Council (ERC) under EU's Horizon 2020 program (grant agreement No. 681312).

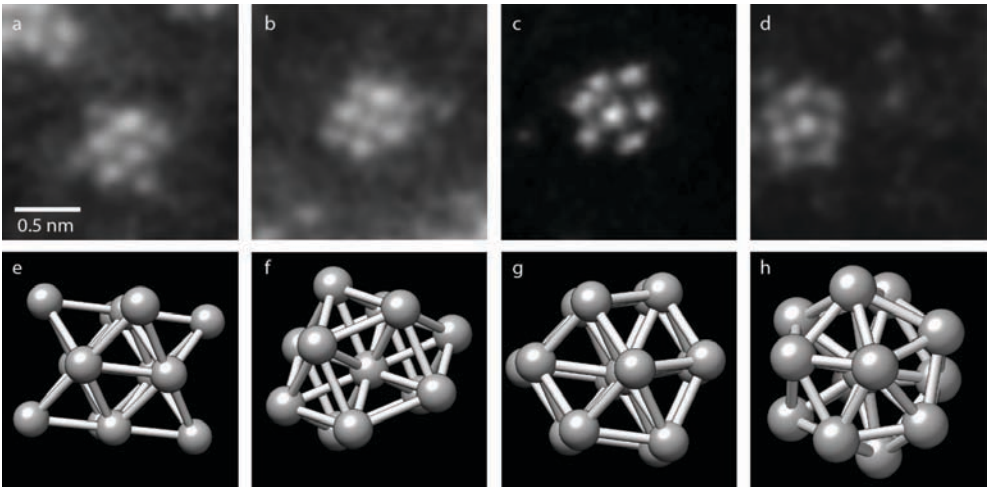

Figure 1. Experimental denoised STEM images (top) and atomic models (bottom) of four different crystalline structures for clusters in the 11-15 atom range, all recorded with similar microscope parameters at 350°C. The fcc cuboid cluster was stable for 18.37s (cumulative dose of $4.6 \cdot 10^6$ e/Å^2). The fcc cubooctahedral cluster was stable for 18.21 s ($5.3 \cdot 10^6$ e/Å^2). Other structures are typically stable for less than a second. a,e: A 13-atom cuboid single fcc unit cell missing one corner atom. b,f: A 13 atom fcc cubooctahedron with one atom displaced. c,g: A 15-atom hcp cluster . d,h: A 13-atom icosahedron core surrounded by 5 atoms.

Efficient First Principles Simulation of Electron Scattering Factors for Transmission Electron Microscopy

Toma Susi[1], Jacob Madsen[2], Ursula Ludacka[1], Jens J. Mortensen[2], Timothy J. Pennycook[1,3], Zhongbo Lee[4], Jani Kotakoski[1], Ute Kaiser[4] and Jannik C. Meyer[1]

[1] *University of Vienna, Faculty of Physics, 1090 Vienna, Austria*
[2] *Technical University of Denmark, Department of Physics, Kgs. Lyngby, Denmark*
[3] *Max Planck Institute for Solid State Research, Center for Electron Microscopy, Stuttgart, Germany*
[4] *Ulm University, Electron Microscopy Group of Materials Sciences, Ulm, Germany*

Electron microscopy is a powerful tool for studying the properties of materials down to their atomic structure. In many cases, the quantitative interpretation of images requires simulations based on atomistic structure models. These typically use the independent atom approximation (IAM) that neglects bonding effects.

With the development of better instrumentation, bonding effects have become measurable, making efficient simulation of the full electrostatic potential of materials ever more important. Such analysis requires a description beyond the IAM, and can provide insights not only into the atomic configuration but also into the electronic structure of a material. The difference between the IAM and a first principles simulation is in many cases large enough to be directly detectable in high-resolution transmission electron microscopy images and electron diffraction intensities.

Since all electrons and the nuclear cores contribute to the scattering potential, simulations that go beyond this approximation have relied on computationally highly demanding all-electron density functional theory (DFT), often Wien2k. We describe a new method to generate *ab initio* electrostatic potentials when describing the core electrons by projector functions within the GPAW code. This allows us to recover the exact (frozen) core electron density. Our approach is a simple and accurate way to calculate the electrostatic potential in the sample and the subsequent electron scattering factors.

We combine this with an interface to quantitative image simulations as implemented in the PyQSTEM package, also written in the Python programming language. We

show how the electrostatic potential derived from projector-augmented wave DFT gives a description of electron scattering equal to orders of magnitude more expensive all-electron methods, and in excellent agreement with experiment on graphene and hexagonal boron nitride. In addition, we show that experimental electron diffraction patterns of graphene and hexagonal boron nitride (hBN) can be simulated with a near-perfect match only when bonding effects are taken into account.

The current implementation [1] further provides a convenient computational workflow starting from a structure model all the way to high-quality images or diffraction patterns in one simple script. Our work further opens the way for the treatment of large systems with defects, such as impurities or grain boundaries [2].

References:

[1] T. Susi *et al*, arXiv (2018) 1803.05338.

[2] T.S. and M.T. acknowledge the Austrian Science Fund (FWF) for funding via project P 28322-N36.

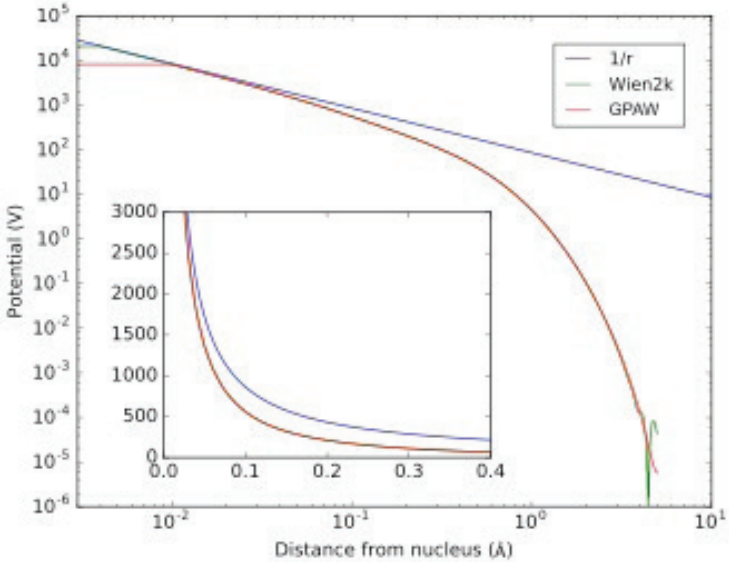

Figure 1. Comparison of GPAW-derived electrostatic potential to Wien2k and to the pure Coulomb potential of the nucleus of a C atom in the center of a 10 Å box.

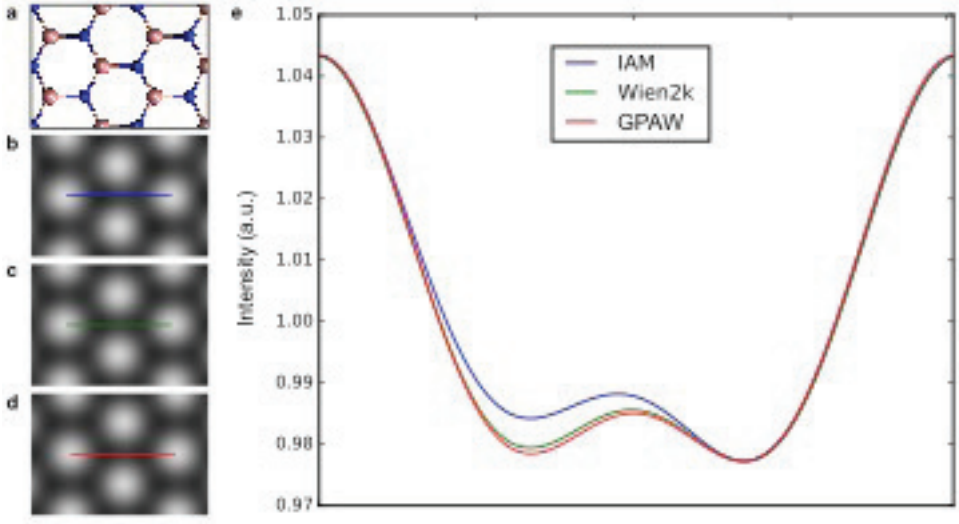

Figure 2. Comparison of different simulation methods for the 80 kV HRTEM image of hBN for a defocus value of -9 nm. a) Cropped view of the hBN stucture model (boron is pink, nitrogen blue). b) Independent atom model (IAM). c) Wien2k. d) GPAW, this work. e) Profiles over the colored lines in b-d, showing that the present GPAW potential results in an even smaller asymmetry over the B and N atoms than previously obtained with Wien2k.

HRTEM and HAADF–STEM Study of Translation States and Cation Ordering on Basal Plane Inversion Boundaries in ZnO with III+, VI+ and V+ Dopants

Vesna Ribić[1], Aleksander Rečnik[2], Goran Dražić[3], Zorica Branković[1], Goran Branković[1] and Nina Daneu[4]

[1] *Institute for Multidisciplinary Research, University of Belgrade, Belgrade, Serbia*
[2] *Department for Nanostructured Materials, Jožef Stefan Institute, Ljubljana, Slovenia*
[3] *Department of Materials Chemistry, National Institute of Chemistry, Ljubljana, Slovenia*
[4] *Advanced Materials Department, Jožef Stefan Institute, Ljubljana, Slovenia*

ZnO is used as a ceramic varistor, a catalyst, and in numerous electronic and chemical applications. In order to enhance its properties for these purposes it is frequently doped with metal oxides. So far, ZnO is known to produce inversion boundaries (IBs) with many metal oxides, such as In_2O_3, Fe_2O_3, Mn_2O_3, Ga_2O_3, SiO_2, SnO_2, TiO_2 and Sb_2O_3, causing polarity inversion across the interface. Owing to local charge compensation mechanism, following Pauling's rule of electroneutrality, dopants show different ordering in the IB–plane depending on their oxidation state [1].

We investigated the translation states and cation ordering in basal plane IBs in ZnO ceramics using high-resolution electron microscopy methods HRTEM and HAADF–STEM. Stacking configuration is best studied in [100] projection. Analyzing possible translations we identified three possible modes of translation that produce basal plane head–to-head (→|←) IBs in ZnO: (i) IB with βγβγ|α|βαβα stacking of cation sublattice, as observed with Sb–doping [1], (ii) IB with αγαγ|α|βαβα, as observed with In–, Fe– and Sn–doping [2] and (iii) IB with βαβα|γ|βαβα as observed with Mn-doping [3].

All these translations produce and octahedral IB–layer comprising dopant cations in the exact ratios that satisfy Pauling's principle of electroneutrality. Such distribution of cations has been confirmed by concentric electron probe method for three types

of dopants [4] showing that In^{3+} atoms occupy 1.095±0.053 of a monolayer, Sn^{4+} atoms 0.504±0.038 of a monolayer, whereas Sb^{5+} atoms occupy 0.326±0.040 of the IB layer, indicating that III+ dopants conform full monolayer, VI+ dopant ½, and V+ dopants ⅓ of the IB layer. Structurally, distribution of cations can be studied in [120] projection. Employing HRTEM and HAADF–STEM methods we confirmed an uniform occupancy of the IB layer in the case of In–doping, and honeycomb ordering of Zn^{2+} and Sn^{5+} in the case of Sn–doping, whereas the cation distribution appears disordered in the case of Sn–doping.

To further study the in–plane distribution of cations with different oxidations states samples will be prepared by atomic–layer deposition (ALD) and their stable configurations will be theoretically investigated by ab–initio calculations within the frame of density functional theory (DFT).

References:

[1] A Rečnik *et al*, J. Am. Ceram. Soc. **84** (2001), 2657–68.
[2] A Goldstein *et al*, ACS Nano **7** (2013), 10747–10751.
[3] J Hoemke *et al*, J. Am. Ceram. Soc. **100** (2017), 4252–62.
[4] A Rečnik *et al*, J. Mater. Sci. **47** (2012), 1655–68.

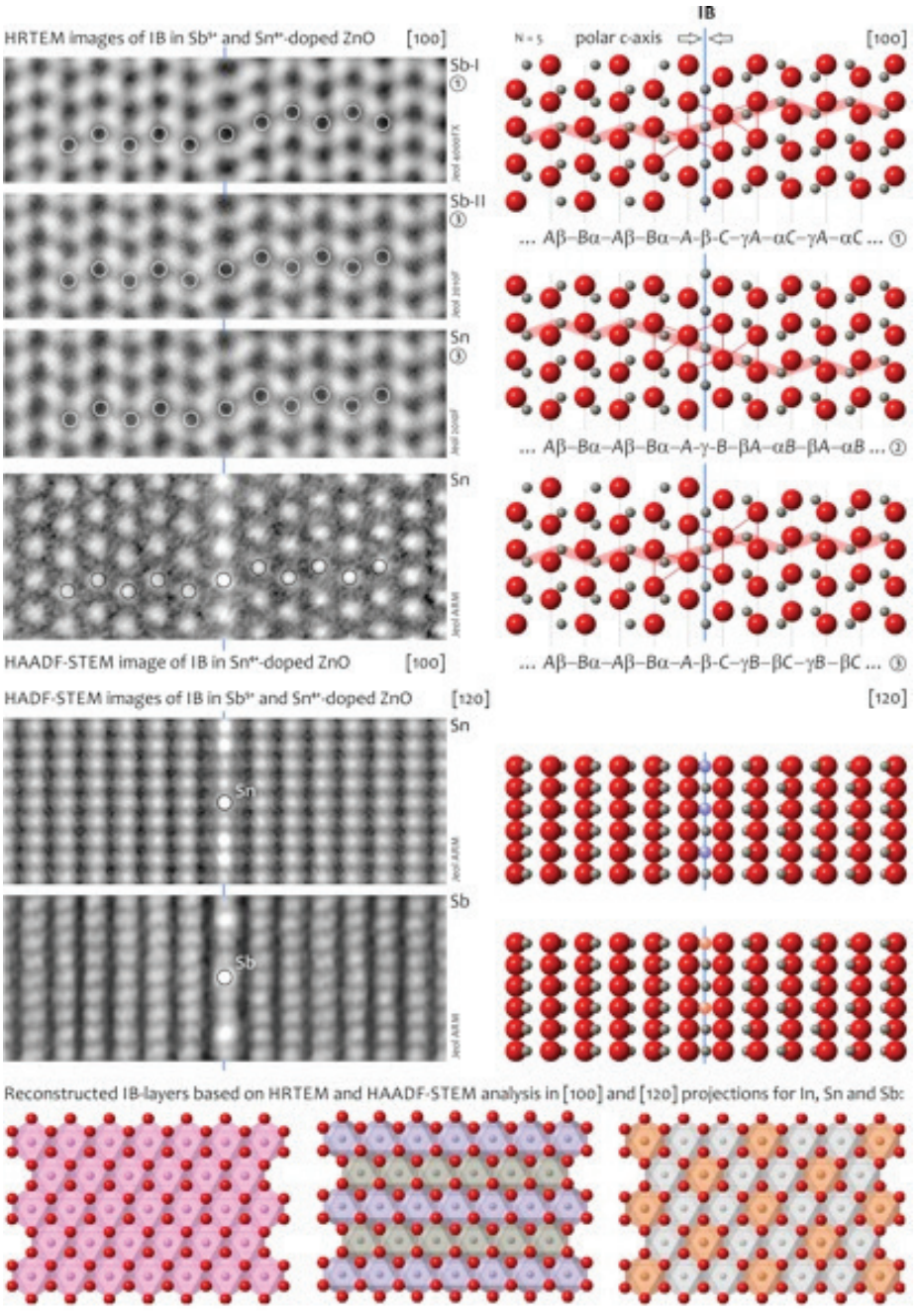

Figure 1. Structural analysis of IBs in ZnO doped with In^{3+}, Sn^{4+}, and Sb^{5+}. Note that average oxidation state per IB octahedral site is III+ controlling local in–plane ordering.

Study of Ge and SiGe Nanoparticles Formed by RTA and Laser Pulse Annealing of SiGeO Amorphous Films Obtained by RF Sputtering

Valentin S. Teodorescu[1], Adrian V. Maraloiu[1], Corneliu Ghica[1], Andrei Kuncser[1], Ionel Stavarache[1], Ana-Maria Lepadatu[1], Magdalena L. Ciurea[1], Nicu D. Scarisoreanu[2], Andreea Andrei[2] and Maria Dinescu[2]

[1] *National Institute for Materials Physics, Bucharest-Magurele, Romania*
[2] *National Institute for Lasers, Plasma and Radiation, Bucharest-Magurele, Romania*

Ge and SiGe nanoparticles (NPs) embedded in different dielectric matrices are interesting for applications in optoelectronics and memory devices. [1]. The NPs formed by annealing of amorphous GeSiO thin films are of particular interest due to some special features of the formation mechanism. This study was performed on amorphous RF films co-deposited on Si wafer substrates, using Si, Ge and SiO_2 as a targets, or Ge and SiO_2 targets. Structural investigations were performed by cross-sectional transmission electron microscopy (XTEM) using a Jeol ARM 200F microscope.

Ge or SiGe nanoparticles were obtained by rapid thermal annealing (RTA) of SiGeO amorphous films, via a nucleation and crystal growth process. A much faster annealing was performed on similar films by laser pulse annealing using 266 nm radiation of Nd-YAG laser with a pulse duration of 7 ns and different laser fluences. Since the nanosecond scale of the laser pulse annealing is the time scale of the duration of NPs nucleation it is useful for revealing of the features of the NPs formation mechanism.

At the same time, Ge diffusion in the SiO_2 amorphous matrix leads to different morphologies depending on the initial film compositions. Interesting feature of the Ge containing film is the loss of the Ge due to the gas state diffusion of the GeO molecules [2]. This leads to different morphology and composition of the film sections after annealing.

Figure 1 shows XTEM images of the SiGe-SiO_2 amorphous film annealed by RTA at 700°C, 800°C and 1000°C for 8 minute. Nanoparticles of different size and

morphology are obtained depending on the RTA temperature. In the top part of the film the NPs are not present. The EDX measurements taken from this part of the film show a lower content of Ge in the SiO_2 matrix. In the case of RTA annealing at 1000°C some nanovoids are observed, formed by aggregations of vacancies and probably filled by molecular GeO gas, produced at a higher rate than the diffusion can evacuate them through the film surface. Void formation does not take place at lower temperature annealing.

On the other hand, Figure 2 shows the results of laser pulse annealing. A single laser pulse with the fluence of 100 mJ/cm^2 was used. Ge or SiGe NPs were formed in the heated top part of the films, corresponding to the laser radiation absorption length. However, voids are formed only in the case of SiGe-SiO_2 films and not for the Ge-SiO_2 films. In the case of SiGe-SiO2 film, the amorphous SiGeO matrix composition is different compared to the case of Ge-SiO2 film, and the mechanism of SiGe NPs formation is different compared to the Ge NPs formation.

The laser pulse annealing reveals also the very fast diffusion of Ge in the hot solid SiO_2 matrix. Under laser pulse irradiation, the Ge diffusivity is estimated to be similar to the liquid state [3]. A high Ge diffusivity was also evidenced in the case of normal thermal annealing of Ge implanted SiO_2 films [4].

Refereences:

[1] I Stavarache *et al*, Applied Surface Science **309** (2014), 168.
[2] V Bayer and J von Borany, Physical Review B **77** (2008), 014107.
[2] VS Teodorescu *et al*, Beilstein Journal of Nanotechnology **6** (2015), 893.
[4] L Chen *et al*, Nanotechnology **28** (2017), 035707.

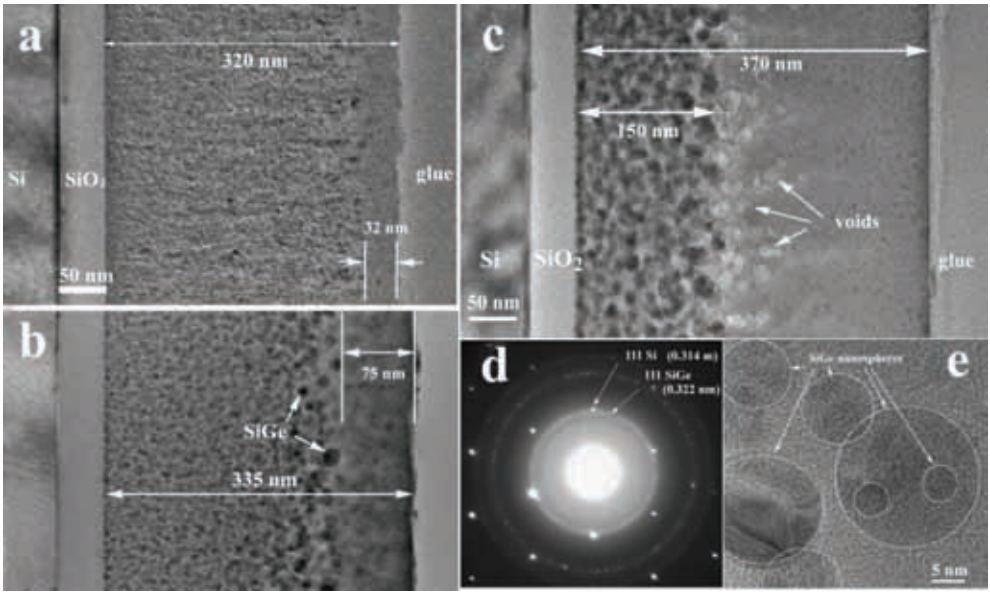

Figure 1. SiGe-SiO_2 films after different RTA annealing temperatures: **a-** film annealed at 700°C; **b-** film annealed at 800°C; **c-** film annealed at 1000°C, **d-** SAED pattern of the film area imaged in **c**; **e-** detail of spherical crystalline SiGe NPs formed after annealing at 1000°C.

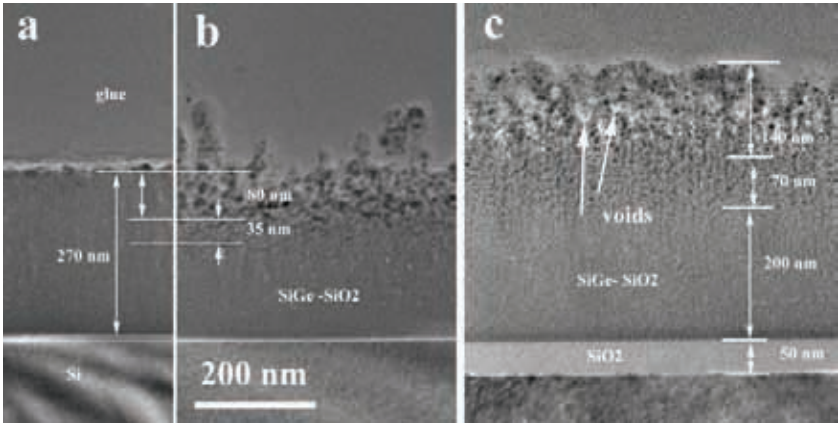

Figure 2. Ge and SiGe nanocrystallites formed after 7 ns laser pulse annealing with 266 nm radiation. **a** – XTEM image of the Ge-SiO_2 as deposited film, **b** – Ge NPs formed by laser annealing of Ge-SiO_2 film after laser pulse irradiation with the fluence of 100 mJ/cm^2. ; **c** – GeSi nanoparticles formed in GeSi-SiO_2 amorphous film after the laser pulse annealing to the same fluence as in **b**. Nanovoids are observed in the top part of the laser annealed film. The film temperature estimation during the laser pulse irradiation is about 700°C, less than the Ge melting point.

Study of Structural Defects in $Ga_{2-x}Fe_xO_3$ Thin Layers

Corinne Bouillet[1], Xavier Devaux[2], Anna Demchenko[1], Christophe Lefevre[1], François Roulland[1], Nathalie Viart[1]

[1] *Institut de Physique et Chimie des Matériaux de Strasbourg (IPCMS), UMR 7504 CNRS, Université de Strasbourg, 23 rue du Læss BP 43, 67034 Strasbourg, France*

[2] *Institut Jean Lamour, UMR 7198 CNRS - Université de Lorraine, Campus ARTEM 2, allée André Guinier, BP 50840 F54011 NANCY Cedex, France*

The aim of the study is to unveil the polarization switching mechanisms in multiferroic $Ga_{2-x}Fe_xO_3$ ($1 \leq x \leq 1.4$), (GFO) thin films. GFO crystallizes in the noncentrosymmetric orthorhombic space group $Pc2_1n$ [1], its polarization has been determined by calculation [2] and the polarization vector is along the [010] direction of the GFO cell and points from the Ga_2 octahedral site towards the Ga_1 tetrahedral site as shown in Figure 1.

GFO thin films have been deposited by pulsed laser deposition and radio frequency sputtering on yttrium stabilized zirconia (YSZ) substrates. The structural studies performed by resonant X rays scattering and transmission electron microscopy allowed to determine the electric polarization state of the layers. It has been shown that the two different growth methods lead to different polarization states. In the case of GFO thin layer elaborated by PLD, the polarization direction points towards the surface, whereas it points towards the substrate when the GFO layer is elaborated by radio frequency sputtering [3].

In order to study specifically the polarization reversal mechanisms, a GFO layer was first grown by radio frequency sputtering on a YSZ substrate, then covered by a GFO layer grown by PLD (Figure 2). The polarization domains boundaries of the bilayer have been observed by high angle annular dark field scanning transmission electron microscopy (HAADFSTEM) coupled with electron energy loss spectroscopy map at the atomic scale in order to study their structural and chemical nature. Observations were performed on a JEOL ARM 200F Cold FEG microscope, operating at 80kV, equipped with a spherical aberration corrector on the condenser lens, allowing to

have a probe size of 0.15 nm. The EELS mapping were acquired thanks to a Gatan GIF Quantum ER. As observed in the case of the GFO elaborated by sputtering, the growth starts with few Fe atomic layers followed by the expected composition of GFO. In the PLD part of the sample, different configurations of polarization have been observed, head to head or head to tail. Figure 3 presents a typical 2D defect at the interface between head to head polarization domains. Such polarization domains boundary is associated to cations stacking fault whereas, in the case of head to tail domains boundaries, only a shift in the unit cell was observed from one domain to the other, similar to antiphase boundaries.

As a perspective to this study and in order to propose a polarization reversal mechanism, it will be helpful to investigate at the atomic scale, the structural change of the GFO layer next to the domain boundaries by in-situ biasing TEM.

References:

[1] SC Abrahams, JM Reddy and JL Bernstein, J. Chem Phys. **42** (1965), 3957.
[2] D Stoeffler, J. Phys. Condens. Matter **24** (2012), 185502
[3] C. Lefevre *et al*, Small Methods **1** (2017), 1700234.

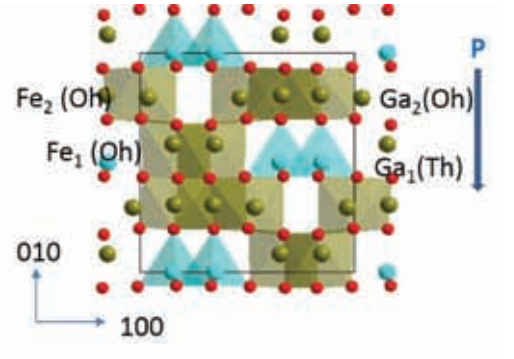

Figure 1. Crystal structure of GFO. The polarization orientation is given by the blue arrow.

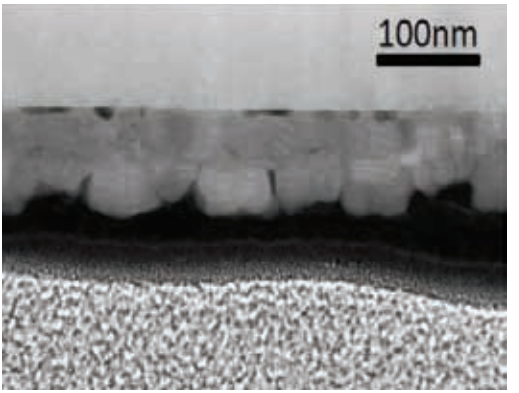

Figure 2. Global view of the GFO layer grown in a two steps method (sputtering followed by PLD).

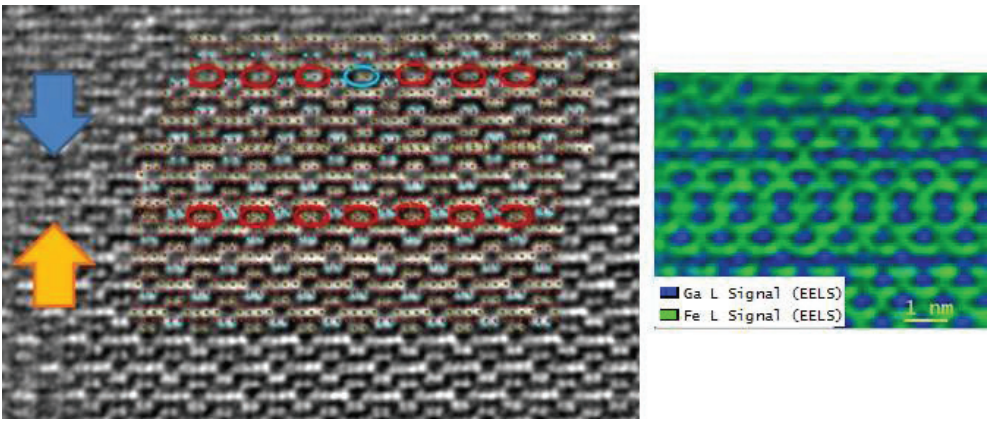

Figure 3. Typical defect at the interface between two head to head polarization domains and its EELS map.

Analysis of Coatings With Scented Microcapsules

Rastko Milošević[1], Nemanja Kašiković[1], Živko Pavlović[1], Urška Stanković Elesini[2], Tomislav Cigula[3] and Raša Urbas[2]

[1] *University of Novi Sad, Faculty of Technical Sciences, Department of Graphic Engineering and Design, Novi Sad, Serbia.*
[2] *University of Ljubljana, Faculty of Natural Sciences and Engineering, Department of Textiles, Graphic Arts and Design, Ljubljana, Slovenia.*
[3] *University of Zagreb, Faculty of Graphic Arts, Department of Printing Plates, Zagreb, Croatia.*

In the graphic and the printing industry, different coatings are used for enhancing the visual and protective properties of the prints, while the application of various types of microcapsules enables the production of so called functional coatings [1,2]. At present, microcapsules are used in different industries, such as in medicine, pharmacy, agriculture, biotechnology, electronics, chemistry, construction, food, printing and textile industry [2,3]. Microcapsules can be deposited on various substrates, using various transfer techniques, but prior to the application, they need to be mixed with the appropriate printing ink or varnish [3]. They are mainly transferred by coating or by different printing techniques (e.g. most often screen or flexo printing), which enable microcapsules' deposition on the specific areas of the substrate [4]. This research aims to determine basic characteristics of the functional coatings with scents, produced by a manual coating technique using water-based varnish in which fragranced microcapsules in water suspension were added, as well as to investigate how different concentrations of the microcapsules in the coating layers affect the physical and the surface characteristics of the coated samples. Conducted scanning electron microscopy (SEM) and atomic force microscopy (AFM) analyses of the produced functional coatings revealed that the application of the microcapsules, especially their higher concentrations in the varnish, significantly affected physical and surface characteristics of the coatings.

For the coating process, a commercially available transparent foil was used as a substrate, on which was deposited a mixture of the water-based varnish (Cinkarna Celje, Slovenia) and the water suspension of fragranced microcapsules with

essential oils of sage, rosemary and lavender in their core. The water suspension of microcapsules was premixed with the varnish prior the coating process. The mixture of the varnish and the fragranced microcapsules was applied using a manual coating technique (BYK 4-sided applicator, Germany) in three different microcapsules' mass concentrations in the varnish (0% – CV_0% sample, 1% – CV_1% sample and 15% – CV_15% sample) and a 200 μm deposition thickness setup of the coater. After the coating process, samples were dried for 24 hours (at 25°C and 55% rel. humidity) before analyses. An image analysis, using scanning electron microscopy (SEM; JSM 6060 LV, Jeol, Japan) of the fragranced microcapsules (Figure 1a) and the coated samples (Figures 1b–d) was performed for obtaining the morphology and the determination of the microcapsules' size/volume distribution, using an image analysis software (ImageJ, USA). The surface characteristics of the samples (Figure 2) were determined by the atomic force microscopy (AFM, VeeCO di CP II, Digital Instruments, USA), and software for scanning probe microscopy (SPIP, Denmark). Standard roughness parameters, root-mean-square height roughness (S_q), skewness (S_{sk}), and kurtosis (S_{ku}) were used for the characterization of surface roughness properties of the coated samples (Table 1). Besides adding value to the final printed product, deposited microcapsules also change the basic properties of the coated samples to a certain level. The higher concentrations of the fragranced microcapsules in the varnish produced thicker and heavier prints. It led to the generation of more irregularities on the surface of the samples (Figure 1c and d), that significantly increased the samples' surface roughness (S_q) (Figure 2b and c). The coatings made with just the varnish, had relatively flat and uniform surface structure (Figure 2a), while on the other hand, the coatings with the fragranced microcapsules in the mass concentration of 1% in the varnish (CV_1% sample), produced surfaces with rougher surface structure. Increase of the microcapsules concentration in the varnish (up to 15%; e.g. CV_15% sample), caused an even higher increase of the S_q surface roughness parameter value, but skewness S_{sk} and kurtosis S_{ku} parameters decreased, as a result of the generation of new valleys (along with the appearance of new peaks) which balanced the surface structure of the coated samples (Table 1). From the presented analyses it can be concluded that the coating process with varnishes and different fragranced microcapsules' concentrations, changed original, flat coated surfaces into rougher surfaces with more irregularities [5].

References:

[1] H Kipphan in "Handbook of Print Media", ed. H Kipphan, (Springer-Verlag, New York) p.142.

[2] SK Gosh in "Functional coatings by Polymer Microencapsulation", ed. SK Gosh, (Wiley-VCH, Weinheim) pp. 3, 153, 177, 235.

[3] R Urbas *et al*, Iranian Polymer Journal **26** (2017), 541.
[4] M Starešinič, B Šumiga and B Boh, Tekstilec **54** (2011), 80.
[5] The authors acknowledge funding from the Serbian Ministry of Science and Technological Development, Grant No. 35027, and support by Cinkarna Celje, Slovenia, that provided materials.

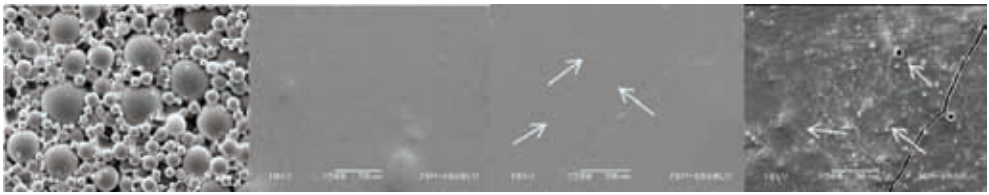

a) b) c) d)

Figure 1. The appearance of (a) fragranced microcapsules in water suspension and surfaces of the coated samples: (b) CV_0%, (c) CV_1%, (d) CV_15%, with white arrows pointing at microcapsules (SEM; 1000× and 500× magnification).

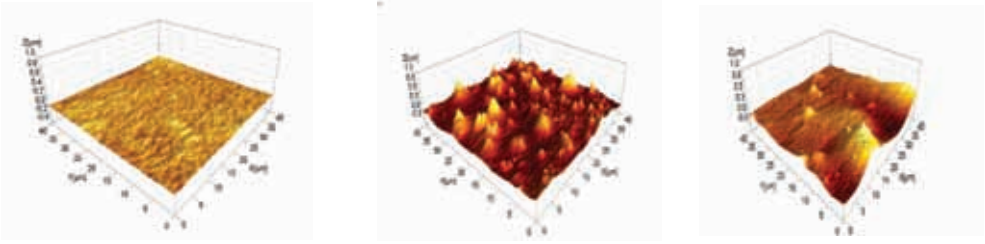

a) b) c)

Figure 2. 3D renderings of the AFM data: (a) CV_0%, (b) CV_1%, (c) CV_15% (AFM; 40×40 μm).

	CV_0%	**CV_1%**	**CV_15%**
S_q [nm]	43.18	61.94	92.71
S_{sk}	0.36	1.98	1.32
S_{ku}	8.02	15.49	6.16

Table 1. Measured surface roughness parameters of coated samples with varnish and different microcapsules' concentrations.

Potentials, Implementation and Perspectives of Atomic Force Microscopy for Characterization of Drug Delivery Nanosystems

Ines Nikolic[1], Danijela Randjelovic[2], Snezana Savic[1]

[1] *University of Belgrade, Faculty of Pharmacy, Department of Pharmaceutical Technology and Cosmetology, Belgrade, Serbia*
[2] *University of Belgrade, Institute of Chemistry, Technology and Metallurgy, Department of Microelectronic Technologies, Belgrade, Serbia*

Research and development of biocompatible nanosystems represent contemporaneous approach in drug carrier design, aiming to take advantage of their unique physicochemical and biological properties. Progress in this field has brought various types of delivery systems, with highly set expectations [1]. Bearing this in mind, there is a strong need for wide-spectrum characterization techniques, enabling us to take a deeper insight into the real structure of the systems being investigated. Atomic force microscopy (AFM), a characterization method with many potentials, but not fully exploited, which has just recently been introduced into the field of investigation of the nanosized drug delivery systems, is the only technique that can provide three-dimensional display and topography. Sample preparation for AFM analysis does not require particular procedures (although some adjustments and variations are needed). Moreover, it is a non-destructive technique, which is extremely important because of the fragile nature of the samples. Therefore, AFM is completely suitable for obtaining relevant scientific results in this field [2].

The aim of our study was to perform AFM analysis of several types of novel drug nanocarriers differing in their properties and applicability (high-energy nanoemulsions, low-energy nanoemulsions, and microemulsions (MEs) as nanostructured colloids), which are liquid/soft samples by their nature, in order to visualize their inner structure, and to compare and totalize results obtained through some other techniques.

AFM analysis was carried out applying AutoProbe CP-Research SPM (TM Microscopes-Bruker), using 90 μm large area scanner. Only 10 μL of the sample was placed on circular mica substrate (Highest Grade V1 AFM Mica Discs, Ted

Pella Inc., Redding, California, USA) and dried in vacuum. Due to the nature of the samples, noncontact mode was applied.

Implementation of AFM enabled us to directly observe the inner structures of developed systems and to get the impression of the morphology of dispersed droplets, pointing out the differences that originate from the preparation technique and fundamental principles of formation of these nanosystems (Figures 1 and 3). On the one hand, we confirmed results on average droplet size obtained through laser diffraction and dynamic light scattering technique in all sample types, but on the other hand, broader size distribution and some aggregates formed in the inner phase of low-energy nanoemulsions, which remained undiscovered by these two commonly used sizing techniques, were revealed (Figure 2). In addition, providing a direct insight into the oil-surfactant-water contact, AFM gave an evidence line for the proposed theory that explains the mechanism of nanoemulsification of low-energy nanoemulsion (Figure 3).

Even though for comprehensive characterization of drug delivery nanosystems a variety of experimental approaches and complementary characterization techniques are needed, AFM proved to be highly multifunctional, gathering pieces of information that are hardly accessible, throwing more light to the intrinsic structure of the investigated samples. How far can we go? The possibilities even for *in vivo*/*ex vivo* experiments should be underlined as special advantages, broadening the perspectives of this method in nanomedicine. Direct drug carrier – cell interactions investigation is imposed.

References:

[1] V Jankovic in "Instrumentalne metode – ključ za razumevaje nanotehnologije i nanomedicine", ed. B Nikolić, (Engineer Academy of Serbia and Institute for Nuclear Sciences *Vinca*, Novi Sad) p. 792

[2] J Sitterberg *et al*, European Journal of Pharmaceutics and Biopharmaceutics 74 (2010), 2.

[3] The authors acknowledge the Ministry of Education, Science and Technological Development of the Republic of Serbia for supporting this research through the projects TR34031 "Development of micro- and nanosystems as carriers for drugs with anti-inflammatory effect and methods for their characterization" and TR 32008 "Micro-, Nanosystems and Sensors for Applications in Power Industry, Process Industry and Environmental Protection".

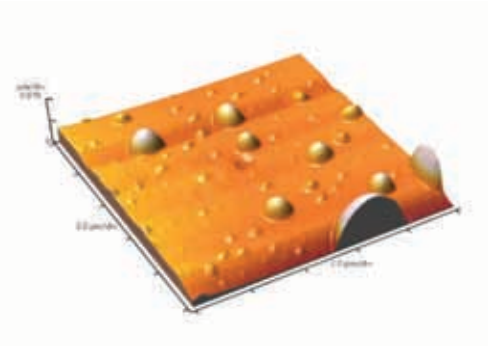

Figure 1. Ideally spherical nanodroplets in a microemulsion

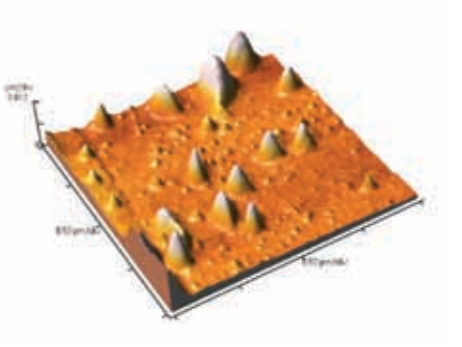

Figure 2. Broader size distribution in a low-energy nanoemulsion revealed by AFM

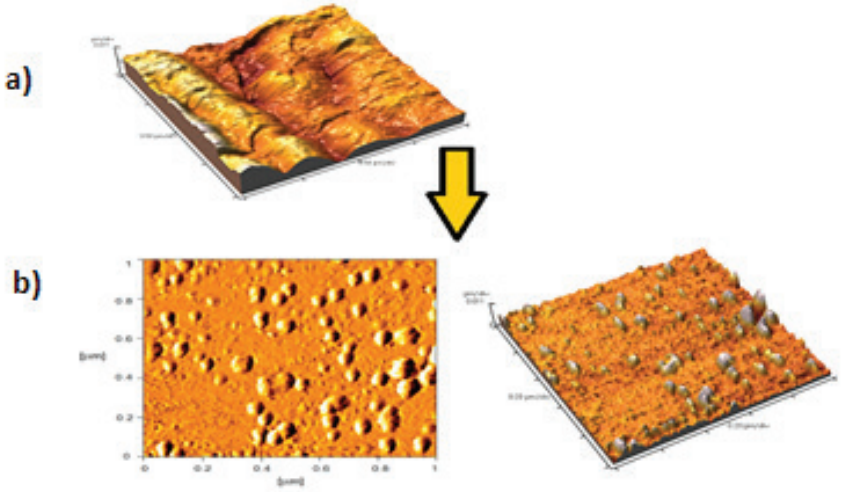

Figure 3. Phase transition/exploding from myelinic liquid-crystalline structures (a) to the nanodroplets (b) during low-energy nanoemulsification process

Epitaxial Growth of Metastable (P–type) Al–Mn–Si Quasicrystal from the Stable (F–type) Al–Cu–Fe Quasicrystalline Surface

Blaž Leskovar[1], Sašo Šturm[2], Zoran Samardžija[2], Bojan Ambrožič[2], Boštjan Markoli[1], Iztok Naglič[1]

[1] *University of Ljubljana, Faculty of Natural Sciences and Engineering, Department of Materials and Metallurgy, Aškerčeva cesta 12, 1000 Ljubljana, Slovenia*

[2] *Jožef Stefan Institute, Department for Nanostructured Materials, Jamova cesta 39, 1000 Ljubljana, Slovenia*

Metastable quasicrystals (Qcs) were first discovered in Al–Mn alloys in 1984 by Shechtman, who received the Nobel Prize in Chemistry 2011 for this discovery [1]. Soon after the discovery of metastable Qcs, stable forms were identified too [2]. According to their diffraction patterns, which displays intense, distinct spots, Qcs are classified as icosahedral (i-), octagonal (o-), decagonal (d-) or dodecagonal (dd-) phases. The atomic positions are ordered, but with rotational symmetries, *e.g.* five- (i-), eight- (o-), ten- (d-) or twelvefold (dd-), which are not found in standard crystals. These symmetries forbid a periodic structure and, instead, enforce quasi-periodicity [3, 4]. IQcs are the only ones that are quasiperiodic in all three spatial directions. Their structure consists of 6 intersecting fivefold axes, 10 threefold axes and 15 twofold axes. Theoretically, three types of iQcs exist and are described by P– (primitive), F– (face–centred), and I– (body–centred), but only F– and P– type icosahedral structures have been grown experimentally [1, 5].

Structures of stable Al65Cu20Fe15 (iQc–AlCuFe) phase (F–type) and metastable Al73Mn21Si6 (iQc–AlMnSi) phase (P–type) are very similar[5-7]. Along with that, their quasilattice constants are also very close to each other with 0.445 nm for stable iQc–AlCuFe phase and 0.460 nm for metastable iQc–AlMnSi phase [7]. The difference between quasilattice constants is only 3.4 %. Therefore, the aim of this investigation was to evaluate the possibility that a stable iQc–AlCuFe phase could serve as a substrate for the nucleation of the metastable iQc–AlMnSi phase in a rapidly solidified Al–Mn–Si alloy. This might enable us in the future to control

the size and distribution of in-situ formed iQc phases in alloy systems similarly as in conventional alloys which contain crystalline phases. Such attempts were not yet found in the literature.

Synthesized aluminium alloys, that form metastable and stable iQc phase while casting into a copper mould, were prepared in the electric-furnace. Castings were characterized by light optical microscopy (LOM), scanning electron microscopy (SEM) and energy dispersive x-ray spectroscopy (EDS) for micro- and macro-chemical analysis. Electron backscattered diffraction (EBSD) and transmission electron microscopy (TEM) were used to determine the structure of the phases present in the microstructure. Details regarding samples preparation and characterization are published elsewhere [8].

In order to evaluate a nucleation effect of metastable iQc–AlMnSi phase on the surface of stable iQc–AlCuFe phase, a small particle of stable iQc–AlCuFe phase with a diameter between 2 and 3 mm was placed on the bottom of the mould cavity. The Al–Mn–Si alloy melt was then cast into the mould. On the clean particle surfaces the formation of a thin layer of different phase was observed, see Fig. 1a. EBSD patterns acquired from the iQc–AlCuFe particle and thin layer confirm the presence of 5-fold (white pentagon), 3-fold (white triangle) and 2-fold (white ellipse) axes that are characteristic for icosahedral symmetry group. The axes are arranged in such a way that the 5-fold axis is surrounded by five 3-fold axes and five 2-fold axes [9]. The SAED patterns of particle and thin layer indicate that the particle represents the stable iQc–AlCuFe phase and thin layer the metastable iQc–AlMnSi phase. It was also found that fivefold symmetry axes and (110000) planes are parallel in both phases.

These results confirm that stable iQc–AlCuFe phase can serve as an effective substrate for the nucleation of metastable iQc–AlMnSi phase.

References:

[1] D Shechtman *et al*, Physical Review Letters **53** (1984), 1951-1953.
[2] A-P Tsai, A Inoue and T Masumoto, Japanese Journal of Applied Physics **26** (1987), L1505.
[3] W Steurer, Zeitschrift für Kristallographie-Crystalline Materials **219** (2004), 391-446.
[4] W Steurer, Chemical Society Reviews **41** (2012), 6719-6729.
[5] A-P Tsai, Science and technology of advanced materials **9** (2008), 013008.
[6] A-P Tsai, Chemical Society Reviews **42** (2013), 5352-5365.
[7] R W Cahn and P Haasen in "Physical metallurgy" Vol. 1 (North Holland, Amsterdam).
[8] B Leskovar *et al*, Scripta Materialia **150** (2018), 92-95.
[9] D Naumović *et al*, Physical review letters **87** (2001), 195506.

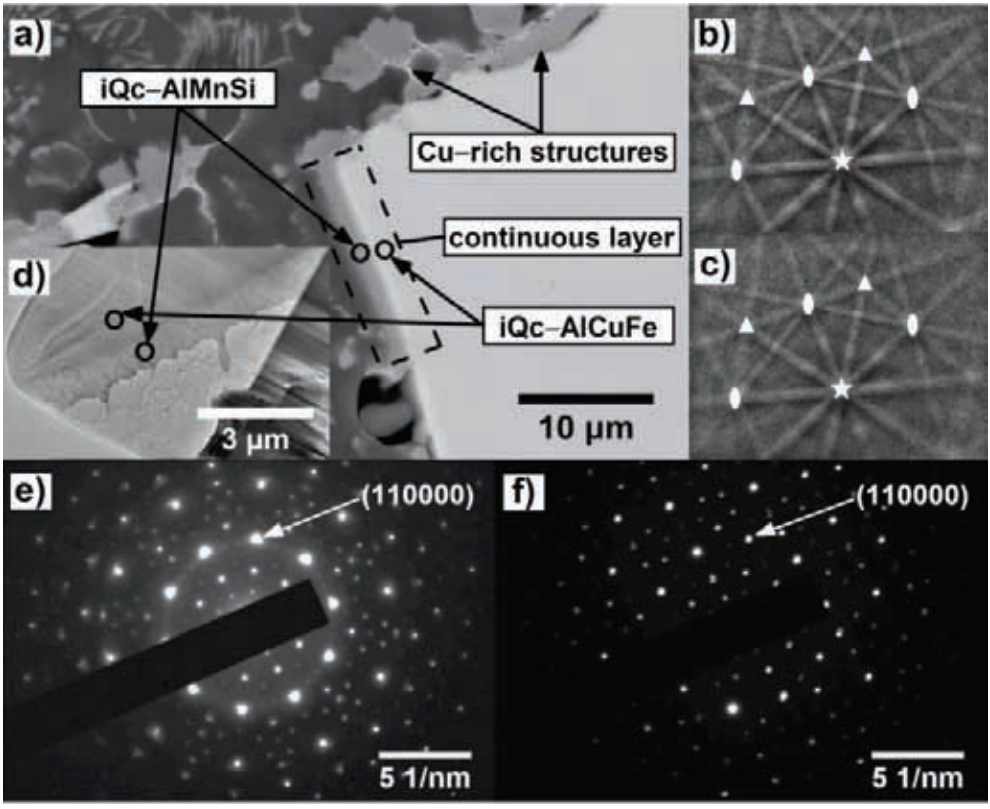

Figure 1. a) BE image of the Al–Mn–Si alloy with the embedded iQc–AlCuFe particles. The left faceted surface of iQc particle is covered with a continuous layer of iQc–AlMnSi phase (area denoted by the dashed box). Black arrows going over the uneven curvaceous top right surface of iQc–AlCuFe indicate that dissolution of particle started and that Cu-rich structures were formed. b) EBSD pattern of stable iQc–AlCuFe and c) a layer of metastable iQc–AlMnSi phase, with marked the 5-fold (white five-pointed star), 3-fold (white triangle) and 2-fold (white ellipse) axes. d) Bright field image of TEM sample containing iQc phases and α–Al matrix. e) Selected area electron diffraction (SAED) patterns of the stable iQc–AlCuFe phase and f) the metastable iQc–AlMnSi phase. Circles in Fig. 1a denote the iQc phases, whereas the circles in Fig. 1d denote the location where SAED patterns were taken.

Morphology and Structure of TiO_2 Thin Films and Nanostructures Deposited on ZnO Nanorods for Photovoltaic Application

Andreja Gajović[1], Ivana Panžić[1], Krunoslav Juraić[1], Nikša Krstulović[2], Domagoj Belić[1], Milivoj Plodinec[1,3], Davor Gracin[1], Ana Šantić[1], Marc Gregor Willinger[3]

[1] *Ruđer Bošković Institute, Bijenička 54, 10000 Zagreb, Croatia*
[2] *Instutute of Physics, Zagreb, Croatia*
[3] *Fritz Haber Institute of Max Planck Society, Berlin, Germany*

Nanostructured titanium dioxide is known as a material with excellent physical and chemical properties, such as high specific surface area, high photo-activity and environmental stability as well as low cost synthesis. TiO_2 exists in three different crystalline phases: anatase, rutile and brookite, but it was found that anatase (Eg ~ 3.2 eV) is more photo-active than other modifications. It is widely used for photovoltaic applications, primarily as electron transporting layer in perovskite and dye sensitized solar cells due to suitable band gap for acceptance of electrons from active layer of solar cells. However, by combination of high reactivity of TiO_2 together with the large binding energy of ZnO, the process of electron transfer between the corresponding conduction and valence bands can be facilitated in the composite system.

With the aim to prepare high performance TiO2@ZnO core–shell nanostructure for photovoltaic application, in this work TiO_2 was deposited on ZnO nanorods by pulsed laser deposition (PLD) and magnetron sputtering (MS). We studied influence of the preparation parameters to crystal structure and morphology of nanocomposite and correlate them with the optical and electrical properties.

ZnO nanorods (ZNR) arrays were prepared by sol-gel procedure followed by annealing of nanorods to obtain crystallinity. TiO_2 thin films were prepared on ZNR using PLD in Ar or vacuum and by reactive MS with the aim to select the preference deposition procedure. The structural phase of TiO_2 were preliminary studied by confocal micro-Raman spectroscopy (mRS), while morphology and crystal structure on nanoscale were studied by high resolution electron microscopy; JEOL-ARM300 microscope in HAADF-DF mode and FEG-SEM JEOL JSM-700F.

The optical properties are evaluated by UV-vis spectroscopy, while for electrical characterization impedance spectroscopy was applied.

Raman spectroscopy results indicated that TiO_2 thin films prepared by MS and PLD were amorphous after deposition (Fig. 1). The SEM images show that heating of the samples after deposition did not influence the morphology of TiO_2. The annealing temperature for crystallization were optimised to obtain anatase structure, since mRS study showed the formation of rutile already at temperature between 450 and 500 °C (Fig. 1). It was shown that morphology of the TiO_2 layers obtained by PLD considerably depend on preparation atmosphere and the number of pulses (Fig. 2). In the case of preparation by MS the attention should be focused on reactive magnetron atmosphere as well as on the pre-treatment of the ZNR substrate, while it was shown that morphology of the MS deposited TiO_2 depend on deposition duration (Fig. 3). The obtained phase composition and morphology of the TiO_2 will be discussed in the frame of the preparation parameters, while optical and electrical properties of prepared TiO_2@ZnO core–shell nanostructure will be discussed in the view of structure and morphology of the obtained TiO_2 layers.

References:

[1] This work has been supported by Croatian Science Foundation under the project IP-2014-09-9419 and by Croatian-Germany DAAD bilateral project.

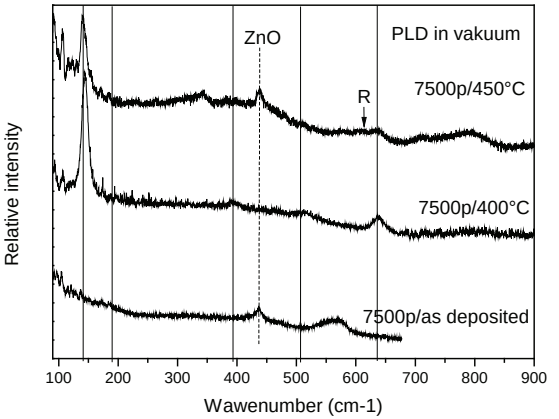

Figure 1: Raman spectra of TiO_2 deposited by PLD: a) in 30 Pa argon and b) in vacuum. Full lines denoted the positions of anatase Raman bands, position of ZnO band from nanorods are denoted by dotted line, while position of rutile band is denoted by arrow.

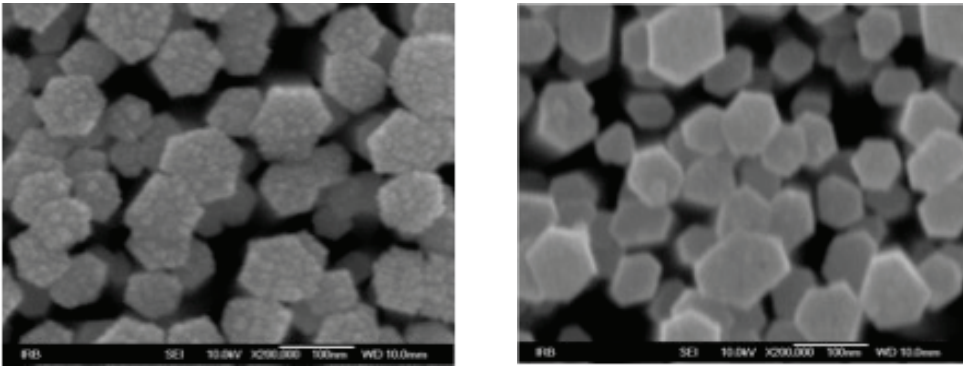

Figure 2: SEM of TiO_2 deposited by PLD: a) 5000 pulses, vacuum and b) 7500 pulses, Ar.

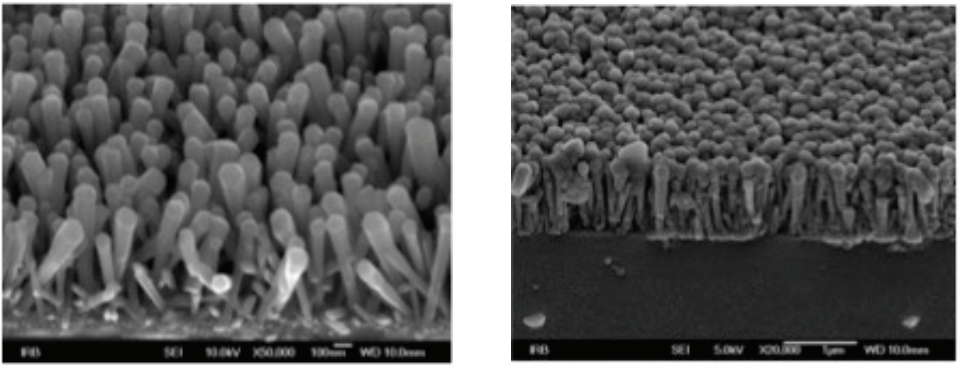

Figure 3: SEM of TiO_2 deposited by magnetron sputtering:
a) 1h deposition and b) 3 h deposition.

Mapping Twins in B_4C using ASTAR Electron Precession System on Transmission Electron Microscope

Andrei C. Kuncser[1], Corneliu Ghica[1], Ionel Mercioniu[1], Oleg Vasylkiv[2] and Petre Badica[3]

[1] *National Institute of Materials Physics, Laboratory of Atomic Structures and Defects in Advanced Materials, Magurele, Romania*
[2] *National Institute of Materials Science, Tsukuba, Ibaraki, Japan*
[3] *National Institute of Materials Physics, Laboratory of Magnetism and Superconductivity, Magurele, Romania*

A novel EBSD-like technique suitable for most Transmission Electron Microscopes (TEM) is used for identification of nanostructure in hard materials. The advantages of ASTAR crystallographic analysis system over conventional electron diffraction are the fine spatial localization (few nm) of the diffraction pattern as well as a suitable redistribution of the diffraction spot intensities by precession.

During TEM observations, a twin-like structure is observed in B_4C. This material is considered the third hardest material after diamond and cubic BN. As the micro/nano-structure (e.g. phases, defects, quality of grain boundaries) is directly related to the mechanical properties of the materials, in this work the structure of twins in B_4C has been analyzed using the ASTAR equipment installed on the JEM 2100 TEM microscope.

The analysis setup implies a nanobeam diffraction (NBD) spot controlled by NanoMEGAS DigiSTAR precession unit via deflection coils and allows a fine probing (few nm order) of a precisely defined area from the sample. From each probed point a diffraction pattern is obtained on the focus screen of the microscope and recorded by an external camera. The diffraction series spatially correlated with a corresponding image is processed with a proprietary suite of programs. The aim of the processing is to generate theoretical diffraction patterns of the candidate crystal phase/phases, to fit the theoretical data on the experimental data and to show the results in terms of crystal phase and/or orientation. It is to be mentioned that with a suitable post-processing of the data after the fitting process, information not only about the phase and orientation but also about the grain boundaries and grain size distributions can be obtained.

In order to get information about a potential twin structure, in the fitting process only the rhombohedral B_4C crystal phase has been considered (only that specific phase provided reliable fitting results). The quality of the results has been checked by the index parameter (the quality of fitting) and by the orientation reliability parameter (which provides a measure of the uncertainty between the two highest quality values of the index). Both parameters were controlled within reasonable limits for extraction of reliable results.

In Figure1(a) is shown the TEM-Bright Field image with the contrast suggesting the presence of the twins. Figure1(b) is the B_4C orientation map obtained after processing with the NanoMEGAS software suite. The (hkl) orientation of each colored stripe is the same, i.e. (-2-1-1), but there is a rotation (missorientation) of around 60 degrees around *c*-axis between green and purple stripes (colors are related to specific points on the pole figures). Missorientation is depicted in Figure1(c). The twinning plane is of the type (100) and a schematic drawing of the crystallographic twin model is presented in Figure1(d).

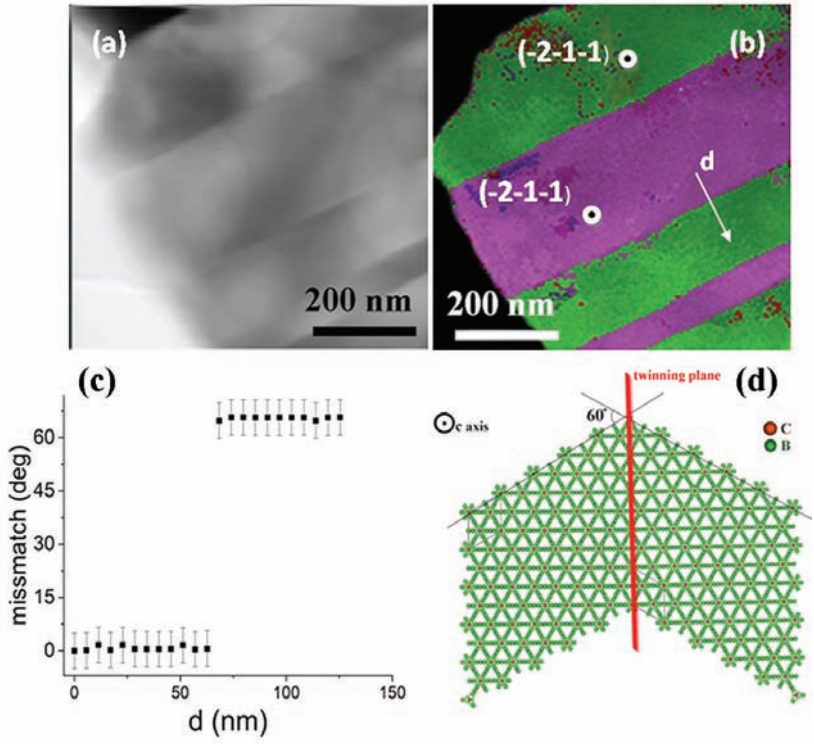

Figure 1. (a) Bright-Field TEM image of the analyzed area; (b) Orientation mapping results: both green and purple stripes have the same (hkl); (c) Missorientation (rotation) of ~60 degrees around c-axis; (d) schematic drawing of the model for the twin in B4C.

Influence of Zr Concentration on the Morphology and Structure of $BaTi_{1-Y}Zr_yO_3$ Particles

Valentin A. Maraloiu[1], Ioana D. Vlaicu[1], Marjeta M. Maček Kržmanc[2], Ionel Mercioniu[1] and Daniela Ghica[1]

[1] *National Institute of Materials Physics, 405A Atomistilor Str., 077125 Magurele-Ilfov, Romania*

[2] *Advanced Materials Department, Jožef Stefan Institute, Jamova cesta 39, Ljubljana 1000, Slovenia*

In order to produce efficient piezoelectric nanogenerators or other self-powered nanosystems, the decrease of piezoelectric constant with the size of particle has to be overcomed. Already, a piezoelectric generator based on (001) oriented $BaTiO_3$ micro-platelets to capture eolian energy was produced, but the obtained volume power density (only 105 μW cm^{-3}) was modest [1]. This value is considered low compared to volume power density produced by a nanogenerator based on $BaTiO_3$ thin film with low tetragonality deposited on plastic substrate [2]. Other lead-free piezoelectric materials show promising results. Recent investigations on $Ba(Zr_{0,2}Ti_{0,8})O_3$-$(Ba_{0,7}Ca_{0,3})TiO_3$ (BZT-BCT) system demonstrated that a d_{33} piezoelectric constant higher than 620 pC/N can be obtained. A value of d_{33}=1500-2000 pC/N is expected for the monocrystalline form of this morphotropic composition [3, 4]. Tests made on BZT-BCT nanowires obtained from electrospinning evidenced a high volume power density (338 μW cm^{-3}) [5]. Based on this data, it is expected that nano- and micro-platelets can be promising candidates to produce lead-free energy harvesting devices with high efficiency.

The present work investigates the influence of Zr concentration on the morphology and structure of $BaTi_{1-y}Zr_yO_3$ (y=0-1) particles. The particles were obtained using topochemical conversion from molten salt solution. Various techniques of electron microscopy (SEM, TEM, SAED, EDX) were used to characterize the samples.

TEM images illustrate that the platelets are cubic or rectangular and that they have a uniform thickness. It can be noticed that for the highest concentration of Zr (y=0.4) the platelets are thinner. SAED patterns indicate the platelets are monocrystalline.

Combining the data obtained from XRD, SEM and TEM led to a general view on the effects produced by the substitution with Zr ions over the morpho-structural properties of $BaTi_{1-y}Zr_yO_3$ (y=0-1) compounds.

Zr content has a minor effect over the morpho-structural properties for nominal concentrations up to y=0.075. For concentrations $y \geq 0.1$, a supplementary crystalline phase of $BaZrO_3$ is detected which leads to the conclusion that the solubility limit for Zr ions in $BaTiO_3$ crystalline structure was reached. Also, for Zr content up to y=0.075 the tetragonality of particles and the morphology of the template are kept.

References:

[1] T Gao *et al*, J. Mater. Chem. A **3** (2015) 9965-9971.
[2] K-L Park *et al*, Nano Lett. **10** (2010) 4939-4943.
[3] W Liu and X Ren, Phys. Rev. Lett. **103** (2009) 257602.
[4] M Acosta *et al*, Phys. Rev. B **91** (2015) 104108.
[5] W Wu *et al*, J. Mater. Chem A **1** (2013) 7332-7338.
[6] The authors I.D. Vlaicu, D. Ghica, A.V. Maraloiu and I.F. Mercioniu acknowledge that the studies in this work were supported by a grant of the Romanian National Authority for Scientific Research and Innovation, CCCDI-UEFISCDI, project number 49/2016 within PNCDI III - M-ERA NET Program.

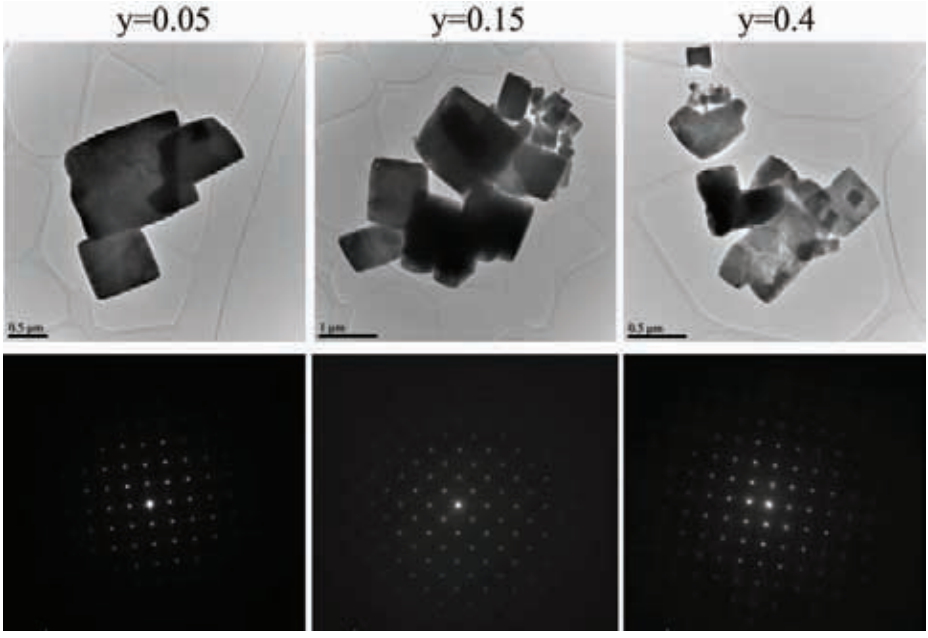

Figure 1. TEM images and SAED patterns showing the morphology and crystalline structure of $BaTi_{1-y}Zr_yO_3$ particles, where y= 0.05, 0.15 and 0.4.

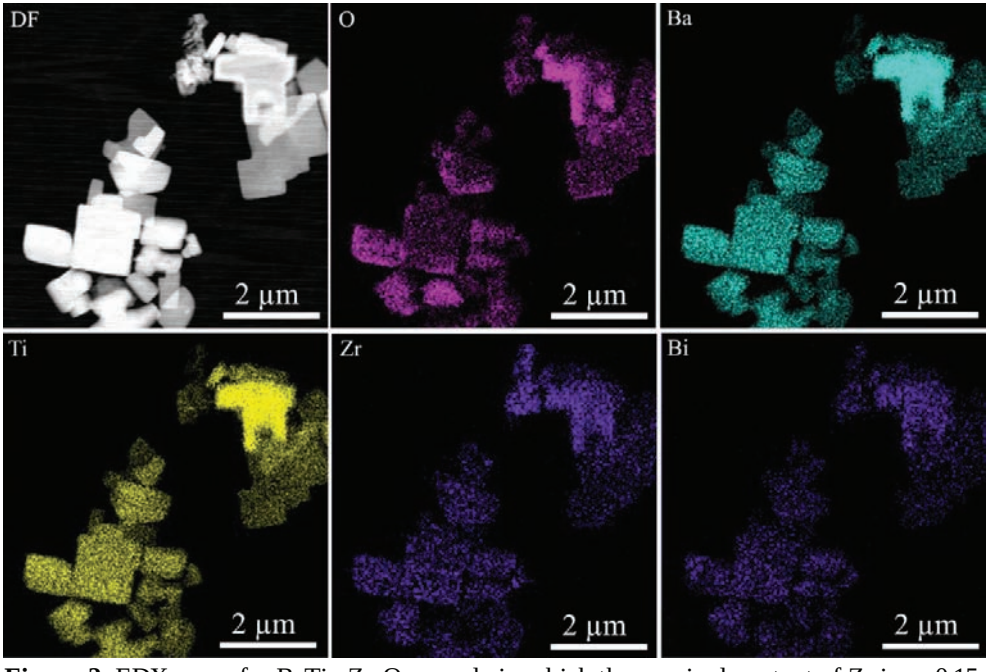

Figure 2. EDX maps for $BaTi_{1-y}Zr_yO_3$ sample in which the nominal content of Zr is y=0.15.

From Titania to Titanates: Phase and Morphological Transition

Bojana Simović[1], Aleksandra Dapčević[2], Jelena Zdravković[3], Jugoslav Krstić[4] and Goran Branković[1]

[1] *Institute for Multidisciplinary Research, University of Belgrade, Belgrade, Serbia*
[2] *Faculty of Technology and Metallurgy, University of Belgrade, Belgrade, Serbia*
[3] *Innovation centre Faculty of Technology and Metallurgy, University of Belgrade, Belgrade, Serbia*
[4] *Institute of Chemistry, Technology and Metallurgy, Department of Catalysis and Chemical Engineering, University of Belgrade, Belgrade, Serbia*

Regarding their extraordinary properties, such as biological and chemical stability, photocatalytic activity, cost-effectiveness, the titanium-based nanomaterials are the subject of an intense research. Although titania is well known as a photocatalyst, the titanates are promising candidates for the wide range of applications including ion exchange, high adsorption capacity toward organic molecules and radioactive toxic metal ions [2], in photovoltaics, H- and Li-storage, gas sensors, etc. The hydrothermal process became a very important way to obtain these materials in nanostructural form since the discovery of anatase-based alkaline hydrothermal treatment reported by Kasuga *et al.* [1].

In this work, nine products were obtained by modifying the experimental conditions (6, 12 and 18 h at 110, 135 and 160 °C) of hydrothermal treatment of starting nanoanatase in less alkaline medium (5 mol dm^{-3} NaOH solution) than usual. Specimens are labeled as T_{T-t}, where T is temperature of the treatment and t is duration of the treatment. The step-by-step optimization of this simple and costless procedure was necessary in order to obtain a pure titanate phase and to finally distinguish the titanates from titania in terms of structure and microstructure. The nanocrystalline samples were characterized by HRTEM/SAED, XRPD, EDS, TG, UV-VIS and BET techniques.

According to XRPD and HRTEM, the complete conversion of anatase to pure titanate phase was achieved after energetically the most intensive treatment, *i.e.* 18 h at 160 °C. Among other products, a certain amount of anatase remained, with its decreasing content as the temperature and time of hydrothermal treatment increases. This increment significantly improves the solubility of TiO_2 promoting the changes in morphology from the approximately spherical anatase nanoparticles into elongated titanate nanosheets (Fig. 1). Based on EDS and TG, the $Na_{0.4}H_{1.6}Ti_2O_5 \cdot H_2O$ formula could be assigned to T_{160_18}. The HRTEM/SAED revealed the shortening of interplanar distances along *a*axis because of the dehydratation due to the high vacuum of the TEM chamber and high energy of the electron beam irradiation confirming the layered structure of $Na_{0.4}H_{1.6}Ti_2O_5 \cdot H_2O$ (Fig. 2). Because of the poor characterization of titanate nanosheets found in literature, the optical and textural properties of products were also investigated. A blue shift toward lower wavelength is observed with the temperature increasing being the most pronounced for the T_{160_18} (Fig. 3). This is the consequence of full transformation of TiO_2 into $Na_{0.4}H_{1.6}Ti_2O_5 \cdot H_2O$. For the same reason, the values of specific surface areas decreased with the temperature increasing.

As shown in this work, the structure, morphology and texture of samples strongly depend of the conditions of hydrothermal treatment. The production of single phase titanate and its detailed microscopic characterization finally allowed the clarification of long-standing confusion between titania and titanates.

References:

[1] T Kasuga *et al*, Langmuir **14** (1998), p. 3160.
[2] Y Zhang *et al*, RSC Advances **5** (2015), p. 79479.
[3] The authors acknowledge funding from the Ministry of Education, Science and Technological Development of the Republic of Serbia, Grant Numbers III45007 and III45019. The support of the bilateral cooperation with Slovenia is also gratefully acknowledged (Project No. 451-03-3095/2014-09/32).

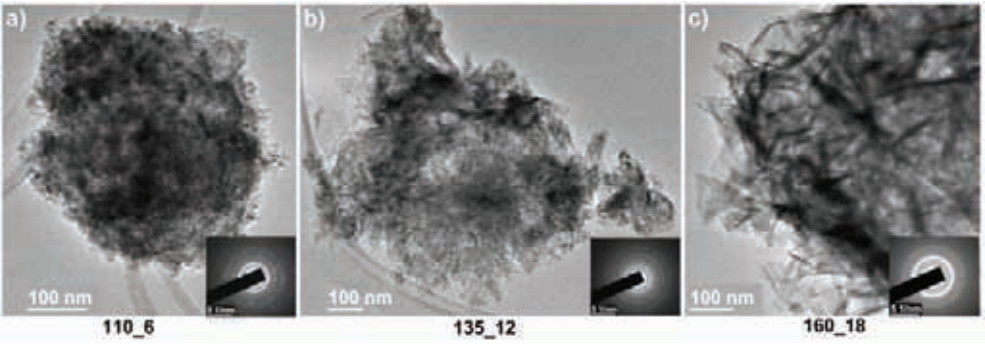

Figure 1. TEM and SAED of selected T_{T_t} samples: a) T_{110_6}, b) T_{135_12} and c) T_{160_18}.

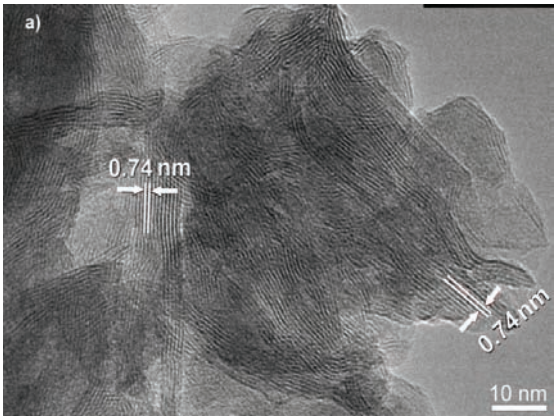

Figure 2. HRTEM image of the T_{160_18} titanate nanosheets showing its layered nature, curving of thin layers and reduction of interlayer spacing of (200) lattice planes from 0.90 to 0.74 nm.

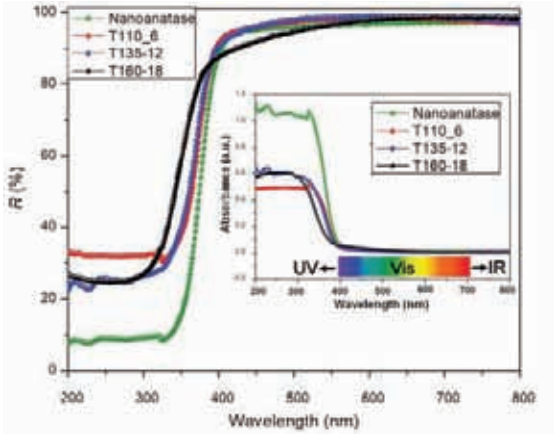

Figure 3. UV-Vis diffuse reflectance and absorption spectra of selected samples.

Sunlight-driven Photocatalytic and Photo-electrochemical Activity of ZnO/SnO_2 Composite

Smilja Marković[1], Ivana Stojković Simatović[2], Ana Stanković[1], Srečo Škapin[3], Lidija Mančić[1], Slavko Mentus[2,4] and Dragan Uskoković[1]

[1] *Institute of Technical Sciences of SASA, Belgrade, Serbia*
[2] *University of Belgrade, Faculty of Physical Chemistry, Belgrade, Serbia*
[3] *Institute Jožef Stefan, Ljubljana, Slovenia*
[4] *Serbian Academy of Sciences and Arts, Knez Mihajlova 35, 11000 Belgrade, Serbia*

Due to their high photoactivity, photostability, chemical inertness, simple syntheses procedures as well as low cost, semiconductor materials such as TiO_2, ZnO, V_2O_5, and SnO_2, are recognized as materials with a great potential for photoelectrochemical and photocatalytic applications. In particular, they can be used as photoanode in the process of photoelectrolysis of water, or to initiate decomposition of different organic or biological pollutants in water under light irradiation [1]. Which wavelength of light will be absorbed depends on the semiconductor band gap; semiconductors with a wide band gap (> 3 eV) can absorb light in the UV range only, while those with a narrow band gap (< 3 eV) can be activated by visible light. Current trend in photo(electro)catalysis is to develop efficient semiconductors which can be activated by absorbing natural sunlight. During the years, various approaches have been developed to modify optical properties of semiconductors thus to be capable to absorb sunlight, for example: the incorporation of transition metal ions or defects into the crystal structure, the particles' surface sensitization, hydrogenation, coupling of semiconductors with different band gap energies, etc. [2].

In this work, to enhance photo(electro)catalytic activity of ZnO, we prepared composite with SnO_2. ZnO/SnO_2 composite was prepared by high-energy ball milling of commercially available ZnO and SnO_2 powders in a 0.9:0.1 molar ratio [3]. The oxides were milled during 2 h in planetary ball mill with the angular velocity of the vessels of 400 rpm. Stainless steel vessels and balls were used, while the balls to powder weight ratio was 10:1. The phase composition and crystal structure were analyzed by XRD and Raman spectroscopy. XRD patterns were recorded at

Philips PW-1050 over a 2θ range 10–70° with a step of 0.05° and a counting time of 5 s. The μ-Raman spectra were recorded in the frequency interval of 50–1200 cm^{-1} (DXR Raman microscope, Thermo Scientific). The particles morphology and size distributions were examined by FE–SEM (Ultra plus, Carl Zeiss, Germany), TEM (JEOL 2100), and laser diffraction particle size analyzer (Mastersizer 2000; Malvern Instruments Ltd., U.K.); elemental mapping was performed by EDXS analysis (JEOL ARM 200CF equipped with JEOL centurion 100). Optical properties were studied by UV–Vis diffuse reflectance (Thermo Scientific, Evolution 600 UV–Vis spectrophotometer) and photoluminescence spectroscopy (Horiba Jobin Yvon Fluorolog FL3–22 *spectrofluorometer*). The photocatalytic activity of ZnO/SnO_2 composite was tested for a degradation of methylene blue dye under direct sunlight illumination with intensity of about 1000 lux. The pollutants concentration during degradation was monitored by the UV-Vis spectrophotometer and calculated according to the maximum absorbance value. The total organic carbon (TOC) was determined by the TOC Analyser Multi N/C (Analytik Jena, Austria). The photoelectrochemical performance was tested under lamp which simulates sunlight (Osram Ultra Vitalux lamp, 300 W), by cyclic voltammetry CV using Gamry PCI4/750 in the three-electrode quartz cell composed from the working electrode, platinum foil as the counter electrode and saturated calomel electrode (SCE) as the reference electrode. All the results obtained for ZnO/SnO_2 composite are compared with the ones for pristine ZnO powder.

According to the XRD analysis, composite powder is of high crystallinity, consisted of hexagonal ZnO and tetragonal SnO_2 phases, without any other crystal phases. Results of HRTEM, EDXS mapping and FE–SEM showed that after milling surface of ZnO crystals is covered with small spheroidal particles of tin oxide. Figure 1 shows the FE–SEM micrograph of ZnO/SnO_2 powder.

The cyclic voltammogram was measured in 1 M KCl at 20 $mV \cdot s^{-1}$, under dark and during illumination. For pristine ZnO it was measured that the potential decreased from -0.310 to -0.292 V versus SCE in dark and light, respectively; while for ZnO/SnO_2 the onset hydrogen evolution potential decreased from -0.351 V versus SCE in dark to -0.337 V versus SCE during illumination. What's more, at the potential of -0.7 V versus SCE, the current during illumination of photoanode increased about 40 % in the case of composite material, while for the pristine ZnO it increased just about 10 %, Figure 1.

When ZnO/SnO_2 was used MB dye solution was completely de-colorized after 40 min, whereas the time necessary for the de-colorization of 50% of the dye was $t_{1/2}$ = 3.85 min.

Raman and PL results implicate that the enhanced photo(electro)activity of ZnO/SnO_2 as compared to pristine ZnO is due to the surface defects which contributes

to the visible light absorption. The presence of Zn_i point defects contributes to the visible light absorption due to the defect level located in the band gap, at 0.22 eV below the conductive band (narrowing band gap to about 3.15 eV or 400 nm). These defects also promote charge transfer and suppress electron-hole recombination [3,4].

References:

[1] T Majumder *et al*, Energy Technology **4** (2016), 950.
[2] R Lamba *et al*, Talanta **131 (**2015), 490.
[3] S Marković *et al*, RSC Advances **7** (2017), 42725.
[4] This study was supported by the Ministry of Education, Science and Technological Development of the Republic of Serbia under Grant no III45004 and the Serbian Academy of Sciences and Arts through the project F-190 “Electrocatalysis in the contemporary processes of energy conversion”.

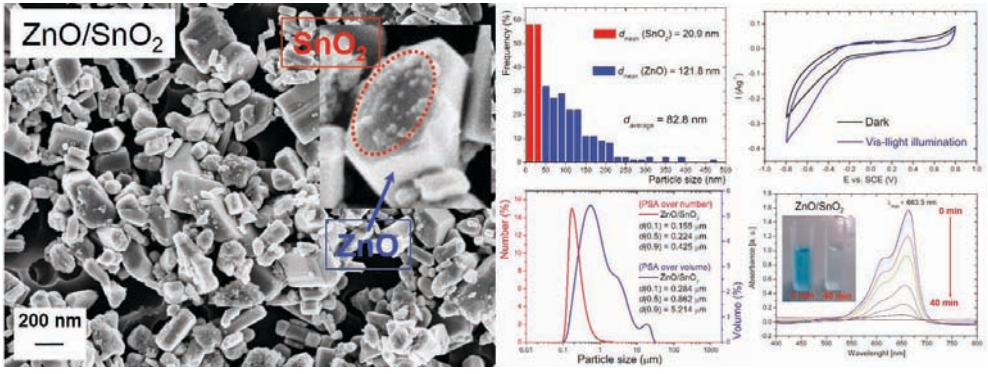

Figure 1. FE–SEM micrograph, particle size distributions, and photo(electro)catalytic activities of ZnO/SnO_2 composite.

Synthesis and Characterization of $Na_{0.4}MnO_2$ as a Positive Electrode Material for an Aqueous Electrolyte Sodium-ion Energy Storage Device

Lazar Rakočević[1], Mirjana Novaković[2], Jelena Potočnik[2], Dragana Jugović[3] and Ivana Stojković Simatović[1]

[1] *University of Belgrade, Faculty of Physical Chemistry, Belgrade, Serbia*
[2] *University of Belgrade, Vinča Institute of Nuclear Sciences, Serbia*
[3] *Institute of Technical Sciences of SASA, Belgrade, Serbia*

Due to the increasing use of batteries in everyday life and in industry, there is a need for developing cheaper batteries than the widely used lithium ion batteries. Lower price and higher abundance of sodium compared to lithium mineral resources intensified the development of Na-ion batteries. Aqueous lithium/sodium rechargeable batteries have attracted considerable attention for energy storage because they do not contain flammable organic electrolytes as commercial batteries do, the ionic conductivity of the aqueous electrolyte is about two orders of magnitude higher than in non-aqueous electrolyte and the electrolyte salt and solvent are cheaper. Various materials such as manganese oxides, vanadium oxide and phosphates have been used as electrode materials (cathodic and anodic) in sodium batteries due to high sodium intercalation ability in both, organic and aqueous electrolytes. The most frequently used type of manganese oxides are Li–Mn–O or Na–Mn–O systems due to their tunnel or layered crystal structures which facilitate the lithium/sodium intercalation-deintercalation [1, 2].

In this work, a glycine-nitrate method (GNM) was applied for the synthesis of cathode material $Na_{0.4}MnO_2$. Aqueous solutions of $NaNO_3$ and $Mn(NO_3)_2{\cdot}4H_2O$ were mixed in appropriate volume ratios in order to obtain desired stoichiometry and solid glycine was added in order to obtain a precursor solution with the molar ratio of glycine to nitrate was 1.2:1. The precursor solution was placed in a glass beaker and heated in an oven at 200°C until spontaneous ignition occurred. The ash, resulted from the combustion, was heated at 800 °C for 4 h.

The phase composition and crystal structure were analyzed by XRD on a Philips PW-1050 over a 2θ range 10–70° with a step of 0.05° and a counting time of 5

s. The particle morphology was examined by SEM/FIB (FEI SCIOS Dual Beam microscope) and TEM (FEI Talos F200X microscope) while elemental mapping was performed by EDS analysis. The electrochemical performance was tested by cyclic voltammetry (CV) using Gamry PCI4/750 in a three-electrode cell, consisting of a working electrode, platinum foil as the counter electrode and a saturated calomel electrode (SCE) as the reference electrode in saturated aqueous solution of $NaNO_3$. The working electrode was prepared by mixing 85 wt% $Na_{0.4}MnO_2$ powder, 15 wt% acetylene black and 5 wt% poly(tetrafluoroethylene) (PTFE) binder in N-methyl-2-pyrrolidone and, after homogenization in an ultrasonic bath, the suspension was transferred onto glassy carbon support.

The phase structure of the product annealed at 800 °C was identified as orthorhombic $Na_{0.4}MnO_2$ (JCPDS 27–0749) with tunnel structure which consists of MnO_6 octahedral units shared by corners and/or edges [3]. Also, some additional peaks were observed and identified as Mn_2O_3. TEM and SEM micrographs of obtained $Na_{0.4}MnO_2$ powder material are shown in Fig. 1. Uniform rod-like shaped particles can be observed, with average length and width of 300 nm and 80 nm, respectively. EDS analysis revealed that sample contained Na, Mn, and O in an appropriate ratio.

The cyclic voltammogram were performed in a saturate aqueous solution of $NaNO_3$ at scan rate of 20-400 mVs^{-1} within the voltage range from -1.30 to 1.35 V vs. SCE. The shape of CVs and peak positions were similar for all rates which means that the intercalation/deintercalation process of Na^+ is reversible even at high rates of charging/discharging. The specific capacity ($mAh\ g^{-1}$) was calculated as the area under redox peaks of CVs recorded at 20 mVs^{-1} (equivalent to 33 C). The initial discharge capacity of $Na_{0.4}MnO_2$ in $NaNO_3$ solution was 50 $mAhg^{-1}$ while after 15th cycles the values increased by 9%. During cycling, this material demonstrated great efficiency (the ratio of capacity charge and discharge) of ~95%. This indicates that the material synthesized by glycine-nitrate method can be used in aqueous rechargeable sodium batteries [4].

References:

[1] J Liu *et al*, Green Energy & Environment **3** (2018), 20.
[2] F Hu and M Doeff, Journal of Power Sources **129** (2004), 296.
[3] S Liua *et al*, Journal of Power Sources **196** (2011), 10502.
[4] This study was supported by the Ministry of Education, Science and Technological Development of the Republic of Serbia under Grant no III45014 and III45005 and the Serbian Academy of Sciences and Arts through the project F-190 “Electrocatalysis in the contemporary processes of energy conversion”.

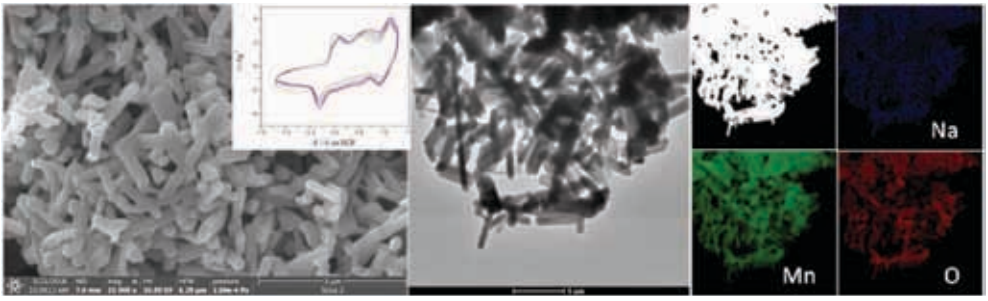

Figure 1. (Left) SEM micrograph of sample with CV in inset; (Middle) TEM micrograph of samples; (Right) HAADF STEM micrograph of samples with appropriate EDS maps of Na, Mn and O distribution.

Metal Nanoparticles-PANI Nanocomposites and their Applications

Una Stamenović[1], Vesna Vodnik[1] and Mojca Otoničar[2]

[1] *Vinča Institute of Nuclear Sciences, University of Belgrade, P. O. Box 522, 11001 Belgrade, Serbia*
[2] *Jožef Štefan Institute, Department of Advanced Materials, Jamova 39, 1000 Ljubljana, Slovenia*

Characteristic physicochemical properties, as the effect of their nano - dimensions and diversity of their possible applications, make metallic nanoparticles (NPs) one of the main colloidal materials studied in the nanoscience field. Its development depends on the improvement of the existing synthetic procedures in order to gain stable and uniform metallic NPs with different sizes and shapes, since NPs' features (optical, electrical, catalytical, *etc*.), and therefore their applications, depend on particles' morphology. The necessities could be fulfilled within materials such nanocomposites are, *ie*., by the incorporation of metallic NPs into the polymer matrix, whereby not only polymer matrix will have a positive effect on the NPs characteristics, but metal NPs could significantly improve polymers' properties. A special group of functional materials with advanced features and accordingly promising applications are nanocomposites with metal NPs (gold (Au), silver (Ag), and copper (Cu)) and intrinsically conductive polymers, such as polyaniline (PANI). As biocompatible materials with unique properties, good conductivity and electrochemical activity, these nanocomposites were the subject of our researches [1-3].

Nanocomposites designated as Au-PANI, Ag-PANI, and Cu-PANI, were synthesized by the simple *in situ* oxidative polymerization of aniline to PANI by metal ions [1-3]. These typical oxido-reduction reactions begin with atomic (metal ions) and molecular (aniline monomer) precursors in an appropriate molar ratio, in order to achieve simultaneous reduction of metal ions to NPs and oxidation/polymerization of aniline to PANI. This type of nanocomposite' formation has certain advantages over other chemical or electrochemical polymerization processes, that are associated to reduced number of reactants, since metal ions such Au^{3+}, Ag^{+}, and Cu^{2+} have

satisfactory standard electrode potentials (+1,498, +0,8, and +0,34 V, respectively), that will easily induce aniline oxidation, while formed PANI chains act as surfactants that will stabilize metal NPs through charge transfer. Additionally, it is less demanding, either in the process itself, or in the post-synthetic treatment (concerning the cleaning of the sample).

Based on our findings [1-3], as well as existing literature data, experimental conditions have great influence on the nanocomposites' features firstly reflected through their morphology (size and shape of metallic NPs and PANI chains), and consequently possible applications. For example, changing the reaction medium (water/methanol), pH of the reaction mixture, as well as the molar ratio between reactants [1], has a significant effect on the structure and morphology of the final products. These factors control the duration of the polymerization induction period, which will further affect the other stages of the polymerization, and finally nanocomposites' characteristics. Thus, the architecture of formed AgNPs varies from 7 nm to 150 nm in sizes and from spheres, through triangular nanoplates, to polyhedral shapes, while PANI chains are formed either in the shape of fibers or granules. Besides, their conductivity, electrocatalytic activity, and possible application for oxygen reduction reaction (ORR) differ, and vary depending on AgNPs dispersion throughout PANI matrix.

Similar behavior was recognized with Au-PANI nanocomposite [2]. It was shown that the molar ratio between Au^{3+} ions and aniline is crucial for the nature of the final product - just for the defined proportion between these two reactants, the final product is Au-PANI nanocomposite, with granular morphology and incorporated Au nanorods. Additionally, even though this nanocomposite have similar or half smaller mass fraction of metal NPs, compared to Ag-PANI nanocomposites mentioned above (~29 wt% compared to ~20 and ~45 wt%), its electrical conductivity is several order of magnitudes higher. The main reason could be the dispersity of NPs throughout PANI matrix and their morphology. Namely, since the electrical conductivity of nanocomposites is narrowly correlated to its network geometry, AuNPs adsorbed on the PANI chains surface could act as charge trapping sites that participate in the charge transport through PANI matrix, enabling the formation of infinite conductive pathways, unlike Ag-PANI nanocomposites, where these pathways are interrupted by polyvinylpyrrolidone non-conductive islands [1].

Besides they are electrocatalytically active, metal/PANI nanocomposites also show significant antimicrobial activity [3]. Our findings considering Cu-PANI nanocomposite, with fibrilar PANI chains morphology and spherical CuNPs with 10 nm in diameter, pointed out that small amount of this composite for short contact time (all compared to the literature data) can inhibit the growth and kill representative microbes - *Escherichia coli*, *Staphylococcus aureus*, and *Candida albicans*. There

is a synergistic antimicrobial effect of nanocomposite' constituents, that is a combination of several different action mechanisms: a) physical and electrostatic interaction between nanocomposite and microbial cell wall; b) as a steric stabilizator, PANI chains network increases effective concentration of strong antimicrobial agent - CuNPs, and contact interface between nanocomposite and microbes; c) additional antimicrobial effect of released Cu^{2+} ions.

The electrochemical and antimicrobial activity of these nanocomposites, regardless metal mass fraction, NPs' size, shape, and PANI morphology, is related to the particles' surface effects, *ie*., reactive (111) crystallographic planes present on the particles surface. These nanocomposites proved to be promising Pt-free electrocatalysts and antimicrobial agents.

Reference

[1] U Stamenović *et al*, Article in Press.
[2] U Bogdanović *et al*, ACS Applied Materials and Interfaces **7** (2015), 28393.
[3] U Bogdanović *et al*, ACS Applied Materials and Interfaces **7** (2015), 1955.
[4] This work was supported by grants from the Ministry of Education, Science and Technological Development of the Republic of Serbia (No. 172056 and 45020).

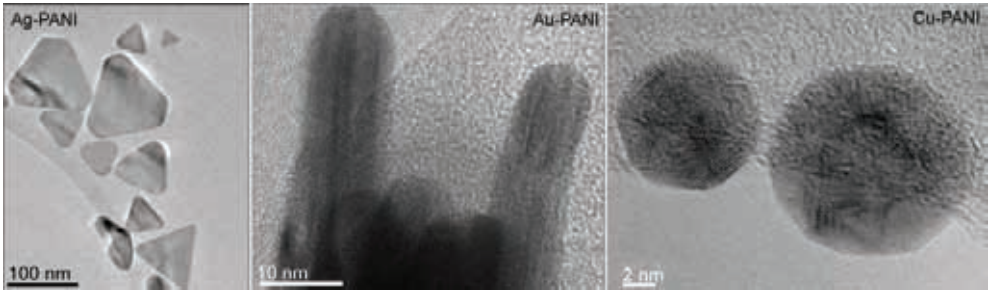

Figure 1. TEM images of metal nanoparticles-PANI nanocomposites.

Morphology of Nanotubular Oxide Layer Formation on Titanium and Titanium Alloy Using Electrochemical Anodization

Dragana R. Barjaktarević[1], Ivana D. Dimić[1], Ivana Lj. Cvijović-Alagić[2], Veljko R. Đokić[1] and Marko P. Rakin[1]

[1] *Faculty of Technology and Metallurgy, University of Belgrade, Karnegijeva 4 11120 Belgrade, Serbia*
[2] *Institute of Nuclear Sciences "Vinča", University of Belgrade, P.O. Box 522, 11001, Belgrade, Serbia*

Behavior of metal biomaterials is governed by surface properties, which is a crucial factor in interactions of the implant material with the surrounding tissue. The implant often needs some kind of modification to optimize and improve biological and mechanical properties of the surface. One of the most commonly used methods is the electrochemical anodization, a simple process used to form nanotubular oxide layer on the metal surface by oxidation [1]. In order to form nanotubular oxide layer on UFG commercially pure Ti and Ti-13Nb-13Zr alloy (coarse-grained, CG, and ultrafine-grained, UFG, obtained by high pressure torsion) the material surface was modified using chemical surface treatments, electrochemical anode oxidation. Anodization was done in 1M H_3PO_4 + NaF electrolyte, at room temperature. The anodization was performed during 30, 60, 90 and 120 minutes, for the desired potential of 25 V with a scan rate of 100 mVs^{-1}. The aim of the work was determining the influence of anodization time on morphology of nanotubular oxide layer. In order to analyze characteristics of the nanotubular oxide layer, Scanning Electron Microscope (SEM) MIRA3 TESCAN was used. The SEM operated at an accelerating voltage of 20 keV. As a result of the anodic oxidation highly ordered nanotubular layers were obtained.

The homogeneous morphology of nanotubular oxide layer was formed during 90 and 120 minutes, while inhomogeneous nanotubular oxide layer was formed during 30 and 60 minutes. There is a bimodal distribution size of nanotubes with diameters in the range of 40-100 nm for the CG TNZ alloy and in the range of 60-100 nm for the UFG TNZ alloy. Wall thickness was approximately 20 nm for the CG TNZ alloy and approximately 30 nm for the UFG TNZ alloy. Increasing anodization time

increased the diameter and the wall thickness of the formed nanotubular oxide layer [2]. As can be seen in Figure 1, nanotubes formed on UFG TNZ surface have not regular and homogeneous morphology for shorter anodizing time, while increasing anodizing time caused the formation of homogeneous morphology. On the other hand, nanotubes formed on the CG TNZ surface did not have compact pore and homogeneous morphology for shorter anodizing time, while increasing anodizing time led to the formation of nanotubes with compact pore and homogeneous morphology. It is obvious that the nanotubes are open on the top. Also, Figure 1 shows that the nanotubular oxide layer on the UFG TNZ surface needs less time for formation. The bimodal feature observed in the diameter distribution of nanotubes could be ascribed to the difference in the growth rate and dissolution rate of each nanotube [3]. The non-uniform surface morphology of nanotubes may be conditioned by dual $\alpha'+\beta$ phase microstructure of the alloy in the case of phases etched primarily by the electrolyte. Figure 2 shows that nanotubular oxide layer was formed on UFG commercially pure Ti only during 60 minutes.

References :

[1] KH Kim *et al*, Dent. Mater. J. **28** (2009), 20-36.
[2] H Tsuchiya *et al*, Electroch. Acta **52** (2006), 94–101.
[3] XJ Feng *et al*, Acta Biomater. **4** (2008), 318–323.

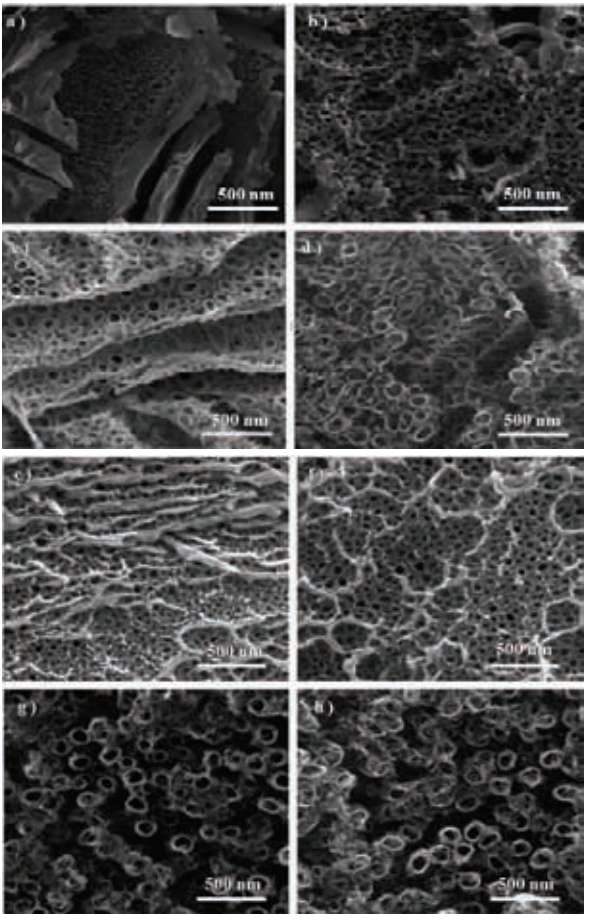

Figure 1. SEM micrographs of the nanotubular oxide layer formed on the CG Ti–13Nb–13Zr alloy (a), (b), (c), (d) and UFG Ti-13Nb- 13Zr alloy (e), (f), (g), (h) in $1H_3PO_4$ + NaF for 30, 60, 90 and 120 minutes, respectively for both materials.

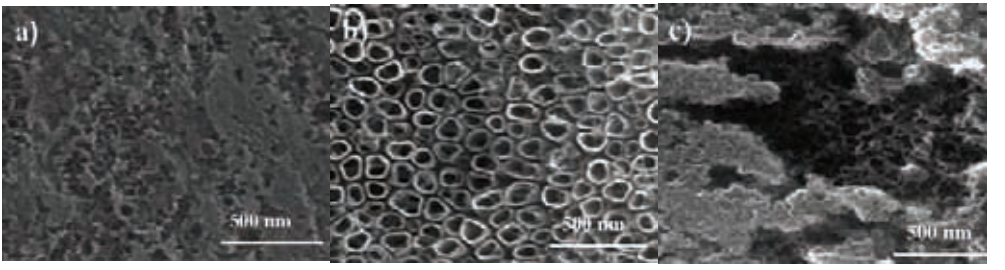

Figure 2. SEM micrographs of the nanotubular oxide layer formed on the UFG cpTi (a), (b), (c), (d) in $1H_3PO_4$ + NaF for 30, 60 and 90 minutes.

Depth Analysis of Thin Films Using StrataGem Program

Jelena Potočnik, Maja Popović, Mirjana Novaković, Davor Peruško, Zlatko Rakočević

University of Belgrade, INN Vinča, Mike Petrovića Alasa 12-14, 11351 Belgrade, Serbia

The investigation of multilayered nano-structures can be of great interest since their characteristics can be, most of the times, much better than the ones typical of the single components [1]. Titanium (Ti) has been investigated as a biomedical material due to its good mechanical strength, excellent biocompatibility, high acidic corrosion resistance, etc. [2-4]. These characteristics of Ti are similar to those of zirconium (Zr) [5]. The alloys' enhanced mechanical and corrosion resistance make these two elements excellent candidates for different applications, especially in the biomedical field. The aim of this work was to obtain Ti/Zr layered sample depth using SEM-EDS system as well as StrataGem software package [6]. An attempt was made to estimate the range of the method by comparison with results obtained from TEM analysis. StrataGem software was used to fit the experimental K-values by use of plots of theoretical K-values against thickness.

The sample was deposited in a Balzers Sputtron II system. Si wafer was used as a substrate. Multilayer was deposited at the deposition rate of 8 nm min^{-1} for Ti and 11 nm min^{-1} for Zr. The deposited structures consisted of 30 alternate Ti and Zr layers, 15 of each, with a total thickness of ~ 500 nm. The first layer deposited on the substrate was Zr and the outermost Ti. In this paper, results of characterization of Ti/Zr layered thin film in terms of elemental composition and film thickness with SEM-EDS (FEI SCIOS 2) using StrataGem software are presented. The thicknesses are compared to those obtained on the basis of cross-section TEM (FEI TALOS F200X) imaging of the sample.

On the cross-sectional TEM image (Fig. 1) a multilayered structure is observed. The thickness was measured to be 480 nm, while the thicknesses of Ti and Zr layers were approximately 16 nm and 18 nm, respectively. EDS elemental mapping of Ti/Zr layers deposited onto Si substrate is presented in the inset of the Fig. 1. Titanium, zirconium and silicon are presented with different colors: Ti (green), Zr (red) and Si (blue).

According to StrataGem depth analysis of the composition of the sample, the dependences K of the value of the primary electron beam and the thickness of the deposited layers were determined. Experimental and fitted K-values for the analyzed sample are shown in Fig. 2a. It can be seen that the K-values calculated for TiLα, TiKβ, ZrLα, ZrKα and SiKβ fit the experimental data quite satisfactorily. In the Fig. 2b are presented dependences on film thickness of measured and fitted K-values for the Ti and Zr layers measured at 5 kV and 30 kV electron beam. It can be noted that, at a value of 5 kV electron beam, the thickness values of Ti and Zr layers are approximately 16 and 21 nm respectively (according to the experimental K-value). The obtained values are in good agreement with the values measured by TEM. It is noted that for the values of electron beam voltage of 30 kV, thicknesses of the deposited layers are significantly higher. This could be explained by the fact that electrons penetrate deeper into a thin layer and obtain information within much greater depth. For experimental K-values, the thickness of Ti layer is about 225 nm, while the thickness of the Zr layer is 245 nm. Since the resulting thin layer consists of 15 layers of Ti and 15 layers of Zr, then it can be concluded that the average thickness of the Ti layers in the sample is 15 nm, while the average layers thickness of Zr is 17 nm [7].

References:

[1] AV Demchishina *et al*, Appl. Surf. Sci. **342** (2015), 127.
[2] H Michelle Grandin, S. Berner, M. Dard, Materials **5** (2012), 1348.
[3] G Bolata *et al*, Electrochim. Acta **88** (2013), 447.
[4] D Peruško *et al*, Mater. Manuf. Process. **32** (2017), 1622.
[5] S Berner *et al*, Eur. Cell. Mater. **17** (2009), 16.
[6] StrataGem Version 6.7.0. – Thin Film Analysis.
[7] This work was financially supported by the Ministry of Education Science and Technological Development of the Republic of Serbia, project no. III 45005.

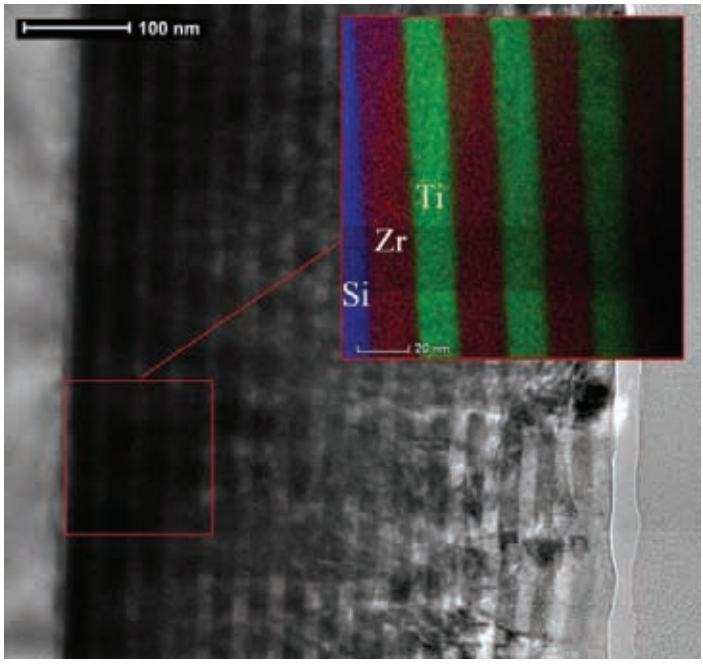

Figure 1. Cross-sectional TEM image of Ti/Zr layers deposited onto Si substrate. The EDS color mapping wherein elements are distinguished by color: Si (blue), Zr (red) and Ti (green) is given in inset.

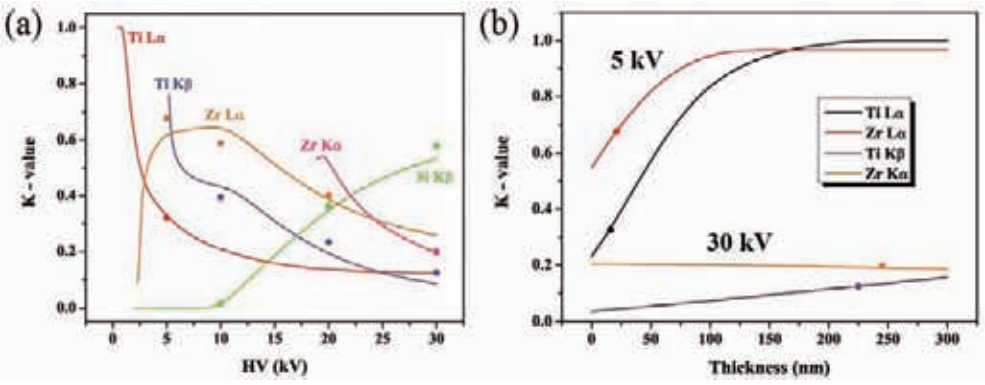

Figure 2. Results obtained using StrataGem program: (a) dependence on primary electron energy of measured and fitted K-values and (b) dependence on film thickness of measured and fitted K-values for the Ti and Zr layers.

Improvement of Density and Influence of Sb Doping on Structural Properties of Perovskite $BaSnO_3$

Jelena Vukašinović[1], Milica Počuča-Nešić[1], Danijela Luković Golić[1], Slavica M. Savić[2], Zorica Branković[1], Nikola Tasić[1], Aleksandra Dapčević[3], Slavko Bernik[4], Matej Kocen[4] and Goran Branković[1]

[1] *Institute for Multidisciplinary Research, University of Belgrade, Belgrade, Serbia*
[2] *Biosense Institute, University of Novi Sad, Novi Sad, Serbia*
[3] *Faculty of Technology and Metallurgy, University of Belgrade, Belgrade, Serbia*
[4] *Jožef Stefan Institute, Ljubljana, Slovenia*

Perovskite-type materials are widely important class of materials due to their interesting physical properties, such as superconductivity, ferromagnetism, ferroelectricity, piezoelectricity, and many others [1]. Barium stannate ($BaSnO_3$) is crystalizing in an ideal cubic structure, and has good chemical and thermal stability at high temperatures up to 1200 °C. Undoped $BaSnO_3$ is an n-type semiconductor with a band gap of ~3.1 eV [1]. $BaSnO_3$ finds application as dielectric ceramic material, transparent conducting oxide (TCO), resistor, photocatalyst, photoanode material, gas sensor for many gases, protonic conductor. Doping with antimony (Sb) can improve the electrical conductivity and enhance density during sintering [1-4].

In this work samples of $BaSn_{1-x}Sb_xO_3$ (x = 0.04, 0.06, 0.08, 0.1) were prepared by mechanochemically assisted solid state method. Precursor powders $BaCO_3$, SnO_2 and Sb_2O_3 were mechanochemically activated in isopropanol for 8h. After drying prepared powders were calcined at 900 °C for 4h in air. Calcined powder were mounted into a carbon die and subsequently sintered by spark plasma sintering (SPS) at 1200 °C for 5 minutes. Structural properties of the obtained ceramic samples of ($BaSn_{1-x}Sb_xO_3$) were completely characterized by X-ray diffraction (XRD), scanning electron microscopy (SEM), energy dispersive X-ray spectroscopy (EDS) and atomic force microscopy (AFM). Electrical properties of the ceramic $BaSn_{1-x}Sb_xO_3$ samples were determined by measuring the current-voltage characteristics at room temperature and elevated temperatures in different mediums (air, silicon oil). The

XRD analysis showed the formation of the cubic perovskite $BaSnO_3$ as a major phase and Ba_2SnO_4 as a secondary phase. The content of tetragonal secondary phase of Ba_2SnO_4 was approximately the same in all samples. This confirmed that presence of Sb did not influence the forming of Ba_2SnO_4. Ionic radius of Sb^{3+} (0.076 nm) is larger than ionic radius of Sn^{4+} (0.069 nm), and it incorporation by lattice leads to the increase of lattice parameter [4]. The cubic lattice parameter *a* was estimated to be 0.41287(9), 0.41301(9), 0.41321(9) and 0.41302(4) nm for x =0.04, 0.06, 0.08 and 0.1, respectively. The relative densities were 95.2 %, 84.2 %, 85.9 % and 79.2 % for x =0.04, 0.06, 0.08 and 0.1, respectively The SEM images of the fractured surfaces of the obtained ceramics revealed that all samples were well-densified, with the trend of reducing a grain size with increasing of Sb concentration. The AFM images showed the existence of various particles shapes, with the particle size of around 36 nm.

References:

[1] M Hiroshi *et al*, Chemistry of Materials **25** (19) (2013), 3858.
[2] Y Masahiro *et al*, Materials Science and Engineering B **173** (2010), 29.
[3] L Wenzhong *et al*, Sensors and Actuators **80** (2000), 35.
[4] Y Daisuke *et al*, Materials Science and Engineering B **173** (2010), 33.
[5] The authors would like to acknowledge the financial support of the Ministry of Education, Science and Technological Development of the Republic of Serbia, project III 45007.

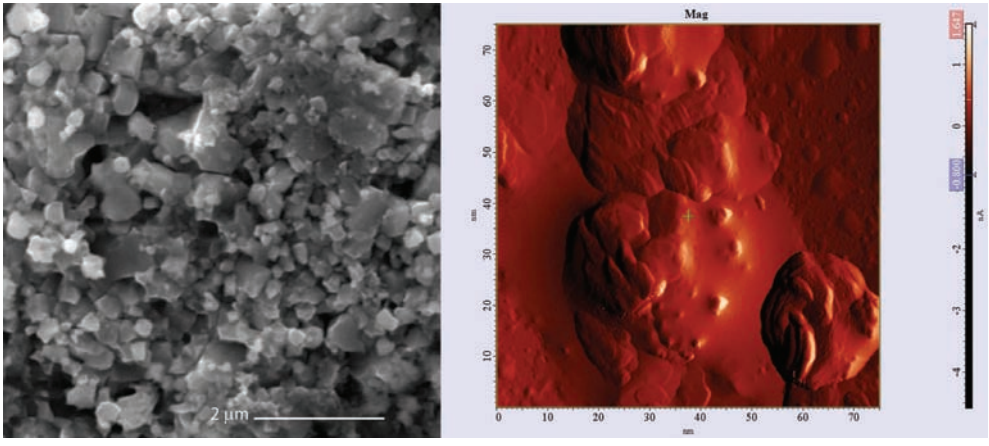

Figure 1. SEM image of fractured surface of $BaSn_{0.92}Sb_{0.08}O_3$ (left) and AMF image of crashed pellet of $BaSn_{0.92}Sb_{0.08}O_3$ (right).

Perovskite Thin Films in Tunable Microwave Technologies

Jelena Vukmirovic[1], Elvira Djurdjic[2], Andrea Nesterovic[1], Ante Bilusic[3], Zeljka Cvejic[2] and Vladimir V. Srdic[1]

[1] *Department of Materials Engineering, Faculty of Technology, Novi Sad, Serbia*
[2] *Department of Physics, Faculty of Sciences, Novi Sad, Serbia*
[3] *Department of Physics, Faculty of Science, University of Split, Croatia*

Advances in microelectronics, demand miniaturization of electronic components and ferroelectric thin films, are recognized as good potential candidates for broad range of applications such as capacitors, sensors, memories, etc. Microwave tunable devices based on thin film technology intrigued scientists in last few decades [1]. Architecture of tunable devices is quite complicated and it demands fabrication of complex shaped thin films as well as specifically designed electrodes. In order to prepare 2-dimensional electronic devices huge number of thin film deposition techniques were considered. Inkjet printing is relatively novel technique suitable for preparation of complex shaped thin films. In comparison to lithography, inkjet printing is less precise, but much cheaper technique with huge potential application in thin film technology and electrode production. Both methods were considered for preparation of tunable microwave devices.

Barium titanate based materials, doped by strontium and zirconium are known as materials with high tunability [2,3]. For this investigation barium titanate thin films with addition of different concentrations of strontium and zirconium were prepared by sol gel method in acidic environment. Barium carbonate, strontium acetate, zirconium oxychloride and tetrabutyl-orthotitanate were used as precursors and glacial acetic acid and 2-methoxy ethanol were used as solvents. Thin films were deposited at previously cleaned platinized silicon substrates by spin coating technique, calcined at 500 °C and sintered at different temperatures up to 1000 °C. The prepared thin films were structurally characterized before deposition of electrodes for tunable measurements. Uniformity and surface of the thin films were examined by scanning electron microscopy. Microscopy confirmed that the obtained thin films have well-defined structure and smooth surface without cracks.

XRD analysis confirmed changes in crystal structure of barium titanate thin films by dopants addition, followed by peak displacement. Additional investigation of changes in structure was done by Raman spectroscopy. The influence of dopants and the phase composition were noticed by monitoring the 306 cm^{-1} peak in Raman spectra for all systems. This peak position is characteristic for barium titanate tetragonal phase. The replacement of part of barium ions by strontium and titanium ions by zirconium changed the shape of this peak and also lowered its intensity. All this indicates the changes in structure compared to pure barium titanate.

The second goal of this investigation was deposition of metal conductive electrodes suitable for microwave tunable measurements. Schematic review and cross section of considered designs of the device are showed in Fig. 1 and Fig. 2, respectively. Electrodes were prepared by two different techniques: inkjet printing and photolithography. Inkjet printing is less precise technique and preparation of electrodes with weight <50 μm is not possible. Electrodes obtained by photolithography are more precise and suitable for tunable microwave measurement.

References:

[1] N Setter *et al*, J. Appl. Phys. **100** (2006), 51606.
[2] P Bao *et al*, J. Phys. D. Appl. Phys. **41** (2008), 63001.
[3] V Buscaglia *et al*, J. Phys. Condens. Matter. **26** (2014), 65901.

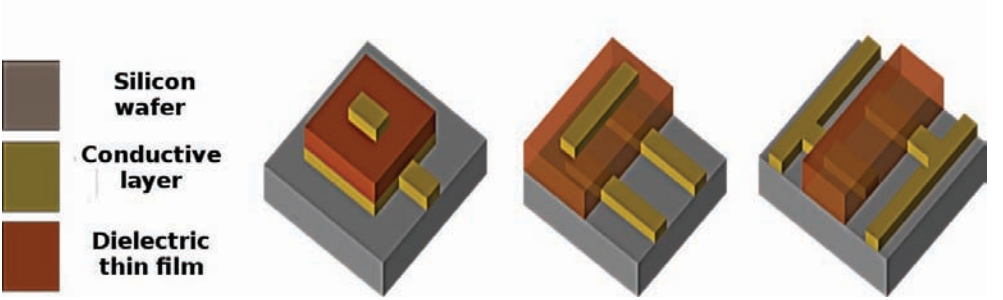

Figure 1. Scheme of different designs of thin films for microwave tunable measurements

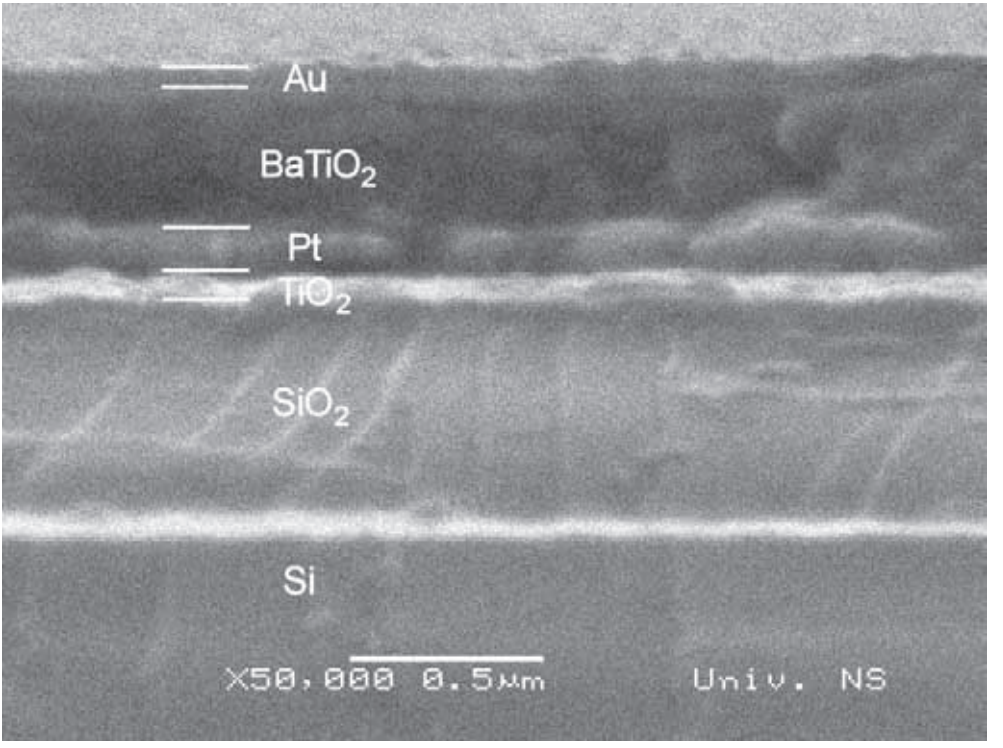

Figure 2. SEM micrograph of barium titanate based thin film (cross section) designed for tunable measurements.

Synthesis, Structure, Morphology and Properties of Biphasic $ZnO–ZnMn_2O_4$

Lidija Radovanović[1], Predrag Vulić[2], Željko Radovanović[1], Bojana Balanč[1], Bojana Simović[3], Ivana Zeković[4], Miroslav Dramićanin[4] and Jelena Rogan[5]

[1] *Innovation Center of the Faculty of Technology and Metallurgy, University of Belgrade, Belgrade, Serbia.*
[2] *Faculty of Mining and Geology, Department of Crystallography, Petrology and Geochemistry, University of Belgrade, Belgrade, Serbia.*
[3] *Institute for Multidisciplinary Research, University of Belgrade, Belgrade, Serbia.*
[4] *Vinča Institute of Nuclear Sciences, University of Belgrade, Belgrade, Serbia.*
[5] *Faculty of Technology and Metallurgy, Department of General and Inorganic Chemistry, University of Belgrade, Belgrade, Serbia.*

Transition metal oxides are important materials that have found many applications, as capacitors, sensors or in energy storage [1]. Synthesis of these compounds has been realized by various methods, such as hydro(solvo)thermal synthesis, precipitation, microwave synthesis or sol-gel synthesis [2]. Recently, the thermolysis of coordination compounds as precursors has been considered as a new approach in obtaining functional nanosized materials. [3]. In this way, by selecting the proper precursor, it is possible to control the phase composition, morphology and particle size of a resulting material [3].

The biphasic powder composed of ZnO (zincite) and $ZnMn_2O_4$ (hetaerolite), (**I**) has been obtained by thermolysis of bimetallic complex $[MnZn_2(dipya)_3(tpht)_3(H_2O)_4]\cdot 2H_2O$ (dipya = 2,2'-dipyridylamine, tpht = dianion of 1,4-benzenedicarboxylic acid) at 450 °C during 1 h in air atmosphere. Scanning Electron Microscopy (SEM) was used to investigate the morphology of **I** (Figure 1). It can be observed that the morphology consists of deformed spherical grains of ZnO with an average diameter of 67 nm and elliptical grains of hetaerolite whose average diameter and length were 156 and 290 nm, respectively. The X-ray powder diffraction (XRPD) was applied to investigate the structure of **I**. In Figure 2 two-phase Rietveld refinement

pattern of **I** is presented (ZnO to $ZnMn_2O_4$ phase-ratio of 62:38 wt. %). The main crystallographic data and Rietveld refinement parameters for ZnO phase are: hexagonal, space group $P6_3mc$, a = 3.2574(1), c = 5.2175(2) Å, V = 47.945(3) Å^3; for $ZnMn_2O_4$ phase are: tetragonal, space group $I4_1/amd$, a = 5.7299(3), c = 9.3000(8) Å, V = 305.34(3) Å^3; R_{wp} = 4.80 %, R_p = 3.82 %, R_{exp} = 3.80 % and χ^2 = 1.5960. UV-Vis-NIR absorption spectrum was measured in order to investigate the direct band gap (E_g) of **I**. Due to the existence of two phases in **I**, two different E_g values of 2.4 and 3.3 eV for $ZnMn_2O_4$ and ZnO phase, respectively, were determined using Kubelka-Munk function. The mean size, polydispersity index (PDI) and zeta potential of spherical grains were measured using Zetasizer Nano Series, Nano ZS. The mean size was 418.6±53.1 nm while PDI value was found to be 0.354±0.099. Relatively high values of PDI and low apostate value of zeta potential (–6.55 mV) are indications of incipient instability of colloidal dispersion of **I**, probably due to the formation of agglomerates [4, 5]. Photoluminescence measurements were carried out at room temperature on Fluorolog-3 Model FL3-221 spectrofluorimeter system upon excitation at 350 nm, in order to study the optical properties of **I**. This analysis revealed one band centred at 422 nm in the blue region of the visible part of the spectrum, which can possibly be associated with defects in the crystal structure of the ZnO phase [6].

References:

[1] C Yuan *et al*, Angewandte Chemie International Edition **53** (2014), 1488.
[2] CNR Rao and B Raveau in "Transition Metal Oxides: Structure, Properties, and Synthesis of Ceramic Oxides" 2nd edition (WILEY-VCH, New York).
[3] MY Masoomi and A Morsali, Coordination Chemistry Reviews **256** (2012), 2921.
[4] R Greenwood and K Kendall, Journal of the European Ceramic Society **19** (1999), 479.
[5] M Staiger *et al*, Journal of Dispersion Science and Technology **23** (2002), 619.
[6] H Zeng *et al*, Advanced Functional Materials **20** (2010), 561.
[7] The authors acknowledge funding from the Ministry of Education, Science and Technological Development of the Republic of Serbia, Grant Number III45007.

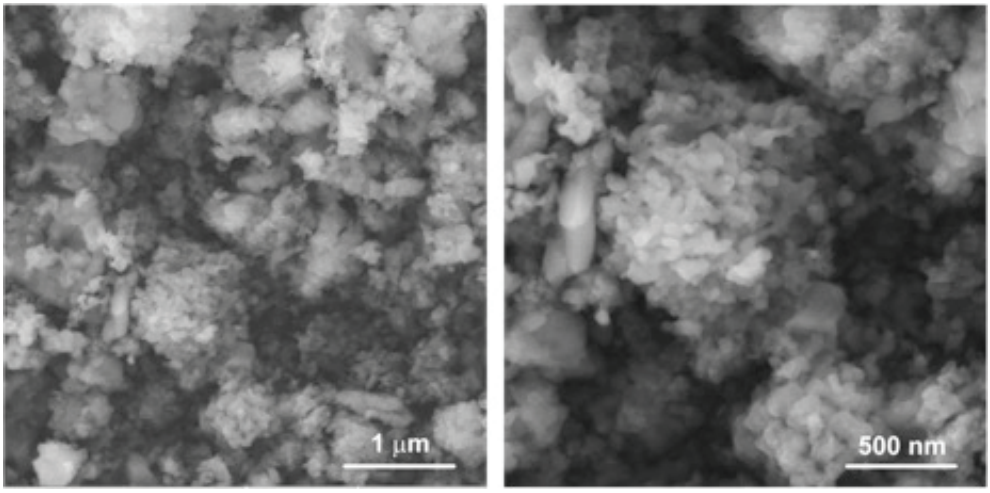

Figure 1. SEM images of **I**.

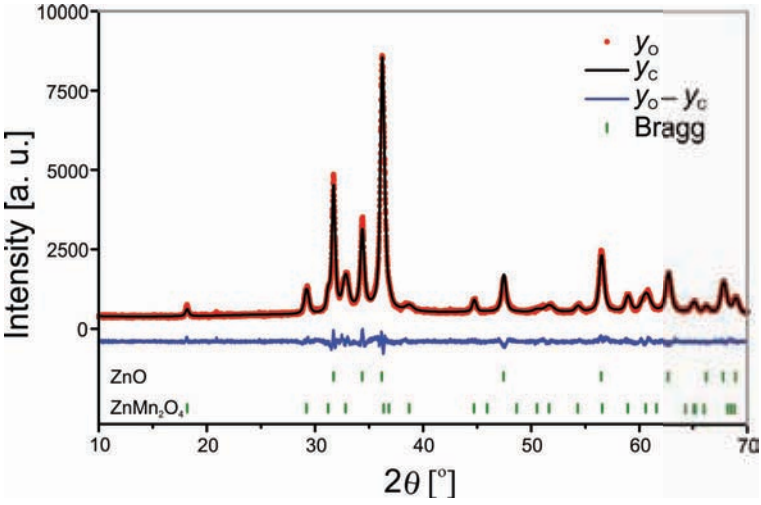

Figure 2. Rietveld refinement pattern of **I**.

Electron Microscopy Characterization of TiO_2 Nanotubes Sensitized with CdS Quantum Dots

Andjelika Bjelajac[1], Rada Petrović[2], Veljko Djokic[2], Kassioge Dembele[3], Simona Moldovan[3,4], Ovidiu Ersen[3], Gabriel Socol[5], Ion N. Mihailescu[5], Djordje Janaćković[2]

[1] *University of Belgrade, Innovation center of Faculty of Technology and Metallurgy, Karnegijeva 4, 11000 Belgrade, Serbia*

[2] *University of Belgrade, Faculty of Technology and Metallurgy, Karnegijeva 4, 11000 Belgrade, Serbia*

[3] *Institut de Physique et Chimie des Materiaux de Strasbourg, UMR 7504CNRS - Université de Strasbourg, 23 rue du Loess, BP 43, 67037 Strasbourg cedex 02, France*

[4] *Groupe de Physique des Matériaux UMR CNRS 6634, Université de Rouen, INSA Rouen, Avenue de l'Université – BP12, 76801 Saint Etienne du Rouvray, France*

[5] *National Institute for Lasers, Plasma, and Radiation Physics, Lasers Department, «Laser-Surface-Plasma Interactions» Laboratory, PO Box MG-54, RO-77125, Magurele, Ilfov, Romania*

Nanotechnology serves well in terms of obtaining the materials of required property. However it needs to be accompanied by an adequate technique that enables the characterization of nanostructures. Electron microscopy can provide the insight into the structure of nanosized materials. One of the materials whose nanosizing proved effective in enhancement of its feature is titanium dioxide (TiO_2). Herein, field emission electron microscopy (FESEM) was used to analyse the morphology of TiO_2 films supported on fluorine doped tin oxide (FTO) glass. The films were obtained by anodization of titanium films sputtered on FTO until reaching total transparency [1]. Next step was annealing of the films in air at 450 °C to induce the crystallization of TiO_2 [2]. Such annealing did not cause any morphological change of TiO_2 film [1]. Thus, Fig. 1 gives an overview of the annealed films structure. The obtained films consisted of highly ordered ~3.6 μm long and ~60 nm wide TiO_2 nanotubes (NTs). The open porosity was a requirement for further deposition of CdS quantum dots (QDs). The aim of CdS deposition is to enhance the absorption properties of TiO_2 films that can be used as photoanodes in QDs sensitized solar cells [3].

The deposition was performed by immersing the TiO_2 films in CdS sol. CdS QDs were synthetized using mercapto-silane (MS) that enabled stabilization of the CdS sol preventing the agglomeration and preserving the quantum effect of the CdS nanoparticles. What is more, MS served as a binding reagent to TiO_2 surface due to its bifunctionality [4].

Transmission electron microscopy (TEM) was used for characterization of the CdS/TiO_2 nanocomposites. Fig. 2 shows typical scanning TEM micrographs of the film's fragment obtained by scratching the film's surface with a diamond needle. By observing the images, the presence of ~ 5 nm sized nanoparticles within the NTs is evident. Using high resolution TEM it was possible to measure the interplanar distance of the detected particles and also of TiO_2 nanotube. By comparing the values to those of the characteristic for CdS and TiO_2, it can be concluded that TiO_2 consists of anatase phase, whereas CdS nanoparticles show to be both in cubic and hexagonal phase. This study proved that electron microscopy is a powerful method for analysing the structure of NTs/nanoparticles composite. [5]

References:

[1] A Bjelajac *et al*, Digest Journal of Nanomaterials and Biostructures **10** (2015), 1411-1418.
[2] DAH Hanaor and C. C. Sorrell, Journal of Materials Science **46** (2011), 855–874.
[3] H Wang *et al*, J. Phys. Chem. C **114** (2010), 16451-16455.
[4] A Bjelajac *et al*, Ceramics International **41** (2015), 7048–7053.
[5] The Serbian authors acknowledge with thanks the financial support of the Ministry of Education, Science and Technological Development, Republic of Serbia through the Project III 45019. The French Institute in Belgrade supported the research done in IPCMS. The Romanian authors acknowledge with thanks the partial financial support of this work in the frame of the contract POC-G 135/23.09.2016. M.V. was supported by Czech Ministry of Education, Youth and Sports (grant LG15050).

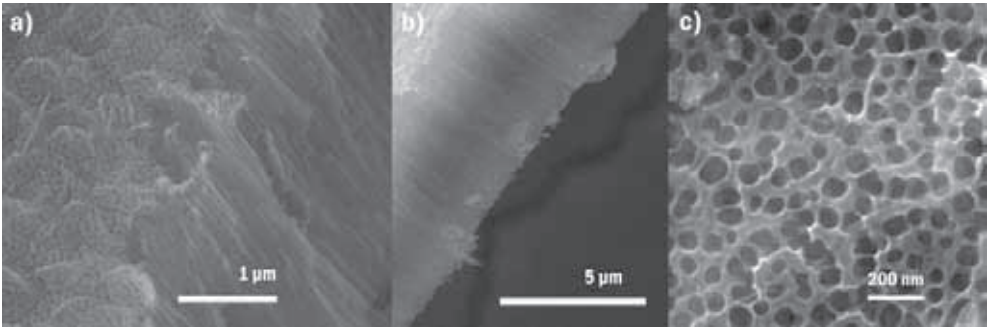

Figure 1. SEM micrographs of the annealed TiO_2 film: a) side view showing the nanotubular structure, b) lateral view revealing the thickness of the film, c) top view enabling the measurement of the pore diameter

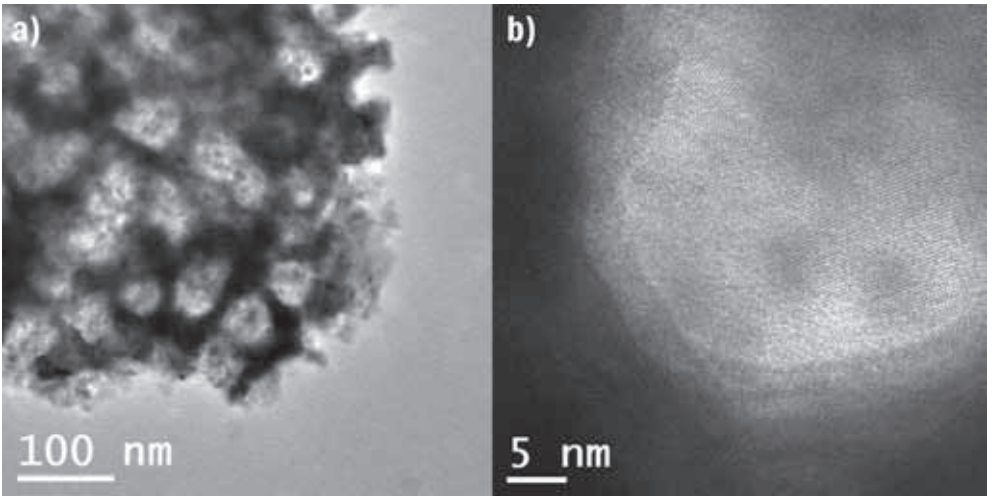

Figure 2. a) STEM and b) HRTEM micrographs of the TiO_2/CdS composite.

Cathodically Protonated TiO_2 Nanotube Arrays Decorated with Pd Nanoparticles as Highly Efficient and Stable Electrocatalysts for the Hydrogen Evolution Reaction

Uroš Lačnjevac[1], Rastko Vasilić[2], Tomasz Tokarski[3], Grzegorz Cios[3], Piotr Żabiński[4], Nevenka Elezović[1] and Nedeljko Krstajić[5]

[1] *Institute for Multidisciplinary Research, University of Belgrade, Kneza Višeslava 1, 11030 Belgrade, Serbia*
[2] *Faculty of Physics, University of Belgrade, Studentski trg 12-16, 11000 Belgrade, Serbia*
[3] *Academic Centre for Materials and Nanotechnology, AGH University of Science and Technology, al. A. Mickiewicza 30, 30-059 Krakow, Poland*
[4] *Faculty of Non-Ferrous Metals, AGH University of Science and Technology, al. A. Mickiewicza 30, 30-059 Krakow, Poland*
[5] *Faculty of Technology and Metallurgy, University of Belgrade, Karnegijeva 4, 11000 Belgrade, Serbia*

The expensive platinum group metals such as platinum and palladium are inevitable components of highly active cathodes for the hydrogen evolution reaction (HER) in acidic media. However, the Pt or Pd loading is still high, which prevents widespread commercialization of water splitting systems employing these cathodes. Hence, designing new synthesis methods for the nanocomposite HER catalysts and developing advanced supporting structures is very important for achieving low noble metal content at no cost in activity [1].

To address this critical issue, herein, we have introduced a novel and straightforward approach to deposit Pd nanoparticles (NPs) on the anodically formed TiO_2 nanotube array support (Pd@TNT). In the two-step synthesis procedure, air-annealed TNT arrays are first cathodically protonated (H-TNT) and then partially reoxidized by Pd(II) ions through a galvanic-displacement-type reaction in a $PdCl_2$ solution while being decorated with the disperse metallic Pd deposit [2]. Field emission scanning electron microscopy (FESEM) analyses reveal that the average tube lengths of the TNT structures prepared at anodization times of 30 and 80 min are 12.2 and 21.5 μm, respectively, while their pore diameter is about 100 nm. Backscatter electron

(BSE) FESEM imaging demonstrates that the TNT arrays preserve their open-pore nanostructure upon the deposition of Pd NPs (Fig. 1a). Scanning transmission electron microscopy high-angle annular dark-field (STEM HAADF) characterizations show that the size of the Pd NPs attached to the inner tube walls is not uniform, but distributed over a relatively wide range of 3–80 nm (Fig. 1b). The BSE FESEM/STEM HAADF analysis of the cross-section of Pd@TNT bulk films and thin membranes further reveals that the surface density of Pd NPs is the highest at the top surface, but gradually decreases towards the tube bottoms. The Pd content and the width of the Pd-populated zone in the Pd@TNT samples are found to critically depend on the average tube length.

The Pd@TNT composites display remarkable apparent and mass activity for the HER in 1 M $HClO_4$. The most active sample (Pd@TNT-80) containing only 12 μg cm^{-2} of Pd exhibits a lower HER overpotential at higher current densities than a commercial Pt/C catalyst (Fig. 2). More importantly, it also shows a negligible loss in activity during chronopotentiometric and potential cycling stability tests. The exceptional performance of the Pd@TNT cathodes is ascribed to the unique properties of the three-dimensional protonated TNT semiconducting structures that exhibit high conductivity in the cathodic direction and act as an interactive support for abundant Pd catalytic sites, while in the anodic direction they inhibit current passage and prevent the degradation of the Pd catalyst.

References:

[1] C Ray *et al*, Chemical Communications **52** (2016), 6095.
[2] U Lačnjevac *et al*, Nano Energy **47** (2018), 527.
[3] This work was financially supported by the Ministry of Education, Science and Technological Development of the Republic of Serbia through the project No. 172054. The networking support by COST action MP1407 is greatly appreciated. The authors would also like to express their gratitude to Vesna Vukojević and Prof. Dragan Manojlović of Faculty of Chemistry, Department of Analytical Chemistry, University of Belgrade, for performing ICP analysis.

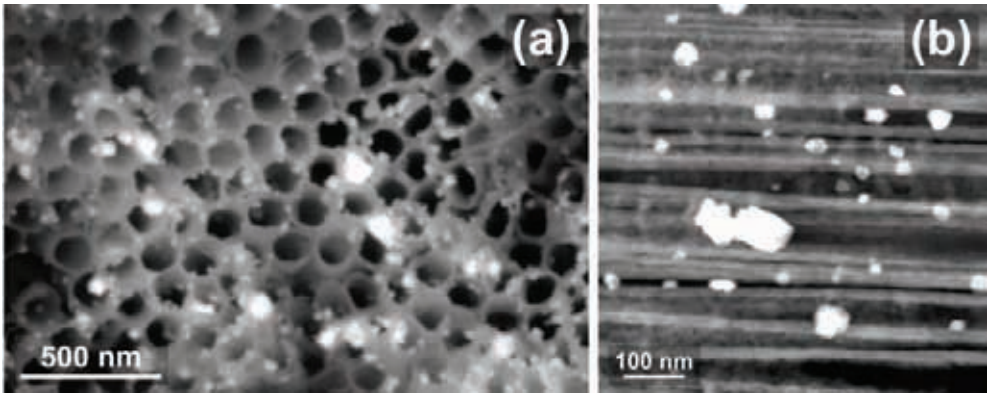

Figure 1. (a) BSE FESEM image of the top surface of the Pd@TNT structures; (b) HAADF STEM image of Pd NPs attached to the inner tube walls.

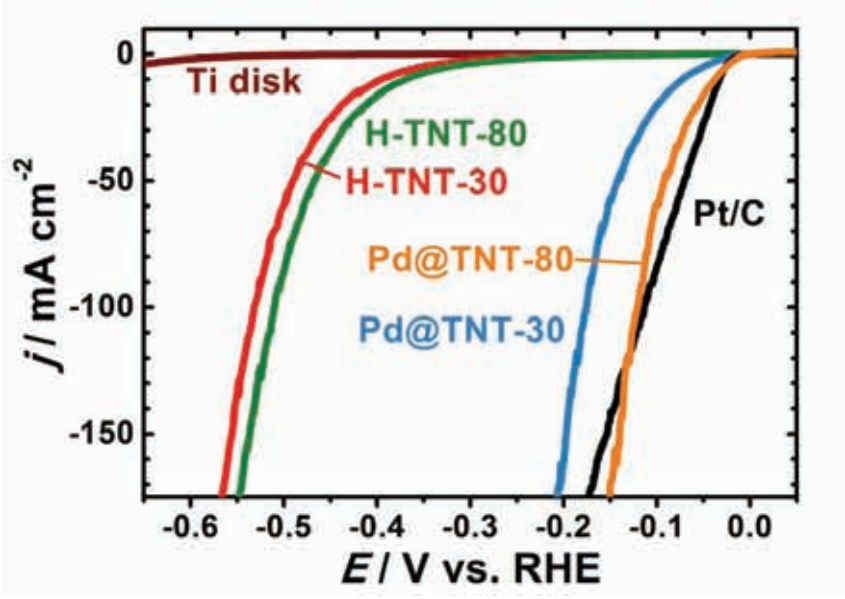

Figure 2. Polarization curves for the HER in 1 M $HClO_4$ recorded at a sweep rate of 1 mV s^{-1} on various samples (marked in the figure).

Elemental Mapping in (Alpha$_2$/O)-Phase Lamellae of a Gamma-TiAl Alloy

Heike Gabrisch[1], Tobias Krekeler[2], Uwe Lorenz[1], Marcus Willi Rackel[1], Martin Ritter[2], Florian Pyczak[1] and Andreas Stark[1]

[1] *Helmholtz-Zentrum Geesthacht, Department of Metal Physics, Max-Planck-Str.1, 21502 Geesthacht, Germany*

[2] *Technische Universität Hamburg, Betriebseinheit Elektronenmikroskopie BEEM, Eißendorfer Straße 42, 21073 Hamburg, Germany*

Gamma-Titanium aluminides are promising structural light-weight materials for applications in aircraft engines. In addition to the main constituents, Ti and Al, they often contain β-stabilizing elements for improved creep strength and oxidation resistance [1].

It has been found that the addition of Nb to γ-Ti-aluminides induces the formation of the orthorhombic O-phase in the alloy's microstructure. While the O-phase has been known in Nb-rich α_2-based Ti-aluminides since the late 1980ies the finding in γ-based alloys is new [2]. Using in-situ High Energy X-Ray diffraction we followed the formation of the O-phase from the parent α_2 phase during annealing at 550-650°C [3]. Transmission electron microscopy (TEM) imaging showed that the O-phase is located within the α_2 lamellae of lamellar (α_2+γ)-colonies. The orthorhombic distortion of the hexagonal lattice can be observed directly in atomically resolved images [4]. A point of discussion is the role of niobium in the formation of the O-phase. Here we compare the microstructures obtained after annealing for different durations to explore whether Nb agglomeration precedes the O-phase formation.

The alloy Ti-42Al-8.5Nb was produced by powder metallurgy starting from pure elements [5] and was annealed for 8 h and 168 h at 550 °C to form the orthorhombic phase. Specimens for TEM investigations were prepared by standard methods [4]. High-angle annular dark-field (HAADF) imaging was performed at the Helmholtz Zentrum Geesthacht with the FEI-Titan 80-300kV TEM operated at 300kV. Atomic resolution HAADF-STEM imaging was conducted at the CNMS, at Oakridge National Laboratory using the Nion UltraSTEM 100 dedicated aberration-corrected

STEM at 100 kV. Elemental energy dispersive x-ray spectroscopy (EDX) mapping was performed at the BEEM facility of the Technical University Hamburg using a SuperX detector system attached to an FEI-Talos F200XTEM operated at 200kV with a probe current of 1 nA.

A summary of the results obtained after annealing for 168 h is given in Fig. 1. Fig. 1a illustrates the orientation relationship between parallel close-packed planes and directions of phases in the (α_2+γ) colonies. The bright field image in Fig. 1b shows a section of a (α_2+γ) colony in α_2-[0001] orientation. A striking feature within α_2/O-phase laths is the appearance of bright and dark facets that are differently tilted regions of the crystal lattice. Imaging under z-contrast condition (STEM mode, L=195mm) shows that a network of dark lines on bright background covers the facets across facet borders (Fig. 1c). Elemental maps taken from a smaller section of such a region (95 x 95 nm) demonstrate that the dark lines in Fig. 1c correspond to increased Ti and Al content whereas the brighter regions have a higher niobium concentration. For illustration, the maps of Nb and Ti are shown in Figs. 1d and e. The effect for Al is weaker but identical to that of Ti (not shown). Fig. 1f shows a STEM image of the same specimen (550 °C, 1 week) at atomic resolution where the orthorhombic distortion of the lattice is recognized within the brighter patches. It can be seen that the lattice is less distorted in the darker regions between bright patches. Fig. 1f is also an example for the two O-phase domains where the lattice is distorted along two different <11-20> directions of the hexagonal lattice of the parent phase α_2 (indicated by arrows).

We compared these findings to the results obtained from the sample annealed for 8 h. In both annealing states, substantial amounts of the O-phase are present within the alloy's microstructure but elemental segregation is only observed after the longer annealing time. These findings indicate that Nb diffusion only sets in after the O-phase has been formed.

References:

[1] F Appel, M Oehring, and R Wagner, Intermetallics **8** (2000), 1283-1312.
[2] D Banerjee *et al*, Acta metall. **36** (1988), 871-882.
[3] MW Rackel *et al*, Acta Materialia **121** (2016), 343-351.
[4] H Gabrisch *et al*, Acta Materialia **135** (2017), 304- 313.
[5] R Gerling, H Clemens and FP Schimansky, Advanced Engineering Materials **6** (2004), 23-38.
[6] Atomic resolution HAADF STEM imaging was conducted using the Nion UltraSTEM 100 (U100) dedicated aberration-corrected STEM at the Center for Nanophase Materials Sciences, which is a DOE Office of Science User Facility.

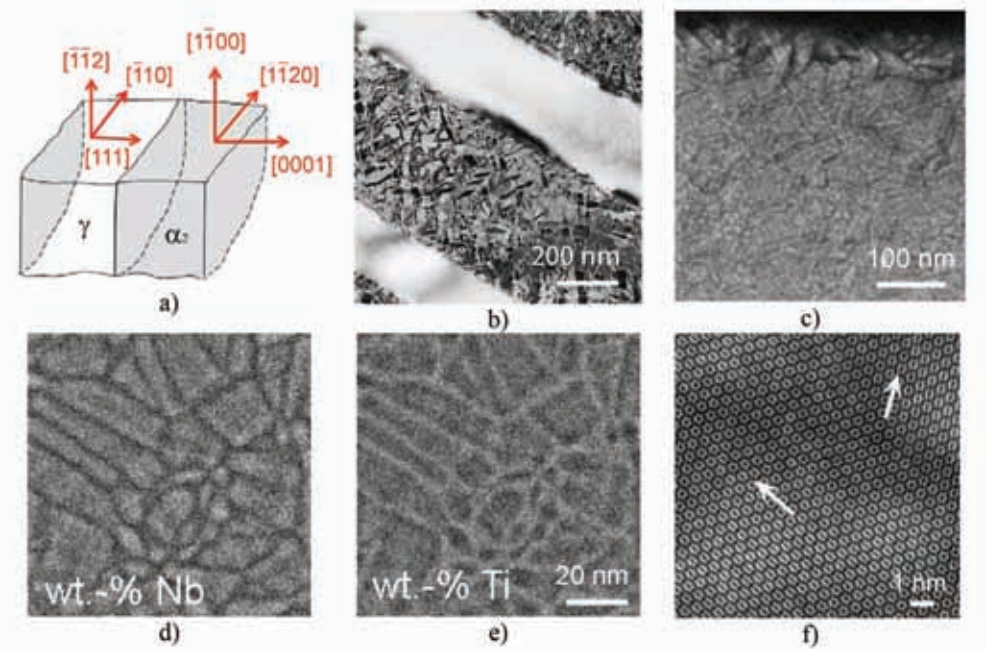

Figure 1. Images of specimen annealed for 168 h at 550°C. a) Orientation relationship between the α_2 and γ phases in lamellar colonies. b) Lamellar colony in the α_2-[0001] viewing direction. The bright phase is γ, the darker lamellae are a mixture of the α_2 and O-phase. c) HAADF image of the α_2/O-phase region showing details within the α_2/O-phase lamellae. d) and e) EDX maps using the Nb-L and Ti-K signals. f) STEM image at atomic resolution illustrating orthorhombic distortion in the brighter regions of STEM image.

Various Structures of ZnO Grown by Vapor - Liquid - Solid Method

Danilo D. Kisić, Miloš T. Nenadović, Jelena M. Potočnik and Zlatko Lj. Rakočević

University of Belgrade, Vinča Institute of Nuclear Sciences, Laboratory of Atomic Physics, Belgrade, Serbia

ZnO is one of the most studied semiconducting materials. It is a wide band gap semiconductor (3.37 eV), with wurtzite crystal structure [1,2]. ZnO can be synthesized into a number of different forms, such as nanowires, nanorods, nanoflowers, nanobelts [3-5]. A number of studies proved strong correlation between the materials properties and its structure. In this study, ZnO structures grown by Vapor-Liquid-Solid (VLS) method were analyzed by field emission scanning electron microscopy (FESEM), energy dispersive X-ray spectroscopy (EDS) and X-ray spectroscopy (XPS).

ZnO nanorods were synthesized by chemical vapour deposition process using the vapour liquid solid mechanism. The deposition was performed on MTI GSL 1600X furnace, home adapted for VLS deposition. ZnO nanorods were grown on monocrystal silicon substrate of the (100) orientation, coated with 5 nm gold layer. A zinc-oxide powder was used as a deposition source, positioned in the furnace heating zone at 1350 °C. Argon was used as a carrier gas, and the flow rate was set to 50 standard cubic centimeters per minute (sccm). System pressure was set to 0.1 mbar during the deposition. Substrates were positioned at 5 different distances from the source materials, starting with 17 cm, with a step of 1 cm. From the FESEM images (Fig 1.), we can see that largest rod structures were synthesized in the first position (Fig. 1a), i.e. on the substrate closest to the source material. The diameters of the rods are in the range from 1 μm to 4 μm. In the second position (Fig. 1b), the structures merged during growth, so that the structure appears as a layer with irregular boundaries. In the third position (Fig. 1c), the micro rods and nanorods are partly merged, so that surface is comprised of large irregular structures from 2 μm to more than 8 μm in diameter. For the sample in position 4 (Fig. 1d), very dense irregular rod structures, from 700 nm to 900 nm in diameter are observable. In the

fifth position, quite regular hexagonal small scale nanorods were formed, although lateral sides of the nanorods are quite irregular. The diameters range from 70 nm to 100 nm. EDS analyses confirmed presence of Zinc, Oxygen and Carbon for all five samples. The atomic concentrations of Zn and O are almost equal for the first 4 samples, while for the 5th sample, atomic concentration of O is much higher. For the 5th sample, Si was also detected, which suggests that layer is very thin, so that Si as the substrate was detectable.

ZnO structures were grown by VLS method. The substrates were positioned at 5 different distances from the source material. FESEM analysis has shown that ZnO structures formed depend on the distance from the source material. EDS quantitative analysis confirmed presence of Zn and O, in almost equal atomic concentrations for all samples except for the 5th. In the case of 5th sample, O concentration was much higher than that of Zn. This could be the case because of the small nanostructures, so that the surface where oxygen is always in excess and defects are denser makes much higher influence on the EDS spectrum.

References:

[1] T Kiyoshi, Y Akihiko and Sandhu Adarsh in “Wide bandgap semiconductors: fundamental properties and modern photonic and electronic devices” (Springer, New York), p. 357.
[2] Ü Özgür *et al*, Journal of Applied Physics **98** (2005), 041301.
[3] ZL Wang, Mater Today **7** (2004), 26.
[4] ZL Wang, Materials Science Engineering R **64** (2009), 33.
[5] Y Wang *et al*, Separation and Purification Technology **62** (2008), 727.

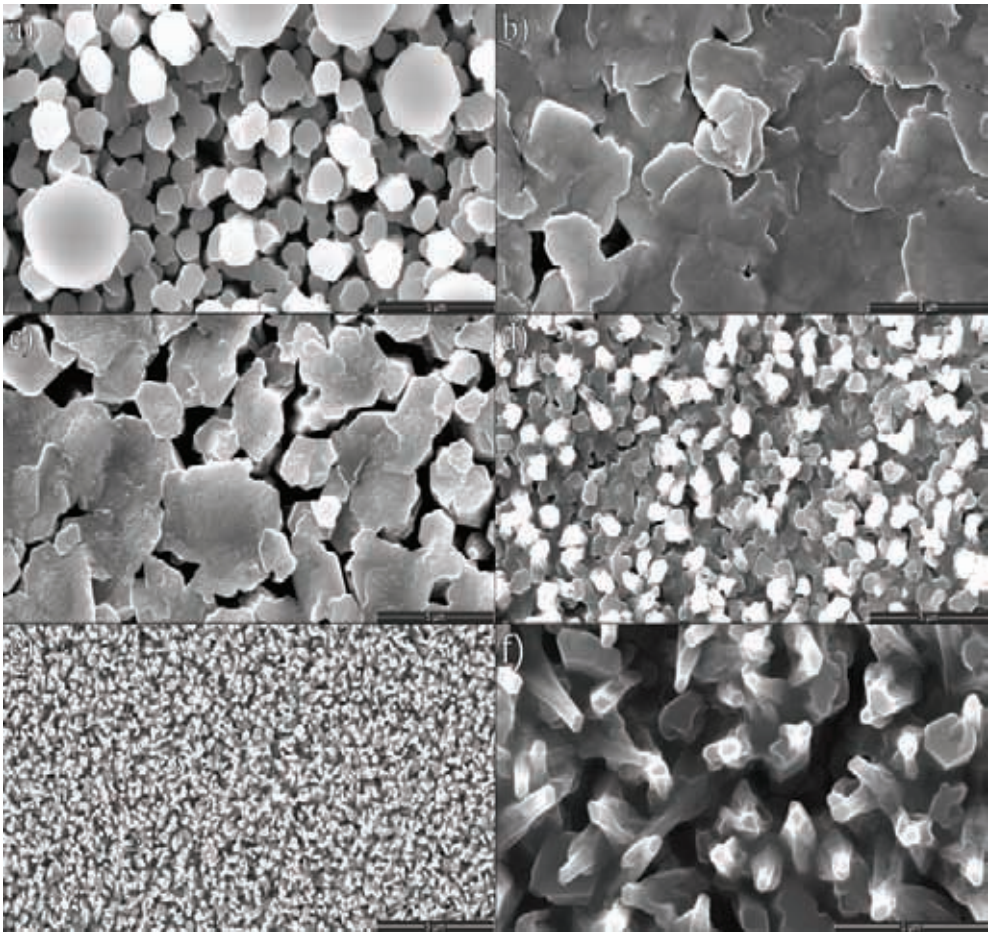

Figure 1. FESEM micrographs of ZnO structures grown by VLS method; a) sample in position 1; b) sample in position 2 c) sample in position 3 d) sample in position 4 e) sample in position 5 f) sample in position 5 - higher magnification.

Influence of Generation Time on Optical Properties of Gold Nanoparticles

Nataša Nastić, Jaroslava Švarc-Gajić and Zorica Stojanović

Department of Applied and Engineering Chemistry, Faculty of Technology, University of Novi Sad, Novi Sad, Serbia

The interest in gold nanoparticles initiated numerous research related to their synthesis, physical properties, and their application in different areas [1,2]. Nowadays, colloidal gold is irreplaceable in chemical and biological research, studies on cancer, catalysis, and technology of electrical and optical devices [3]. Synthesis of gold nanoparticles often involves toxic and expensive physical and chemical methods.

In this study, gold nanoparticles were generated in a house-made electric arc discharge device. The electrodes were made of gold (99.9999%) wire (j=1 mm). The electric arc discharge system consisted of a control system which maintained a constant distance between the electrodes (2 mm), a power supply system and amperometer which controlled the arc discharge parameters, halogen bulbs used as resistors, a glass container with deionized water and a magnetic stirrer. Gold nanoparticles were generated by electric arc in 0.2 mM HCl solution. Initial voltage and current were in the range 40–70 V and 20±5 A, respectively. The current intensity was maintained constant during generation step, while increasing the power accordingly. During arc discharge the surface layer of gold electrodes evaporated and condensed in the water, creating a gold suspension. Gold disperse systems obtained at different generation times (5-150 min) were characterised by photometric and spectrophotometric techniques. Transmission spectra were recorded by photoeletric photometer using four different filters, whereas absorption spectra were recorded using spectophotometer.

With increase in generation time the intensity of color of gold disperse systems changed from light purple (5 min) to dark red (150 min) (Fig. 1) indicating increase in concentration, but also different particle sizes. The color of colloidal gold systems depends both on concentration and the size of nanoparticles. With increase in gold concentration (through increase in generation time) color became darker.

Spectrophotometric and photometric characterisation of gold suspensions provided indirect insight in particle size distribution and gold content. Absorption spectra was measured by using four different filters and, as expected, the highest absorptions in the range 510-540 nm were measured when using green and blue filters, as complement to red-colored gold disperse systems. With increase in generation time absorption maximum shifted from 534 to 527 nm indicating the change in particle size distribution (Fig. 2). The size of particles has major influence on bioactivity and properties of gold nanoparticles, thus it is recommended to conduct detailed particle size distribution characterisation, as well as quantification for more thorough characterisation of nano gold disperse systems.

References:

[1] JK Lung *et al*, Journal of Alloys and Compounds **434** (2007), p. 655-58.

[2] BN Khlebtsov and NG Khlebtsov, Colloidal Journal **73** (2011), p. 118-27.

[3] JF Hainfeld *et al*, Journal of Pharmacy and Pharmacology **60** (2008), p. 977-85.

[4] The authors acknowledge funding from the project TR 31014 financially supported by the Serbian Ministry of Education, Science and Technological Development.

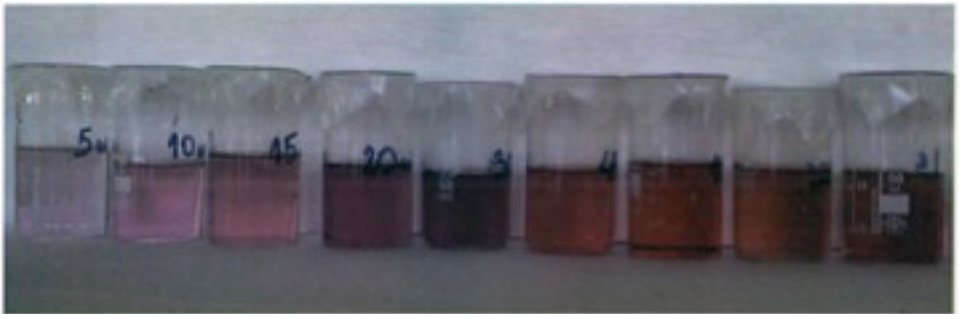

Figure 1. Gold disperse systems obtained at different generation time (5-150 min).

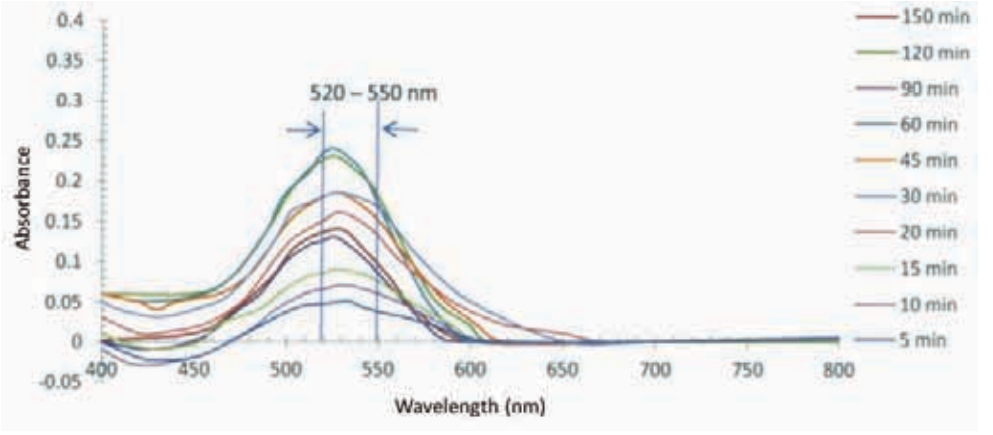

Figure 2. Absorption spectra of gold disperse systems obtained at different generation time.

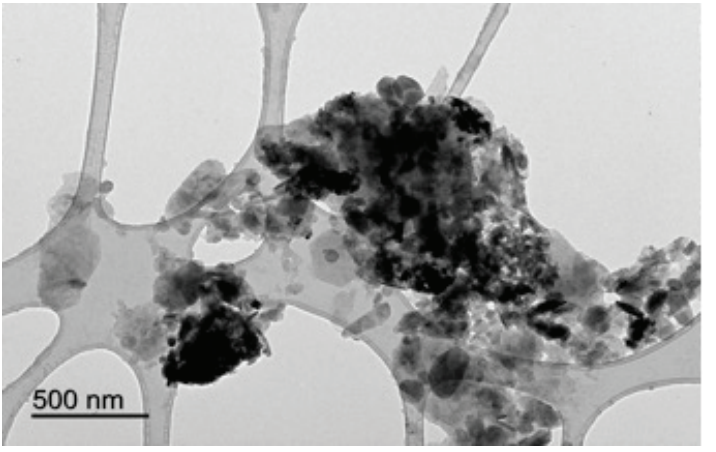

Figure 3. TEM micrograph of colloidal gold nanoparticles.

Problems in Obtaining High-Density, Pure-Phase $BiFeO_3$ Ceramics

Nikola I. Ilić, Jelena D. Bobić, Adis S. Džunuzović, Mirjana M. Vijatović Petrović and Biljana D. Stojanović

Institute for Multidisciplinary Research, University of Belgrade, Materials Science Department, Belgrade, Serbia

Multiferroic materials exhibit at least two of the so-called ferroic properties (ferroelectric, (anti)ferromagnetic and ferroelastic) in the same time. They are very interesting from the theoretical point of view because of a different nature of those properties, but coupling between the properties opens up huge possibilities for application as magnetoresistors, memory devices, sensors and many other devices [1].

Being ferroelectric up to 830 °C and antiferromagnetic (weakly ferromagnetic) up to 370 °C, bismuth ferrite ($BiFeO_3$) is one of the very few room-temperature single-phase multiferroic materials and one of the most studied ceramic materials in the last two decades. $BiFeO_3$ has also good potential to be used as a pigment, catalyst, photocatalyst or solar cell material [1,2].

However, because of specific obstacles in obtaining pure, dense and highly resistive ceramics, harnessing of those properties is still far from being achieved and the possibility of its application as a multiferroic material is arguable. High volatility of bismuth above 800 °C and thermodynamic instability of $BiFeO_3$ between 447 °C and 767 °C make the densification of $BiFeO_3$ ceramics very difficult, especially by conventional methods. High leakage currents in $BiFeO_3$ (originating mostly from oxygen and bismuth vacancies) disable ceramic samples to be polarized and to exhibit ferroelectric properties. Spiral structure of magnetic moments lowers the coupling between ferroelectric and magnetic orders [3,4].

$BiFeO_3$ ceramic materials presented in this study were synthesized by auto-combustion method with idea to lower the temperature needed for effective sintering in order to prevent volatilisation and improve the density and phase composition. Auto-combustion is a type of sol-gel route which enables high homogeneity in solutions stabilized by organic compounds, which oxidize vigorously producing

the ash powders as a wanted product. Because of such fast reaction, the defects are incorporated into structure enabling solid state sintering to take place at lower temperatures and more quickly. Presented microstructures are illustrating the usual problems that occur during the synthesis of powders and processing of ceramic materials. Powders tend to agglomerate, and although the agglomerates can be destroyed by milling (Figure 1), this process often disturbs the phase composition of ceramics synthesized from the milled powders. Because of a wide range of temperatures at which bismuth evaporates and secondary phases form, it is important to conduct heating and cooling of samples very fast (quenching), but even this way some secondary phases are formed (Figure 2) and densification is not complete (Figure 3).

The study presents the evolution of the mentioned problems during attempts to overcome them by modification of the synthesis conditions, by using different treatments of the powders and by modification of the sintering process.

References:

[1] W Eerenstein, ND Mathur and JF Scott, Nature **442** (2006), 759.
[2] G Catalan, JF Scott, Advanced Materials **21** (2009), 2463.
[3] MS Bernardo *et al*, Journal of the European Ceramic Society **31** (2011), 3047.
[4] T Rojac *et al*, Journal of the American Ceramic Society **97** (2014), 1993.
[5] The authors would like to acknowledge the financial support of the Ministry of Education, Science and Technological Development of the Republic of Serbia, project III 45021.

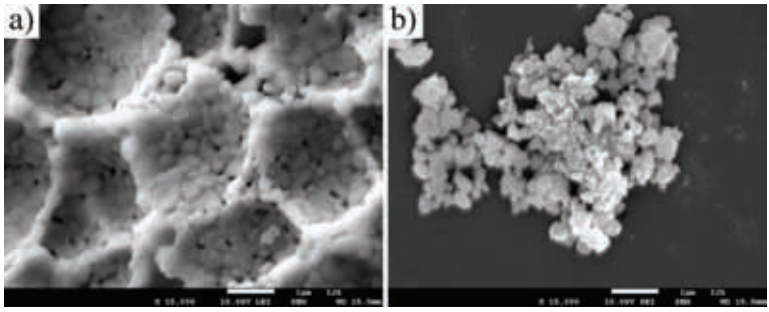

Figure 1. Microstructure of as prepared (a) and milled (b) $BiFeO_3$ powder.

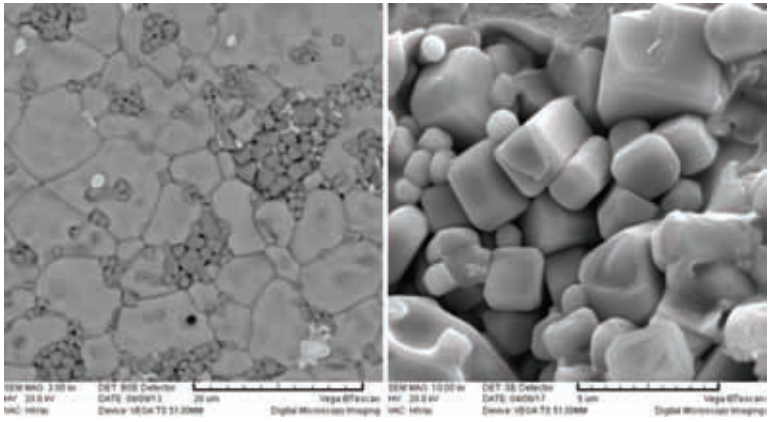

Figure 2. Secondary phases in $BiFeO_3$ ceramic samples.

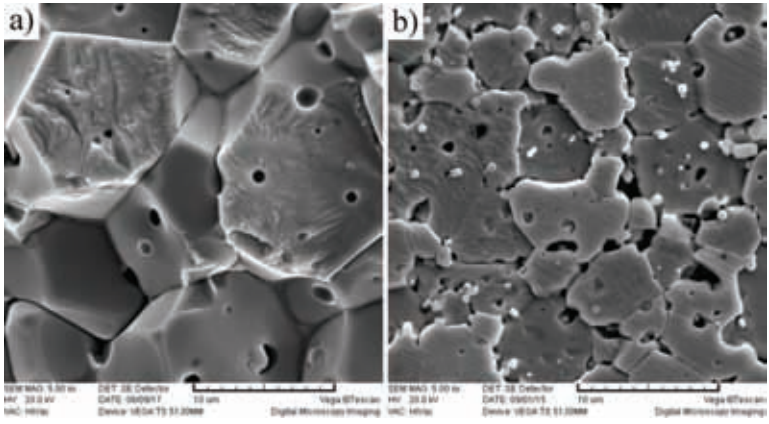

Figure 3. Porosity in $BiFeO_3$ ceramic samples: a) fracture, b) polished and chemically etched surface.

Synthesis, Calcination and Characterization of $CoMoO_4$ Nanopowders by GNP Method

Milena Rosić[1], Dejan Zagorac[1], Maria Čebela[1], Dragana Jordanov[1], Jelena Zagorac[1], Jelena Luković[1], Aleksandra Zarubica[2] and Branko Matović[1]

[1] *Institute for Nuclear Sciences, Centre of Excellence-CextremeLab Vinca, University of Belgrade, Belgrade, Serbia*

[2] *Department of Chemistry, Faculty of Science and Mathematics, University of Niš, Višegradska 33, 18000 Niš, Serbia*

Molybdates are of interest in various applications, e.g. catalysts [1], catalyst precursors [2], optical and electrode materials [3,4] and supercapacitors [5,6]. Synthesizing nanopowders of $CoMoO_4$ could improve their properties thereof, since; various properties of materials differ from bulk to nanostructure. Metal molybdate nanostructures are well suited for energy-storage devices because they are environmentally safe and exhibit enhanced performance compared to their corresponding oxides. Nanosized $CoMoO_4$ powder was synthesized by glycine nitrate procedure (GNP). We focused on the chemical synthesis method for producing nanoparticles in a simple, quick, and inexpensive way, the method which effectively in the first step of the preparative process produces nanosized metal molybdate powders. The synthesized samples were investigated by DTA, X-ray diffraction (XRD), Fourier transform infrared (FT-IR) spectra, Field emission scanning electron microscopy (FESEM), and nitrogen adsorption method. The photocatalytic activity of obtained $CoMoO_4$ nanopowders was estimated by the photocatalytic degradation of crystal violet in aqueous solution. This work has provided simple and effective method for controlling the composition and morphology of $CoMoO_4$ powders, which revealed a potential new approach in inorganic synthesis methodology. DTA curve for the synthesized powder of $CoMoO_4$ indicates formation of β-$CoMoO_4$ in the temperature range 360 to 416 °C and the possibility of forming α-$CoMoO_4$ and polymorphic transition $\beta \rightarrow \alpha$ at 913 °C. XRD pattern of the obtained nanopowder shows that $CoMoO_4$ crystallizes in the monoclinic space group C2/m, No.12. Presence of single-phase α and β crystalline forms of the $CoMoO_4$ compound was confirmed by X-ray diffraction (XRD). Volumes of the unit cells of the two structural types

decrease with increasing temperature. The prepared $CoMoO_4$ nanopowder exhibited agglomeration tendency and it is characterized by inhomogeneous microstructure with partial allocations of grains and almost ordered shapes. The polyhedral grains of different sizes and plate-like crystals 3–47 nm in size, grown on irregular grains, are forming grape-like structure, with interstices and voids between them. A sponge-type morphology involving large numbers of irregular connected pores is attributed to the large amount/ volume of gases escaping out of the reaction mixture during the combustion. On the other hand, large individual spherical and polyhedral grains which are regular in shape are present. The observed grains have smooth and non-porous surfaces. The specific surface areas of all $CoMoO_4$ samples are within 15 and 24 $m^2 g^{-1}$ confirming mainly mesoporous structure. The above GNP method is technically simple, quick, and suitable for low-cost preparation of high-quality $CoMoO_4$ nanopowder of significant specific surface area. The photocatalytic testing of the $CoMoO_4$ nanopowders showed that these nanostructured materials can be promising solutions in photocatalytic processes oriented toward green chemistry and sustainable development. This stands especially for samples activated at higher temperatures probably due to their beneficial properties (particular single α-phase modification, large pore radius/diameter, great pore volume and acceptable specific surface area, typical arranged morphology and specific surface functional groups).

References:

[1] YJ Zhang, I Rodrıǵuez-Ramos and A Guerrero-Ruiz, Catal. Today **61** (2000), 377–382.
[2] R Kojima and K-I Aika, Appl. Catal. A—Gen. **215** (2001), 149–160.
[3] V Volkov *et al*, Chem. Mater. **17** (2005), 291–300.
[4] N Sharma *et al*, Chem. Mater. **16** (2004), 504–512.
[5] LQ Mai *et al*, Nat. Commun. **2** (2011), 381–385.
[6] GK Veerasubramani *et al*, Int. J. Hydrogen Energy **39** (2014), 5186–5193.

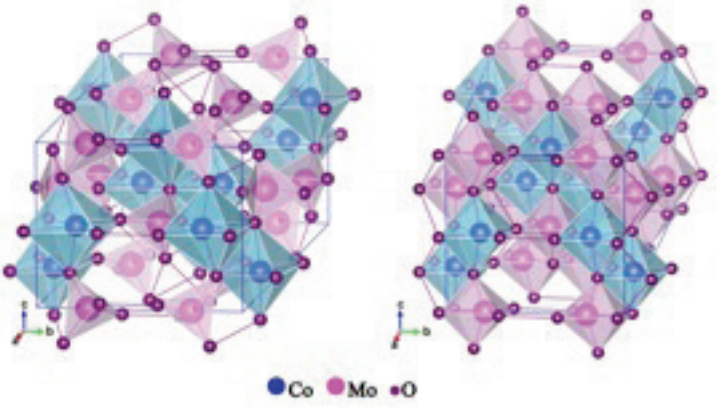

Figure 1. Structure of a) β-$CoMoO_4$ (synthesized and calcinated samples at 450 °C) and b) α-$CoMoO_4$ (samples at 1000 °C).

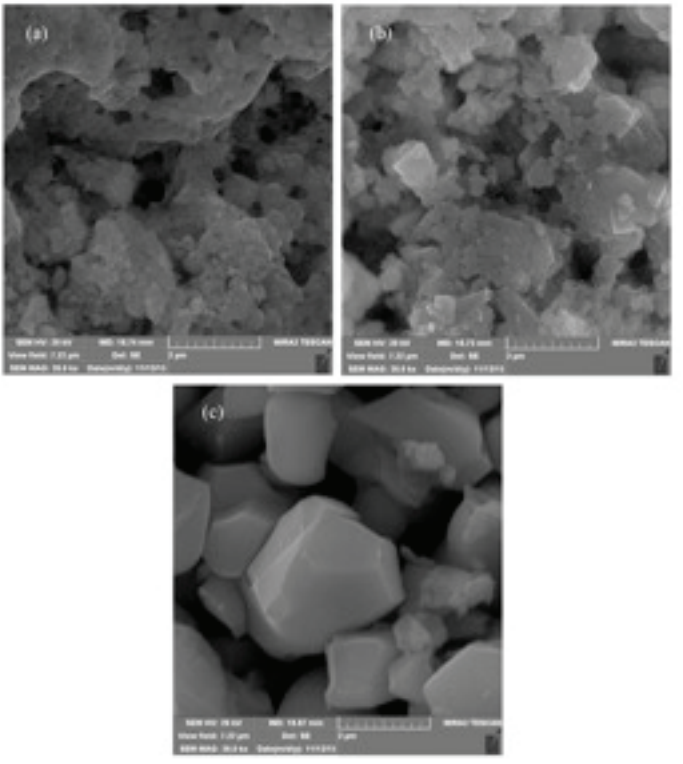

Figure 2. FESEM images of $CoMoO_4$ samples: a) as prepared; b) calcinated at 450 °C and c) calcinated at 1000 °C.

Polyacrilic Acid and Chitosan Assisted Solvothermal Synthesis of Up-converting $NaYF_4$: Yb,Er Particles

Marina Vuković[1], Ivana Dinić[1], Lidija Mančić[2], Marko Nikolić[3], Mihailo Rabasović[3] and Olivera Milošević[2]

[1] *Innovation Center of the Faculty of Chemistry, University of Belgrade, Serbia*
[2] *Institute of Technical Sciences of SASA, Belgrade, Serbia*
[3] *Photonic Center, Institute of Physics Belgrade, University of Belgrade, Belgrade, Serbia*

There is a growing interest for development of a facile and reproducible approach for the synthesis of biocompatible lanthanide doped up-converting nanoparticles (UCNPs) for deep tissue imaging and targeted drug delivery [1]. Synthesis of such particles is usually performed through the decomposition of organometallic compounds, followed either with a ligands exchange or with a biocompatible layer coating [2,3]. In this work, biocompatible $NaYF_4$:Yb,Er (17 mol% Yb; 3 mol% Er) nanoparticles were synthesized by one-pot hydrothermal processing with an assistance of chitosan (Ch) or *polyacrylic acid* (PAA). Obtained powders were analyzed by X-ray powder diffraction (XRPD, Bruker D8 Discovery), field emission scanning electron microscopy (FE-SEM, *Zeiss*, DSM 960), transmission electron microscopy (TEM, JEOL JEM 2010), Fourier transform infrared (FTIR, Thermo Scientific Nicolet 6700) and photoluminescence (PL, Spex Fluorolog with C31034 cooled photomultiplier) spectroscopy.

The results showed that although both powders crystallize in the same crystal arrangement (cubic, *Fm-3m*), particles size, shape and optical properties are dependent on the polymer used. Powder which synthesis was performed in the presence of Ch is composed from spherical, monodispersed particles which size is of about 120 nm, Fig.1a. TEM observation revealed coexistence of much smaller crystallites on the surface of these particles, Fig. 1b. On the other hand, PAA functionalized UCNPs were consisted of very thin foils (~6 nm) sized around 10 μm in both in-plane directions, Fig.1c. Degree of the UCNPs functionalization was investigated using FTIR analysis. The obtained results confirm the presence of corresponding

PAA or Ch functional groups on the UCNPs surface, indicating that these could be used in biomedical field. The up-conversion luminescent spectra of the synthesized particles demonstrated both, green emissions in the range of 520–550 nm (assigned to the $^2H_{11/2} \rightarrow {}^4I_{15/2}$ and $^4S_{3/2} \rightarrow {}^4I_{15/2}$ electronic transitions) and red emission (assigned to $^4F_{9/2} \rightarrow {}^4I_{15/2}$ electronic transitions) of Er^{3+} ion, Fig.2. Since more intense emission was observed for $NaYF_4$:Yb,Er monodispersed spherical particles obtained through Ch assisted synthesis than those obtained in the presence of PAA, former are additionally tested to check their citotoxicity and internalization capacity in human gingival fibroblasts (HGF) cells. MTT assay shows that viability of HGF cells was highly preserved after 24 h exposure to Ch functionalized UCNPs, being above 90% over the whole investigated concentration range (10–50 μg/mL). The homemade nonlinear laser scanning microscope used in this study comprises Ti:Sapphire laser (Coherent, Mira 900-F) capable to operate in femto-second (FS) pulse mode and continuous wave (CW) mode. FS mode at 730 nm was used for visualization of the unlabeled cells while CW radiation at 980 nm was used for the excitation of Ch functionalized UCNPs in cells. The results presented in Fig.3 confirm that observed fluorescence spots are related to the non-specific uptake of UCPNs through cell membrane, indicating that these could be used as new cell labeling agents in the future [4].

References:

[1] A Sedlmeier and H Gorris, Chem. Soc. Rev. **44** (2015), 1526.
[2] X Chen, D Peng, Q Ju and F Wang, Chem. Soc. Rev. **44** (2015), 1318.
[3] Z Gu *et al*, Adv. Mater. **25** (2013), 3758.
[4] This work was financially supported by the Ministry of Education, Science and Technological Development of Serbia project OI 172035.

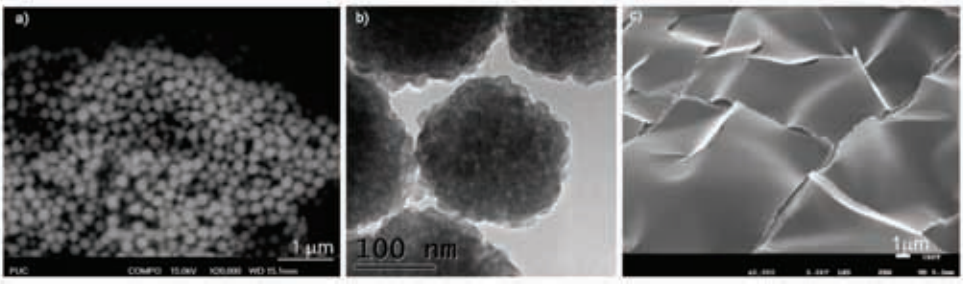

Figure 1. a) SEM and b) TEM images of Ch functionalized $NaYF_4$:Yb,Er particles; c) SEM image of PAA functionalized $NaYF_4$:Yb,Er particles.

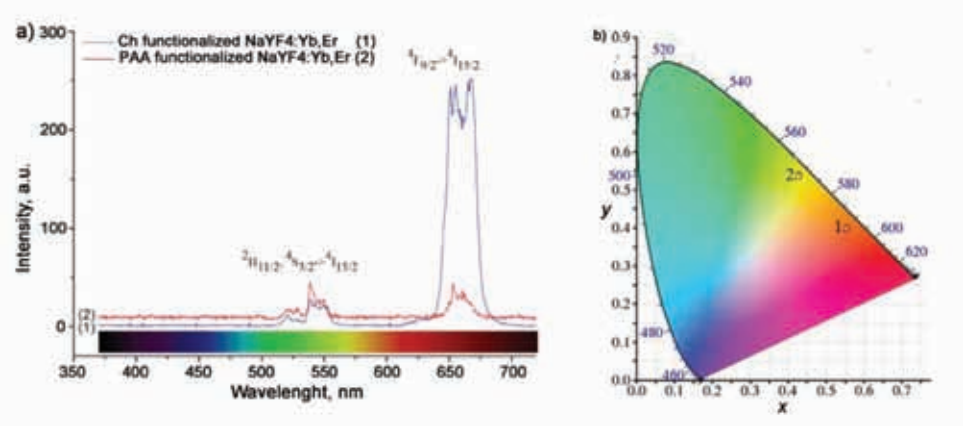

Figure 2. a) Emission spectra and b) corresponding CIE diagram of Ch- and PAA- functionalized $NaYF_4$:Yb,Er particles.

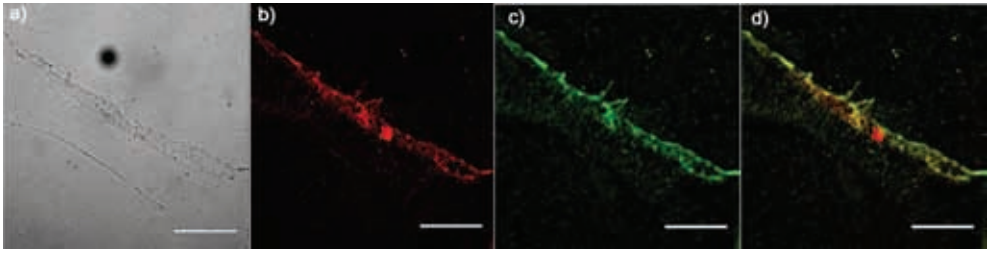

Figure 3. Laser scanning images of HGF following 24 h incubation with 10 µg/ml of Ch functionalized $NaYF_4$:Yb,Er: a) bright field image of cells; b) cells auto-fluorescence; c) up-conversion emission of the Ch- functionalized $NaYF_4$:Yb,Er particles and d) their positioning in cells revealed through co-localization of the b and c. The scale bars correspond to 50 µm.

Alkali Activated Slag as Adsorbents for Cu^{2+} Removal from Wastewaters

Irena Nikolić[1,2], Dijana Đurović[2], Ivana Milašević[2], Smilja Marković[3], Ljiljana Veselinović[3], Vuk V. Radmilović[4], Ivona Janković-Častvan[5], Velimir R. Radmilović[5,6]

[1] *University of Montenegro, Faculty of Metallurgy and Technology, Podgorica, Montenegro*
[2] *Institute of Public Health of Montenegro, Podgorica, Montenegro*
[3] *Institute of Technical Sciences of SASA, Belgrade, Serbia*
[4] *Innovation Centre, Faculty of Technology and Metallurgy, University of Belgrade, Belgrade, Serbia*
[5] *Faculty of Technology and Metallurgy, University of Belgrade, Belgrade, Serbia*
[6] *Serbian Academy of Sciences and Arts, Belgrade, Serbia*

The removal of heavy metals from wastewaters is presently a global imperative primarily due to their well-known toxic nature and detrimental effects on the environment, and more importantly, on human health. Currently, special attention is paid to the use of novel slag based materials – alkali activated slag (AAS) as potential novel adsorbents [1]. Our previous studies have shown that electric arc furnace slag (EAFS) can be successfully used as a precursor for the production of AAS [2]. Generally, alkaline activation involves a chemical reaction between solid aluminosilicate materials and a highly alkaline activator. The alkali activation mechanism of slag involves the dissolution of slag in a highly alkaline [3], which is followed by the condensation and hardening processes. Dependent on the pH and type of alkaline activator, calcium (alumina) silicate hydrate or *C–(A)–S–H* gel has been identified as a reaction product of slag alkali activation [4].

The objective of this research was to investigate the removal of Cu^{2+} from aquatic solution using alkali activated slag (AAS) obtained by alkaline activation of EAFS. The AAS sample was synthesized at a constant solid to liquid mass ratio of 4:1, using an alkali activator prepared by mixing 10M NaOH and Na_2SiO_3 (water glass: Na_2O = 8.5%, SiO_2 = 28.5%, density of 1.39 kg/m^3) solutions in a mass ratio of 2:1. The paste obtained by alkali activation was cast in a plastic mold and cured for 48 h

at 65 °C. For the purpose of batch adsorption experiments, hardened AAS samples were crushed. The batch adsorption tests were performed by mixing solid AAS samples with solution containing Cu^{2+} at the solid to liquid ratio of 0.4:1 at initial Cu^{2+} concentration of 100 ppm, for a period of 35 min. Sample characterization (XRDP, FTIR and SEM/EDS) before and after the adsorption test was carried out as to further illustrate the effectiveness of AAS as an adsorbent.

Microstructural and chemical investigations were carried out using the FEI Helios NanoLab 660 SEM/FIB dual beam system, equipped with the EDAX energy dispersive spectrometer (EDS) and the FEI TITAN Themis^3 300, equipped with the Super-X EDS system controlled with Bruker Esprit software.

The results of morphological investigations reported in our previous study [2] have shown that alkaline activation leads to the partial dissolution of EAFS and the formation of a C–(A)–S–H gel. Thus, the microstructure of AAS is heterogenous and comprises of unreacted EAFS and the reaction product, the C–(A)–S–H gel [2]. Scanning electron back scattered micrographs of the AAS sample after adsorption and appropriate EDS maps of element distribution are given in Fig. 1. It is evident that newly formed platelets on the surface of AAS particles are present (Fig. 1a inset). The cross-section of an AAS particle after the adsorption test (Fig. 1b) and appropriate EDS maps indicate that AAS particles are uniformly covered with the platelets containing Cu, O and S. Scanning transmission electron micrographs (STEM) in high angle annular dark field (HAADF) mode along with appropriate EDS maps indicate that there is a relationship between the distribution of Cu, S and O (Fig. 2). X-ray powder diffraction as well as Fourier Transform Infrared (FT–IR) spectroscopy of metal loaded AAS samples indicated that Cu^{2+} ions have been attached on the surface of AAS in the form of a posnjakite crystal phase.

References:

[1] L Bláhová *et al*, Inżynieria Mineralna **18** (2017), 59.
[2] I Nikolić et al, Materials Letters **133** (2014), 251.
[3] D Krizan and B Zivanovic, Cement and Concrete Research **32** (2002), 181.
[4] W Chen and HJH Brouwers, Journal of Material Science **42** (2007), 428.
[5] The authors acknowledge the support of Centre for Nanoanalysis and Electron Microscopy (CENEM), Friedrich-Alexander University Erlangen-Nürnberg, Erlangen, Germany.

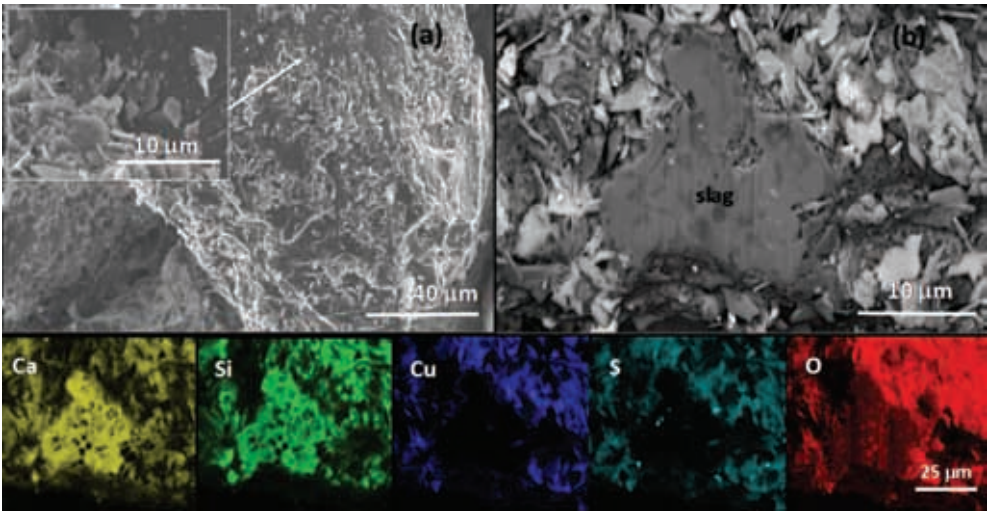

Figure 1. Scanning electron back scattered micrographs of AAS sample in a) top view and b) cross-section along with with appropriate EDS maps.

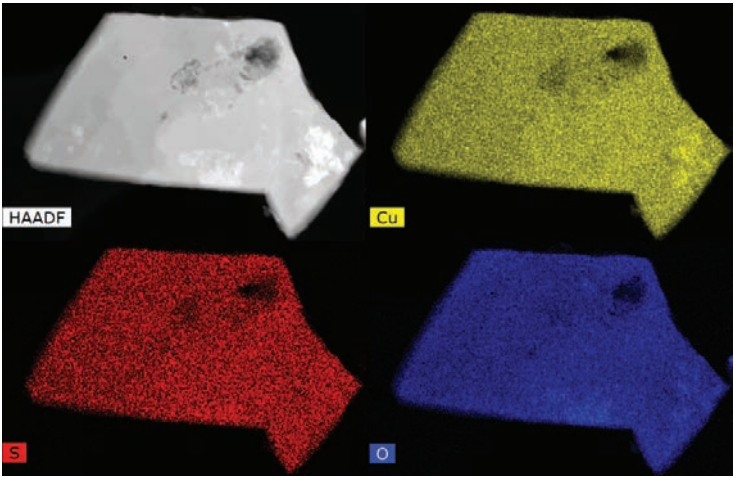

Figure 2. HAADF STEM micrograph of platelet and corresponding EDS maps of Cu, S and O distribution.

Nanostructured Boehmite Powders as Efficient Absorbent in Water Treatments

Marija Milanović[1], Ivan Stijepović[1], Vesna Vasić[2], Dragana Kukić[2], Marina Šćiban[2]

[1] *University of Novi Sad, Faculty of Technology, Department of Materials Engineering, Bulevar cara Lazara 1, 21000 Novi Sad, Serbia*
[2] *University of Novi Sad, Faculty of Technology, Department of Biotechnology and Pharmaceutical Engineering, Bulevar cara Lazara 1, 21000 Novi Sad, Serbia*

Boehmite (AlOOH) is partly dehydrated aluminum hydroxides which is an important precursor for the preparation of advanced catalysts, coatings, membranes, alumina and alumina-derived ceramics [1]. Boehmite can be also employed as a removal reagent of aqueous phosphate and metal cations, both of which cause a significant pollution of water [2]. It has a layered structure with adjacent layers being bound by hydrogen bonds and could transform into active alumina phases after being heated between 400 °C and 700 °C without altering the morphology. Nanocrystalline boehmites and derived transition alumina phases, are extremely important materials with high porous structure, average crystallite on nanoscale and large surface area which enable their adsorption properties. Boehmite is mainly obtained either by hydrolysis of Al-alkoxides or by precipitation of aluminium salts using organic additives to control the morphology of the desired phases, which is often environmentally undesirable. We have synthesized the nanocrystalline boehmite powders with high surface area and specific textural properties at low temperature with use of a low-cost and non-toxic glucose as a surfactant.

Nanocrystalline boehmite powders were synthesized starting from sodium aluminate solution prepared from Bayer liquor, using the procedure we previously reported [3]. In brief, glucose was added in the starting solution as a surfactant. The neutralization of the starting solution was performed with the use of 1M sulphuric acid. The obtained white precipitate was separated by vacuum filtration, washed with distilled water and dried at 110°C for 3 h. The obtained powders have high specific surface area (around 350 m^2/g) and narrow pore size distribution (pore size around 5 nm) [4]. The phase purity and phase structure were examined using following anal-

ysis methods: XRD, FTIR, SEM/TEM and BET. The morphology of the boehmite powder is shown in Figure 1.

In the present study, the removal efficiency of aqueous Cu^{2+} and Cr^{3+} with boehmite have been investigated. The aqueous solutions, to which 50 mg/l of chromium and copper ions were added, had been adjusted to pH 4 in the case of Cu^{2+} and pH 2 for Cr^{3+} ions. Then, the specified dosage of boehmite powders were employed for investigation of ions adsorption (0.05, 0.1, 0.25, 0.5, 1, 1.5 and 2.5 g/l). The results have shown that the removal rate of Cr^{3+} with boehmite is greater than of divalent Cu^{2+} cation and it exceeds the 71% of removal using the highest loading capacity of boehmite (2.5 g/l).

Ongoing work is focused on investigations of boehmite nanopowders as a possible recyclable reagents for the removal–regeneration of aqueous cations [5].

References:

[1] X Wu, B Zhang and Z Hu, Powder Technology **239** (2013), 155.
[2] F Karouia *et al*, Powder Technology **237** (2013), 602.
[3] Z Obrenovic *et al*, Ceramics International **37** (2011), 3253.
[4] Z Obrenović *et al*, Hemijska Industrija **68 (3)** (2014), 357.
[5] The authors acknowledge funding from the Serbian Ministry of Education, Science and Technological Development under the Project III45021.

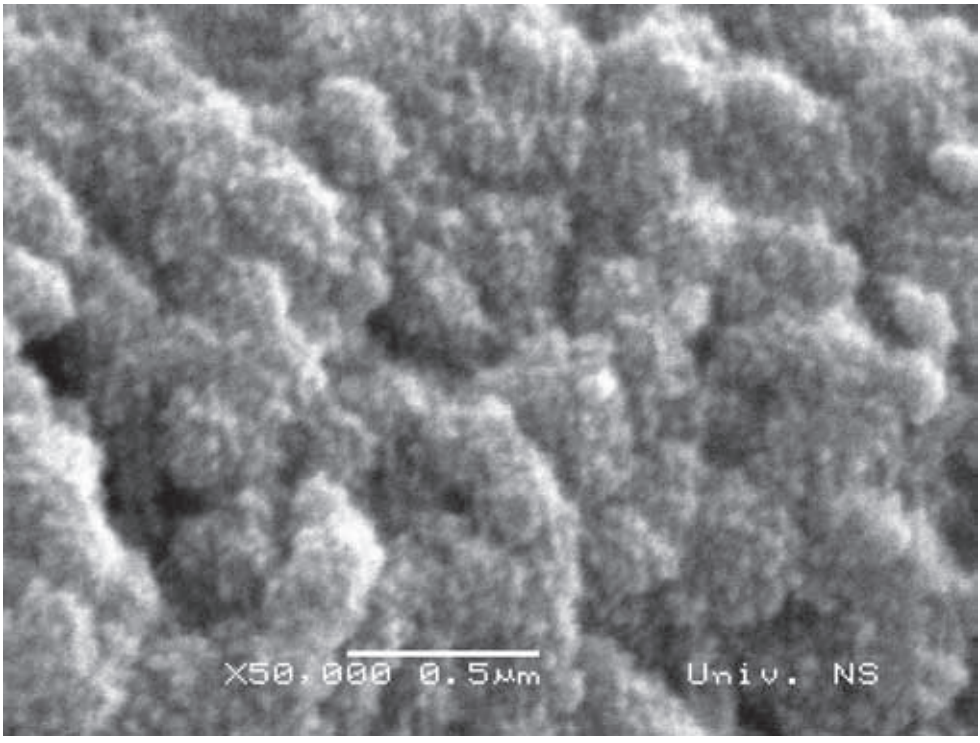

Figure 1. SEM image of nanostructured boehmite powder obtained at 70°C.

The Effect of Alkaline Activator Molarity and Aging Time on the Structure of Inorganic Polymer

Marija Ivanović[1], Ljiljana Kljajević[1], Jelena Gulicovski[1], Bratislav Todorović[2], Adela Egelja[1], Vladimir Pavlović[3] and Snežana Nenadović[1]

[1] *Institute of Nuclear Sciences Vinča, Department of Materials Science, University of Belgrade, Serbia*
[2] *Faculty of Technology of Leskovac, University of Niš, Serbia*
[3] *Institute of Technical Sciences of the Serbian Academy of Sciences and Arts, Knez Mihailova 35/IV, University of Belgrade, 11000 Belgrade, Serbia*

The goal of this research was to produce an environmental friendly, energy saving inorganic polymer using a metakaolin as a precursor. The clean technology which conserve the natural environment was employed for the production of these materials. The used kaolinite is clay obtained from Rudovci, Lazarevac, Serbia. Physicochemical properties of kaolin were investigated in previous work by Nenadović et al. [1]. Metakaolin (MK) was prepared by calcining kaolinite at 750 °C for 1 h. The influence of alkali activation, i.e. different concentration of NaOH as a component of alkali activator mixture on the process of polymerization of metakaolin is investigated. The alkaline solution was prepared from sodium silicate and 2M, 4M, 6M and 8 M NaOH (analytical grade) (volume ratio Na_2SiO_3/NaOH = 1.6). The inorganic polymer (IP) samples were formed from metakaolin and the four different alkaline solution (solid/liquid ratio was about 1), which were mixed for 15 min and then left at room temperature for one day. Finally, the mixture was kept in a sample drying oven for 2 days at 60 °C. Process of aging time of inorganic polymer samples at 7^{th}, 14^{th}, 21^{st} and 28^{th} days is followed by some analytical methods (XRD, FTIR). X-ray diffraction (XRD) and Fourier transformation infrared spectroscopy (FTIR) were used for characterization of metakaolin and metakaolin based inorganic polymers. After 28^{th} days when the aging time were finished, on the surface of the samples were used scanning electron

microscopy (SEM) with energy dispersive spectroscopy (EDS). XRD analysis almost of all inorganic polymer samples revealed their amorphous-like structure with the position of an amorphous halo in the range 18°-32°, which indicates short range ordering of the reference sample with crystalline admixture of SiO_2 (α-quartz, ICSD 89). The FTIR spectra of all samples shows a strong peak at ~1000 cm^{-1} which is associated with Si–O–Si asymmetric stretching vibrations and is the finger print of the geopolymerization [2,3]. The FT-IR results show a shift of the Si-O or Si-O-X bands as the molarity of activator increasing during polymerization process, where X can be Si or Al. Both methods and XRD, as well as FTIR, show greater sensitivity to monitoring the effects of molarity, than the aging time within the same molarity to structural changes in inorganic polymer. SEM micrographs (Fig.1) showed a denser matrix, and a lower content of unreacted metakaolin particles due to increasing of molarity of NaOH. Structural reorganization of inorganic polymer samples occurs during the curing or aging in accordance with a polymerization mechanism.

References:

[1] S Nenadović, *et al*, Environ. Earth. Sci.**73** (2015), 7669.
[2] JW Phair, JSJ Van Deventer, Int. J. Miner. Process. **66** (2002), 121.
[3] P Innocenzi, J. Non Cryst. Solids, **316** (2003), 309.

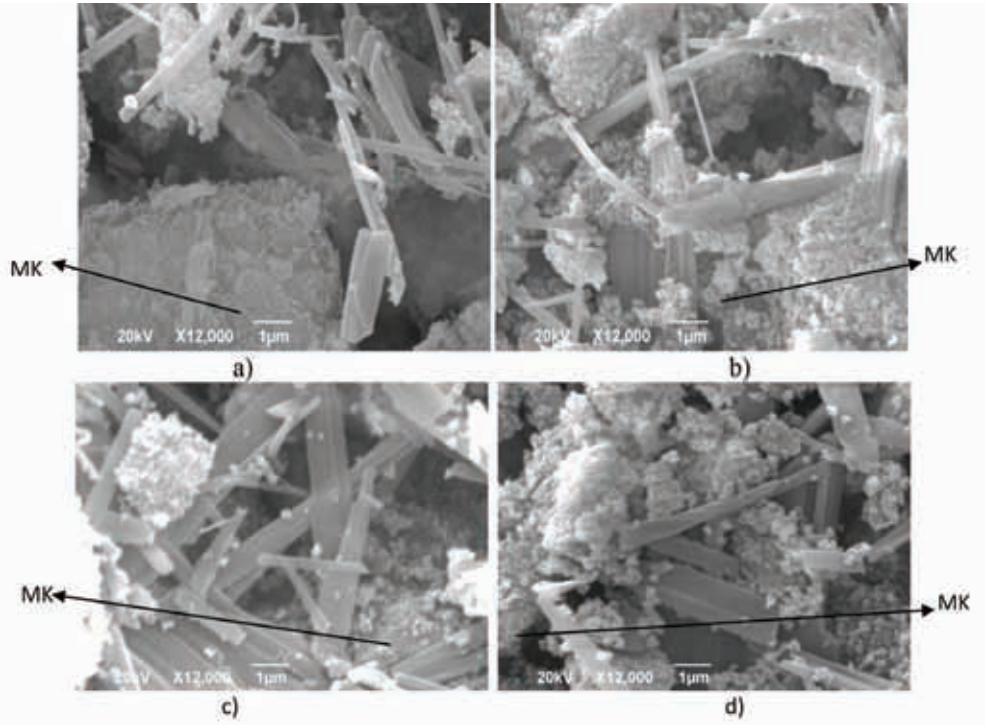

Figure 1. SEM micrographs of inorganic polymer: a) 2M NaOH b) 4M NaOH b) 6M NaOH d) 8M NaOH.

SEM-EDS and AFM Study of a Novel Magnetic Polymer/Bentonite Nanocomposite

Bojana M. Marković[1], Ivan S. Stefanović[1], Jasna V. Džunuzović[1], Danijela V. Ranđelović[1], Bojan Kostić[2], Aleksandra B. Nastasović[1]

[1] *University of Belgrade, Institute of Chemistry, Technology and Metallurgy, Njegoševa 12, Belgrade, Serbia*
[2] *University of Belgrade, Faculty of Mining and Geology, Đušina 7, 11000 Belgrade, Serbia*

Magnetic polymer microspheres consisting of a polymer and inorganic magnetic nanoparticles have been successfully used for separation of toxic and radioactive pollutants [1]. Bentonite as well has been proved as an excellent adsorbent for heavy metals and organic pollutants removal from wastewaters [2]. In order to combine favorable characteristics of magnetite nanoparticles (easy separation using magnetic field), bentonite (large surface area, high chemical and mechanical stability, low-cost and easily available) and macroporous copolymer (selectivity, possibility of additional functionalization, high sorption rate and capacity, recycling capability) a novel magnetic polymer/bentonite nanocomposite was synthesized [3].

Magnetized bentonite (MB) nanoparticles were synthesized as described in the literature [4]. Poly(glycidyl methacrylate-*co*-ethylene glycol dimethacrylate) (PGME) and a novel poly(glycidyl methacrylate-*co*-ethylene glycol dimethacrylate)/ magnetized bentonite nanocomposite (PGME/MB) were prepared by suspension copolymerization [1]. For the synthesis of PGME/MB, 10 wt% of MB nanoparticles was added additionally. Particles with an average diameter in the range <100 μm were used for subsequent characterization via scanning electron microscopy with energy-dispersive X-ray spectroscopy (SEM-EDS) and atomic force microscopy (AFM). SEM-EDS analysis was performed on JEOL JSM-6460LV instrument. AFM characterizations were performed with AutoProbe CP-Research SPM (TM Microscopes-Veeco) using non-contact AFM mode, at the scan size (2 × 2) μm^2.

The morphology of surface and cross-section of PGME and PGME/MB was examined using SEM analysis (Figure 1). As seen, PGME and PDME/MB particles have regular spherical shape. The SEM micrographs of PGME particles cross-

sections show highly developed internal porous structure composed of a large number of globules interconnected with channels and pores. On the other hand, the PGME/MB surface is rather smooth with low porosity which can be due to the clogging of surface pores.

The SEM-EDS analysis enabled investigation of the elements distribution of PGME/MB sample at a depth of 100–1000 nm from the surface. Qualitative SEM-EDS analysis confirmed the presence of all expected elements. The obtained results also indicate that, although predominantly present at the particle surface, the MB nanoparticles were also embedded in the bulk to a certain extent. The spectra at gray and bright areas on the surface of sample PGME/MB were collected. Bright and gray areas confirmed the presence of Fe, Si and Al atoms.

The 3D AFM images of the top view of samples PGME and PGME/MB were shown in Figure 2. Comparing the images, one may notice the clear difference in PGME and PGME/MB morphology, i.e. macroporous PGME surface and less porous PGME/MB surface, fully covered with a layer of MB nanoparticles.

SEM-EDS analysis proved that MB particles were incorporated on the interior surface of the particles as well as on the exterior. The AFM images confirmed the influence of MB nanoparticles incorporation on the size and morphology of PGME/MB [5].

References:

[1] BM Marković *et al*, J. Alloy. Compd. **705** (2017), 38-50.
[2] HH Murray, Acta Geodyn. Geomater. **138** (2005), 131-138.
[3] AM Gutierrez, TD Dziubla and JZ Hilt, Rev. Environ. Health **32** (2017), 111-117.
[4] Z Lou *et al*, J. Taiwan. Inst. Chem. E. **49** (2015), 199-205.
[5] The authors acknowledge funding from the Ministry of Education, Science and Technological Development of the Republic of Serbia (Projects III 43009 and ON 172062).

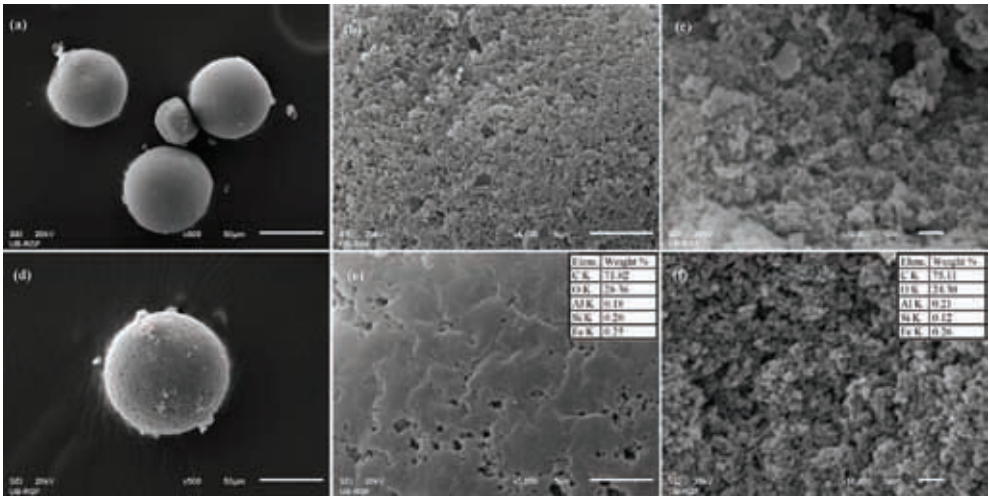

Figure 1. SEM microphotographs of: PGME particles (a), particle surface (b), particle cross-section (c) and PGME/MB particles (d), particle surface (e) particle cross-section (f).The insert tables showed the EDS results.

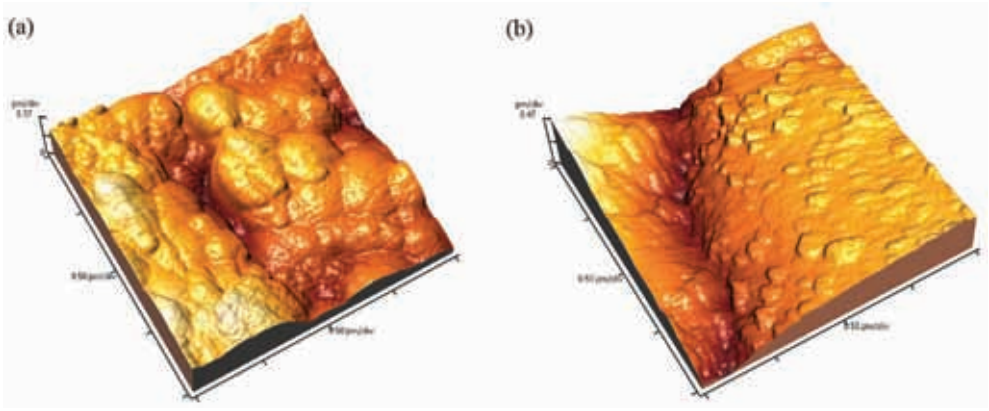

Figure 2. The 3D AFM images of: (a) PGME and (b) PGME/MB.

Ultra-fine Grained Structure and Fracture Mode in Low Carbon Steel Subjected to Severe Plastic Deformation

Marko Vilotić, Leposava Šidjanin and Dragan Rajnović

Department of Production Engineering, Faculty of Technical Sciences, University of Novi Sad, Novi Sad, Serbia

In the past twenty years, research in the field of severe plastic deformation (SPD), has been developing rapidly [1]. Now, SPD has become an effective method of producing ultra-fine grains with submicron and nanostructure, even in steel bulk semi-products with a significant increase in mechanical properties. From an engineering point of view, at the Department of Production Engineering, Faculty of Technical Sciences, University of Novi Sad, one discontinuous SPD method has been developed for upsetting square shaped billet by V-shape dies compression (VSDC). In fact, the VSDC is a multistage process in which the sample is removed from the die after the first compression turn, rotated for 90°, and then returned into the dies, Fig.1 [2]. Experimental application of this method was verified using a normalized carbon steel rod with 0.14% C (EN steel designation C15E). The samples of 14×14×70 mm were compressed up to eighteen turns on a hydraulic press without lubrication. The influence of the processing parameters on the microstructural changes and the fracture mode were evaluated by SEM-JSM6460LV and STEM-FEI Tecnai (F20). The TEM samples (cross-sections) were prepared by FIB (Quanta 3D FEG) with an in-situ lift-out technique.

The starting SEM and TEM micrographs of the undeformed low carbon steel are shown in Fig. 2 (ac). The microstructure consists of 85% ferrite and 15% pearlite, with average ferrite grain size of 19.1 μm. The TEM micrographs with the corresponding diffraction patterns of the ferrite region after the second, eighth, and twelfth turn are presented in Fig. 3 (a-c), respectively. After the second turn (Fig. 3a) the ferrite grain consists of parallel elongated bands having a width of 0.20.3 μm. The band boundaries are predominantly in low-angle misorientation. It is also apparent that inside the band the interior dislocations cells are present. After the eighth and twelfth turns in the samples, the equiaxed grains with an average size of 150 to 300 nm were

formed, Fig. 3 (b,c). The presence of equiaxed grains with high angle boundaries is confirmed by ring patterns with large numbers of reflections and TEM contrast of grain boundaries. It should be noted that the grain refinement up to the eighteenth turn is not significant, compared to the refinement up to the twelfth turn. These results were also confirmed by average microhardness variation from 137 HV for the unprocessed samples, up to 250 HV after the fourteenth turn. Moreover, the microhardness values up to the eighteenth turn remained almost the same.

In Fig. 4, the SEM results of the fractured surfaces (macro and micro) for undeformed, and VSDC deformed samples via fourteenth and eighteenth turns are presented. They contain dimples, showing a ductile fracture. Under tensile stresses these dimples in all samples originate from nucleation, growth, and coalescence of microvoids. However, the macro fracture mode changed from the cup and cone for the undeformed sample, via the spiral mode for the fourteenth turn sample, into the fracture mode by the shear instability, as an indication of the plastic deformation limit, after the eighteenth turn.

References:

[1] F Samadpour *et al*, Materials Science & Engineering A **718** (2018), 412.
[2] M Vilotić "Severe Plastic Deformation in Material Multi-stage Upsetting Processes", Doctoral thesis, Faculty of Technical Sciences, University of Novi Sad, (2015).

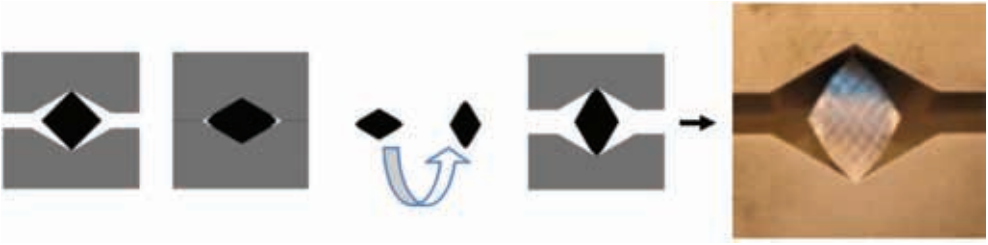

Figure 1. (a) Schematics of upsetting by V-shape dies and (b) sample inside the V-shape die.

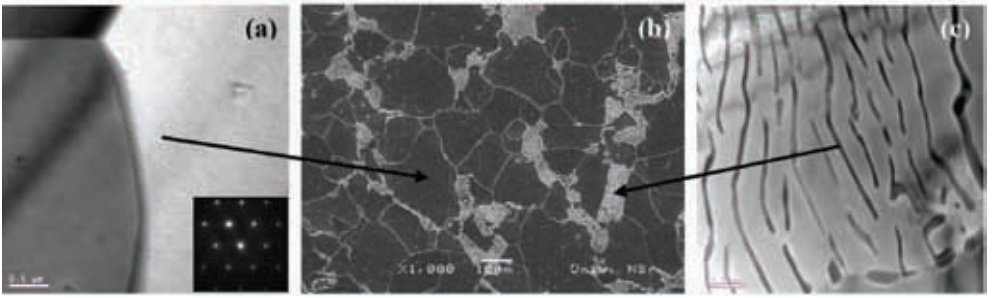

Figure 2. TEM (a,c) and SEM (b) micrographs of the undeformed low carbon steel.

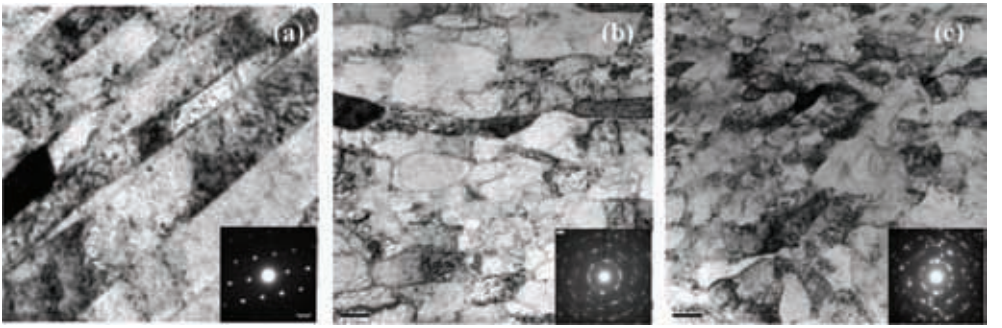

Figure 3. TEM micrograph after: (a) second, (b) eighth and (c) twelfth VSDC turn.

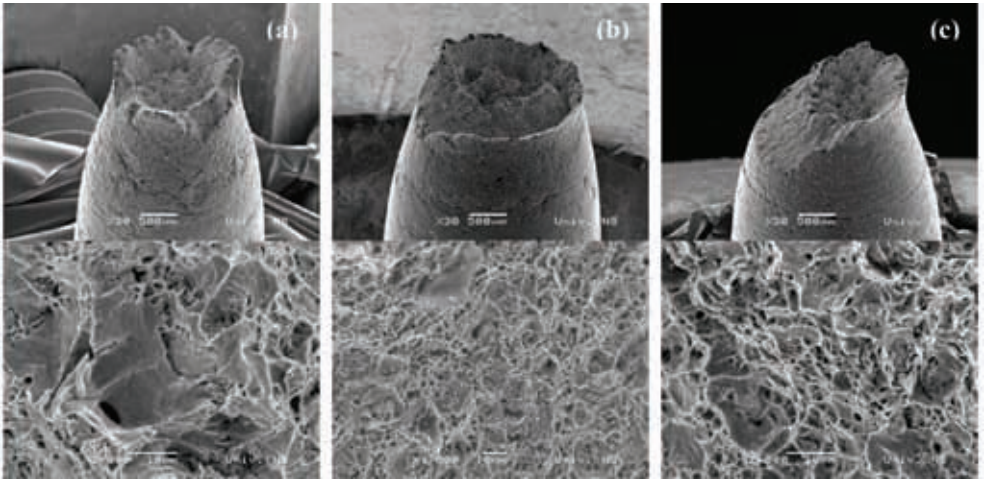

Figure 4. Fracture mode of low carbon steel: (a) undeformed, and after (b) fourteenth and (c) eighteenth VSDC turn.

Microstructure of Nanolayered CrAlN/TiSiN Coating

Aleksandar Miletić[1], Peter Panjan[2], Miha Čekada[2], Lazar Kovačević[1], Pal Terek[1] and Branko Škorić[1]

[1] *Faculty of Technical Sciences, University of Novi Sad, Novi Sad, Serbia*
[2] *Jožef Stefan Institute, Ljubljana, Slovenia*

Ceramic thin films, such as TiN and CrN have been widely used to improve surface properties of mechanical components. Their properties can be enhanced by addition of Al which results in formation of TiAlN and CrAlN films, which are characterized by high hardness (≈ 30 GPa) , high temperature stability (up to 900 °C for TiAlN and 1000 °C for CrAlN), and high oxidation resistance [1].

Nowadays, the majority of research is dedicated to nanocomposite and nanolayered coatings. TiSiN is one of the most widely studied nanocomposite coatings. It is composed of TiN nanocrystals surrounded by amorphous Si_3N_4 tissue, and is characterized by superhardness (> 40 GPa), high oxidation resistance (≈ 850 °C) and thermal stability up to 1100 °C. Nanolayered coatings consist of few nm thin layers comprised of two or more materials, e.g. TiAlN/TiSiN [2].

For practical applications, coating hardness should be accompanied by appropriate toughness, thermal stability, and oxidation resistance, which can be challenging to achieve in one coating. In order to meet these challenges, in this research, CrAlN and TiSiN layers were deposited alternatively to produce CrAlN/TiSiN coating. Industrial magnetron sputtering unit with two CrAl and two TiSi targets was used for coating preparation. More details about the used deposition equipment can be found in our previous work [2]. Conventional and high-resolution TEM along with XRD were used for microstructural analysis. Chemical and phase compositions were assessed by X-ray photoelectron spectroscopy.

XRD and XPS analysis revealed that CrAlN/TiSiN coating consist of fcc-$Cr_{1-x}Al_xN$, fcc-TiN and SiN_x phases. Formation of Cr_2N and AlN phases with hexagonal lattice was not observed.

Bright field TEM image shown in Figure 1a reveals fine grained microstructure with grain width between 25 and 50 nm, and length between 100 and 250 nm.

The SAED pattern shown in the inset corresponds to fcc structure. The strongest diffraction came from {111} and {200} planes. Individual layers can be distinguished from a higher magnification BF TEM image shown in Figure 1b, brighter layers correspond to TiSiN. Thickness of layers was 6.3 nm and 1.0 nm for CrAlN and TiSiN, respectively. Unlike in our previous research [2], where TiSiN layers blocked the growth of TiAlN crystals to size of 5 nm in TiAlN/TiSiN coating, in this research we observed only disturbances in crystal growth (Figure 2). Namely, slight changes in growth direction and large number of dislocations were revealed. It is these disturbances which lead to the fine-grained structure observed in Figure 1a. Presence of such a structure resulted in high hardness of 34 GPa and high toughness expressed as the ratio H^3/E^{*2} of 0.33 GPa.

References:

[1] X Ding *et al*, Thin Solid Films **516** (2008), 5716.
[2] A Miletić *et al*, Surface and Coatings Technology **241** (2014), 105.
[3] This research was supported by the Serbian Ministry of Science and Technological Development and by the Slovenian Research Agency (ARRS) which the authors gratefully acknowledge.

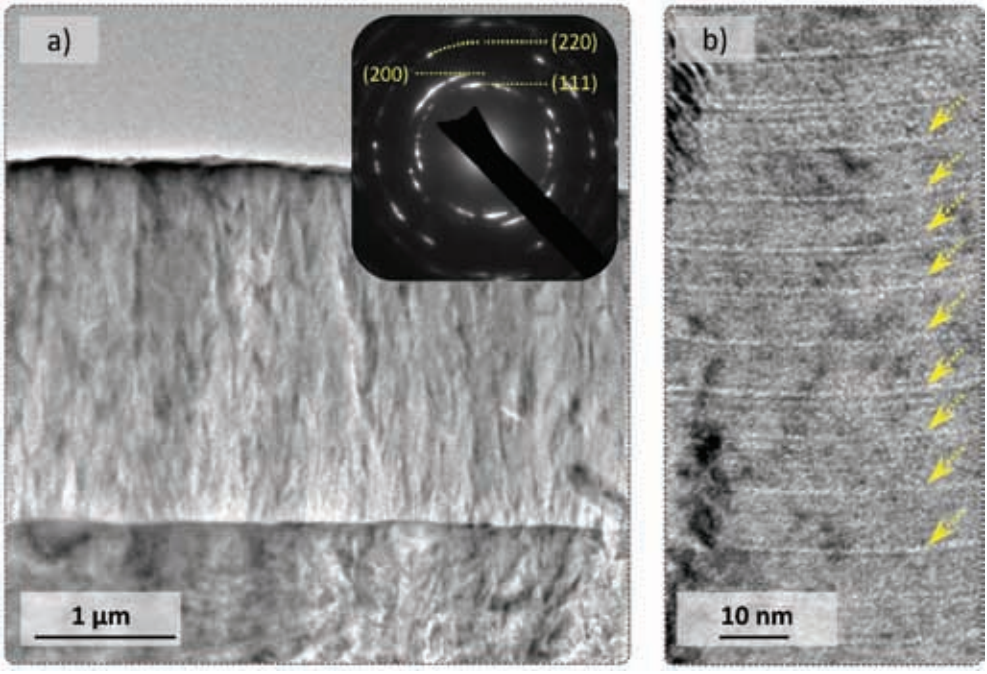

Figure 1. Bright field TEM micrographs of CrAlN/TiSiN coating: a) lower magnification image with the electron diffraction pattern shown in the inset, b) higher magnification image, arrows indicate TiSiN layers.

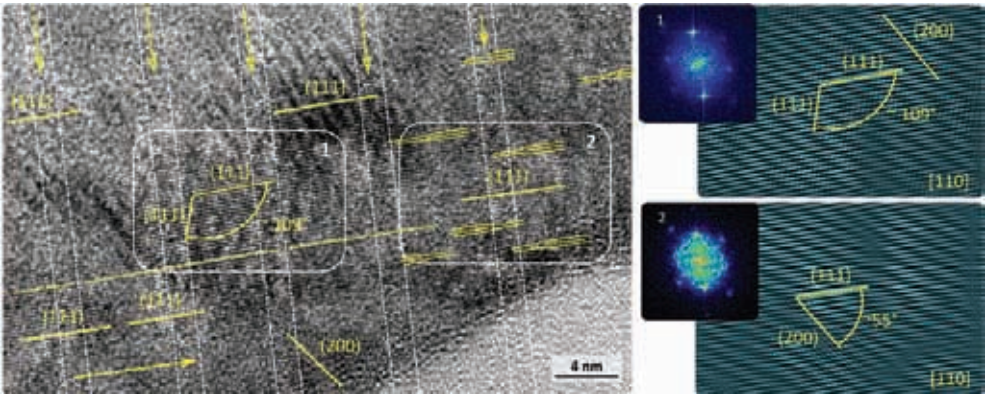

Figure 2. High resolution image of CrAlN/TiSiN coating along with FFT patterns and inverse FFT images of selected areas. Solid arrow indicates coating growth direction, dashed arrows indicate TiSiN layers.

Synthesis and Characterization of $MnCo_2O_4$ Porous Spinel Oxide

Vesna Antunović[1], Dijana Jelić[1], Zoran Nedić[2], Marija Ilić[3], Aleksandar Lolić[4]

[1] *Department of Pharmacy, Faculty of Medicine, University of Banja Luka, Banja Luka, Bosnia and Herzegovina*
[2] *Faculty of Physical Chemistry, University of Belgrade, Belgrade, Serbia*
[3] *Faculty of Mining and Geology, University of Belgrade, Belgrade, Serbia*
[4] *Faculty of Chemistry, University of Belgrade, Belgrade, Serbia*

This work presents an investigation on spinel structured material that consist of Mn(II) and Co(II) combined in the formula $MnCo_2O_4$, where Mn(II) occupies tetrahedral and Co(II) octahedral sites of crystal structure. Such spinel structured material, $MnCo_2O_4$ was synthesized by citrate-gel combustion (CGC) technique, carefully chosen as the method of synthesis is very important for producing a material with desirable physico-chemical characteristics. The CGC method of synthesis is well known for production of nanodispersed simple or complex oxides, catalyst and superconductors [1]. This sol-gel auto combustion technique is quite common, provides a very good homogeneity of samples, very easy control of stoichiometry and delivers production at low cost. The proposed method involved nitrate salt as oxidizer and citric acid as a reducing agent (fuel). The molar ratio of nitrate salt precursors was set to 0.5:0.5. The choice of fuel, as well as the ratio of oxidizer/ fuel affects morphology of spinel porous material [2]. The molar ratio of citric acid versus nitrate groups was 1:3.6. In preparation of $MnCo_2O_4$, aqueous ammonia (1 M) was added into mixture of $Mn(NO_3)_2$, $Co(NO_3)_2$ and citric acid aqueous solution (in order to adjust the to pH=7), subsequently followed by water evaporation and heating under constant stirring until a light pink sol was formed. The sol turned into gel and this was finally calcinated for 2h at 450 ºC. The equation of combustion of citric acid is $2C_6H_8O_7 + 9O_2 = 12CO_2 + 8H_2O$. Since the temperature needed to complete combustion of remaining carbon residues is unknown, the heating at a constant temperature of 500° C was prolonged for approximately 30 minutes, which was enough to obtain carbon-free oxides. After calcination, a black powder of $MnCo_2O_4$ nanoparticles was obtained. The physico-chemical characterization of as-prepared

material was performed by means of X-ray diffraction (XRD) and scanning electron microscopy (SEM). A representative X-ray diffraction pattern of the as-prepared final product is shown in Fig. 1. Obtained X-ray spectrum shows to be in good agreement with standard pattern of spinel structure of $MnCo_2O_4$ (JCPDS card no. 23-1237) regarding some of the diffraction peak positions. The most intense lines of 2θ at 18.53°, 30.47°, 35.99°, 43.64°, 54.30°, 57.84°, 63.45° in XRD spectrum are in good agreement with the angles 18.55°, 30.54°, 35.995°, 43.759°, 54.336°, 57.909° and 63.622° in JCPDS card of $MnCo_2O_4$. As-prepared $MnCo_2O_4$ shows some nosier XRD spectrum than standard pattern of spinel structure of $MnCo_2O_4$ and there are no impurity peaks. These noises are due to the low crystallite size of the prepared material. Debye-Scherrer formula was used to calculate the average crystallite size of the prepared $MnCo_2O_4$ which around 19 nm [3,4]. SEM image (Fig. 2) shows porous morphology of $MnCo_2O_4$ material. Homogeneity of oxide mixtures was also visible which means that a fine dispersion of Mn and Co oxides prevailed, probably achieved due to the equal molar ratio of Mn and Co oxides in the mixture. Elemental composition analysis of this porous spinel material obtained from energy dispersive spectroscopy (EDS) further confirms the existence of Mn, Co and O with calculated composition of 2.21 wt%, 2.99 wt% and 11.33wt%, respectively (Fig. 3). The synthesis of this porous material proved to be inexpensive, fast and environmentally friendly and the material could be potentially used as an electrochemical sensor, especially in the field of heavy metal detection.

References:

[1] A Sutka and G Mezinks, Frontiers of Material Science **6 (**2012), 128.
[2] C Li *et al*, Nature Communications **6** (2015), 1
[3] M Velmurugan and SM Chen, Scientific Reports **7** (2017), 1.
[4] R Tholkaooiyan and K Vishista, Physica B **448** (2014), 177.

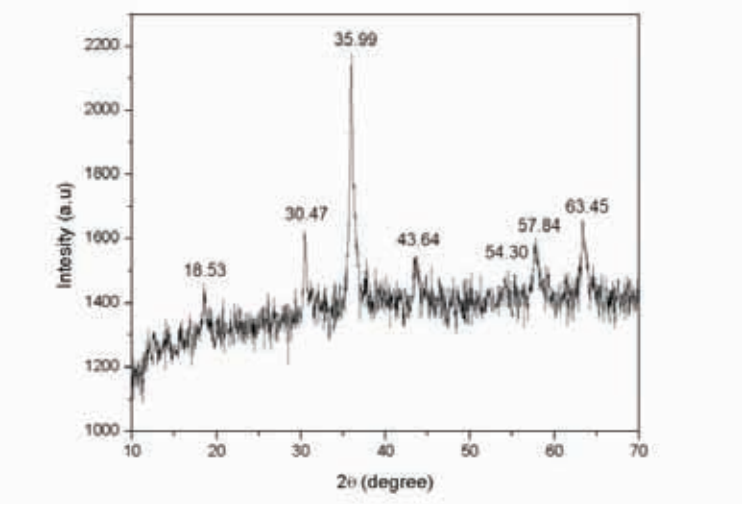

Figure 1. XRD pattern of $MnCo_2O_4$ spinel oxide.

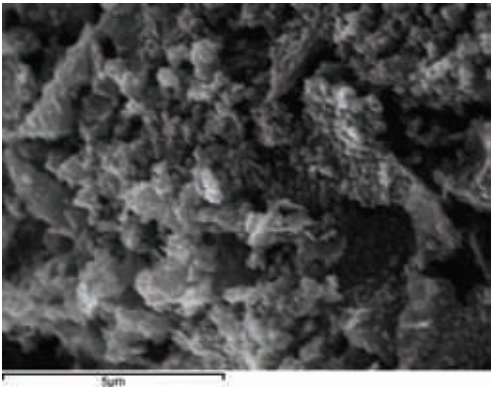

Figure 2. SEM image of prepared porous $MnCo_2O_4$.

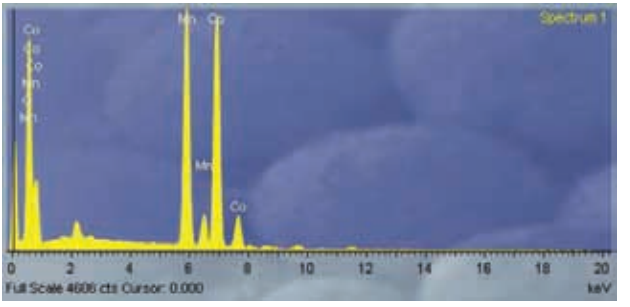

Figure 3. EDS spectrum of prepared $MnCo_2O_4$.

Fabrication Of $NiFe_2O_4$ Nanofibers/Net Via Combined Sol-Gel and Electrospinning Method

Aleksandar Grujić[1], Vladan Ćosović[1], Jasna Stajić-Trošić[1], Aleksandar Ćosović[2], Mirko Stijepović[2] and Tomáš Žák[3]

[1] *Institute of Chemistry, Technology and Metallurgy, University of Belgrade, Belgrade, Serbia.*
[2] *Faculty of Technology and Metallurgy, University of Belgrade, Belgrade, Serbia.*
[3] *Institute of Physics of Materials of the Czech Academy of Sciences, Brno, Czech Republic.*

Magnetically soft ferrites with cubic spinel lattice structure have been widely used in diverse applications for a number of years [1, 2]. With the rapid development of nanoscience and nanotechnology one dimensional (1D) and quasi-one dimensional (QID) nanostructured magnetic materials (nanofibers, nanotubes, nanowires, nanowhiskers, etc.) have gained considerable attention. This is due to their distinctive chemical and physical properties which offer significant potential for production and design of innovative electromagnetic devices, sensing elements and catalysts. Electrospun magnetic nanofibers are particularly interesting because they are relatively inexpensive and easy to produce with controlled diameter and with modified composition and/or surface [2].

In the current study, Ni-ferrite ($NiFe_2O_4$) magnetic nanofibers/net were prepared using combined electrospinning [3] and sol-gel method [4] adopted from literature [5]. The ferrite sol was obtained from aqueous solutions of $Ni(NO_3)_2 \times 6H_2O$ and $Fe(NO_3)_3 \times 9H_2O$. Citric acid was used as chelating agent and ammonium hydroxide was used to regulate pH value. After the subsequent water removal, the ferrite gel was obtained. In the next step, the ferrite gel was mixed with a solution of polyvinylpyrrolidone (PVP) in acetic acid so as to prepare a solution for electrospinning process. The nanofibers were produced by means of an electrospinning apparatus with the vertical configuration in order to allow the production of nanoweb in a static way (plate collector). The applied process conditions were: solution flow rate 0.5 ml/h; distance between the needle tip and electrode 15 cm; voltage 28 kV, number of

syringes 1. The electrospun fibers were firstly dried and then calcinated at 700° C for 5 h in order to remove an organic component as well as to initiate a reaction between present oxides which produces Ni-ferrite magnetic nanofibers.

Morphology and microstructure of the electrospun composite fibers were studied both before and after the calcination using JEOL JSM 6610LV scanning electron microscope (SEM). Phase composition was determined using Fourier-transform infrared (FT-IR) spectroscopy, X-Ray diffraction analysis (XRD) and ^{57}Fe Mossbauer spectroscopy (MS). All phase composition analyzes were carried out at ambient temperature. The FT-IR spectra of the nanofibres were recorded by a BOMEM spectrometer (from the Hartmann & Braun, MB series) with 4 cm^{-1} resolution, using a transmission mode between 4000 and 400 cm^{-1}. The XRD diffraction patterns were obtained using PAN analytical X'Pert PRO MPD X-ray diffractometer with CoKα radiation. The XRD pattern fitting was done using Full Prof software and ICDD database. The Mössbauer spectra were taken in the standard transmission geometry using a ^{57}Co(Rh) source and the calibration was done against an α-iron foil. The CONFIT software package was used for MS spectra analysis [6]. Room temperature magnetic hysteresis loop measurements were carried out on EG&G Vibrating sample magnetometer (VSM) with the magnetic field strength of 2 T. In order to gain better insight into the magnetic behavior of the obtained Ni-ferrite nanofibers/net at elevated temperatures thermomagnetic measurements (TM) were carried out. The thermomagnetic curves were measured on the EG&G vibrating sample magnetometer in the field of 4 kAm^{-1} in vacuum. The heating and cooling rate was 4°C min^{-1} with 30 min delay at maximum of 800°C.

As expected the diameter of electrospun fibers is directly proportional to the viscosity of the starting solution and the applied parameters of electrospinning process. The obtained SEM results show that the prepared Ni-ferrite magnetic fibers represent a net structure that resembles a space within the polymer composite fibers that was initially occupied by the ferrite gel. The SEM micrograph of typical net structure is presented in Figure 1. The FT-IR analysis indicate presents of broad band with a maximum at 584 cm^{-1}, 1270 cm^{-1}, 1638 cm^{-1}, 2852 cm^{-1} and 2922 cm^{-1}. The results of XRD phase composition analysis confirm that the pure $NiFe_2O_4$ material was obtained. The results of MS analysis confirm the formation of $NiFe_2O_4$ phase with nanocrystalline structure. The observed set of sextets with decreasing splitting and intensity along with fairly small paramagnetic doublet reveal existence of a crystallite size distribution, while latter also points out to presence of superparamagnetic fraction of the $NiFe_2O_4$ with very small crystallite size <13 nm. The room temperature magnetic hysteresis loop exhibits characteristic "S" shape, typical for a magnetically soft material, with values of magnetic properties within the expected range for this type of material. The obtained thermomagnetic curves

essentially illustrate temperature dependence of the total magnetic moment of the studied material under an applied external magnetic field. They reveal sudden drop for the heating curve and vice versa sharp increase for the heating curve at about 570°C which corresponds to the Curie temperature of $NiFe_2O_4$ phase. The observed increase of total magnetic moment during the cooling stage of measurements can be also, to some extent, attributed to field cooling as well as overall decrease in thermal energy.

References:

[1] A Ćosović *et al*, Journal of Mining and Metallurgy Section B: Metallurgy **49** (2013), 271.
[2] S Thenmozhi *et al*, Materials Science and Engineering B **217** (2017), 36.
[3] A Sutka and G. Mezinskis, Frontiers of Materials Science **6** (2012), 128.
[4] H Wu *et al*, Journal of Advanced Ceramics **1** (2012), 2.
[5] D Li, T Herricks and Y Xia, Applied Physics Letters, **83** (2003), 4586.
[6] T Žák and Y Jirásková, Surface and Interface Analysis **38** (2006), 710.
[7] This work has been supported by the Ministry of Education, Science and Technological Development of the Republic of Serbia (Projects TR34011, III45019, TR34023, ON172037) and by European Regional Development Fund through CEITEC- Central European Institute of Technology (project CZ.1.05/1.1.00/02.0068).

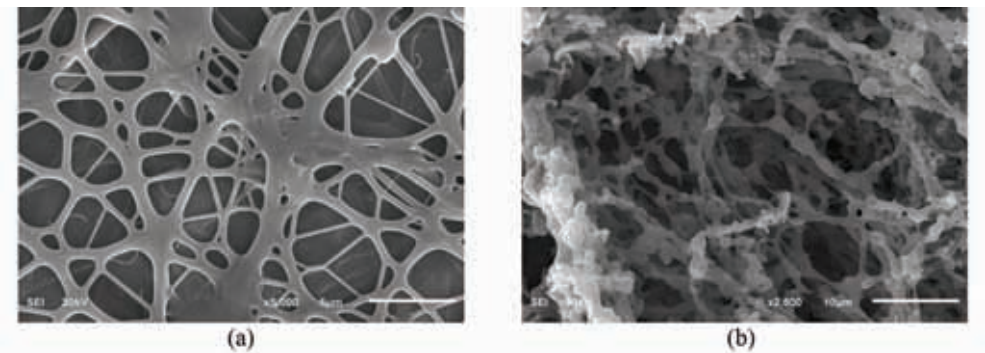

Figure 1. The SEM micrographs of the obtained net structures (a) after drying and (b) after calcination.

TiO_2 Nanoparticle Deposition on Solid CP-Ti Substrate through Spraying Water Colloid in the Arc Plasma

Vladimir Pavkov[1], Milovan M. Stoiljković[2], Vesna M. Maksimović[1], Ivana Lj. Cvijović-Alagić[1], Jovan Ciganović[2] and Mila R. Vranješ[3]

[1] *Laboratory of Material Science, Vinča Institute of Nuclear Sciences, University of Belgrade, Belgrade, Serbia*
[2] *Laboratory of Physical Chemistry, Vinča Institute of Nuclear Sciences, University of Belgrade, Belgrade, Serbia*
[3] *Laboratory of Radiation Chemistry and Physics-Gamma, Vinča Institute of Nuclear Sciences, University of Belgrade, Belgrade, Serbia*

Surface modification techniques are an important area of biomaterials research and biomedical engineering of titanium-based materials. Coatings composed of titanium dioxide are stable and non-toxic to the environment or humans. Moreover, titanium dioxide is well known for its antibacterial properties [1]. Different authors have reported that titanium dioxide induces the precipitation of bone-like apatite particles or calcium phosphates on its surface making it a suitable candidate for bone replacement and hard-tissue reconstruction [1, 2]. In most of the biosensing applications, where TiO_2 plays a role of an interface layer, its surface needs to be additionally functionalized in order to achieve selective binding of biological molecules. The functionalization process can be achieved by physical adsorption of a bioreceptor or by its chemical binding. Nowadays, TiO_2 films and coatings can be obtained using a number of well-established vapor or liquid-based deposition techniques [1, 2].

The present study describes an improved method for TiO_2 coating deposition onto the commercially pure (CP) Ti substrate by spraying colloidal solution of TiO_2 nanoparticles in the electric discharge plasma. The success of the proposed deposition method is investigated by characterization of the deposited coating morphology using a scanning electron microscope (SEM) and 3D surface morphology analyzer (*i.e.* optical profilometer).

Aerosol generation: Colloidal water solution of TiO_2 nanoparticles with a concentration of 0.24 M and 10^{17} particles/ml and with agglomeration number of 1402 was

used for spraying [3]. The spray was produced using Meinhard pneumatic nebulizer, Type A, coupled with the Scott-type cloud chamber, Figures 1 and 2. The supporting argon gas flow was 2 dm^3/min and the aerosol yield is about 0.03 ml of liquid per 1dm^3 of argon. According to the nebulizer system used, it can be assumed with high certainty that the most of the aerosol droplets are approximately 10 μm in size. Spraying time was 1 min.

Direct current arc plasma (DCP): Direct current arc discharge was used to generate spatially and temporarily stabilized atmospheric pressure plasma [4]. The argon stream carrying the aerosol enters tangentially to the circular cavity of the arc discharge and forms a vortex around the plasma column, see Figure 1. The arc column, about 2.5 mm in diameter, reaches temperatures ranging from 9000 K in the center of the vortex to 6000 K at the vortex periphery.

CP-Ti workpiece: A ring-shaped CP-Ti workpiece was fixed coaxially inside the circular cavity (see insert in Figure 1). The current carrying plasma channel passes orthogonally through the ring and heats it. Aerosol vortex interacts with the plasma inducing in that way droplets desolvation followed by partial melting of TiO_2 solids and their evaporation. As a result, deposits are formed on the CP-Ti workpiece, Figures 3 and 4.

SEM images presented in Figures 3 and 4 show morphology of the TiO_2 film deposited on the CP-Ti substrate surface at various distances from the plasma center. It could be seen that the size of the TiO_2 particles deposited on the substrate surface increases with the increase of the distance from the center of the workpiece.

Conducted investigations confirmed that stable titanium dioxide layer can be successfully deposited on the CP-Ti surface by applying this simple and cost-effective method. Nevertheless, the described method provided a good dispersion of the titanium dioxide nanoparticles onto the substrate surface enabling in that way the formation of the continuous layer [5].

References:

[1] L Visai *et al*, International Journal of Artificial Organs **9** (2011), 929.
[2] M Dominik *et al*, Biosensors and Bioelectronics **93** (2017), 102.
[3] M Boni *et al*, Colloids and Surfaces A: Physicochemical and Engineering Aspects **519** (2017), 238.
[4] M Stoiljković *et al*, Spectrochimica Acta Part B **65** (2010), 927.
[5] The authors acknowledge funding from the Ministry of Education, Science and Technological Development of the Republic of Serbia through the Grants Nos. OI172019, OI174004, OI172056 and III45012.

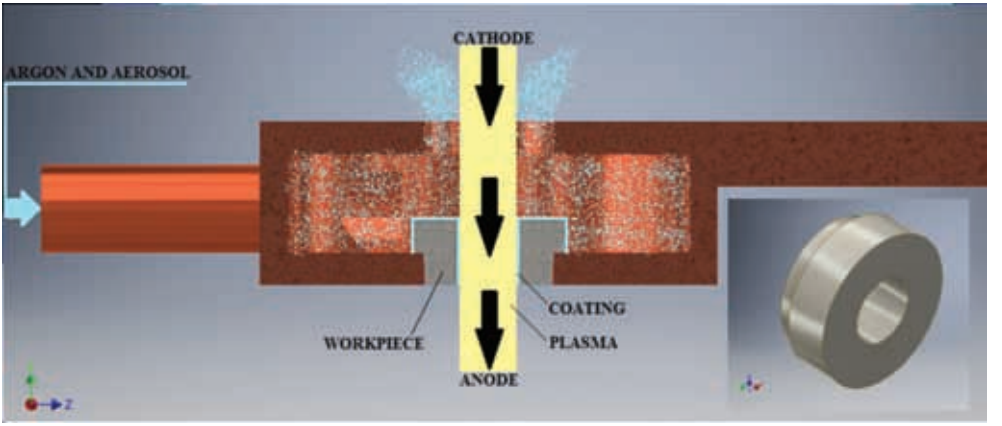

Figure 1. Illustration of the applied set-up. The insert represent illustration of the ring-shaped CP-Ti workpiece.

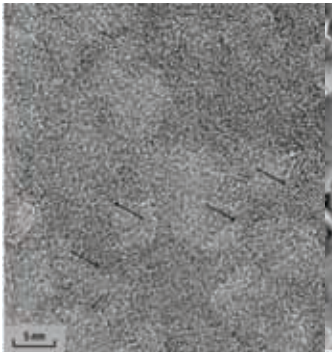

Figure 2. TEM image of the TiO_2 colloidal nanoparticles.

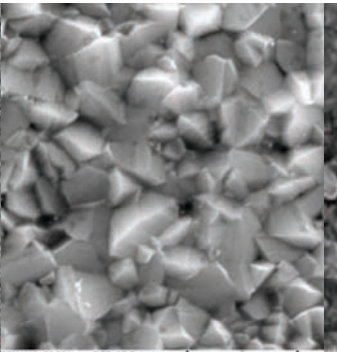

Figure 3. Surface morphology of the TiO_2 deposit close to the outer edge of the workpiece.

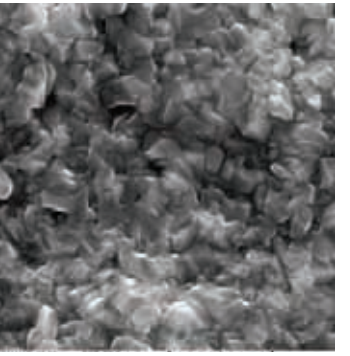

Figure 4. Surface morphology of the TiO_2 deposit close to the inner edge of the workpiece.

Bioactive Hydroxyapatite/Chitosan/Gentamicin Composite Coating Electrodeposited on Titanium

Milena Stevanović[1], Marija Đošić[2], Ana Janković[1], Maja Vukašinović-Sekulić[3], Vesna Kojić[4] and Vesna Mišković-Stanković[3]

[1] *Innovation center of Faculty of Technology and Metallurgy, Karnegijeva 4, Belgrade, Serbia*
[2] *Institute for Technology of Nuclear and Other Mineral Raw Materials, Bulevar Franš d'Eperea 86, Belgrade, Serbia*
[3] *Faculty of Technology and Metallurgy, University of Belgrade, Karnegijeva 4, Belgrade, Serbia*
[4] *Faculty of Medicine, Oncology Institute of Vojvodina, University of Novi Sad, Dr Goldmana 4, Sremska Kamenica, Serbia*

Titanium (Ti) is the most widely used implant material due to its high corrosion resistance, and good mechanical properties. The biocompatibility and bioactivity of titanium can be significantly improved by the modification of its surface through the deposition of bioceramic coating on Ti [1]. Materials of choice were hydroxyapatite (HAP), chitosan (CS) and gentamicin because of their good properties. HAP is well known for its outstanding biocompatibility, chemical composition similar to natural bone and its ability to promote osseointegration. Improvement of mechanical and antimicrobial properties of the coating was achieved by addition of CS, biocompatible, natural polymer [2]. In order to improve antibacterial properties, and to avoid the occurrence of various inflammatory processes during implantation, a broad spectrum antibiotic gentamicin was added [3]. The combination of good mechanical properties of Ti, the bioactivity of HAP and good adhesion properties of CS enables the production of bone tissue implants with improved biological functions.

Cathodic electrophoretic deposition process (EPD) was employed for assembling composite HAP/CS and HAP/CS/Gent coating on Ti substrate (Figure 1.). EPD was carried out at the constant voltage on pure Ti plates from an aqueous suspension. The aim was to produce homogenous bioactive coatings with improved mechanical properties and remarkable antibacterial effects. Obtained coatings were characterized by Fourier transform infrared spectroscopy (FT-IR), X-ray photoelectron

spectroscopy (XPS) and field emission scanning electron microscopy (FE-SEM). Antibacterial properties of coatings were tested against two bacteria strains – *Staphylococcus aureus* and *Escherichia coli*, by agar diffusion test. Evaluation of relative cytotoxicity of obtained coatings was performed using MTT test. The ability of coatings to promote osseointegration was tested using ALP assay.

Obtained results confirmed the successful deposition of HAP/CS and HAP/CS/Gent coatings on Ti using EPD technique. Hydrogen bonding of functional groups of CS and HAP was confirmed by FT-IR analysis which also revealed several bands characteristic for CS. Due to low gentamicin content in HAP/CS/Gent coating, no characteristic bands corresponding to gentamicin were detected. The presence of gentamicin in HAP/CS/Gent was revealed by XPS analysis through the deconvolution of C1s peak that indicated binding of gentamicin to the matrix. Addition of the polymer significantly improved morphology, and bioactivity of thus formed composite. Morphology examination of HAP/CS and HAP/CS/Gent is represented in Figure 2. FE-SEM micrographs confirmed bioactivity of HAP/CS and HAP/CS/Gent after immersion in SBF. The rapid formation of apatite in a relatively short time (after only 7 days) showed coatings ability to promote bonding between natural bone and implants. MTT assay for HAP/CS and HAP/CS/Gent indicated low cytotoxicity against MRC-5 and L929 cell lines. Both composite coatings exhibited strong antibacterial activity against *S.aureus* and *E. coli*, indicating the high potential for biomedical applications. This effect was slightly more pronounced for the samples tested against *S. aureus*, for both HAP/CS and HAP/CS/Gent coatings.

Excellent osteogenic properties, through the promotion of osteoblast differentiation were confirmed by ALP assay. Results were much more pronounced for HAP/CS/Gent coating. Therefore, HAP/CS and HAP/CS/Gent coatings can be considered as an excellent promising candidate for biomedical hard tissue implants [4].

References:

[1] MS Đošić *et al*, J.Ind.Eng.Chem **47** (2017), 336.
[2] V Mišković-Stanković, M Đošić and A Janković, Pat. Appl. No. P-2017/0732, Intellect. Prop. Off. Repub. Serbia, Dated 19.07.2017.
[3] F Pishbin *et al*, ACS Appl. Mater. Interfaces **6** (2014), 8796.
[4] The authors acknowledge funding from the Ministry of Education, Science and Technological Development, Republic of Serbia (Grant No. III 45019).

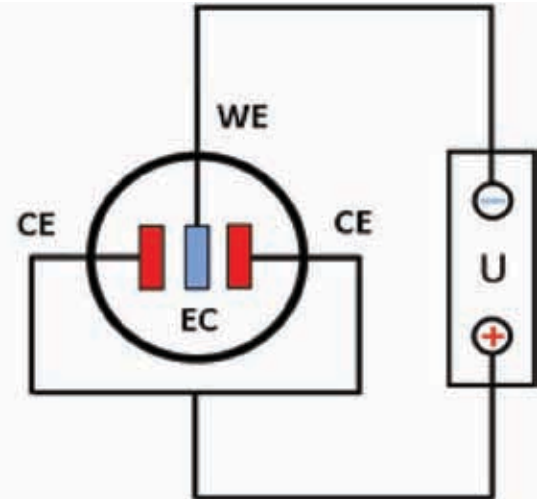

Figure 1. Scheme of electrochemical cell (EC): WE-working electrode, CE-counter electrode.

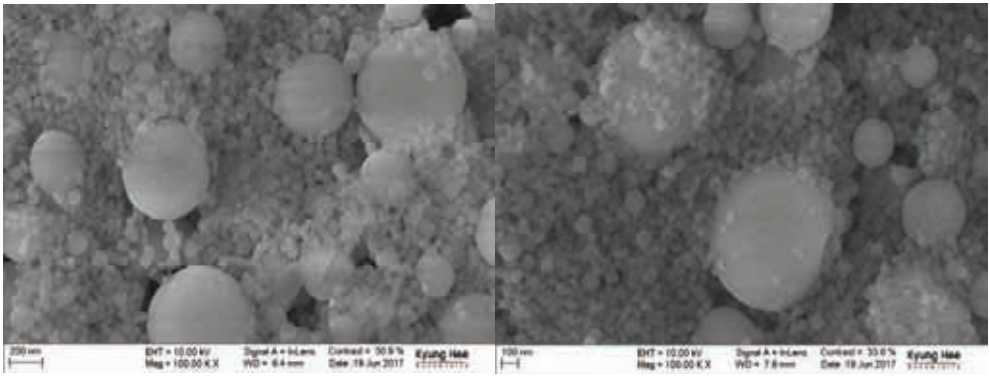

a) b)

Figure 2. FE-SEM micrographs of composite coatings: a) HAP/CS and b) HAP/CS/Gent.

Electrochemical Deposition of Ni in the Liquid Cell: Groundwork Experimental Approach Prior to LC TEM Experiments

Maja Koblar[1,3], Kristina Žužek Rožman[2], Sašo Šturm[2], Miran Čeh[1,2]

[1] *Center for Electron Microscopy and Microanalysis (CEMM), Jožef Stefan Institute, Jamova 39, 1000 Ljubljana, Slovenia.*
[2] *Department for Nanostructured Materials (K7), Jožef Stefan Institute, Jamova 39, 1000 Ljubljana, Slovenia.*
[3] *Jožef Stefan International Postgraduate School, Jamova 39, 1000 Ljubljana, Slovenia.*

Liquid cell transmission electron microscopy (LC TEM) has attracted significant interest in recent years and has been applied to many areas of research, ranging from chemistry to physics, materials science, and biology [1]. Incorporating a three electrode system into a liquid cell additionally enables *in-situ* observation of dynamic electrochemical processes, such as reduction of metallic cations in liquid solutions and subsequent deposition of metal elements at the work electrode at certain applied potential. Depending on the applied potential to the work electrode the morphology of deposited metals may be directly observed in TEM during deposition which provides valuable information on the kinetics and mass transport of material during electrochemical process.

In our work we report on experimental approach and our preliminary results of Ni electrodeposition from aqueous solution on a platinum working electrode in an electrochemical liquid cell [2]. The electrode array of the three electrode system of the electrochemical liquid cell is shown in Figure 1. Since assemblage of liquid cells and carrying out subsequent experiments in TEM is extremely challenging, it is advisable to optimize all experimental parameters prior to TEM analyses. This is why all the experiments were carried 'ex-situ', i.e. using optical microscope (OM) with subsequent SEM analysis.

A $NiSO_4$ starting aqueous solution (1M) was flown through the electrochemical cell at 300 µl/h. It was important that no bubbles were present in the electrochemical cell

during the experiment [3]. The potential between work electrode and Pt reference electrode (Pt_{REF}) was increased with 1 mV/s rate starting from 0 V towards negative potential vs. Pt_{REF} electrode. In our preliminary work the Ni deposition on Pt electrode was observed using OM with recording speed of 16 fps. Figure 2 shows deposition of Ni on Pt work electrode at sequentially applied potentials of 100 mV, 200 mV and 800 mV vs. Pt_{REF} electrode. One can observe that Ni preferentially nucleates at the edges of Pt work electrode. Uneven Pt electrode coverage with deposited Ni was attributed to the presence of appearing and disappearing bubbles, which are formed during electrochemical deposition which temporarily prevent local contact between the solution and the electrode surface. After the OM analysis the electrochemical cell was disassembled and the chips were cleaned with distilled water and air dried. Subsequent scanning electron microscopy / energy dispersive x-ray spectroscopy (SEM/EDS) analysis of the top electrochemical cell chip revealed dendritic growth of metal Ni with high surface to volume ratio and that the deposited Ni is of high purity (Figure 3).

Our preliminary results of Ni deposition from $NiSO_4$ aqueous solution using electrochemical liquid cell showed that it is possible to deposit pure Ni on Pt electrode which exhibits dendritic growth. Since all experimental parameters were successfully optimized ‘ex-situ’, our future experiments will be focused on studies of Ni nucleation and growth on the nano-scale in the TEM.

References:

[1] FM Ross, Science, **359** (2015), 6367.
[2] X Chen *et al*, Acta Mater. **60** (2012), 192.
[3] TJ Woehl and P Abellan, J. Microsc. **265** (2017) p. 135.

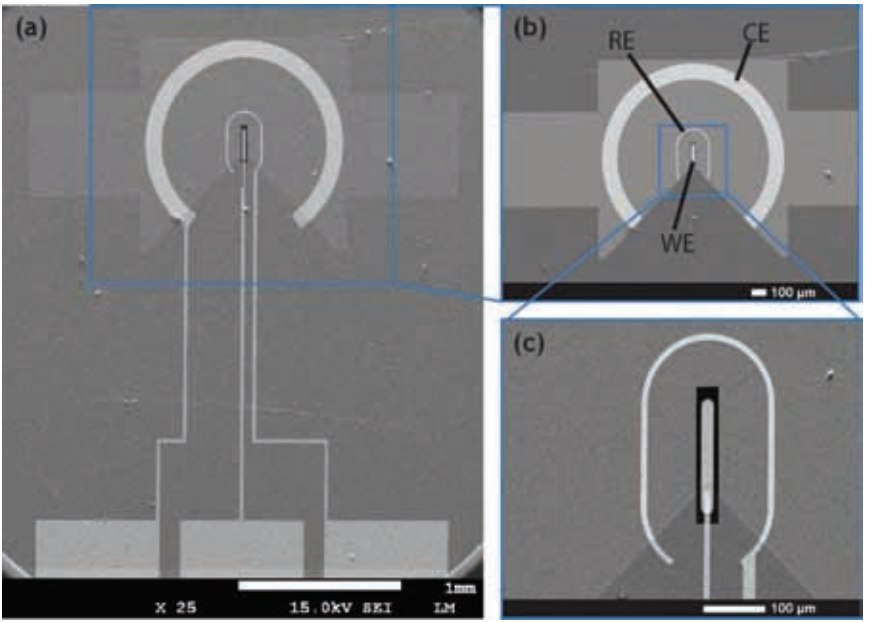

Figure 1. (a) SEM SEI image of top electrochemical chip. (b) A three electrode system: platinum work electrode (WE), reference electrode (RE) and counter electrode (CE). (c). Platinum WE is positioned in between SiN thin film windows.

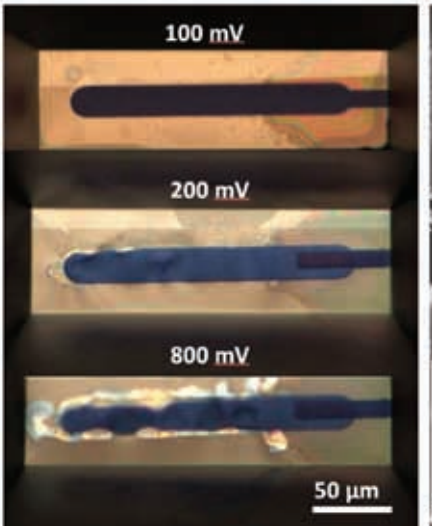

Figure 2. OM images of Ni deposition on platinum work electrode after subsequent increase of applied potential vs. Pt_{REF} electrode.

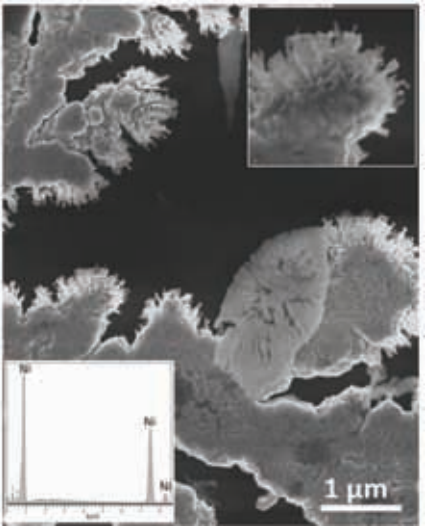

Figure 3. SEM image of Ni deposit. Dendritic growth can be observed (top right inset). EDX spectrum showing only Ni (bottom left inset).

Characterization Of Composite Polymer Membranes Modified By Electrospinning Method

Lana Putić[1], Jasna Stajić-Trošić[1], Branka Pilić[2], Vladan Ćosović[1], Aleksandar Grujić[1]

[1] *Institute of Chemistry, Technology and Metallurgy, University of Belgrade, Belgrade, Serbia*

[2] *Faculty of Technology, University of Novi Sad, Novi Sad, Serbia*

There has been considerable recent interest in membranes and membrane-based separation technologies because of their high separation and energy efficiency, reasonably low costs and easiness of operation. Generally speaking, a membrane essentially acts as a barrier between two phases that allows selective transport of one of the substances from one side to the other [1]. Consequently, pore structure is one of the key parameters that determines transport properties and selectivity of membranes. Nowadays, electrospun membranes are rapidly emerging as promising candidates for the development of high flux membranes due to their interconnected pore structure that enables shorter diffusion path and thus permits a higher flux of permeate [2]. An additional benefit of electrospun membranes is that they retain good mechanical properties even at considerably small thicknesses. Electrospinning is a common, simple and reliable method for producing smooth nanofibers with controllable morphology from a variety of different polymer materials [3]. By careful selection of process conditions and solution parameters highly porous structures of smooth, defect free nanofibers or non-woven membranes can be obtained [4]. Furthermore, owing to their nanoscale diameters and large aspect ratio nanofibers can act as a bond between nano and macrosize elements.

The aim of this study is to investigate the effect of surface modification by deposition of electrospun fibers on functional properties and performance of selected microporous polypropylene/polyethylene (PP/PE) polymeric membranes. Particular attention was paid on mechanical properties of the nanofiber coated membranes as one of the key parameters that could seriously limit their field of application along with the membrane efficiency in terms of reduction of the pore size [5]. The idea is to exploit the advantage that surface modification process using electrospinning

technique offers, which is that fiber diameter, surface area or composition, can be easily adjusted and thus membrane pore size distribution and/or selectivity to certain chemical species can be controlled.

The nanofiber webs were produced by means of a commercial electrospinning apparatus using the static configuration with plate collector and one syringe. The polyamide nanoweb was then coated by applying the previously optimized parameters onto three commercial PP/PE membranes produced by Viledon – Freudenberg Novatexx 2430, Novatexx 2465 and Novatexx 2473 with the thickness of 0.22 mm, 0.31 mm and 0.11 mm, respectively.

Microstructure and morphology of the unmodified and nanofiber coated were studied by field emission scanning electron microscopy (FESEM) using Tescan MIRA3 XM microscope. Thermal Analysis is applied using Differential Scanning Calorimetry (DSC) to investigate if the treatment could affect the arrangement of the polymer chains in terms of crystallinity. Fourier-transform infrared (FT-IR) spectroscopy analyses were conducted in order to confirm the chemical composition of the commercial membranes. The infrared (IR) spectra of studied samples were recorded by a BOMEM spectrometer (Hartmann & Braun, MB series). Tensile strength and elongation measurements are performed using Mark-10 ESM301 force test stand according to ASTM D638.

The results of microstructural and morphological characterization by FESEM reveal that the studied unmodified polymer membranes are composed of the random network of overlapping fibers that create multiply connected pores through which the fluid can flow. Furthermore, the obtained results for the nanofiber coated membranes suggest that nanofiber net with fibers of about 100 nanometer diameter was successfully produced and deposited onto membrane surface. This implies that the membrane pore size for diffusion of fluid is reduced to some extent but on the other hand it can also be concluded that the applied membrane modification process offers a possibility for micro- and ultra-filtration or combination of both. The FESEM micrographs presented in Figure 1 illustrate typical obtained net structures. From the application point of view, a tensile strength of membranes is a very important parameter and can be potentially increased by the applied modification procedure. The results of mechanical tests for the unmodified membranes show the differences in mechanical parameters such as maximum stress, strain and modulus of elasticity. In case of the nanofiber coated membranes, apart from the expected differences in selectivity due to pore size limits, differences in mechanical behavior can be observed as well.

References:

[1] FE Ahmed, BS Lalia and R Hashaikeh, Desalination **356** (2015), 15.

[2] X Song, Z Liu and DD Sun, Advanced Materials **23** (2011), 3256.
[3] Z-M Huang *et al*, Composite Science and Technology **63** (2003), 2223.
[4] Z Li and C Wang in "Effects of working parameters on electrospinning, One-Dimensional Nanostructures", (Springer, Berlin Heidelberg), p. 15.
[5] L Huang *et al*, Journal of Membrane Science **460** (2014), 241.
[6] This work has been supported by the Ministry of Education, Science and Technological Development of the Republic of Serbia (Projects TR34011, III45019 and ON172037).

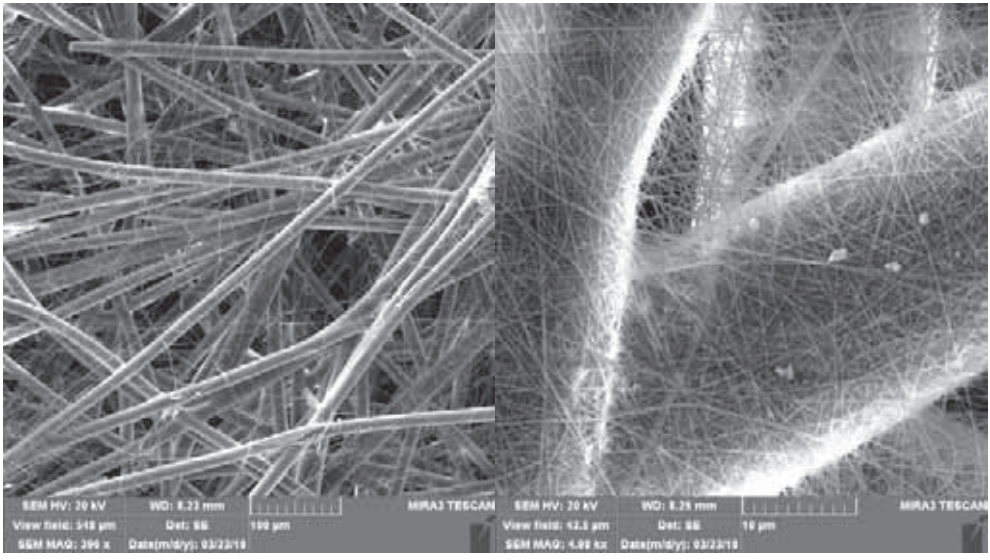

Figure 1. The FESEM micrographs of the membrane surface coated with nanofibers net structures.

Morphology of Poly(urethane-siloxane)/Montmorillonite Nanocomposites

Ivan S. Stefanović, Bojana M. Marković, Aleksandra B. Nastasović, Marija V. Pergal and Jasna V. Džunuzović

Institute of Chemistry, Technology and Metallurgy, Center of Chemistry, University of Belgrade, Njegoševa 12, 11000 Belgrade, Serbia.

Segmented polyurethanes (SPU) are multiblock copolymers consisted of hard (HS) and soft segments (SS). HS usually form crystalline domains that are responsible for good mechanical properties, while SS represent amorphous matrix that contributes to good elastomeric properties, hydrophobicity and inertness of the SPUs [1]. Furthermore, the morphology of the SPUs is one of the main factors that determine their physical and chemical properties. Moreover, thermodynamic incompatibility between HS and SS leads to the formation of microphase separation within the SPUs [2]. Properties of SPUs mostly come from their different composition and microphase separation between segments.

Further improvement of the properties of these materials is the main goal of the research lately. This often includes the addition of different inorganic nano-fillers, such as clay minerals, into a polymer matrix [3]. Dispersion and degree of the delamination of clay particles inside polymer matrix determine which type of polyurethane nanocomposite (PUNC) is obtained. Addition of low quantities of clay nano-fillers usually leads to the improvement of the thermal, mechanical, surface and barrier properties of the SPUs [4].

In this work series of PUNCs was obtained with the *in situ* polymerization method in solvent mixture. The PUNCs were based on α,ω-dihydroxy-poly(propylene oxide)-*b*-poly(dimethylsiloxane)-*b*-poly(propylene oxide) macrodiol (PPO-PDMS-PPO) that represents SS and 4,4′-diphenylmethane diisocyanate (MDI) and 1,4-butanediol (BD) which were selected as the HS. PUNCs were synthesized with different content of HS (from 10 to 60 wt%), with the addition of organomodified montmorillonite clay (Cloisite 30B®) as the nano-filler, in an amount of 1 wt%. The PUNCs are marked so that the last two numbers in title indicate mass.% of HS in

samples [5]. For nanostructural examinations, SEM and TEM analysis were performed on the obtained polymer films. SEM analysis was performed on JEOL JSM-6460LV instrument on the cross-section surface of the samples, at a magnification of 3k ×. TEM analysis was performed on the JEM-1400 Plus Electron microscope, at a magnification of 60k ×.

The morphology of the obtained PUNCs, i.e. dispersion of the clay nanoparticles inside polymer matrix, was investigated by SEM analysis. SEM micrographs show the presence of brighter parts („points“) in the investigated samples, which originate from the addition of clay nanoparticles (Figure 1). In addition, it is observed that the clay nanoparticles are homogeneously dispersed in the polymer matrix and do not form aggregates in the tested samples. This type of morphology increased the degree of the microphase separtion, that led to the better mechanical properties of the investigated samples.

In order to determine clay morphology inside PUNCs, TEM analysis was performed (Figure 2). On the obtained TEM micrographs darker lines represent individual layers of the clay nanoparticles, which are homogeneously dispersed within the lighter polymer matrix. Moreover, clay nanoparticles had predominantly exfoliated morphology with a small number of those that had intercalated morphology in the PUNCs. This indicates mainly complete delamination of the clay nanoparticles within polymer matrix. This occurred due to the reaction between organomodifier from clay and isocyanate groups in prepolymer. Within the polymer matrix, dispersed clay nanoparticles have the length between 50 and 250 nm and the distance between layers greater than 5 nm [5].

Series of the PUNCs based on PPO-PDMS-PPO, MDI, BD and with addition of montmorillonite clay as a nano-filler was successfully synthesized. SEM and TEM analysis confirmed homogeneous dispersion and obtained mixed exfoliated/intercalated morphology of the clay nanoparticles within the polyurethane matrix [6].

References:

[1] W Tang *et al*, Macromolecules **27** (1994), 2814-2819.
[2] R Adhikari *et al*, J. Appl. Polym. Sci. **78** (2000), 1071-1082.
[3] JC Wang *et al*, High Perform. Polym. **21** (2009), 155-171.
[4] MW Ho *et al*, Compos. Struct. **75** (2006), 415-421.
[5] IS Stefanović *et al*, Appl. Clay Sci. **149** (2017), 136-146.
[6] This work was financially supported by the Ministry of Education, Science and Technological Development of the Republic of Serbia (Project No. 172062 and Project No. III 43009).

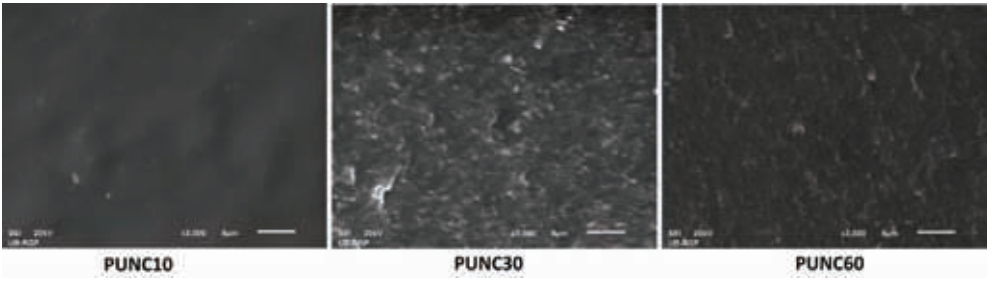

Figure 1. SEM micrographs of cross-section surface of the selected PUNCs with 10, 30 and 60 wt.% of HS (magnification 3k ×).

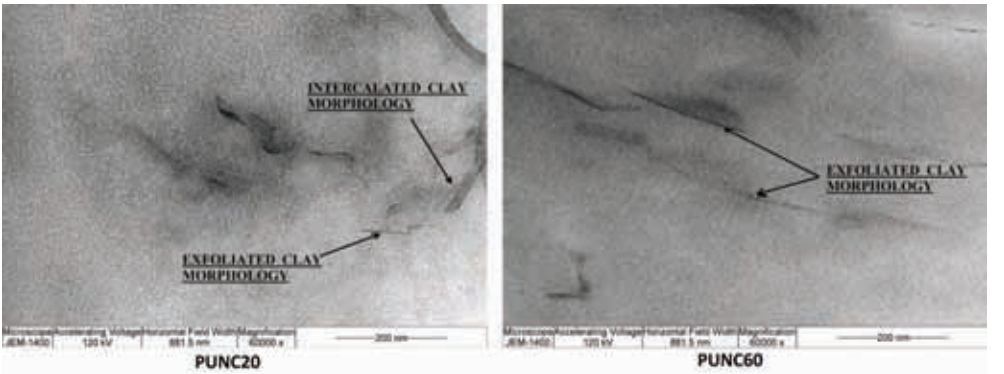

Figure 2. TEM micrographs of the selected PUNCs with 20 and 60 wt.% of HS (magnification 60k ×).

Morphology, Biocompatibility and Antimicrobial Activity of Hydroxyapatite Simultaneously Doped with Silver and Strontium Ions

Djordje Veljovic[1], Zeljko Radovanovic[1], Suzana Dimitrijevic-Brankovic[1], Vesna Kojic[2], Rada Petrovic[1] and Djordje Janackovic[1]

[1] *University of Belgrade, Faculty of Technology and Metallurgy, Department of Inorganic Chemical Technology, Karnegijeva 4, 11120 Belgrade, Serbia.*

[2] *University of Novi Sad, Faculty of Medicine, Oncology Institute of Vojvodina, Put Dr Goldmana 4, 21204 Sremska Kamenica, Serbia.*

Biomaterials based on hydroxyapatite (HAp) due to its approved biocompatibility, possibility for chemical bonding with the hard tissue and also its evident osteogenic potential, are irreplaceable part of dental and orthopedic practice [1,2]. Various cations are usually incorporated in HAp structure instead of calcium and have an important role in a large number of physiological processes in human body. Strontium, as an ion with a dual role in bone metabolism, improves osteoblast differentiation, proliferation and activity and on the other hand simultaneously inhibits osteoclast proliferation, can also affect the changes of the lattice dimensions, particle size, crystallinity and solubility of the synthesized HAp powders. The substitution of optimal amount of calcium ions with strontium is of great interest for development of novel bioceramic materials [3,4]. On the other hand, the incorporation of silver ions in bioceramic structures as an antimicrobial agent could inhibit the bacteria adhesion on the implant surface after incorporation into the body [5]. The aim of this study was to optimize the antimicrobial activity and biocompatibility of silver and strontium doped HAp based bioceramic materials.

HAp powders doped with various amounts of strontium and silver ions related to calcium were synthesized by modified hydrothermal method at 160 ºC for 3 h. For all experiments (Ca+Ag+Sr)/P molar ratio was kept at a constant value of 1.67. After deposition of a thin gold/palladium layer on the powder surface, a TESCAN MIRA 3 XMU field emission scanning electron microscope, operated at

20 keV, was used to analyze the morphology of the obtained powders. Spherically agglomerated nanosized HAp powder (Fig. 1.) doped with 0.4 mol % of Ag and 0.5-5.0 mol % of Sr ions in relation to calcium were successfully synthesized. Energy dispersive spectroscopy (EDS), tip Oxford Inca 3.2, coupled with the scanning electron microscope Jeol JSM 5800, operated at 20 keV, confirmed the presence of Sr and Ag in synthesized powders. Incorporated strontium ions affected the size of primary rod-like particles, and furthermore had the effect on the density, hardness and fracture toughness of sintered samples.

On the basis of the antimicrobial properties against *Staphylococcus aureus* and *Escherichia coli* it can be concluded that strontium could enhance the antimicrobial effect of silver doped bioceramic materials. The *in vitro* cellular biocompatibility tests on MRC-5 human fibroblasts showed that obtained Sr- and Ag-doped HAP materials exhibited no cytotoxic effects and that the cytotoxicity decreased with the prolongation of the incubation time. Biocompatibility tests also revealed that the powder doped with 5.0 mol% Sr and 0.4 mol% Ag had highest stimulatory effect on the growth of the MRC-5 cells and that stimulated cellular proliferation more effectively compared to pure HAp and Ag-doped HAP. The attachment, material/cell interface and the shape of MRC-5 human cells during intimate contact with sintered bioceramic samples was observed by using the JEOL-JSM 6460LV microscope. The shape of the cell in Fig. 2. indicates their excellent spreading over the Ag- and Sr-doped HAp bioceramic material and the position of their cytoplasm extensions indicates good proliferation and adequate metabolic activity.

Based on the powder morphology, examined sinetrability, biocompatibility and antimicrobial activity it could be concluded that simultaneously doped HAp powders with Sr and Ag could be a good basis for processing dense, control porous and scaffold bioceramics as well as bioactive, biocompatible and antimicrobial active ceramic fillers for different composite biodegradable forms.

References:

[1] J Chevalier and L Gremillard, J Eur Ceram Soc **29** (2009), 1245.
[2] Dj Veljovic *et al*, J Biomed Mater Res A **100** (2012), 3059.
[3] Y Li *et al*, Biomater **31** (2010), 9006.
[4] K Lin *et al*, Biomater **34** (2013), 10028.
[5] Z Radovanovic *et al*, App Surf Sci **307** (2014), 513.
[6] The authors wish to acknowledge the financial support for this research from the Ministry of Education, Science and Technological Development, Republic of Serbia through the project III45019.

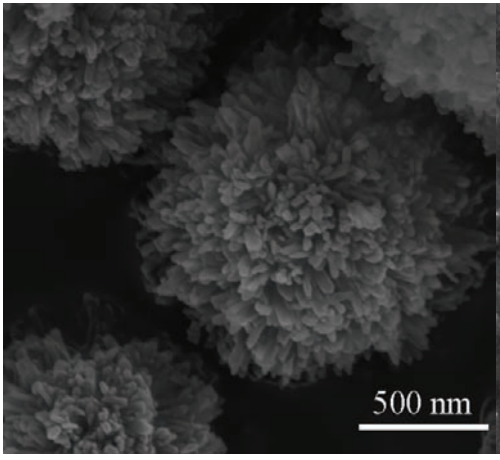

Figure 1. SEM micrograph of HAp powder doped with 3.0 mol% Sr and 0.4 mol% Ag.

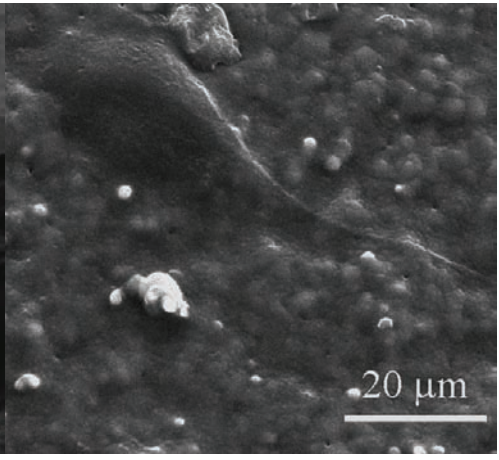

Figure 2. SEM micrograph of MRC-5 cell coupled with sintered HAp bioceramic doped with 5.0 mol% Sr and 0.4 mol% Ag.

Nanocomposite Hydrogels Based on Poly(vinyl alcohol) and Chitosan with Silver Nanoparticles and Graphene Aimed for Wound Dressing Applications

Katarina Nešović[1], Ana Janković[1], Maja Vukašinović-Sekulić[2], Aleksandra Perić-Grujić[2] and Vesna Mišković-Stanković[2]

[1] *Innovation center of the Faculty of Technology and Metallurgy, Karnegijeva 4, Belgrade, Serbia*
[2] *Faculty of Technology and Metallurgy, University of Belgrade, Karnegijeva 4, Belgrade, Serbia*

There is a growing need to improve existing biomedical devices for severe wound dressings that would protect the lesion from physical damage and keep the surrounding local tissue moisturized and at the same act as antibacterial barrier for prolonged periods of time. Bacteria, especially in-hospital strains, are quickly developing resistance towards traditional antibiotics; so many studies are directed towards developing wound dressing based on alternative antibacterial agents. Silver nanoparticles (AgNPs) are long known and used for this purpose, owing to their strong antibacterial and antimycotic activity. A problematic aspect of metallic nanoparticle application is their instability and tendency to agglomerate, thereby altering and incapacitating desirable properties of NPs. This problem is often overcome by using polymer stabilizers such as poly(vinyl alcohol) (PVA) and chitosan (CHI), to bind AgNPs and prevent their aggregation, while allowing their release when applied to the wound site.

PVA is a synthetic biocompatible polymer, used for almost half a decade in various branches of biomedicine, among others for wound dressing applications. Chitosan is a natural biocompatible and biodegradable polysaccharide with intrinsic antibacterial properties and polycationic nature – properties which render it desirable biomedical material in applications such as wound dressings and drug delivery. Graphene (Gr) is a relatively recently discovered material with many extraordinary properties, and it has been shown to improve the mechanical properties, such as tensile strength and elasticity, of polymer-based matrices [1], which is especially desirable for topical applications where wound dressing should retain its structural integrity and mechanical strength over longer periods of time, in order to avoid the need for frequent replacement and thus possible trauma to the wound [2].

In this work, we prepared hydrogels based on PVA, CHI and Gr, and used them as a porous matrix to synthesize silver nanoparticles by an *in situ* electrochemical method [3,4]. The hydrogels were prepared from PVA/CHI/Gr colloid dispersions using a simple and effective freezing-thawing method for gelation, without the use of chemical cross linkers. The hydrogels were then swollen in $AgNO_3$ solution to saturate with Ag^+ ions and subsequently subjected to constant-voltage electrical current, to reduce silver ions and to obtain AgNPs. This electrochemical method is fast and green, as there is no need for the use of any (potentially toxic) chemical cross linkers and reducing agents, rendering the final product non-toxic and safe for medical applications.

The obtained silver/poly(vinyl alcohol)/chitosan/graphene (Ag/PVA/CHI/Gr) were characterized by field-emission scanning electron microscopy (FE-SEM) and energy-dispersive X-Ray spectroscopy (EDS), UV-visible and Raman spectroscopies and X-ray photoelectron spectroscopy (XPS). Additionally, the swelling ability and silver release behavior were monitored in phosphate buffer (PB) at 37 °C. The effect of chitosan content on physico-chemical and biological properties of the nanocomposite hydrogels was also investigated. Antibacterial activity was evaluated using disc-diffusion method and test in suspension, against *Staphylococcus aureus* and *Escherichia coli* bacterial strains.

The results indicated the higher concentration of AgNPs in hydrogels with more chitosan, as determined by UV-vis spectroscopy and EDS analysis. Additionally, the antibacterial activity of hydrogels with higher CHI content was stronger towards both *S. aureus* and *E. coli*. FE-SEM (Figure 1) confirmed smaller sizes of AgNPs with the increase of chitosan content in the hydrogel. Silver release studies indicated diffusion-controlled mechanism with initial burst behavior followed by the period of slower and steadier release up to 28 days. All these results confirmed the strong potential for the use of Ag/PVA/CHI/Gr nanocomposite hydrogels in biomedical applications as topical wound dressings with improved properties. [5]

References:

[1] R Surudžić *et al*, Journal of Industrial and Engineering Chemistry **34** (2016), 250.
[2] J Koehler, FP Brandl and AM Goepferich, European Polymer Journal **100** (2018), 1.
[3] K Nešović *et al*, Corrosion **73** (2017), 1437.
[4] M M. Abudabbus *et al*, Composites Part B: Engineering **140** (2018), 99.
[5] The authors acknowledge funding from the Ministry of Education, Science, and Technological Development of the Republic of Serbia, Grant Number III 45019.

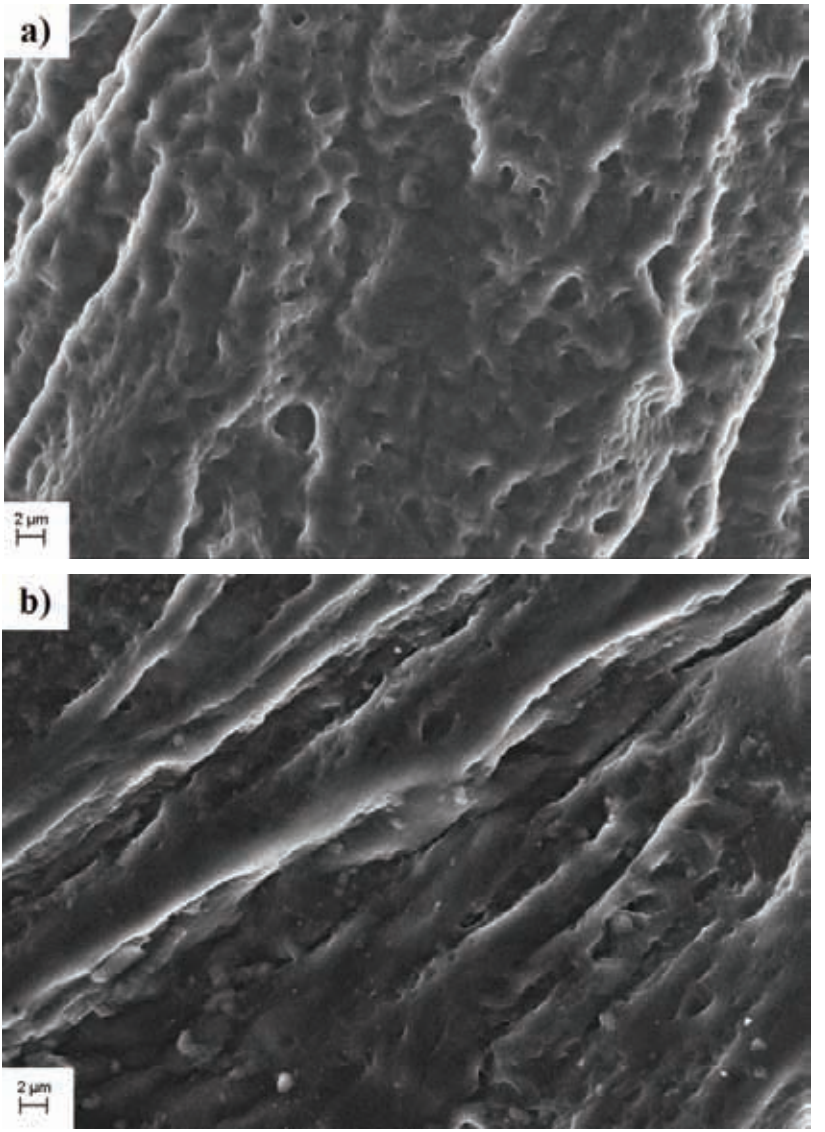

Figure 1. FE-SEM micrographs of a) PVA/CHI/Gr and b) Ag/PVA/CHI/Gr nanocomposite hydrogels

Bacteria-Based Self-Healing System for Concrete Structures

Snežana Vučetić[1], Andrijana Sever Škapin[2], John M. van der Bergh[1], Bojan Miljević[1], Ivan Ristić[1], Siniša Markov[3], Ana Vidaković[3], Olja Šovljanski[3] and Jonjaua Ranogajec[1]

[1] *University of Novi Sad, Faculty of Technology, Dept. of Materials Engineering, Novi Sad, Serbia*

[2] *Slovenian National Building and Civil Engineering Institute, Ljubljana, Slovenia*

[3] *University of Novi Sad, Faculty of Technology, Dept. of Biotechnology and Pharmaceutical Engineering, Novi Sad, Serbia*

The interest in self-healing materials for preventive repair of concrete structures is increasing. The presence of cracks inside the concrete structures is a common phenomenon, which leads to reduction of functionality and service life of concrete structures. The novel bacterial based self-healing approach could be a good solution for the reduction of crack network development inside the concrete structures, thus leading to the growth of its sustainability [1,2].

The motivation of our work was to investigate repair potential (self-healing) of newly prepared cement materials based on encapsulated bacteria. We performed several imaging techniques for detection and evaluation of cracks inside the cement-based concrete structures, as well as to monitor influence of the newly developed materials on the concrete self-healing capacity. The study included the use of the IR (thermographic) camera in localization of the newly developed materials (polymer encapsulated bacteria) in cement prisms, which presents a precondition for self-healing process. The development of this process was imaged by Low Vacuum Scanning Electron Microscopy. The following materials were examined: polymer material (hydrogel), bio-polymer system (bacterial culture *Sporosarcina pasteurii* DSM33 encapsulated in the hydrogel), standard cement mortar specimens (compliant to EN 196-1:2017), standard cement mortar specimens with the addition of polymer material, and standard cement mortar specimens with the addition of bio-polymer system. For these experiments, all bio-polymer systems had been previously frozen using liquid nitrogen and subsequently subjected to fracturing (fresh cross-sections were studied).

The obtained results indicate that in the initial phase of cement hydration no negative effects were caused by the addition of hydrogel/bio-polymer system in cement mortars, regarding the mortar microstructural and mechanical properties. Moreover, the products of hydration were more developed in the case of hydrogel/bio-polymer addition (Figure 1). Also, examination by Low Vacuum Scanning Electron Microscopy of the developed bio-polymer based material has shown that the used bacterial culture was successfully encapsulated (Figure 2).

The presented results have proven that imaging techniques can be very useful for the characterization of the bio-polymer based self-healing concrete. However, it requires specific sample preparation and precisely programmed time of analysis. It leaves room for further optimisation of sample preparation and analysis conditions [3].

References:

[1] D Sun, Advances in Colloid and Interface Science **in press** (2018).
[2] J Xu and X Wang, Construction and Building Materials **167** (2018), 1-14.
[3] The authors would like to acknowledge the funding and support from the Ministry of Education, Science and Technological Development of the Republic of Serbia (contract No. III45008) and the COST Action CA 15202 “Self-healing As prevention Repair of COncrete Structures (SARCOS)”.

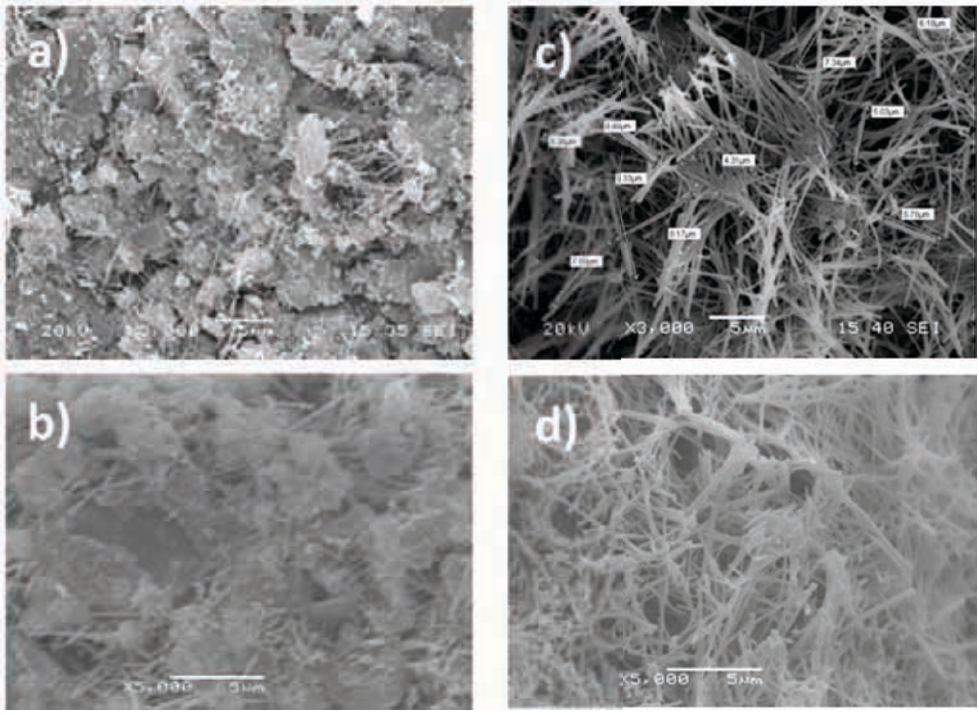

Figure 1. SEM micrographs of standard cement prisms - a) and b); and SEM micrographs of the cement prisms with bio-polymer system - c) and d).

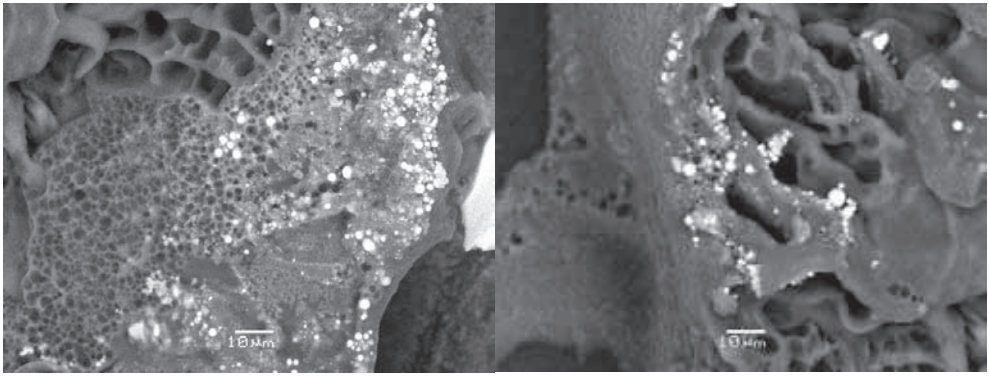

Figure 2. SEM micrographs of encapsulated bacterial culture (white spheres) in bio-polymer system.

Processing and Characterization of Hydroxyapatite/tricalcium Phosphate Biomaterials for Obtaining Scaffolds

Željko Radovanović[1], Saša Vasilijić[2], Djordje Veljović[3], Ivona Janković-Častvan[3], Slavica Lazarević[3], Rada Petrović[3], Djordje Janaćković[3]

[1] *University of Belgrade, Innovation Center of the Faculty of Technology and Metallurgy, Karnegijeva 4, Belgrade 11070, Serbia.*
[2] *University of Defense, Institute for Medical Research Military Medical Academy, Faculty of Medicine of Military Medical Academy, Crnotravska 17, Belgrade 11000, Serbia.*
[3] *University of Belgrade, Faculty of Technology and Metallurgy, Karnegijeva 4, Belgrade 11070, Serbia.*

Calcium phosphates constitute the inorganic part of bones and teeth of mammals. This fact is well known and has encouraged researchers to apply hydroxyapatite (HAp, $Ca_{10}(PO_4)_6(OH)_2$) and α- and β-TCP tricalcium phosphate (TCP, $Ca_3(PO_4)_2$) as implant materials [1,2]. Their similarity to the inorganic part of hard tissues was confirmed [3], highlighting their biocompatibility and osteoconductivity and in addition bioactivity of HAp and bioresorbability of TCP [1,4]. The biphasic forms (BCP): HAp/*β*-TCP and HAp/*α*-TCP and triphasic form HAp/*β*-TCP/*α*-TCP are of particular interest because they have proved to be even better biomaterials than pure, single phases [4,5].

Hydroxyapatite (HAp) powders doped with Si^{4+}, Ag^{+}, Cu^{2+} and Zn^{2+} were synthesized by a hydrothermal method, at a Ca/P ratio of 1.50, in order to obtain biomaterial with an antimicrobial effect (powders: HAp, Si-HAp, Ag-HAp, Cu-HAp, AgCuSi-HAp and AgZnSi-Hap). Doping with silicon ions was aimed at stabilizing the TCP phase during calcination [6]. On the other hand, copper and zinc are micronutrients that at low concentrations are necessary for the functioning of many processes in humans, but at large concentrations are toxic [7–9]. The synthesized powders were calcined at 1100 and 1150 °C in order to obtain powders suitable for scaffold processing.

Analyses of all powders, undoped and doped HAp and HAp/α-TCP, were performed by Field emission scanning electron microscopy (FESEM), Energy-dispersive X-Ray spectroscopy (EDS) and X-Ray diffraction (XRD).

The cytotoxicity of the powders calcined at 1150 °C was evaluated based on their action on metabolic activity, cell proliferation, production of reactive oxygen species (ROS) and necrosis of L929 cell. The Si-HAp powder had reduced metabolic activity, while the AgCuSi-HAp powder significantly decreased the proliferative activity of L929 cells, which indicate their potential cytotoxic effect. However, confirmation of cytotoxic activity in these materials was not obtained at the level of cell necrosis and was not accompanied by significantly higher production of ROS.

References:

[1] SV Dorozhkin, Ceramics International **41** (2015), 13913.
[2] E Champion, Acta Biomaterialia **9** (2013), 5855.
[3] LL Hench, Journal of the American Ceramic Society **81** (1998), 1705.
[4] SV Dorozhkin, Acta Biomaterialia **8** (2012), 963–977.
[5] Y Xie *et al*, Biomaterials **27** (2006), 2761.
[6] B Jokic *et al*, Materials Letters **74** (2012), 155.
[7] KM Hambidge and N Krebs, The Journal of Nutrition **137** (2007), 1101.
[8] AS Prasad, British Medical Journal **326** (2003), 409.
[9] BR Stern and R Bonnie, Journal of Toxicology and Environmental Health, Part A **73** (2010), p. 114.
[10] The authors acknowledge funding from the Ministry of Education, Science and Technological Development of the Republic of Serbia, Grant Number III45019.

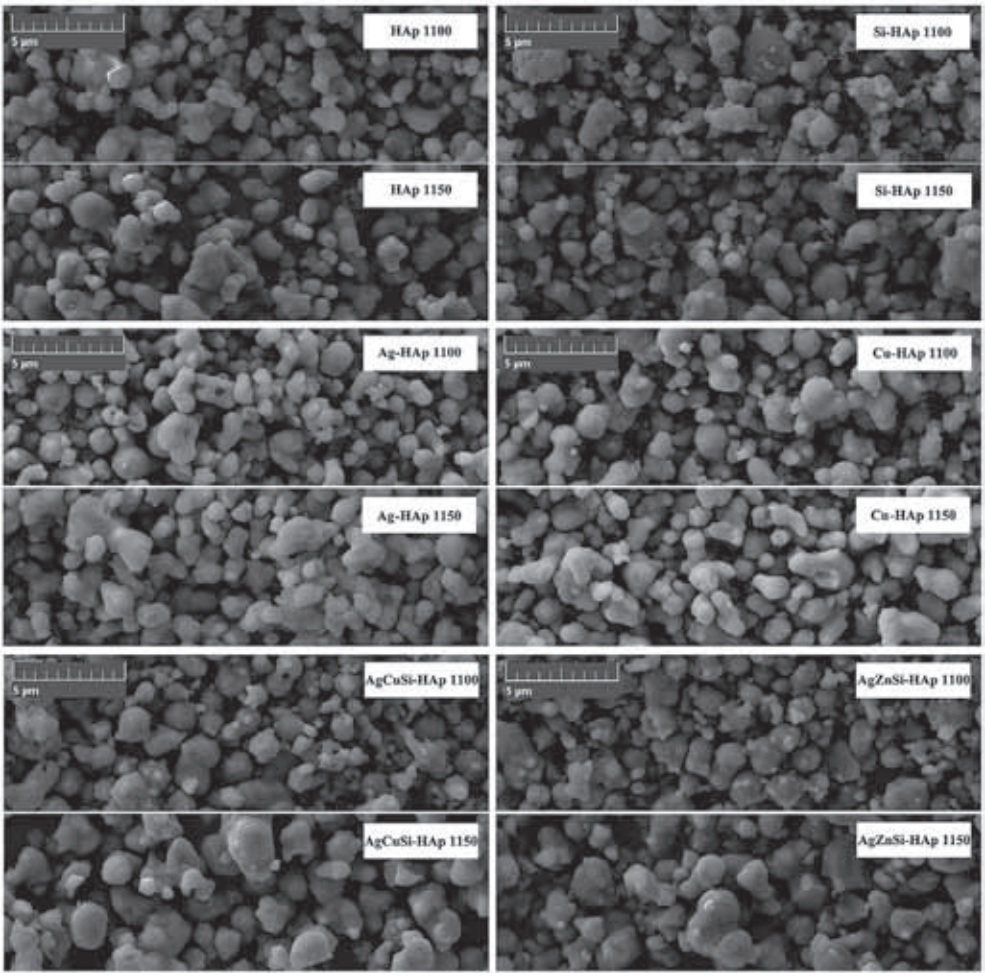

Figure 1. SEM images of powders calcined at 1100 and 1150 °C.

Synthesis of Phosphate Based Bioactive Glass-ceramics Scaffolds

Vladimir S. Topalović[1], Srđan D. Matijašević[1], Jelena D. Nikolić[1], Marija S. Đošić[1], Veljko V. Savić[1], Sonja V. Smiljanić[2], Snežana R. Grujić[2]

[1] *Institute for the Technology of Nuclear and Other Mineral Raw Materials, 86 Franchet d' Esperey St, 11000 Belgrade, Serbia*
[2] *Faculty of Technology and Metallurgy, University of Belgrade, Karnegijeva 4, 11000 Belgrade, Serbia*

In recent years, because of dissolution behavior, bioactivity and biocompatibility, there is an expanding interest for development and application of phosphate-based glasses as biomaterials in medicine [1, 2]. These glasses are preferable than silica-based glasses because of their more controllable dissolution rate [3, 4]. A number of techniques have been developed to fabricate bioactive porous glass–ceramic scaffolds for application in bone tissue engineering [5-7]. In this paper, the 3D macroporous bioactive glass–ceramic scaffolds based on $42P_2O_5$•40CaO•5SrO•$10Na_2O$•-$3TiO_2$ (mol %) glass were prepared by polyurethane (PU) foam replication technique and analyzed.

The appropriate batch composition of raw materials was melted at 1250 °C for 0.5 h in a Pt crucible. Obtained glass samples were transparent, without visible residual gas bubbles. In order to obtain desired particle size (< 5μm), the glass sample was ground at 400 rpm during 1h in a SFM-1 Desk-Top Planetary Ball Miller, MTI Corporation.

The polymeric template used for scaffolds preparation was a commercial PU sponge. The sponge cubes were soaked into the glass slurry, compressed, dried and thermally treated (650 °C, 1h) in order to remove the organic phase and to obtain macroporous glass-ceramic scaffolds. The sintering temperature for glass was chosen according to DTA and HSM experiment performed previously [8].

Scaffolds structure and morphology were analyzed by stereo microscope (EU Instruments) and a scanning electron microscope (MIRA X 3 TESCAN). The phase composition of the sintered scaffold was determined by XRD analysis using a Philips PW-1710 automated diffractometer.

Figure 1, shows the structure of PU sponge, used as scaffolds template that exhibits 3-D network of pores, which vary in size from 100 to 600 μm. In Figure 2, the SEM micrograph of PU skeleton coated with glass particles is shown. As may be seen in Figure 3, the morphology of the scaffold sintered at T = 650 °C for 1h remains highly porous without significant decrease of the pore size. The images revealed that the pore struts are well sintered.

XRD analysis of the powdered scaffold showed that during sintering the glass particles crystallized and the crystalline phases determined are: $Ca(PO_3)_2$, β-$Ca_3(PO_4)_2$, α-$Ca_2P_2O_7$ and β-$Ca_2P_2O_7$ (Figure 4). For β-$Ca_3(PO_4)_2$ and β-$Ca_2P_2O_7$ the bioactivity, i.e. the ability to promote the formation of apatite (HAP) layer after reaction with the surrounding body fluid has been reported [9]. The obtained phase composition and the microstructure of as-prepared scaffold indicated its possible application as a bioactive material for bone tissue engineering [10].

References:

[1] EA Abou Neel *et al*, Journal of Materials Chemistry **19** (2009), 690.
[2] C Vitale-Brovarone, E Verne and P Appendino, Journal of Materials Science: Materials in Medicine **17** (2006), 1069.
[3] MN Rahaman *et al*, Acta Biomaterialia **7** (2011), 2355.
[4] N Lakhkar *et al*, Journal of Biomaterials Applications **25** (2011), 877.
[5] C Vitale-Brovarone *et al*, Journal of Materials Science: Materials in Medicine **15** (2004), 209.
[6] T Livingston, P Ducheyne, and J Garino, Journal of Biomedical Materials Research **62** (2002), 1.
[7] J Jones, L Ehrenfried and LL Hench, Biomaterials **27** (2006), 964.
[8] V Topalović *et al*, Proceedings of Thirteenth Young Researcher's Conference, Materials Science and Engineering (2014), 7.
[9] T Kitsugi *et al*, Biomaterials **16** (1995), 1101.
[10] The authors are grateful to the Ministry of Education and Science, Republic of Serbia for financial support (Projects TR 34001 and OI 172004).

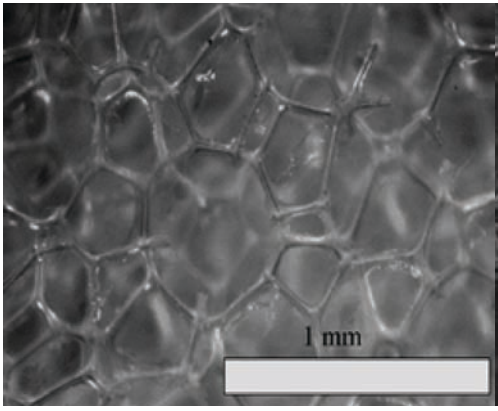

Figure 1. Bare PU sponge.

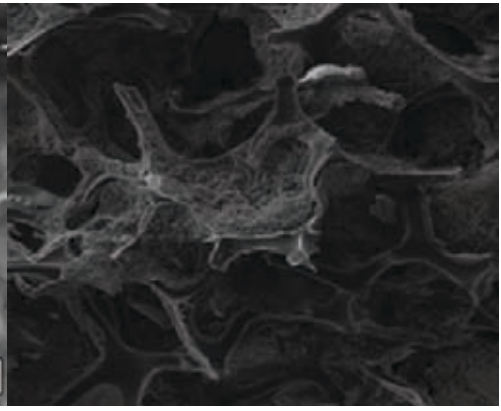

Figure 2. SEM micrograph of PU sponge covered with glass particles.

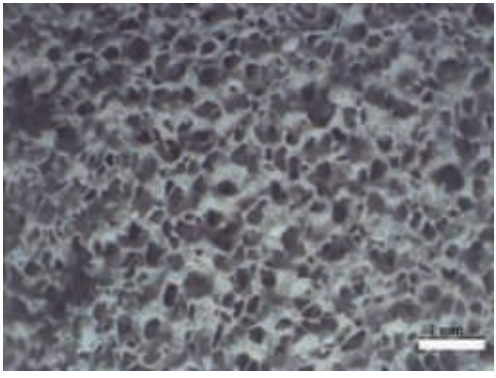

Figure 3. Sintered glass-ceramics scaffold structure.

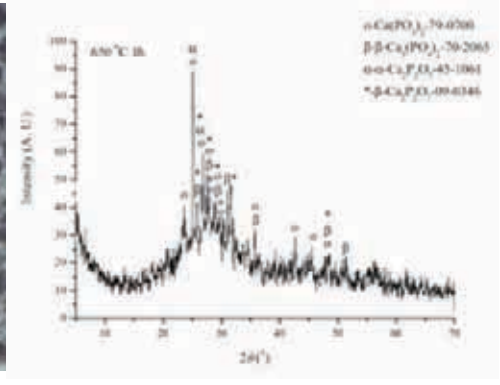

Figure 4. XRD pattern of the sintered scaffold.

Assessment of Three Microscopic Techniques in Observing Morphology of Pygidial Glands of Ground Beetles

Marija Nenadić[1], Aleksandar Krmpot[2], Nikola Vesović[1], Mihailo Rabasović[2], Srećko Ćurčić[1], Danica Pavlović[2], Vesna Lačković[3], Svetlana Savić-Šević[2] and Dejan Pantelić[2]

[1] *Institute of Zoology, University of Belgrade - Faculty of Biology, Belgrade, Serbia*
[2] *Institute of Physics, University of Belgrade, Belgrade, Serbia*
[3] *Institute of Histology and Embryology "Aleksandar Đ. Kostić", University of Belgrade - Faculty of Medicine, Belgrade, Serbia*

Pygidial glands represent an exocrine glandular system situated in abdomen of ground beetles and other representatives of the suborder Adephaga within the order Coleoptera [1]. This system plays a major role in the defense against predators [2] by discharging its products (secretions) outwards. It includes two sets of secretory lobes, collecting canals, collecting reservoirs and efferent ducts [1,3]. From a biological point of view, observing pygidial glands of ground beetles is important in taxonomy and promising due to potential medical significance of the secretions [4,5]. In order to better understand glandular functional mechanisms, it is necessary to examine the morphological aspects in detail.

Morphology of pygidial gland structures of certain ground beetle species (Insecta: Coleoptera: Carabidae) has been observed via three different microscopic techniques. Scanning electron microscopy (SEM), two-photon excitation fluorescence (TPEF) microscopy and conventional light microscopy (LM) were applied in order to identify complementarity of different methods of investigating the above-mentioned morphological structures. It is indisputable fact that the highest information content (level of details) on external morphology of biological structures is obtained by SEM. Examination of soft, fragile structures by SEM includes preparation of samples in a *series of alcohol/acetone* solutions of *increasing* concentrations up to 100% followed by a critical point drying (CPD), which is a well-established method for dehydrating biological tissues. In the case of pygidial glands of ground beetles, it has been noticed that tissue drying was excessive, resulting in the irreversible damage.

Samples somewhat changed their shape and their volume shrunk, precluding detailed analysis (Fig. 1a). This is not the case when CPD is omitted, and dehydration is applied only through a *series of ethanol* solutions of *increasing* concentrations (30, 50, 70, 90 and 100%) (Fig. 1b).

Concerning simplicity of different techniques, undeniable advantage must be given to LM (Fig. 2a), although the flaw of this technique is its insufficient informativity regarding a detailed insight into micro- and nanostructures of pygidial gland system (e.g., arrangement of reservoir myofibrils; diameter of collecting and efferent ducts; diameter, thickness and a more detailed structure of radial canals of secretory lobes). Additional three-dimensional information is obtained by TPEF (Fig. 2b). On the basis of all advantages/disadvantages of the three microscopy techniques compared, it can be concluded that the combination of SEM and TPEF enables the most detailed morphological and anatomical surveys of analyzed biological structures [6].

References:

[1] A Giglio *et al*, ZooKeys 100 (2011), 193-201.
[2] K Dettner, Annual Review of Entomology **32** (1987), 17-48.
[3] DJ Forsyth, Transactions of the Zoological Society of London **32** (1972), 249-309.
[4] M Nenadić *et al*, Bulletin of Entomological Research **106** (2016), 474-480.
[5] M Nenadić *et al*, The Science of Nature **103** (2016), 34.
[6] This study is financially supported by the Serbian Ministry of Education, Science and Technological Development (Grants Nos. ON173038, ON171038 and III45016).

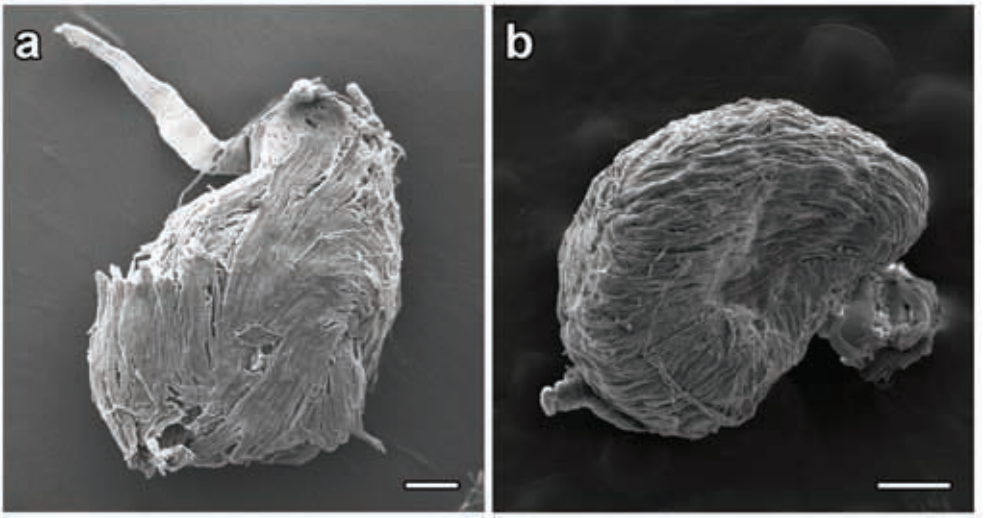

Figure 1. Morphology of a muscle-coated collecting reservoir of pygidial glands of ground beetle species *Laemostenus* (*Pristonychus*) *punctatus* (Dejean, 1828). SEM image after treating sample with CPD (a) and without this procedure (b). Scales: 200 μm.

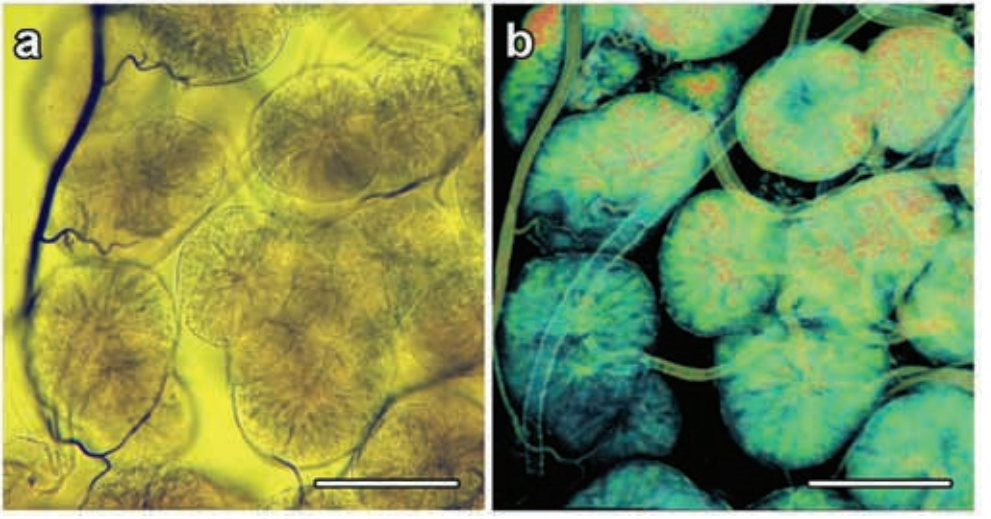

Figure 2. Pygidial gland secretory lobes associated with afferent ducts of ground beetle species *Carabus* (*Eucarabus*) *ullrichii* Germar, 1824. Comparison of images taken using LM (a) and TPEF microscopy (b). Scales: 100 μm.

Electron Tomography Analysis of Human Islet Amyloid Polypeptide crystalline structures in *Drosophila Melanogaster*

Ling Xie[1], Xiaohong Gu[2], Kenta Okamoto[3], Gunilla T Westermark[2] and Klaus Leifer[1]

[1] *Department of Engineering Sciences, Applied Materials Sciences, Uppsala University, SE-75121, Uppsala, Sweden*
[2] *Department of Medical Cell Biology, Uppsala University, SE-75123, Uppsala, Sweden*
[3] *Department of Biology Physics, Uppsala University, SE-75123, Uppsala, Sweden*

In human, more than 30 different proteins can misfold and form amyloid. Examples of amyloid proteins are amyloid beta precursor protein (AβPP) and human islet amyloid polypeptide (hIAPP). Both these form long slender fibrils (10 nm in diameter and more than 1um long) in man. AβPP deposits in brain and is a cardinal finding in Alzheimers dementia and hIAPP is a polypeptide hormone that deposits in pancreas and leads to destruction of the insulin producing beta cells [1].

The structural analysis on the misfolded protein aggregations provide important data to understand the driven force of protein aggregation and how the proteins are expressed in different biological environments. In this work, we have applied electron tomography (ET) technique on transmission electron microscopy (TEM) to study the three dimensional (3D) structure of hIAPP aggregates in Drosophila model.

Expression of human islet amyloid polypeptide (hIAPP) in neurons of Drosophila melanogaster leads to the formation of aggregates in the fat body tissue surrounding the brain. We determined the structure of these membrane-encircled non-amyloid-like aggregates using ET. In Figure 1., a crystalline structure of hIAPP protein aggregate was observed and 3D lattice of hIAPP granules were constructed of two unit cells, a body centered tetragonal (BCT) and a triclinic unit cell. A 5-fold twinned structure was observed and it is comprised of the cyclic twinning of the BCT and triclinic unit cells.

We selected 30 protein granules along the (001) and (101) lattice planes in BCT structures and the (001) and (100) lattice planes in triclinic structures and used the

single particle analysis algorithm to average the contrasts of the selected particles generating the classifications. From the class-averaged particles, we clearly discerned the protein granules were interconnected by thin filament like structures. This observation indicates that the interaction between the two nearest hIAPP granules in both unit cells is not only governed of the van der Waals forces but potentially also by filament-like structures that can connect the nearest neighbors. Such directional interactions between the nearest neighbors cogently explain the formation of our observed crystalline structures. Hence, our 3D structural analysis provides novel insight into the aggregation process of hIAPP in the fat body tissue of Drosophila melanogaster.

The multifunctional fat body tissue can be used for the storage of protein and also for detoxification. To determine if aggregates can be recycled, 30 days old hIAPP female flies were starved for 24 hours and 48 hours. Investigation after starvation showed a complete disappearance of aggregates and supports our theory that formation of aggregates represents an important biological function. In summary, this observation of aggregate morphology together with the structural analysis shows aggregates evolve in a dynamic way during the life span of the Drosophila melanogaster.

References *:*

[1] JD Sipe *et al*, Amyloid-Journal Protein Fold. Disord. **21** (2014), 221–224.

[2] The authors acknowledge funding from VR K2016-02297 (GTW) Family Ernfors Research Fund, Swedish Diabetes Foundation.

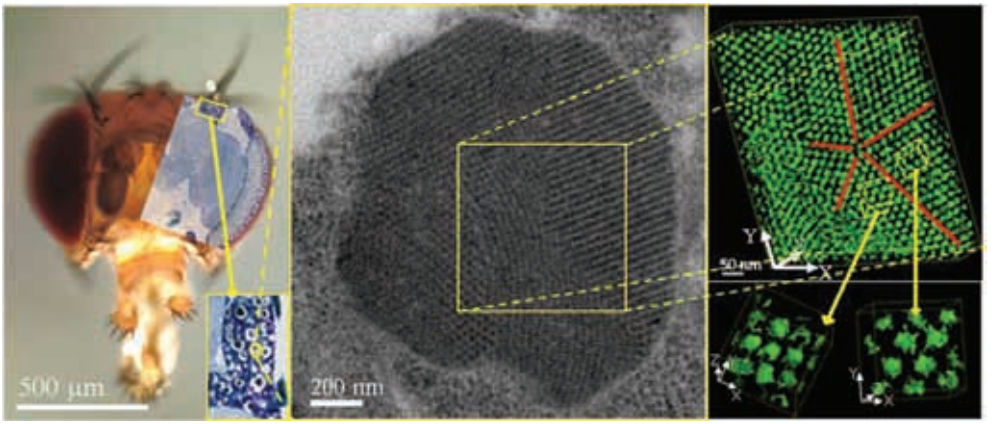

Figure 1. (Left) 2D optical image of a Drosophila head, (Middle) 2D TEM image of Amyloid peptides aggregates, (Right) Segmented protein aggregates in 3D volume showing 5 fold twining structure.

Metformin and Itraconazole Combination is Effective Against Fibrosarcoma in Hamsters

Kosta J. Popović[1], Dušica J. Popović[2], Dušan Lalošević[2], Dejan Miljković[2], Ivan Čapo[2], Jovan K. Popović[3]

[1] *Department of Pharmacy, Faculty of Medicine, University of Novi Sad, Novi Sad, Republic of Serbia*
[2] *Department of Histology and Embryology, Faculty of Medicine, University of Novi Sad, Novi Sad, Republic of Serbia*
[3] *Department of Pharmacology, Toxicology and Clinical Pharmacology, Faculty of Medicine, University of Novi Sad, Novi Sad, Republic of Serbia*

We have carried out small-scale research on anticancer effects of metformin and itraconazole combination. Possibilities of synergistic anticancer metformin-itraconazol interactions and multitargeting safe therapy, based on the previous separate preclinical investigations, are the main reasons for antitumor testing of their combination on our experimental fibrosarcoma model in hamsters. Our aim was to give modest contribution to accelerated development of effective, safe and a low-cost adjuvant anticancer treatment with nontoxic drugs that are already registered for other indications.

Metformin exhibited anticancer effects *in vitro* in number of various cancer cell lines. The anticancer effects of metformin were explained by different mechanisms [1, 2]. In our previous experiment, we found anticancer effects of metformin on BHK-21/C13 fibrosarcoma in hamsters [3]. In diabetic patients, metformin is usually comedicated with the most common and safest antimicotic agent itraconazole, since fungal infections are frequent in diabetes. This combination is nontoxic in humans. Itraconazole, like metformin, possesses anticancer properties. Multiple common or diverse mechanisms of anticancer action of metformin [3] and itraconazole [4] were identified.

24 Syrian golden hamsters of both sexes, weighing approximately 100 g, were randomly allocated to 4 equally sized groups. 2 x 10^6 BHK-21/C13 cells in 1 ml were injected subcutaneously into the animals' back. The first group started peroral treatment with physiological solution, the second with metformin 500 mg/kg daily, the

third with itraconazole 250 mg/kg daily and the fourth with a combination of metformin 500 mg/kg and itraconazole 250 mg/kg daily, via a gastric probe 3 days before tumor inoculation. After 3 weeks, when the tumors were approximately 2 cm in the first group, all animals were sacrificed. The blood was collected for glucose and other analyses. The tumors were excised and weighed and their diameters were measured (Figure 1). The tumor samples were pathohistologically (HE) and immunohistochemically (Ki-67, CD 31, COX IV, GLUT-1, iNOS) assessed (Figure 2) and the main organs toxicologically analyzed. Tumor volume was determined using the formula $LxS^2/2$, where L was the longest and S the shortest diameter. Ki-67-positive cells in the tumor samples were quantified. Images were taken and processed by software UTHSCSA Image Tools for Windows Version 3.00. Statistical significances were determined by the Student´s *t*-test.

Peroral treatment with a metformin and itraconazole combination significantly inhibited fibrosarcoma growth in hamsters without toxicity. This was verified by significantly decreased tumor weight and volume and by reduced proliferation status of tumor cells, shown by Ki-67 staining on hamster tumor sections. Pathohistological and immunohistochemical evaluation revealed a decrease in tissue penetration, an expansion of necrosis and hemorrhagic areas and a reduction of vasculature in all analyzed slices of tumors (Figure 2) treated with the combination of metformin and itraconazole, when compared with control group.

Our results led us to conclude that administration of metformin in combination with itraconazole may be candidate for an effective and safe nontoxic anticancer adjuvant and relapse prevention treatment [5].

References:

[1] X Sui *et al*, Mol Pharm **12** (2015), 3783.
[2] B Dirat *et al*, Mol Cancer Ther **14** (2015), 586.
[3] DJ Popović *et al*, Eur Rev Med Pharmacol Sci **21** (2017), 5499.
[4] H Tsubamoto *et al*, Oncol Lett **14** (2017), 1240.
[5] The authors acknowledge funding from the Republic of Serbia, Autonomous Province of Vojvodina, Provincial Secretariat for High Education and Scientific Research, Grant No. 142-451- 2469/2017 (JP) and Republic of Serbia, Ministry of Education, Science and Technological Development, Grants No. 171039 (JS) and 172013 (DM).

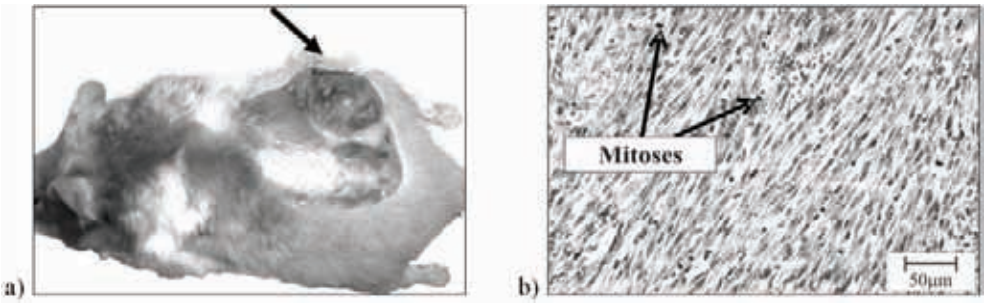

Figure 1. a) BHK fibrosarcoma in hamster; b) mitoses.

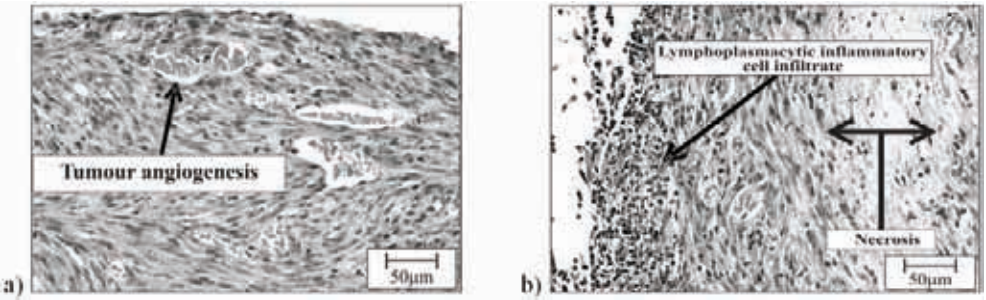

Figure 2. BHK fibrosarcoma: a) tumour angiogenesis; b) lymphoplasmacytic inflammatory cell infiltration and tumour necrosis.

Synergistic Anticancer Interaction of Metformin and Caffeine on Fibrosarcoma in Hamsters

Dušica J. Popović[1], Dušan Lalošević[1], Dejan Miljković[1], Kosta J. Popović[2], Ivan Čapo[1], Jovan K. Popović[3]

[1] *Department of Histology and Embryology, Faculty of Medicine, University of Novi Sad, Novi Sad, Republic of Serbia*
[2] *Department of Pharmacy, Faculty of Medicine, University of Novi Sad, Novi Sad, Republic of Serbia*
[3] *Department of Pharmacology, Toxicology and Clinical Pharmacology, Faculty of Medicine, University of Novi Sad, Novi Sad, Republic of Serbia*

We investigated the effect of metformin and caffeine on fibrosarcoma in hamsters. We were guided by the idea that the use of nontoxic repurposed drugs in arrangement with other medication should be effective against cancer, with decreased toxicity.

Based on the separate *in vitro* evidence of metformin's [1] and caffeine's [2] antifolate activity, we perceived a possible synergistic anticancer effect of these drugs. The finding that caffeine enhanced pemetrexed's antifolate activity in the four studied mesothelioma cell lines was important for our research motivation [2]. Like metformin, caffeine can induce apoptosis in various human cancer cell lines, such as neuroblastoma [3], lung [4] and pancreatic [5] adenocarcinomas, leukemia cells [6] and non-small lung carcinoma [7]. Furthermore, caffeine enhances the toxicity of radiation and sensitivity of cancer cells to chemotherapy [8].

32 Syrian golden hamsters of both sexes, weighing approximately 100 g, were randomly allocated to 3 experimental and 2 control groups, with a minimum of 6 animals per group. 2 x 10^6 BHK-21/C13 cells in 1 ml were injected subcutaneously into the animals' back in 4 groups. The first experimental group started peroral treatment with metformin 500 mg/kg daily, the second with caffeine 100 mg/kg daily and the third with a combination of metformin 500 mg/kg and caffeine 100 mg/kg daily, via a gastric probe 3 days before tumor inoculation. After 2 weeks, when the tumors were approximately 2 cm in the control group, all animals were sacrificed. The blood was collected for glucose and other analyses. The tumors were excised and weighted and their diameters were measured. The tumor samples

were pathohistologically (HE) and immunohistochemically (Ki-67, CD 31, COX IV, GLUT-1, iNOS) assessed (Figure 1) and the main organs toxicologically analyzed, including the control animals that had received metformin and caffeine. Tumor volume was determined using the formula $LxS^2/2$, where L was the longest and S the shortest diameter. Ki-67-positive cells in the tumor samples were quantified. Images were taken and processed by software UTHSCSA Image Tools for Windows Version 3.00. Statistical significances were determined by the Student´s *t*-test.

Our results show that the combination of metformin and caffeine inhibited fibrosarcoma growth in hamsters without toxicity.

We concluded that the administration of metformin with caffeine might be an effective and safe approach in novel nontoxic adjuvant anticancer treatment.

References:

[1] B Corominas-Faja *et al*, Aging **4** (2012), 480.
[2] SH Min, ID Goldman and R Zhao, Cancer Chemother Pharmacol **61** (2008), 819.
[3] MH Jang *et al*. J Korean Med Sci **17** (2002), 674.
[4] W Qi, D Qiao and JD Martinez, Radiat Res **157** (2002), 166.
[5] B Gururajanna *et al*, Int J Mol Med **4** (1999), 501.
[6] Y Dai *et al*, Cancer Res **61** (2001), 5106.
[7] M Hałas *et al*, Cent Eur J Biol **9** (2014), 727.
[8] S Saiki *et al*, Autophagy **7** (2011), 176.
[9] The authors acknowledge funding from the Republic of Serbia, Autonomous Province of Vojvodina, Provincial Secretariat for High Education and Scientific Research, Grant No. 142-451- 2469/2017 (JP) and Republic of Serbia, Ministry of Education, Science and Technological Development, Grants No. 171039 (BM) and 172013 (SD). The excellent technical assistance and suggestions of el. eng. Mrs. Vesna Popović during the preparation of this work are gratefully acknowledged.

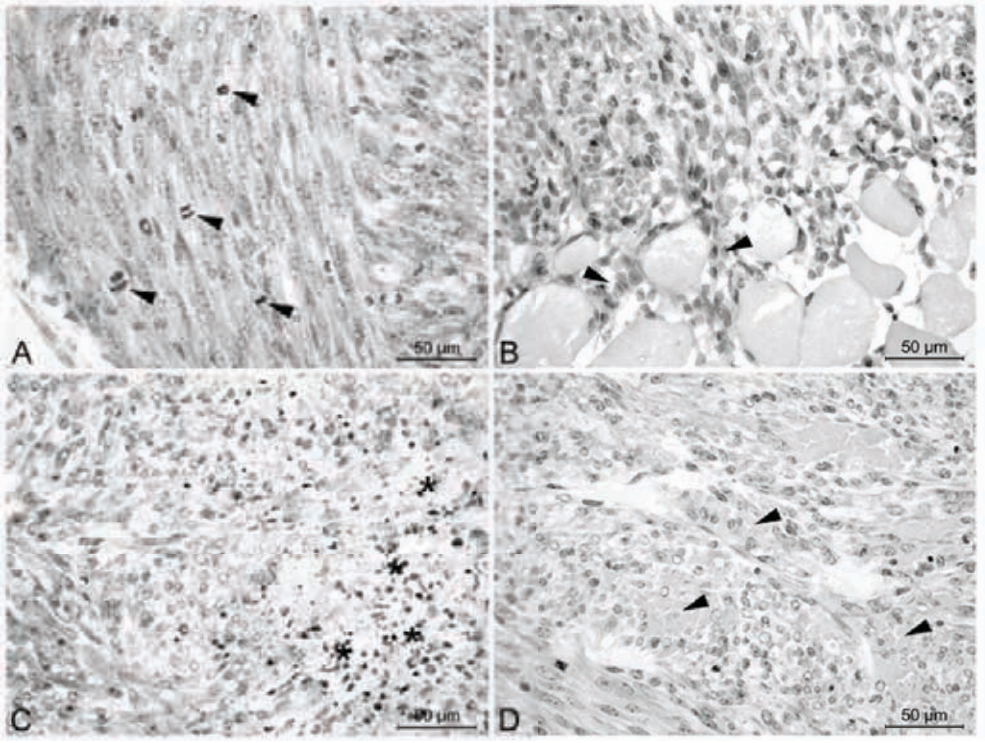

Figure 1. BHK fibrosarcoma: A) mitoses; B) penetration into skeletal striated muscle; C) multiple areas of tumor necrosis; D) tumor vasculature and hemorrhagic areas.

Differential Polarization Laser Scanning Microscopy (DP-LSM) -Technique for Rapid Screening of Cell Walls of Different Plant Species

Jasna Simonović Radosavljević[1], Daniela Djikanović[1], Gabor Steinbach[2], Aleksandra Lj. Mitrović[1], Jelena Bogdanović Pristov[1], Győző Garab[3], Ksenija Radotić[1]

[1] Institute for multidisciplinary study, University of Belgrade, Kneza Višeslava 1, 11000 Belgrade, Serbia
[2] Institute of Biophysics, Biological Research Center, Szeged 6701, Hungary
[3] Institute of Plant Biology, Biological Research Center, Szeged 6701, Hungary

Plant cell walls represent the most abundant, renewable and biodegradable composite on Earth. It forms a large part of the plant body and defines its characteristics. The specific form and function of the cell walls and interaction with the environment are based on variation in its chemical composition and connections between the building macromolecules. The secondary cell walls are rich in biopolymers such as cellulose, hemicellulose and lignin, but the most abundant component is cellulose [1-3].

DP-LS microscopy is a useful and easily applicable technique for rapid screening of cell wall structural order, by mapping the linear dichroism of cellulose fibrils [4]. It allows screening and quantification of the alignment of cellulose fibrils, relative to one another, in cell walls [5]. The goal was to provide new information about structural characteristics of the isolated cell walls among species which may be a basis for their possible applications, such as biofuel and biomaterial industry, but also to understand what plant response to stress is.

We applied DP-LS microscopy to compare alignment of cellulose fibrils in cell walls of spruce, maize and liana (*D.balcanica*).

The confocal fluorescence intensity images were recorded on a Zeiss LSM 410 laser scanning microscope (Carl Zeiss Jena, Jena, Germany) equipped with a differential polarization (DP) attachment [6, 7]. The images were in resolution of 512x512 dots, covering the area of 50x50 and 64x64 μm. Each image consists of two channels: FDLD channel and fluorescence emission channel. FDLD values for dipoles

oriented along the Y axis correspond to 1, while the values of dipoles oriented along the X axis correspond to -1. The FDLD values are in the range from -1 to +1 due to the definition: FDLD = (I1-I2)/(I1+I2). (I1 fluorescence intensity was measured with vertically, I2 with horizontally polarized excitation). The acquired 8-bit TIFF images were set to have a color scale from blue (#0000FF) to yellow (#FFFF00) for the FDLD channel. The samples of isolated cell walls were stained with freshly prepared 2 % (w/v) solution of Congo Red for 1h, followed by rinsing in distilled water three times. Samples were excited at 488 nm, and fluorescence emission was observed above 560 nm.

Distribution of linear dichroism was analyzed on images of the cell wall (Fig. 1). Width of obtained distribution curves indicates degree of linear order in the analyzed structures. The distributions show a quite similar orientation for the three species. However, the narrowest is for maize, corresponding to simpler structure and more regular packing (observed parallel linear structures) of cellulose molecules than in the wood species.

The DP-LSM method is shown to be a simple and rapid way to check the structural complexity in the cell wall through cellulose labeling.

References:

[1] A Bacic, PJ Harris and Stone BA (1988) in: “The Biochemistry of Plants”, ed. J Preiss, (Academic Press, Inc., New York) p. 297-371.
[2] M O’Neill, P Albersheim and A Darvill in “ Methods in Plant Biochemistry”, ed. Dey PM, (Academic Press, London) p. 415–441.
[3] L Salmén and A-M Olsson, Journal of Pulp and Paper Science **24** (1998), 99-103.
[4] G Steinbach *et al*, Cytometry **73A** (2008), 202–208.
[5] A Savić *et al*, Microsc Microanal **22**(2016), 361–367
[6] G Garab *et al*, US Patent 6856391 (2005).
[7] G Steinbach *et al*, Acta Histochem **111** (2009), 316–325.

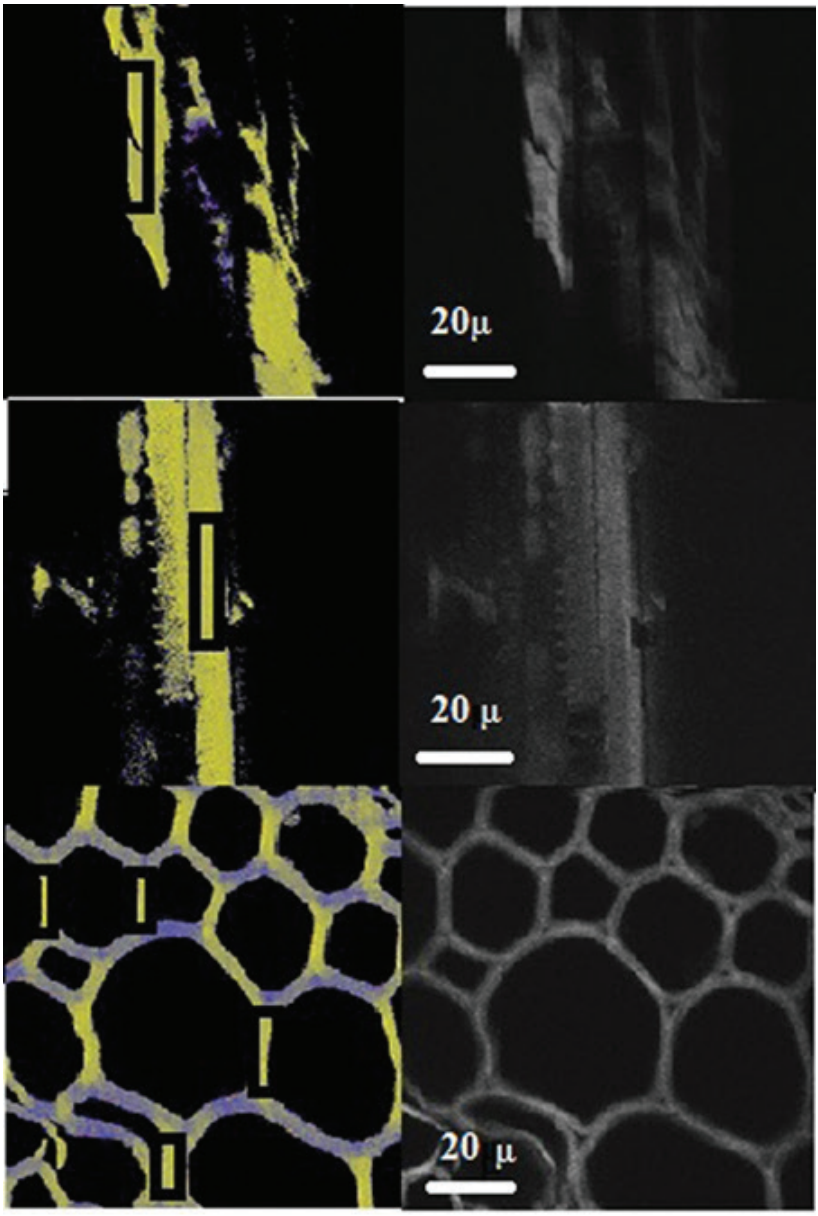

Spruce

Maize

Liana

Figure 1. Confocal fluorescence-detected linear dichroism (FDLD) measurements (left panel), confocal fluorescence intensity (right panel) of the isolated cell walls of spruce, maize and liana stained with Congo Red.

Transmission Electron Microscopy in Evaluation of Curcumin Nanoparticles Cellular Uptake

Tamara Kravic-Stevovic[1], Tamara Martinovic[1], Darko Ciric[1], Verica Paunovic[2], Biljana Ristic[2], Zoran Markovic[3], Biljana Todorovic-Markovic[4], Milica Kosic[2], Jovana Prekodravac[4], Matej Micusik[3], Zdeno Spitalsky[3], Vladimir Trajkovic[2], Ljubica Harhaji-Trajkovic[5] and Vladimir Bumbasirevic[1]

[1] *Institute of Histology and Embryology, School of Medicine, University of Belgrade, Visegradska 26, Belgrade 11000, Serbia*
[2] *Institute of Microbiology and Immunology, School of Medicine, University of Belgrade, Dr Subotica 1, Belgrade 11000, Serbia*
[3] *Polymer Institute, Slovak Academy of Sciences, Dubravska cesta 9, 84541 Bratislava, Slovakia*
[4] *Vinca Institute of Nuclear Sciences, University of Belgrade, P.O. Box522, Mike Petrovica Alasa 12-14, Belgrade 11001, Serbia*
[5] *Institute for Biological Research "Sinisa Stankovic", University of Belgrade, Despot Stefan Blvd. 142, Belgrade 11000, Serbia*

Curcumin, a principal active component of an Indian spice is known for its anticancer properties [1]. With the use of transmission electron microscope (TEM) we here analyzed cellular uptake of blue light (470 nm, 1 W)-irradiated curcumin nanoparticles (NC), using U251 glioma cells as targets. TEM imaging was performed on Morgagni 268D electron microscope (FEI, Hillsboro, OR), operated at 80 kV. Nanocurcumin colloid was prepared using tetrahydrofuran/water solvent exchange method [2]. Tumor cell line U251 were maintained at 37°C in a humidified atmosphere with 5% CO_2, in a RPMI 1640 cell culture medium supplemented with 5% fetal calf serum and 1% penicillin/streptomycin. Cells were detached by the conventional trypsinization procedure, resuspended in culture medium without (control) or with NC (5 μg/ml), and the obtained suspensions were illuminated using the in-house-built blue lamp with 1 W blue LED (465–475 nm) for 1min. After irradiation, cell suspensions were diluted in cell culture medium and transferred to 96-well plates (2 x 10^4 cells/well in 200 μl). After 30 min incubation, cells were fixed in 3% glutaraldehyde, postfixed in 1% osmium tetroxide, dehydrated in graded alcohols, and then embedded in Epon812. The ultrathin sections were

stained in uranyl acetate and lead citrate, and examined with TEM. Although most of the NC were washed in the process of preparation for the TEM analysis, few nanoparticles remained in the intercellular space, but none of them were found in the cytoplasm of NC treated cells in the absence of irradiation. However, nanoparticles were detected in the cytoplasm of NC-treated tumor cells irradiated with the blue light as soon as 30 min after treatment. Having in mind that the intracellular nanoparticles were not observed within vesicles, it seemed that endocytosis was not responsible for their uptake. Importantly, the cell membrane appeared intact on the electron micrographs, arguing against the possibility that NC passively entered the cells through the damaged membrane. In malignant cells with internalized NC disintegrated mitochondria were observed indicating cell damage induced by NC. Our results thus suggest that the blue light irradiation stimulates the cellular uptake of NC. However, it remains to be investigated whether the changes in nanocurcumin itself and/or tumor cells induced by irradiation were responsible for its uptake [3].

References:

[1] WH Lee *et al*, Curr Neuropharmacol **11** (2013), 338–378.
[2] ZM Markovic *et al*, J Serb Chem Soc **79** (2014), 1–11.
[3] The authors acknowledge funding from the Ministry of Education, Science and Technological Development of the Republic of Serbia (grants 41025, 172003, and 173053), by the SASPRO Program project 1237/02/02-b and the People Program (Marie Curie Actions) European Union's Seventh Framework Program under REA grant agreement No. 609427 (grant to ZM). Research has been further co-funded by the Slovak Academy of Sciences.

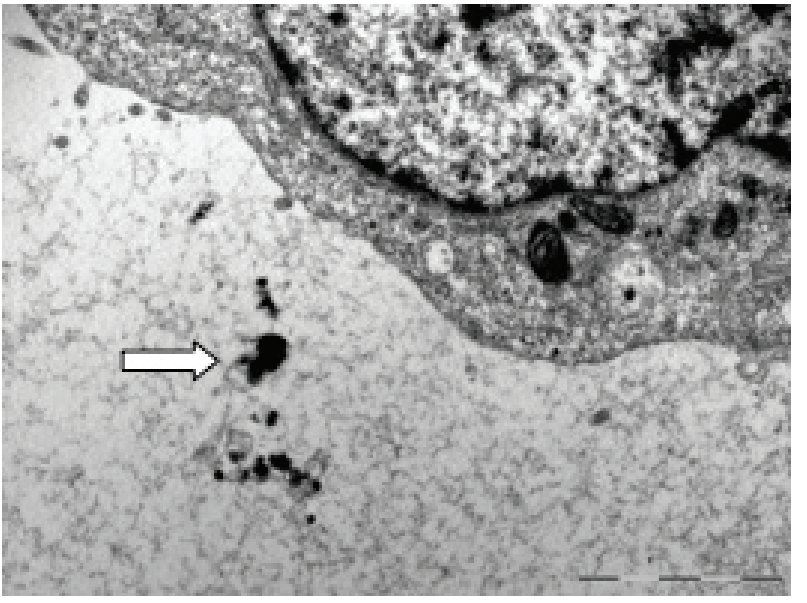

Figure 1. TEM ultramicrograph of U251 cells incubated with NC (5 μg/ml) showing NC out of the cells (arrow); magnification 11000x, scale bar 2 μm.

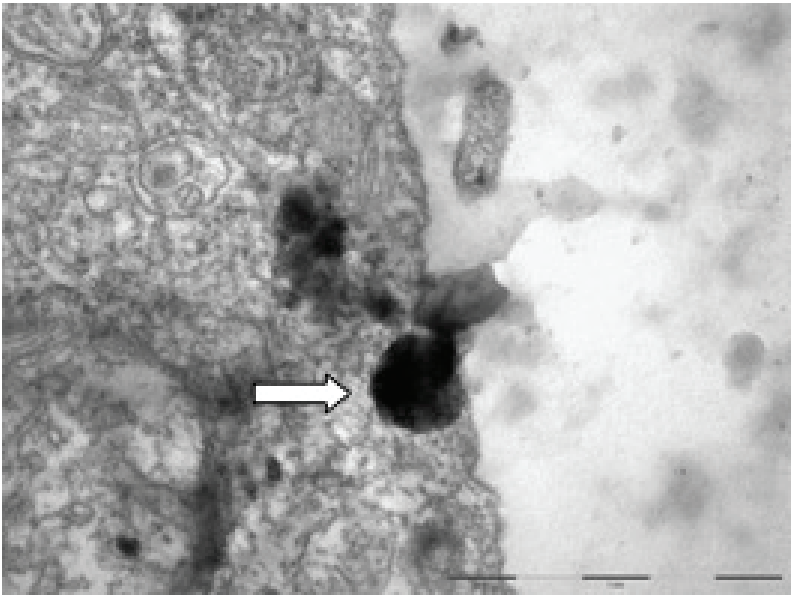

Figure 2. TEM ultramicrograph of U251 cells incubated with NC (5 μg/ml) and irradiated with the blue light (470 nm, 1 W) for 1 min showing NC inside of the cell cytoplasm (arrow); magnification 36000x, scale bar 1 μm.

Polyethylene Glycol Coated Gold Nanoparticles Nerve Tissue Uptake After Spinal Cord Injury

Tamara Martinovic[1], Darko Ciric[1], Tamara Kravic-Stevovic[1], Florentia Papastefanaki[2], Igor Jakovcevski[3,4], Nafsika Poulia[2], Nevena Djogo[3], Florian Schulz[5], Gabrielle Loers[3], Tobias Vossmeyer[5], Horst Weller[5,6], Melitta Schachner[7], Rebecca Matsas[2] and Vladimir Bumbasirevic[1]

[1] *Institute of Histology and Embryology, School of Medicine, University of Belgrade, Visegradska 26, Belgrade 11000, Serbia*
[2] *Laboratory of Cellular and Molecular Neurobiology, Hellenic Pasteur Institute, 127 Vassilissis Sofias Avenue, 11521 Athens, Greece*
[3] *Zentrum für Molekulare Neurobiologie, Universitätsklinikum Hamburg-Eppendorf, Universität Hamburg, Martinistrasse 52, 20246 Hamburg, Germany*
[4] *Experimental Neurophysiology, University Hospital Cologne, Joseph-Stelzmann-Str. 9, 50931 Köln, Germany; German Center for Neurodegenerative Diseases, Ludwig-Erhard-Allee 2, 53175 Bonn, Germany*
[5] *Institut für Physikalische Chemie, Universität Hamburg, Grindelallee 117, 20146 Hamburg, Germany*
[6] *Department of Chemistry, Faculty of Science, King Abdulaziz University, Jeddah, Saudi Arabia*
[7] *Center for Neuroscience, Shantou University Medical College, 22 Xin Ling Road, Shantou, Guandong 515041, People's Republic of China*

Gold nanoparticles (AuNP) are promising candidates for drug delivery in combination with tissue-compatible reagents, such as polyethylene glycol (PEG) [1]. PEG administration in central nervous system injury models have received interest for potential therapy but its low bioavailability prevents clinical application so in this study we used PEGylated 40-nm-AuNPs in order to improve PEG bioavailability [2]. The aim of this study was to analyze cellular internalization of PEGylated AuNP in nervous tissue with the use of transmission electron microscopy (TEM). At early stages after mouse spinal cord injury PEGylated AuNP dispersed in 1µl PBS were injected intraspinally 0.5 mm rostral and caudal to the lesion site, 1 mm deep into the spinal cord. One week after injury, mice were anaesthetized and perfused transcardially with a mixture of 4% paraformaldehyde and 2.5% glutaraldehyde.

Tissue samples were cut at a distance of approximately 1 mm proximal and distal to the center of the lesion, post-fixed in osmium tetroxide, dehydrated and embedded in epon resin. Using a random sampling protocol, ultrathin sections were prepared on a Leica Ultracut UCT microtome, stained with uranyl acetate-lead citrate and examined on a FEI Morgagni 268D transmission electron microscope. Electron-dense particles with an approximate 40-nm diameter size were detected throughout the tissue around the lesion site associated with the plasma membrane or localized intracellularly. We propose that PEG-AuNPs represent a favorable drug-delivery platform with therapeutic potential that could be further enhanced if PEG-AuNPs are used as carriers of regeneration-promoting molecules [3].

References:

[1] F Schulz *et al*, Langmuir **29** (2013), 9897–9908.
[2] I Apostolova, A Irintchev and M Schachner, J Neurosci **26** (2006), 7849–7859.
[3] The authors acknowledge funding from the following grants to R.M.: E.U. FP7 REGPOT NEUROSIGN Project 264083, the Hellenic General Secretariat for Research and Technology Grants SYNERGASIA Noiseplus 09SYN-21-969, the Foundation BNP Paribas, Empeirikion Foundation and the framework action KRIPIS to the Hellenic Pasteur Institute co-funded by the European Regional Development Fund and national resources; and to T.V., H.W., G.L., and M.S. by the Landesexzellenzinitiative (LEXI) of Hamburg Nanotechnology in Medicine (NAME).

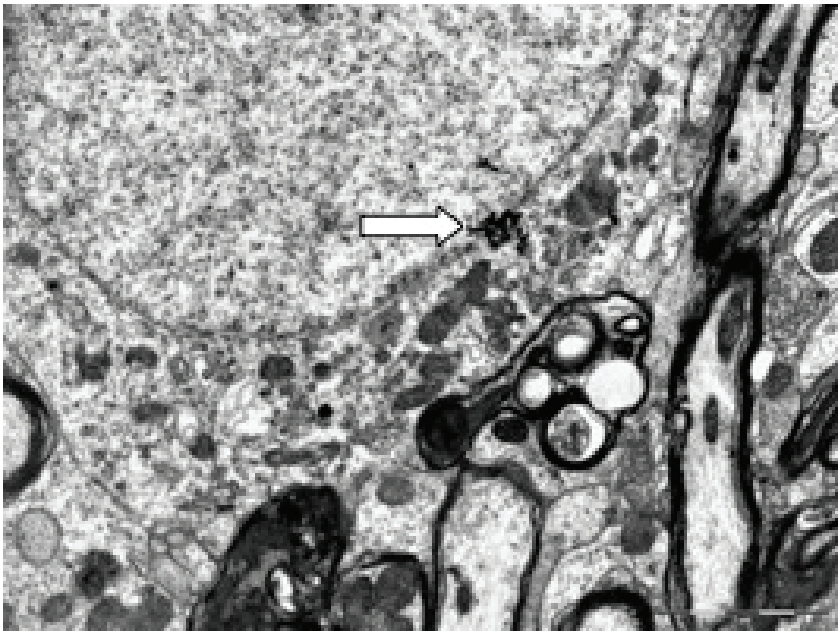

Figure 1. TEM ultramicrograph of a neuron with 40 nm AuNPs observed on nuclear membrane (arrow); magnification 8900x, scale bar 2 μm.

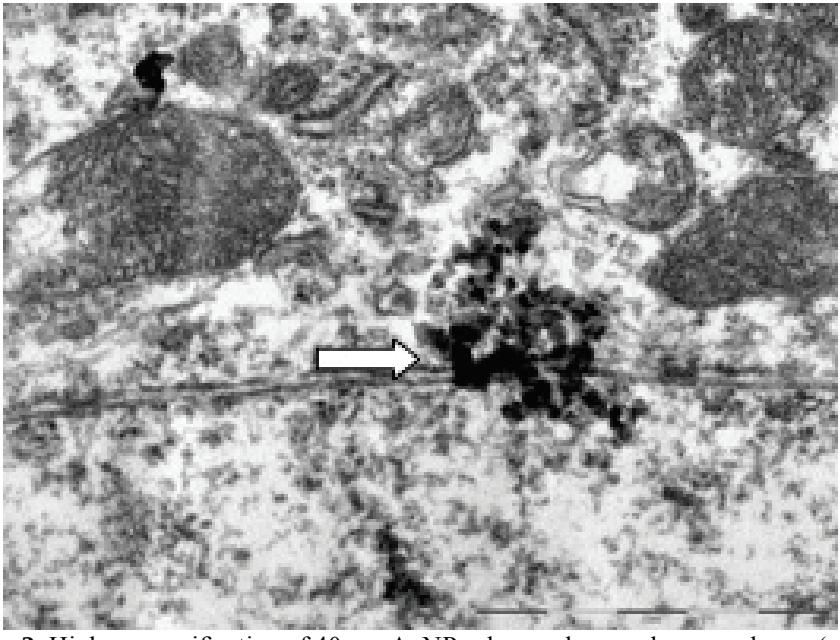

Figure 2. Higher magnification of 40 nm AuNPs observed on nuclear membrane (arrow); magnification 36000x, scale bar 1 μm.

Ultrastructural Analysis of Large Graphene Quantum Dots Internalization in Hepatocytes

Darko Ciric[1], Tamara Martinovic[1], Tamara Kravic-Stevovic[1], Vladislav Volarevic[2], Verica Paunovic[3], Zoran Markovic[4], Bojana Simovic Markovic[2], Maja Misirkic-Marjanovic[3,5], Biljana Todorovic-Markovic[4], Sanja Bojic[2], Ljubica Vucicevic[3,5], Svetlana Jovanovic[4], Nebojsa Arsenijevic[2], Ivanka Holclajtner-Antunovic[6], Momir Milosavljevic[4], Miroslav Dramicanin[4], Miodrag L. Lukic[2], Vladimir Trajkovic[3] and Vladimir Bumbasirevic[1]

[1] *Institute of Histology and Embryology, School of Medicine, University of Belgrade, Visegradska 26, Belgrade 11000, Serbia*
[2] *Centre for Molecular Medicine and Stem Cell Research, Faculty of Medical Sciences, University of Kragujevac, 69 Svetozara Markovica St., 34000 Kragujevac, Serbia*
[3] *Institute of Microbiology and Immunology, School of Medicine, University of Belgrade, Dr Subotica 1, Belgrade 11000, Serbia*
[4] *Vinca Institute of Nuclear Sciences, University of Belgrade, P.O. Box 522, Mike Petrovica Alasa 12-14, Belgrade 11001, Serbia*
[5] *Institute for Biological Research "Sinisa Stankovic", University of Belgrade, Despot Stefan Blvd. 142, Belgrade 11000, Serbia*
[6] *Faculty of Physical Chemistry, University of Belgrade, Studentski trg 12-16, 11000 Belgrade, Serbia*

Graphene, carbon allotrope consisting of a single layer of carbon atoms in a honeycomb structure, has gained considerable attention in nanomedicine as a potential diagnostic and therapeutic tool [1]. Graphene quantum dots (GQD) are graphene sheets with lateral dimensions less than 100 nm, containing one or more graphene layers [2]. Large nanoparticles are mainly eliminated through liver, either by hepatocytes via the biliary system, or by phagocytic Kupffer cells, while smaller nanoparticles are more likely to be excreted in urine, thus enabling fast elimination from the body and preventing excessive accumulation in organs and tissues [3]. Furthermore, the use of large nanoparticles is preferable in treatment of inflamed tissues, which generally present with leaky blood vessels that, as opposed to the vasculature in healthy tissues, allowing selective extravasation of nanomaterials with sizes of up to 400

nm [4]. We investigated the effect of large (40 nm) graphene quantum dots (GQD) *in vitro* in liver cells, macrophages and in lymphocytes using HepG2 hepatocytes, J774 macrophages and Jurkat T cells. Cell cultures were incubated overnight in cell culture medium, and then treated with GQD (100 μg/ml). After 1 h, cells were fixed with 3% glutaraldehyde in cacodylate buffer, postfixed in 1% osmium tetroxide, dehydrated in graded alcohols, and then embedded in Epon812. The ultrathin sections were stained in uranyl acetate and lead citrate, and were examined using a Morgagni 268D electron microscope (FEI, Hillsboro, OR). Large graphene dots were seen in cytoplasm of all the examined cells as electron dense particles with diameter of 20-70 nm. Electron microscopic detection of cellular uptake of large graphene dots by hepatocytes, macrophages and lymphocytes could give reason for the use of large graphene dots in inflammatory disease of liver [5].

References:

[1] D Bitounis *et al*, Adv Mater **25** (2013), 2258–226.
[2] LA Ponomarenko *et al*, Science **320** (2008), 356–358.
[3] M Longmire *et al*, Nanomedicine **3** (2008), 703–717.
[4] LY Rizzo *et al*, Curr. Opin. Biotechnol **24** (2013), 1159–1166.
[5] The authors acknowledge funding from the Ministry of Education, Science and Technological Development of the Republic of Serbia (grants 41025, 175069, 175103, 172003, and 173053) and MP01/12 from the Faculty of Medical Sciences University of Kragujevac, Serbia.

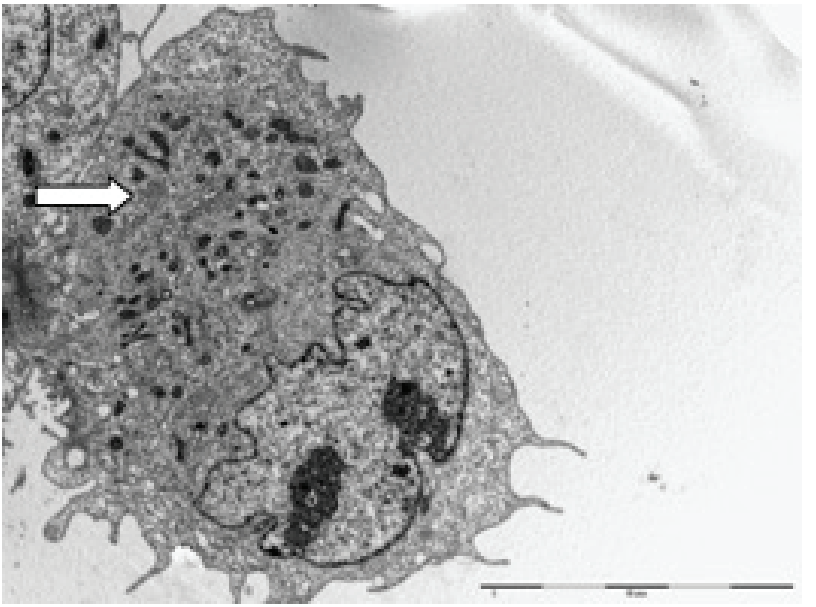

Figure 1. TEM ultramicrograph of HepG2 cell treated with GQD; arrow point at GQD present in intracellular vesicle (diameter 20-70 nm); magnification 3500x, scale bar 10 μm.

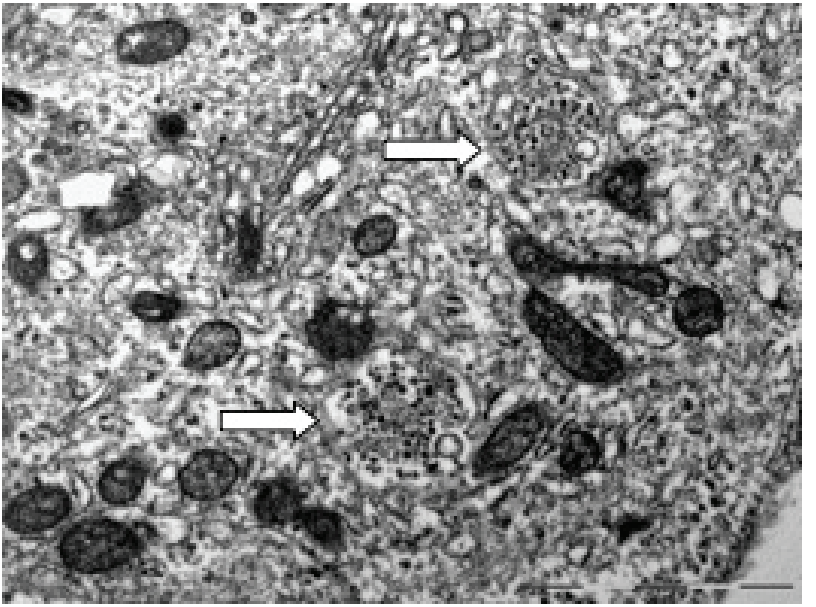

Figure 2. TEM image of the HepG2 cell cytoplasm with GQD present in intracellular vesicle (arrow); magnification 18000x, scale bar 2 μm.

AUTHOR INDEX

Jakovcevski, Igor	igor.jakovcevski@enp.org	269
Janaćković, Đorđe	nht@tmf.bg.ac.rs	174, 237, 246
Janković, Ana		225, 240
Janković-Častvan, Ivona	icastvan@tmf.bg.ac.rs	198, 246
Jannis, Daen	daen.jannis@uantwerpen.be	16
Jelić, Dijana		216
Jerič, Marja	marja.jeric@ijs.si	44
Jordanov, Dragana	djordano@vin.bg.ac.rs	99, 192
Jovanović, Svetlana		272
Jovanović, Vladislava M.	Vlad@tmf.bg.ac.rs	101
Jović, Vladimir D.	vladajovic@imsi.bg.ac.rs	87
Jugović, Dragana	dragana.jugovic@itn.sanu.ac.rs	154
Juraić, Krunoslav	Krunoslav.Juraic@irb.hr	140
Jäger, Wolfgang	wj@tf.uni-kiel.de	61
Kaiser, Ute	ute.kaiser@uni-ulm.de	119
Kaplan, Wayne D.	kaplan@technion.ac.il	24
Kašiković, Nemanja	knemanja@uns.ac.rs	131
Kauppinen, Esko	esko.kauppinen@aalto.fi	90
Kisielowski, Christian	cfkisielowski@lbl.gov	10
Kisić, Danilo D.	dankisic@vin.bg.ac.rs	183
Kljajević, Ljiljana	ljiljana@vin.bg.ac.rs	204
Koblar, Maja	maja.koblar@ijs.si	228
Kocen, Matej	matej.kocen@ijs.si	166
Koh, Ai Leen	alkoh@stanford.edu	27
Kojić, Vesna		225, 237
Komelj, Matej	matej.komelj@ijs.si	113
Kosić, Milica		266
Kostić, Bojan		207
Košir, Mateja		44
Kotakoski, Jani	jani.kotakoski@univie.ac.at	75, 90, 107, 119
Kothleitner, Gerald	gerald.kothleitner@felmi-zfe.at	50
Kovačević, Lazar		213
Knez, Daniel	daniel.knez@felmi-zfe.at	50
Kravić-Stevović, Tamara	tamara.kravic-stevovic@med.bg.ac.rs	266, 269, 272

Vučetić, Snežana	snezanap@uns.ac.rs	243
Vučićević, Ljubica	ljubicavucicevic@hotmail.com	272
Vukašinović, Jelena	jelenavukasinovic03@gmail.com	166
Vukašinović-Sekulić, Maja	vukasinovic@tmf.bg.ac.rs	225, 240
Vukmirović, Jelena	jelenavukmirovic1@gmail.com	168
Vuković, Marina	marinav@chem.bg.ac.rs	195
Vulić, Predrag	predrag.vulic@rgf.bg.ac.rs	171
Wang, Yunzhi	wang.363@osu.edu	58
Weller, Horst	horst.weller@chemie.uni-hamburg.de	269
Westermark, Gunilla T.	gunilla.westermark@mcb.uu.se	255
Willinger, Marc G.	marc.willinger@scopem.ethz.ch	140
Wolf, Daniel	Daniel.Wolf@triebenberg.de	3
Wu, Haijun	wu.haijun@u.nus.edu	35
Xie, Ling	ling.xie@angstrom.uu.se	255
Zabinski, Piotr	zabinski@agh.edu.pl	101, 177
Zagorac, Dejan	dzagorac@vin.bg.ac.rs	99, 192
Zagorac, Jelena	jelena@vin.bg.ac.rs	99, 192
Zarubica, Aleksandra	zarubica2000@yahoo.com	192
Zdravković, Jelena	jtanasijevic@tmf.bg.ac.rs	148
Zeković, Ivana	ivanazekovic@gmail.com	171
Zhao, Xiaoxu	xiaoxu_zhao@u.nus.edu	35
Zheng, Fengshan	f.zheng@fz-juelich.de	7
Zheng, Yufeng	zheng.510@osu.edu	58
Žak, Tomaš	zak@ipm.cz	219
Žužek Rožman, Kristina	Tina.Zuzek@ijs.si	228

ACKNOWLEDGEMENTS

DIAMOND SPONSOR

ThermoFisher SCIENTIFIC

GOLD SPONSORS

Innovation Center of the Faculty of Technology and Metallurgy, University of Belgrade

SCAN LLC / JEOL Ltd

NanoMEGAS

SILVER SPONSORS

Ministry of Education, Science and Technological Development of the Republic of Serbia

Institute of Testing of Materials (IMS

Institute of Nuclear Sciences Vinča, University of Belgrade

NHBG-Žiks Hard LLC

Analysis LLC

ELMINA2018 Conference acknowledges Coca-Cola HBC and Mikrolux LLC for their support.

MEDIA SUPPORT

European Microscopy Society (EMS)

Federation of European Materials Societies (FEMS)

Imaging & Microscopy Journal

CIP - Каталогизација у публикацији
Народна библиотека Србије, Београд

66.017/.018(048)
544.2(048)
621.385.833.2(048)

INTERNATIONAL Conference on Electron Microscopy of Nanostructures ELMINA (1 ; 2018 ; Beograd)
Program ; & Book of Abstracts / First International Conference on Electron Microscopy of Nanostructures ELMINA 2018, August 27-29, 2018, Belgrade, Serbia = Прва међународна конференција о електронској микроскопији наноструктура ELMINA 2018, 27-29 август 2018. Београд, Србија ; [organized by Serbian Academy of Sciences and Arts and Faculty of Technology and Metallurgy, University of Belgrade ; editor Velimir R. Radmilović and Vuk V. Radmilović]. - Belgrade : SASA, 2018 (Belgrade : SASA). - XXIX, 289 str. : ilustr. ; 24 cm

Na nasl. str.: European Microscopy Society and Federation of European Materials Societies. - Tiraž 50. - Bibliografija uz svaki apstrakt. - Registar.

ISBN 978-86-7025-785-6
a) Наука о материјалима - Апстракти b) Нанотехнологија - Апстракти
c) Електронска микроскопија - Апстракти
COBISS.SR-ID 266767116


210
UNIVERSITY
OF BELGRADE
1808-2018